Universidade Federal do Rio Grande – FURG

Instituto de Oceanografia

Programa de Pós-Graduação em Oceanologia

Processos Hidro-Sedimentares na Plataforma Interna sob Influência de Molhes: caso da desembocadura da Lagoa dos Patos

GUILHERME DE OLIVEIRA CRUZ

Tese apresentada ao Programa de Pós-Graduação em Oceanologia, como parte dos requisitos para a obtenção do Título de Doutor.

Orientador: *Prof. Dr. Carlos Augusto França Schettini*

Universidade Federal do Rio Grande (FURG), Brasil

Rio Grande, RS, Brasil

Abril, 2025

Processos Hidro-Sedimentares na Plataforma Interna sob Influência de Molhes: caso da desembocadura da Lagoa dos Patos

Tese apresentada ao PPGO, como parte dos requisitos para a obtenção do Título de Doutor.

por

GUILHERME DE OLIVEIRA CRUZ

Rio Grande, RS, Brasil

Abril, 2025

© A cópia parcial e a citação de trechos desta tese são permitidas sobre a condição de que qualquer pessoa que a consulte reconheça os direitos autorais do autor. Nenhuma informação derivada direta ou indiretamente desta obra deve ser publicada sem o consentimento prévio e por escrito do autor

C957p Cruz, Guilherme de Oliveira

Processos hidro-sedimentares na plataforma interna sob influência de molhes: caso da desembocadura da Lagoa dos Patos / Guilherme de Oliveira Cruz. – 2025. 213 f.

Tese (Doutorado) – Universidade Federal do Rio Grande – Programa de Pós-Graduação em Oceanologia, 2025.

Orientador: Dr. Carlos Augusto França Schettini.

1. Oceanologia. 2. Dinâmica hidro-sedimentar. 3. Intervenção antrópica 4. Plataforma continental. 5.
Sedimentos coesivos. I. Schettini, Carlos Augusto França. II. Título.

CDU 551.46

Catalogação na fonte: Bibliotecário Clériston Ribeiro Ramos CRB10/1889

Ata da defesa

UNIVERSIDADE FEDERAL DO RIO GRANDE - FURG
IO – INSTITUTO DE OCEANOGRAFIA
PROGRAMA DE PÓS-GRADUAÇÃ0 EM OCEANOLOGIA
E-mail: ccpofqg@furg.br – home-page: www.ppgo.furg.br

ATA ESPECIAL DE DEFESA DE TESE DE DOUTORADO – 04/2025

Às quatorze horas do dia vinte e oito de agosto do ano dois mil e vinte e cinco, por Video conferencia: https://meet.google.com/wnh-vrri-iih, Presencial: Sala 5105 – Pav. 5 –FURG/ CARREIROS, reuniu-se a Comissão Examinadora da Tese de **DOUTORADO** intitulada: **"PROCESSOS HIDRO-SEDIMENTARES NA PLATAFORMA INTERNA SOB INFLUÊNCIA DE MOLHES: CASO DA DESEMBOCADURA DA LAGOA DOS PATOS"**, do **Acad. GUILHERME DE OLIVEIRA CRUZ.** A Comissão Examinadora foi composta pelos seguintes membros: Prof. Dr. Carlos Augusto França Schettini - Orientador – (PPGO/IO/FURG); Profa. Dra. Elisa Helena Leão Fernandes - (PPGO-IO/FURG); Prof. Dr. Elirio Ernestino Toldo Jr. - (UFRGS) e Prof. Dr. Mauricio Noermberg – (UFPR). Dando início à reunião, a Coordenadora do PPGO, Profa. Dra. Grasiela Lopes Leães Pinho, agradeceu a presença de todos e fez a apresentação da Comissão Examinadora. Logo após esclareceu que o candidato teria um tempo de 45 a 60 min para explanação do tema, e cada membro da Comissão Examinadora, um tempo máximo de 30 min para perguntas. A seguir, passou à palavra ao candidato que apresentou o tema e respondeu às perguntas formuladas. Após ampla explanação, a Comissão Examinadora reuniu-se em reservado para discussão do conceito a ser atribuído ao candidato. Foi estabelecido que as sugestões de todos os membros da Comissão Examinadora, que seguem em pareceres em anexo, foram aceitas pela Orientadora/Candidato para incorporação na versão final da Tese. Finalmente, a Comissão Examinadora considerou o candidato **APROVADO**, por unanimidade. Nada mais havendo a tratar, foi lavrada a presente ATA, por mim, Clabisnei Moura de Melo – Secretário PPGO, que após lida e aprovada, será assinada pela Comissão Examinadora, pelo Candidato e pela Coordenadora do Programa de Pós-Graduação em Oceanologia

gov.br Documento assinado digitalmente
CARLOS AUGUSTO FRANCA SCHETTINI
Data: 29/08/2025 13:08:06-0300
Verifique em https://validar.iti.gov.br

Prof. Dr. Carlos Augusto França Schettini
Orientador

Elisa Helena Leao Fernandes: 67085148004-03'00' 2025.09.01 08:22:45

Profa. Dra. Elisa Helena L. Fernandes

gov.br Documento assinado digitalmente
ELIRIO ERNESTINO TOLDO JUNIOR
Data: 01/09/2025 10:29:05-0300
Verifique em https://validar.iti.gov.br

Prof. Dr. Elirio Ernestino Toldo Jr.

gov.br Documento assinado digitalmente
MAURICIO ALMEIDA NOERMBERG
Data: 01/09/2025 09:24:21-0300
Verifique em https://validar.iti.gov.br

Prof. Dr. Mauricio Noermberg

Acad. Guilherme de Oliveira Cruz

Profª. Drª Grasiela Lopes Leães Pinho
Coordenadora PPGO

O anegrito da alma

“Até você se tornar consciente, o inconsciente dirigirá sua vida e você o chamará de destino.” - Carl Jung

Índice

ÍNDICE VI

LISTA DE FIGURA VIII

LISTA DE TABELAS XV

LISTA DE ACRÔNIMOS/ABREVIAÇÕES XVII

LISTA DE SÍMBOLOS XVIII

RESUMO XIX

ABSTRACT XX

CAPÍTULO I: INTRODUÇÃO 21

1.1 ÁREA DE ESTUDO 24

2.1 ESTRUTURA DA TESE 27

OBJETIVOS 28

HIPÓTESE 29

CAPÍTULO II: THE DYNAMICS OF THE INNER-SHELF SUSPENDED SEDIMENTS BASED ON ADCP RECORDS AND ROUSE THEORY 30

3.1 ABSTRACT 30

4.1 INTRODUCTION 31

5.1 STUDY AREA 35

6.1 MATERIAL AND METHODS 40

7.1 RESULTS 49

8.1 DISCUSSION 62

9.1 CONCLUSION 71

10.1 ACKNOWLEDGEMENTS 72

CAPÍTULO III: HYDRODYNAMICS OF AN INNER SHELF SHELTERED BY LONG JETTIES 73

1.1 ABSTRACT 73

2.1 INTRODUCTION 74

3.1 STUDY AREA 77

4.1 MATERIALS AND METHODS 81

5.1 RESULTS 88

6.1 DISCUSSION 104

7.1 CONCLUSION 109

8.1 ACKNOWLEDGMENTS 110

CAPÍTULO IV: CIRCULATION AND WATER PROPERTIES IN THE LEEWARD OF LONG JETTIES: THE RIO GRANDE BAR, RS, BRAZIL 111

1.1 ABSTRACT 111

2.1 INTRODUCTION 112

3.1 STUDY AREA 114

4.1 MATERIALS AND METHODS 118

5.1 RESULTS 122

6.1 DISCUSSION 140

7.1 CONCLUSION 143

CAPÍTULO V: SÍNTESE DAS CONCLUSÕES 144

CAPÍTULO VI: REFERÊNCIAS 148

ALGORITMOS E DADOS UTILIZADOS 169

APÊNDICE A 178

APÊNDICE B 195

Lista de Figura

Figure 1 – Cap I. Localização da área de estudo. Em (b) mostra a extensão da plataforma continental com indicação da linha batimétrica. Em (c) a localização do banco de lama extraída de Calliari et al. (2007). Em (d) imagem de satélite do sentinel 2 adquirida no dia 24 de Abril de 2023, mostrando a localização sob condições de vento vindo de nordeste. 27

Figure 1 – Cap II. Location of the study area. The larger panel shows the situation of the continental shelf on a smaller scale with indication of bathymetric lines, and in detail presents the location of the ADCP mooring and buoys RS4 and RS5. The location of the mud bank was extracted from Calliari et al. (2007). The location of the sandy banks was obtained from navy nautical charts. 36

Figure 2 – Cap II. Monthly frequency distribution of wind velocity for the alongshelf and cross-shelf components based on observational data recorded at buoys RS4 (Feb/2019 to Apr/2021) and RS5 (Dec/2016 to Mar/2023). The median value is represented by the black line, and the shades of blue represent the range of percentiles 1-99, 5-95, and 25-75%. The vertical red line in the month of October represents the data observed during mooring from September 17th to November 2nd, 2020 (45 days). 38

Figure 3 – Cap II. Time series of (a) longitudinal and (b) transverse wind velocities, (c) sea level oscillation, average water column velocity (d) longitudinal and (e) transverse, (f) wave height, (g) wave period, and (h) wave propagation direction. 52

Figure 4 – Cap II. Duration curve and frequency distributions of the time series presented in Figure 3 for (a, b) longitudinal and (c, d) transverse wind speed, (e, f) longitudinal and (g, h) transverse current speed, (i, j) wave height, (k, l) wave period, and (m, n) wave

propagation direction. The blue lines represent the observed data during the ADCP mooring, and the orange lines represent the historical data series. 53

Figure 5 – Cap II. Monthly climatology of the alongshore (a) and cross-shore (b) components of the mean water column current, and of the wave height (c), direction (d), and period (e). The median value is represented by the black line, and the shades of blue represent the range of percentiles 1-99, 5-95, and 25-75%. The vertical red line in the month of October represents the data observed during mooring. 56

Figure 6 – Cap II. (a) Temporal indication of accepted and rejected vertical SSC profiles from the validation procedure. The profiles for each criterion are presented with vertical bars, and the points on the bars for the exclusion criteria indicate the overlap with the other criterion. (b) Frequency distributions of mean SSC for each selection category, and (c) relationship between shear stress and mean SSC for each selection category. 57

Figure 7 – Cap II. The left-hand side graphs display the time series of (a) bottom shear stress produced by waves (fuchsia), currents (red), mean wave-current combined (blue) and maximum wave-current combined (green), (b) turbulent diffusion coefficient, (c) root mean square percentage error - RMSPE, (d) sediment size, and (e) particle terminal velocity in suspension. On the right-hand side of each panel, the respective (f, g, h, i, and j) frequency distributions for each parameter from the first column are presented. Valid profile data are shown in blue, and discarded profiles are shown in gray. The frequency distributions are only for valid data. 59

Figure 8 – Cap II. (a) Time series of mean water column SSC obtained from ABS and Rouse model, and (b) the respective relationship between them. (c) and (d) Hovmöller diagrams for SSC distributions derived from ABS and Rouse, respectively. The gray areas in (d) indicates the discarded profiles. 61

Figure 9 – Cap II. Hovmöller plot of longitudinal and transversal velocity along the water column. In (a), red colors indicate currents with northward direction, and blue indicates southward direction. In (b) and (c), red colors indicate currents directed towards the coast, and blue indicates currents directed towards the open ocean. 68

Figure 10 – Cap II. Plots (a, b, c, d, e) show the calculated duration curve for period 1, plots (f, g, h, i, j) for period 2, and plots (k, l, m, n, o) for period 3. In black, the median, and shades of brown and blue indicate the percentiles 1%, 20%, 35%, 65%, 80%, and 99%. T.AS represents alongshelf sediment transport and T.CS represents cross-shelf sediment transport. 69

Figure 1 – Cap III. Location of the anchored ADCPs (#1, #2, #3, #4, and #O), CTD profile collection trajectories (#T1, #T2, #T3, #T4, and #L), the size of the analyzed EOF area, and the location of the cities of Torres, Chuí, and Lagoa dos Patos. The bathymetric contours were obtained from the Brazilian Navy nautical charts. 81

Figure 2 – Cap III. Results of the empirical orthogonal functions (EOFs) analysis. The variance of each EOF is displayed in each graph, along with the average wind direction. The color shades represent the wind magnitude. 89

Figure 3 – Cap III. Monthly frequency distribution of periods of continuous NE wind events, with the median in black and the 1st, 5th, 25th, 50th, 75th, 95th, and 99th percentiles in blue. In (a) and (c), the duration and magnitude of NE wind events when the wind speed exceeds 0 m/s. In (b) and (d), the duration and magnitude of NE wind events when the wind speed exceeds 8 m/s. 91

Figure 4 – Cap III. Time series of average along shelf (a) and cross-shelf current velocities (b) estimated from ADCP data moored at a depth of 20 m. The red lines in (b) indicate the events where the average longitudinal and cross-shelf velocities were negative (onshore). 92

Figure 5 – Cap III. Potential lagrangean displacement of the bottom water layer located 0.9 m above the seabed, with a cell size of 50 cm. Estimated from ADCP data moored at a depth of 20 m and during events where the average longitudinal and cross-shelf velocities were negative. 94

Figure 6 – Cap III. The alongshelf wind component obtained from the RS5 buoy (in blue) and the cross-shelf current intensity index (in red) estimated from ADCP data moored at a depth of 20 m and the longitudinal wind obtained from the RS5 buoy. 95

Figure 7 – Cap III. Results numerical simulation with constant wind speeds of 5 and 10 m/s at 243º, respectively. The black lines represent streamlines and colors indicate current magnitude. The red line shows the average alongshelf velocity of 0 m/s in (a) and (b), and cross-shelf velocity of 0 m/s in (c) and (d). 96

Figure 8 – Cap III. (a) potential Lagrangian displacement of the near bottom (solid lines) and the near surface (dashed lines). (b) and (c) distributions of current vectors of near bottom (b) and near-surface (c). The circles representing a scale of 0.5 m/s. 97

Figure 9 – Cap III. Panels (a) and (f) present the salinity and SSC distribution graphs for the longitudinal section (#L, Figure 1). Panels (b), (c), (d), and (e) show the salinity distributions, while panels (g), (h), (i), and (j) show the SSC distributions for the cross-shelf sections #T1, #T2, #T3, and #T4, respectively. 100

Figure 10 – Cap III. Top panels (a) and (f) show the alongshelf and cross-shelf wind speeds, respectively. Panels (b), (c), (d), and (e) present the Hovmoller diagrams of alongshelf current speed, with red colors indicating westwards currents (away from the jetties) and blue colors indicating eastwards currents. Panels (g), (h), (i), and (j) present the Hovmoller diagrams of cross-shelf current speed. Red colors indicating seawards currents and blue colors indicating landwards currents. 102

Figure 11 – Cap III. Vertical variation of the alongshelf (panels (a), (b), (c), and (d)) and cross-shelf (panels (e), (f), (g), and (h)) current speed. The median is shown in black, and the percentiles of 1, 5, 25, 50, 75, 95, and 99% are shown in blue shades. Panels (i), (j), (k), and (l) present the density profiles closest to the mooring sites, and panels (m), (n), (o), and (p) show the Richardson number, with the dashed line indicating the 0.25 Ri threshold. 103

Figure 12 – Cap III. Cartoons of alongshelf flow at the sheltered area of the Patos Lagoon jetties, driven by a constant alongshelf wind, (a) without and (b) with low salinity water flow through the jetties. Black arrows represent the longitudinal current gradient. The wavy black arrow represents the permeability of the jetties allowing the inflow of brackish water south of the jetty. 107

Figure 13 – Cap III. Diagram illustrating the spatial variability of vortices formed in the shadow zone of the jetty at Lagoa dos Patos. The longitudinal component along the water column, both inside and outside the jetty's influence zone, is represented by blue and red arrows, which also indicate the cross-shelf current component. The thick red arrow represents the surface current moving southward. 108

Figure 1 – Cap IV. Location of the anchored ADCPs (#1, #2, #3, #4), CTD profile collection trajectories (#T1, #T2, #T3, #T4, and #L), and SimCosta Buoys (RS2, RS4 and RS5). The bathymetric contours were obtained from the Brazilian Navy nautical charts. 117

Figure 2 – Cap IV. Time series of alongshore current velocity for the four ADCP measurement points (#1, #2, #3, #4). The solid lines represent the uppermost layer measured by the ADCP, while the dashed lines indicate the bottommost layer. 123

Figure 3 – Cap IV. (a) and (b): vertical profiles of alongshore and cross-shore current components, respectively. The median value is shown by the black line, while the 1st, 5th,

25th, 75th, 95th, and 99th percentiles are displayed through blue shades. The depth at each point and the distance between them are proportional to actual field measurements. (c) Vertical profiles of density (blue) and Richardson number (red) calculated for the same period as the density profile. The red dashed line indicates the 0.25 Ri threshold. 124

Figure 4 – Cap IV. Longitudinal (#L) and transverse (#T1, #T2, #T3, and #T4) sectional distributions of temperature, salinity, suspended sediment concentration (SSC), chlorophyll-a (Chl), and dissolved oxygen (DO) saturation. In the first column plots, the white dashed contour (18°C) indicates the approximate thermocline boundary. In the second column plots, the white contour (28 g kg^{-1}) marks the approximate halocline boundary. In the fifth column plots, the white dashed contour (45%) delineates regions where hypoxic conditions are favorable. 128

Figure 5 – Cap IV. Spatial distribution of temperature, salinity, suspended sediment concentration (SSC), chlorophyll-a (Chl-a), and dissolved oxygen (DO), calculated from data collected in the transverse and longitudinal sections. The first column plots (a-e) show the mean distribution for the upper 2 m water column, while the second column plots (f-j) display the mean distribution from 1 m above the seabed. The white 18°C contour in (a) and 28 g kg^{-1} contour in (b) mark the approximate thermocline and halocline positions, respectively. The white 45% contour in (j) identifies the region prone to hypoxic conditions. 131

Figure 6 – Cap IV. Sentinel-2 satellite image acquired on 2 of November of 2023. The yellow vectors indicate wind direction and intensity. The scale in the lower right corner represents 2 km (spatial reference) and 4 m/s (wind intensity reference). 133

Figure 7 – Cap IV. Sentinel-2 satellite image acquired on 20 of November of 2020. The yellow vectors indicate wind direction and intensity. The scale in the lower right corner represents 2 km (spatial reference) and 4 m/s (wind intensity reference). 135

Figure 8 – Cap IV. Sentinel-2 satellite image acquired on 20 of March of 2021. The yellow vectors indicate wind direction and intensity. The scale in the lower right corner represents 2 km (spatial reference) and 4 m/s (wind intensity reference). 136

Figure 9 – Cap IV. Sentinel-2 satellite image acquired on 24 of April of 2022. The yellow vectors show wind direction and intensity. The scale in the lower right corner represents 2 km (spatial reference) and 4 m/s (wind intensity reference). 137

Figure 10 – Cap IV. Sentinel-2 satellite image acquired on 22 of April of 2023. The yellow vectors display wind direction and intensity. The scale in the lower right corner represents 2 km (spatial reference) and 4 m/s (wind intensity reference). 138

Figure 11 – Cap IV. Sentinel-2 satellite image acquired on 7 of March of 2024, showing water percolation through the jetties into the western jetty's shadow zone. The scale in the lower right corner represents 2 km (spatial reference) and 4 m/s (wind intensity reference). 139

Lista de Tabelas

Table 1 – Cap II. Median and percentile values for the observed data during the ADCP mooring (M) and for the long-term records from the buoys (LT), for alongshore and cross-shore components of wind and currents, and wave parameters. 54

Table 2 – Cap II: Summary of the validation results for vertical SSC profiles, including the total number of profiles and the remaining profiles after selection by the criteria of shear stress (τmwc < 0.05) and positive vertical mean SSC gradient ($dCzdz$ > 0), also indicating the percentage, mean, and maximum SSC for each subset (SSC and C(z) are in kg/m³ and τmwc is in Pa). 58

Table 3 – Cap II. Mean values, standard deviation (σ), and percentiles of shear stress data, turbulent diffusion, RMSPE, sediment size, and particle terminal velocity. 60

Table 4 – Cap II. Oceanographic parameters for periods 1, 2, and 3 as indicated in Figure 10. WL represents the sea level oscillation in meters. U and V denote the mean or maximum longitudinal and transverse velocities, respectively (m/s). τ represents the mean or maximum bottom shear stress produced by waves and currents (Pa). ws is the terminal particle velocity (cm/s), and ds is the mean particle size (μm). 66

Table 1 – Cap III. Selected periods from the time series obtained by the ADCP at point #O, with the respective displacement values (L) along the E/W or N/S axis, and the normalized potential Lagrangian displacement (L) by the event duration. 92

Table 2 – Cap III. Potential Lagrangian displacement (L) in the E/W or N/S axis, and the potential Lagrangian displacement normalized by the duration of the event (L) for ADCPs #1, #2, #3, and #4. 98

Table 1 – Cap IV. Summary of selected periods from Sentinel-2 satellite imagery, with corresponding atmospheric conditions obtained from the ERA5 reanalysis model and

RS4-5 buoys of the SimCosta (SC) project. Current conditions were derived from ADCP data of the SimCosta project's RS2 buoy. Satellite image acquisition time was 13:20 for all dates. 132

Lista de Acrônimos/Abreviações

A

ABS: Acoustic Backscatter Strength

ADCP: Acoustic Doppler Current Profiler

ASAS: Anticiclone Subtropical do Atlântico Sul

C

CAPES**:** Coordenação de Aperfeiçoamento de Pessoal de Nível Superior

Chl-a**:** Clorofila-a

CNPq**:** Conselho Nacional de Desenvolvimento Científico e Tecnológico

CTD: Conductivity, Temperature, Depth.

D

DO: Dissolved Oxygen

E

EOF: Empirical Orthogonal Function

ERA5: Reanálise climática do Copernicus Climate Change Service

F

FLOW: Módulo hidrodinâmico do software Delft3D

FURG: Universidade Federal do Rio Grande

L

LISST: Laser In-Situ Scattering and Transmissometry

N

NTU: Nephelometric Turbidity Unit

O

OBS: Optical Backscatter Sensor

ONR: Office of Naval Research

P

PCA: Principal Component Analysis

PPGO: Programa de Pós-Graduação em Oceanologia

R

Ri: Richardson Number

RMSE: Root Mean Square Error

RMSPE: Root Mean Square Percentage Error

S

SSC: Suspended Sediment Concentratio

Lista de Símbolos

d_{50}	Tamanho médio do floco (m)
d_s	Diâmetro médio do floco (m)
T_n	Período de escala natural
T	Período de onda (s)
h	Profundidade da água (m)
H	Altura de onda (m)
ρ	Densidade da água (Kg/m^3)
g	Gravidade (m^2/s)
ν	Viscosidade cinemática da água (m^2/s)
z_0	Rugosidade de fundo (m)
Re_c	Número de Reynolds para corrente
Re_w	Número de Reynolds para onda
A	Amplitude Orbital do movimento de onda
C_D	Coeficiente de arrasto para vel. Integrada na profundidade
C_{Dm}, C_{Dmax}	Coeficiente de arrasto médio e máximo para o ciclo ondulatório
f_{wr}	Fator de atrito de onda para fundo rugoso
f_{ws}	Fator de atrito de onda para fundo liso
ϕ	Diferença angular entre a direção de onda e corrente
δ	Espessura da camada limite de onda
κ	Constante de Von Karman's (0.41)
a_r, a_s	Coeficiente que prescrevem δ para fluxo turbulento ou suave
u_{*e}	Velocidade de atrito efetiva
$\overline{U}$	Vel. Média integrada na profundidade
U_w	Velocidade orbital de onda (m/s)
τ_m, τ_{max}	Tensão de cisalhamento de fundo médio e máximo (Nm^{-2})
τ_w	Amplitude oscilatória de tensão de cisalhamento de fundo devido às ondas.
u_*	Velocidade de cisalhamento do fluxo (m/s)
ε_s	Coeficiente de difusão turbulenta
C	Concentração (kg/m^3)

Resumo

Este estudo tem como objetivo geral investigar os processos hidrodinâmicos e da dinâmica sedimentar na plataforma interna, tendo como área de observação a plataforma continental do Rio Grande do Sul, Brasil, e na área influenciada pela foz da Lagoa dos Patos. A primeira parte inicia com a análise da dinâmica de sedimentos em suspensão na plataforma interna adjacente à desembocadura da Lagos dos Patos, onde foram utilizados dados de um ADCP e modelagem teórica pela Teoria de Rouse, demonstrando que as trocas com o fundo são a principal fonte de sedimentos em suspensão, com papel secundário da advecção horizontal. Em seguida, os padrões hidrodinâmicos na zona de sombra criada pelos molhes durante um evento de vento intenso de NE foi investigado, identificando a formação de dois vórtices de rotações opostas e destacando a importância da percolação de água através dos molhes na estratificação e intensificação dos gradientes verticais de velocidade sobre essa zona de sombra. Por último, analisa a variabilidade espacial do vórtice formado na zona de sombra dos molhes e seus impactos na distribuição de propriedades físico-químicas e biológicas, utilizando dados de sensoriamento remoto, e dados coletados em campo, revelando que o vórtice modula os gradientes biogeoquímicos, como a formação de máximos subsuperficiais de clorofila, e condições favoráveis a hipóxia abaixo da picnoclina, além disso foi demonstrado que as interações com o fundo constitui o principal mecanismo de acumulação de sedimentos na zona de sombra do molhe.

Abstract

This study's general objective is to investigate the hydrodynamic and sedimentary dynamics processes on the inner shelf, with the observation area being the continental shelf of Rio Grande do Sul, Brazil, and the area influenced by the mouth of Patos Lagoon. The first part begins with an analysis of the suspended sediment dynamics on the inner shelf adjacent to the mouth of the Patos Lagoon, using data from an ADCP and theoretical modeling based on Rouse's Theory, demonstrating that exchanges with the seabed are the main source of suspended sediments, with horizontal advection playing a secondary role. Next, the hydrodynamic patterns within the shadow zone created by the jetties during intense NE wind events were investigated, identifying the formation of two counter-rotating vortices and highlighting the importance of water percolation through the jetties in promoting stratification and intensifying vertical velocity gradients within this shadow zone. Finally, the study analyzes the spatial variability of the vortex formed in the shadow zone of the jetties and its impacts on the distribution of physicochemical and biological properties, using remote sensing data and field measurements, revealing that the vortex modulates biogeochemical gradients, such as the formation of subsurface chlorophyll maxima and conditions favorable to hypoxia below the pycnocline. Additionally, it was demonstrated that interactions with the seabed constitute the main mechanism for sediment accumulation within the jetty shadow zone.

Capítulo I: Introdução

A plataforma continental é a região que conecta a costa ao oceano aberto e desempenha um papel crucial na transferência de materiais dos continentes para os oceanos mundiais, com consequência para a ecologia marinha, a produtividade biológica e o destino da matéria orgânica (Mann e Lazier, 2005). Esta região é uma área chave para a pesquisa interdisciplinar devido à sua importância ambiental, sendo altamente afetada pelas trocas transversais à plataforma de sedimentos, nutrientes, larvas, fitoplâncton e contaminantes originados de várias fontes, incluindo descargas fluviais, emissários, processos de erosão costeira ou deposição atmosférica (Austin et al., 2002; Lentz et al., 2012; Moulton et al., 2023). O transporte de sedimentos, desempenha um papel crucial na distribuição de materiais provenientes da drenagem continental, resultando em mudanças morfológicas no leito marinho (Guillén et al., 2006), criando novos habitats para organismos bentônicos (Williams e Bax, 2001), alterando as relações biogeoquímicas na interface sedimento-água (Lukawska-Matuszewska et al., 2022), ou mesmo liberando materiais tóxicos associados a partículas sedimentares (Palanques e Diaz, 1994).

Na plataforma continental, distingue-se a plataforma externa da interna. A plataforma interna refere-se ao setor costeiro com maior influência de aportes continentais, como o influxo de água doce, e difere hidrodinamicamente da plataforma externa pelo fato de as camadas limite turbulentas da superfície e do fundo ocuparem toda a coluna de água (Lentz, 1995). É também onde se observam os gradientes mais fortes das propriedades da água (Lentz, 1995). As interações sinérgicas entre os processos físicos que ocorrem na plataforma interna desempenham um papel fundamental na determinação da fertilidade da região e na sustentação da produção primária, regulando a

disponibilidade de nutrientes, a turbulência e a mistura vertical da coluna de água (Simpson e Sharples, 2012; Brink, 2016; Moulton et al., 2023). A hidrodinâmica da plataforma é impulsionada pela ação combinada do vento, marés, descarga fluvial e ondas de superfície, interagindo com a batimetria costeira e a geometria da linha de costa (Brink, 2023). Os principais mecanismos que impulsionam a circulação hidrodinâmica na plataforma interna são, portanto, a morfologia da linha de costa, a batimetria, a tensão de cisalhamento do vento, as marés e a descarga fluvial. Os processos que ocorrem na plataforma interna desempenham um papel importante na hidrodinâmica de toda a plataforma, pois é a região onde o escoamento se ajusta à linha de costa e os efeitos de atrito são mais intensos (Brink, 2016).

Devido à proximidade dos aportes continentais e ao balanço radiativo sazonal, o regime de escoamento na plataforma interna tende a ser estratificado (Simpson e Sharples, 2012). O equilíbrio entre a estratificação impulsionada pela pluma de empuxo e a mistura induzida pela turbulência influencia diretamente a distribuição de nutrientes, a produção biológica e a oxigenação das camadas mais profundas. Condições estratificadas limitam as trocas verticais, promovendo a formação de máximos de clorofila-a de subsuperfície (SCM) e intensificando os processos de depleção de oxigênio nas camadas inferiores, podendo levar à hipóxia (Simpson e Sharples, 2012).

Embora a componente da corrente ao longo da plataforma seja tipicamente mais energética e dominante em termos de transporte na coluna de água, apresentando muitas vezes um padrão unidirecional (Brink, 2016), a circulação transversal à plataforma exerce impactos significativos, particularmente nos processos de transferência de material através da plataforma (Brink, 2016). A componente transversal à plataforma, embora menos energética, é mais complexa devido à influência da fronteira costeira e dos mecanismos de forçante transversais (Brink, 2016). Por exemplo, a divergência

transversal do transporte de Ekman na plataforma interna impulsiona tanto a ressurgência (upwelling) quanto a subsidência costeira (downwelling), afetando o transporte de sedimentos, o fornecimento de nutrientes dissolvidos para a plataforma, regulando o tempo de residência, redistribuindo calor e salinidade, determinando balanços biogeoquímicos, transportando organismos planctônicos e removendo contaminantes da região costeira (Gill e Clarke, 1973; Simpson e Sharples, 2012; Brink, 2016; Moulton et al., 2023). Além disso, a presença de um promontório intensifica os processos de mistura transversal na plataforma interna (Russel e Vernell, 2017).

Sendo que, os sedimentos em suspensão em áreas costeiras, excluindo a zona de surf e praias, são essencialmente sedimentos finos coesivos (Winterwerp e van Kesteren, 2004), os quais apresentam relações complexas com a hidrodinâmica (Sahin et al., 2012). A dinâmica sedimentar dos sedimentos coesivos (flocos) é influenciada por diversos fatores interconectados, como a composição e concentração desses sedimentos, a concentração de íons na água (salinidade), o pH, a turbulência e a presença de bactérias e outros organismos (Black et al., 2002), tornando a modelagem numérica desse tipo de sedimento mais desafiadora, além da dificuldade de aquisição de dados síncronos do perfil vertical de SSC.

Diante dessa complexidade, um dos maiores desafios na hidrodinâmica costeira reside na compreensão dos processos que controlam as trocas transversais à plataforma. Embora avanços significativos tenham sido feitos recentemente na compreensão da troca de material transversal à plataforma, o problema da circulação transversal depende muito das condições específicas de cada área (Brink, 2023). Vários fenômenos ocorrem simultaneamente com intensidades variadas em diferentes escalas espaciais e temporais, como forçante de maré, tensão de fundo, tensão de onda ou corrente, deriva de Stokes, efeitos da rotação da Terra e baroclinicidade devido à drenagem continental (Brink, 2016;

Moulton et al., 2023). Além disso, o desenvolvimento econômico muitas vezes requer a expansão da infraestrutura portuária, como a ampliação dos berços de atracação para acomodar mais e maiores navios. Tais transformações necessitam de dragagem de sedimentos, sendo os materiais dragados dispostos na plataforma continental (Marmin et al., 2016; Schettini, 2022). Neste contexto, o estudo destas regiões e a melhoria das técnicas disponíveis para quantificar o transporte de sedimentos são necessários para prever e mitigar perturbações e garantir a sustentabilidade ambiental e econômica destas áreas.

1.1 Área de Estudo

A plataforma continental do estado do Rio Grande do Sul se estende aproximadamente no eixo norte-sul entre o Arroio Chuí (34°S) e Torres (29°S), com uma linha costeira dominada por uma planície costeira arenosa sem feições proeminentes, exceto pela desembocadura da Lagoa dos Patos. Os molhes representam a única obstrução, quase perpendicular à linha de costa, numa extensa praia que se estende entre o Chuí, 215 km a sul, e Torres, 390 km a norte (Fig. 1). Essa configuração única torna essa região um caso de estudo fundamental para a compreensão da dinâmica hidro-sedimentar em ambientes marinhos rasos, com desembocaduras e obstruções ortogonais à linha de costa.

Os molhes da boca da Lagoa dos Patos foram construídos na década de 1910 e estão entre as maiores obras de engenharia costeira da sua época (Motta, 1969; Bicalho, 1983). A motivação para esta construção foi estabilizar a barra da lagoa, garantir a segurança da navegação e dar acesso ao Porto de Rio Grande. A construção começou em

1911 e, na sua configuração final, os molhes estendiam-se por 4 km ao largo da linha de costa (Bicalho, 1983; Motta, 1969; Cunha et al., 2009). O material de construção utilizado foram pedras soltas e, em 2010, os molhes foram modificados com blocos de tetrápodes (Migliorini et al., 2008), resultando numa estrutura permeável, com a porção final localizada numa área de 15 m de profundidade.

Sob condições de vento N-NE, as correntes na plataforma interna fluem para sul (Cruz e Schettini, 2023), criando uma área abrigada a sudoeste dos molhes onde se forma um vórtice horário que, segundo Vinzon et al. (2009) e Franzen et al. (2023), favorece a deposição de sedimentos finos na plataforma interna ao largo da praia do Cassino. Estes estudos basearam-se em simulações numéricas. Embora o escoamento horizontal das correntes seja bem representado, as limitações impostas pelas condições de contorno e esquemas numéricos não permitem a reprodução da complexidade hidrodinâmica desta região.

A sudoeste da desembocadura da Lagoa dos Patos encontra-se a Praia do Cassino, onde ocorrem depósitos de lama inconsolidada na plataforma interna. Durante certos eventos de alta energia, esses depósitos podem ser remobilizados e transportados em direção à costa, resultando potencialmente na deposição de lama na praia, com diversos impactos econômicos, ecológicos e geomorfológicos (Calliari et al., 2001; Calliari et al., 2007; Calliari et al., 2009; Holland et al., 2009). Acredita-se que este processo de transporte de sedimentos transversal à plataforma esteja relacionado com eventos de deposição de lama na praia (Pereira et al., 2011), porém, ainda permanece um fenômeno não resolvido.

A maré local é mista com predominância diurna, apresentando uma amplitude média de 0,3 m, e não desempenha um papel significativo na hidrodinâmica (Moller et

al., 2007). O escoamento é impulsionado principalmente pelo vento local (Soares et al., 2001; Zavialov et al., 2002; Costa et al., 2011; Cruz e Schettini, 2024).

O Rio da Prata possui uma descarga média entre 23.000 e 28.000 m³/s (Urien, 1972), com uma descarga de sólidos em suspensão da ordem de 100 x 10^6 toneladas/ano (Isupova e Mikhailov, 2018), sendo a principal fonte regional de sedimentos para a plataforma. A descarga média da Lagoa dos Patos é de aproximadamente 2.400 m³/s (Vaz et al., 2006), sendo que a descarga média de sólidos em suspensão do Rio Guaíba, principal tributário da Lagoa dos Patos, é de 1,1 x 10^6 toneladas/ano (Andrade et al., 2012)

.

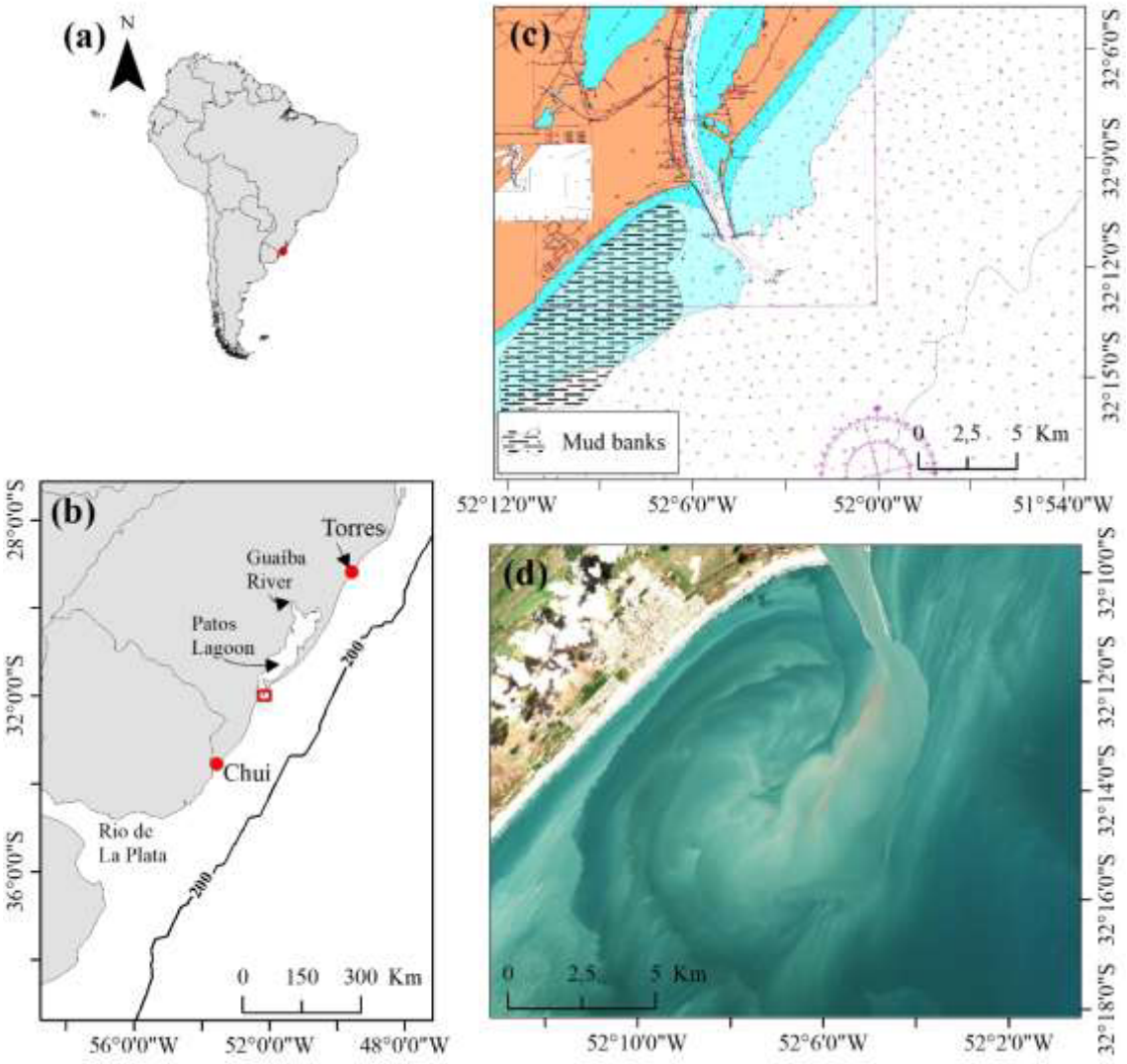


Figure 1 – Cap I. Localização da área de estudo. Em (b) mostra a extensão da plataforma continental com indicação da linha batimétrica. Em (c) a localização do banco de lama extraída de Calliari et al. (2007). Em (d) imagem de satélite do sentinel 2 adquirida no dia 24 de Abril de 2023, mostrando a localização do vórtice sob condições de vento vindo de nordeste.

2.1 Estrutura da Tese

A presente tese está organizada em três capítulos principais (II, III e IV), os quais correspondem aos artigos científicos originais submetidos a periódicos especializados na área de oceanografia física em ambientes marinhos rasos.

O capítulo II, publicado na revista "Continental Shelf", investiga a dinâmica de sedimentos em suspensão na plataforma interna adjacente à desembocadura da Lagoa dos Patos, utilizando dados de um Perfilador Acústico de Efeito Doppler (ADCP) e modelagem teórica dos perfis de sedimento em suspensão, por meio da Teoria de Rouse, para investigar as possíveis fontes, transporte e características do material particulado em suspensão.

O capítulo III, em revisão na revista "Ocean and Coastal Research", investiga os efeitos hidrodinâmicos dos molhes da desembocadura da Lagos dos patos, com base em dados de campo, na região de sombra dos molhes.

O capítulo IV, em revisão na revista "Regional Studies in Marine Science", analisa a variabilidade espaço-temporal de parâmetros físicos, geológicos e biológicos na região de sombra dos molhes da desembocadura da Lagoa dos Patos.

Objetivos

Este estudo tem como objetivo geral investigar os processos hidrodinâmicos e da dinâmica sedimentar na plataforma interna, tento com área de observação a plataforma continental do Rio Grande do Sul, Brasil, e na área influenciada pela foz da Lagoa dos Patos.

Os objetivos específicos são:

1) Analisar a hidrodinâmica e o transporte de sedimentos em suspensão na plataforma interna, ao largo da desembocadura da Lagoa dos Patos (mas afastado da presença dos molhes) (artigo 1);

2) Investigar a hidrodinâmica na zona de sombra formada pelos molhes, analisando os efeitos desta significativa obstrução costeira no escoamento ao longo da costa, nos escoamentos transversais à plataforma e suas consequências para a dinâmica de transporte de materiais em suspensão (artigo 2);

3) Avaliar os efeitos do vórtice formado na zona de sombra do molhe oeste sobre a circulação e na distribuição de propriedades da água (artigo 3).

Hipótese

"Os processos hidro-sedimentares na plataforma interna adjacente à desembocadura da Lagoa dos Patos, RS, são modificados pelos molhes, alterando os gradientes verticais, a distribuição de propriedades de qualidade da água e de materiais em suspensão."

Capítulo II: The dynamics of the inner-shelf suspended sediments based on ADCP records and Rouse theory

3.1 Abstract

The present study investigates the suspended sediment dynamics on the southern Brazilian continental shelf in the fluvial influence region of the Rio de la Plata and Patos Lagoon. Estimates of suspended sediment concentration (SSC) in the water column were obtained using data from a Doppler-effect acoustic Doppler current profiler (ADCP) and were compared with theoretical profiles obtained using Rouse's theory. To construct the theoretical profile, sediment settling velocity and shear velocity are necessary. The former was iteratively estimated to minimize the error between observed and modeled profiles. The latter was obtained from ADCP measurements. The comparison between observed and modeled profiles underwent a validation process considering the shape of the observed profile and environmental energy conditions. For the period of analyzed data,

there was agreement between observed and modeled profiles 56% of the time. When energy conditions were low (39 % of the time), and the gradient profile of SSC had higher concentrations near the surface than bottom (5 %), Rouse's theory did not apply. These results indicate that the main source of sediment in the water column is due to exchanges with the bottom. Although the study area is near the mouth of Patos Lagoon, the role of horizontal advection was negligible. By indirect inference, it was obtained that the median sediment size was 25 μm, with maximum values around 60 μm, which coincides with values suggested in the literature for coastal waters, with a median settling velocity of 0.14 cm/s. During periods of more energetic hydrodynamic conditions, downwelling events were associated with northward longitudinal currents, while upwelling occurred with southward currents. When the flow was directed northward, more material was transported near the bottom compared to southward flow.

4.1 Introduction

Understanding sediment dynamics on the continental shelf is fundamental for comprehending the functioning and evolution of continental margins (Drake and Burk, 1974; Swift, 1974). Sediment transport plays a crucial role in distributing materials arriving from continental drainage, resulting in morphological changes on the seabed (Guillén et al., 2006), creating new habitats for benthic organisms (Williams and Bax, 2001), altering biogeochemical relationships at the sediment-water interface (Lukawska-Matuszewska et al., 2022), or even releasing toxic materials associated with sedimentary particles (Palanques and Diaz, 1994). Additionally, economic development requires the expansion of port infrastructure, such as enlarging docking berths to accommodate more

and larger vessels. Such transformations necessitate sediment dredging, with the dredged materials being disposed of on the continental shelf (Marmin et al., 2016; Schettini, 2022). In this context, studying these regions and improving available techniques for quantifying sediment transport are necessary to predict and mitigate disturbances and ensure the environmental and economic sustainability of these areas.

Suspended sediments in coastal areas, excluding the surf zone on beaches, are essentially cohesive fine sediments (Winterwerp and van Kesteren, 2004), which exhibit complex relationships with hydrodynamics (Sahin et al., 2012), as well as biological activities (Black et al., 2002). One of the main characteristics of cohesive sediments in coastal areas is that they consist of very small particles (< 2 μm); however, due to their cohesive nature, they occur as aggregates or flocs of much larger size (> 50 μm) (Eisma, 1986). Nevertheless, flocs, as sedimentary units, are composed of sediment particles, water, and adsorbed organic matter, and thus, have a lower density of ~1650 kg/m3 for flocs with size ~100 μm, and only the microflocs with size lower than 30 μm approach the effective density of quartz, ~ 2650 kg/m3 (Black et al., 2002).

The formation of these flocs is influenced by various factors, such as the composition and concentration of these sediments, ion concentration in the water (salinity), pH, turbulence, and the presence of bacteria and other organisms (Black et al., 2002). The composition of sediments can affect the formation and stability of these flocs, as the bonding strength between flocs decreases exponentially as the proportion of non-cohesive sediment increases. Flocs formed from a higher concentration of silt are more susceptible to breakage, resulting in a lower terminal particle velocity (Manning et al., 2010). Sediment concentration influences flocculation, as higher concentrations increase the likelihood of particle encounters. The encounter of particles also depends on the turbulence of the medium, but this has a complex relationship with flocculation.

Turbulence can increase the rate of floc formation by increasing the probability of collisions, but when turbulence exceeds a threshold, it can also break already formed flocs or even prevent their formation (Dyer & Manning, 1999; Manning et al., 2010). The presence of ions (salinity) in the water can affect the electric charge of cohesive particles, facilitating or inhibiting floc formation depending on the assembly of clay minerals constituting the sediment (Al Ani et al., 1991). In environments with acidic pH (< 7), particles tend to acquire more positive charges, which can favor flocculation (Couceiro and Schettini, 2010). Bacteria and other organisms can act as binding agents and alter environmental conditions, such as pH, indirectly affecting floc formation (Black et al., 2002).

The shear stress of flow with the bed generated by waves and/or currents is the main source of energy to entrain or maintain sediment particles denser than water in suspension, through the conversion of kinetic energy into turbulent kinetic energy, creating turbulent diffusion. The work required to lift and keep these particles in suspension is directly related to the weight, shape, size, and viscosity of the fluid, as well as thixotropic properties in muddy bottoms (Winterwerp and van Kesteren, 2004). The amount of turbulent energy decreases with distance from the bed, resulting in fewer suspended particles and a vertical sediment concentration profile with an exponential shape (Rouse, 1939).

The vertical profile of suspended sediment concentration (SSC) can be represented by the Rouse model (1939). The equation describing the model represents the balance between the settling velocity of the sediment, which moves the particle towards the bottom, the turbulent diffusion coefficient, which is a measure of the vertical mixing rate, with the sediment concentration rate for each level (z).

$$w_s C(z) + \varepsilon_s \frac{dC(z)}{dz} = 0 \quad (1)$$

where z is the height above the water/sediment interface (m), w_s is the settling velocity of sediment particles (m/s), C is the suspended sediment concentration (kg/m³) at a given level, and ε_s is the vertical turbulent diffusion coefficient for suspended sediments (m²/s).

The use of Acoustic Doppler Current Profilers (ADCP) allows for precise observations of the vertical profile of SSC, providing the $C(z)$ in Eq. 1, as they record acoustic backscatter information (ABS), which has a direct and nonlinear relationship with SSC. ADCP's have proven to be efficient for this purpose in coastal regions (Gartner, 2004; Park & Lee, 2016; Schettini et al., 2013; Yu et al., 2011). This approach has the advantage of enabling data acquisition for long periods with high temporal and spatial resolution (in the vertical) compared to other methods for obtaining SSC, such as water sampling or the use of optical turbidimeters (Downing et al., 1991), at a relatively low cost. However, the use of these other methods for calibration and validation purposes is still necessary.

In the present study, we investigated the dynamics and transport of suspended sediments on the inner continental shelf of Rio Grande – RS, Brazil. Estimates of the vertical and temporal distribution of SSC were obtained using acoustic backscatter data recorded by an ADCP (Acoustic Doppler Current Profiler) and compared with vertical profiles derived from the Rouse model (Boudreau and Hill, 2020). While the ADCP approach provides SSC estimates, the Rouse theory approach enables the assessment of settling velocity and vertical diffusion. The comparison of results allows us to diagnose the relationship between bottom exchange processes and advection. The study area exhibits a complex sedimentary dynamic, influenced by both the freshwater outflows of

the Río de la Plata and the Patos Lagoon. Thus, the SSC estimates and sedimentary characteristics obtained in this study contribute to a better understanding of transport processes and sedimentary dynamics in the region. Furthermore, the methods and algorithms used in this study can be applied to other continental shelves for the analysis of sediment dynamics.

5.1 Study Area

The continental shelf of the state of Rio Grande do Sul extends approximately in a north-south axis between Arroio Chui (34°S) and Torres (29°S), with a coastline dominated by a sandy coastal plain without prominent features except for the mouth of Patos Lagoon. The width of the shelf varies between 100 and 180 km, with a shelf break depth at ~180 m, and a low bottom slope. Near the mouth of Patos Lagoon, the shelf is relatively flat, with the presence of extensive sandy banks to the north and south of the mouth (Fachin, 1998; Corrêa et al., 2019).

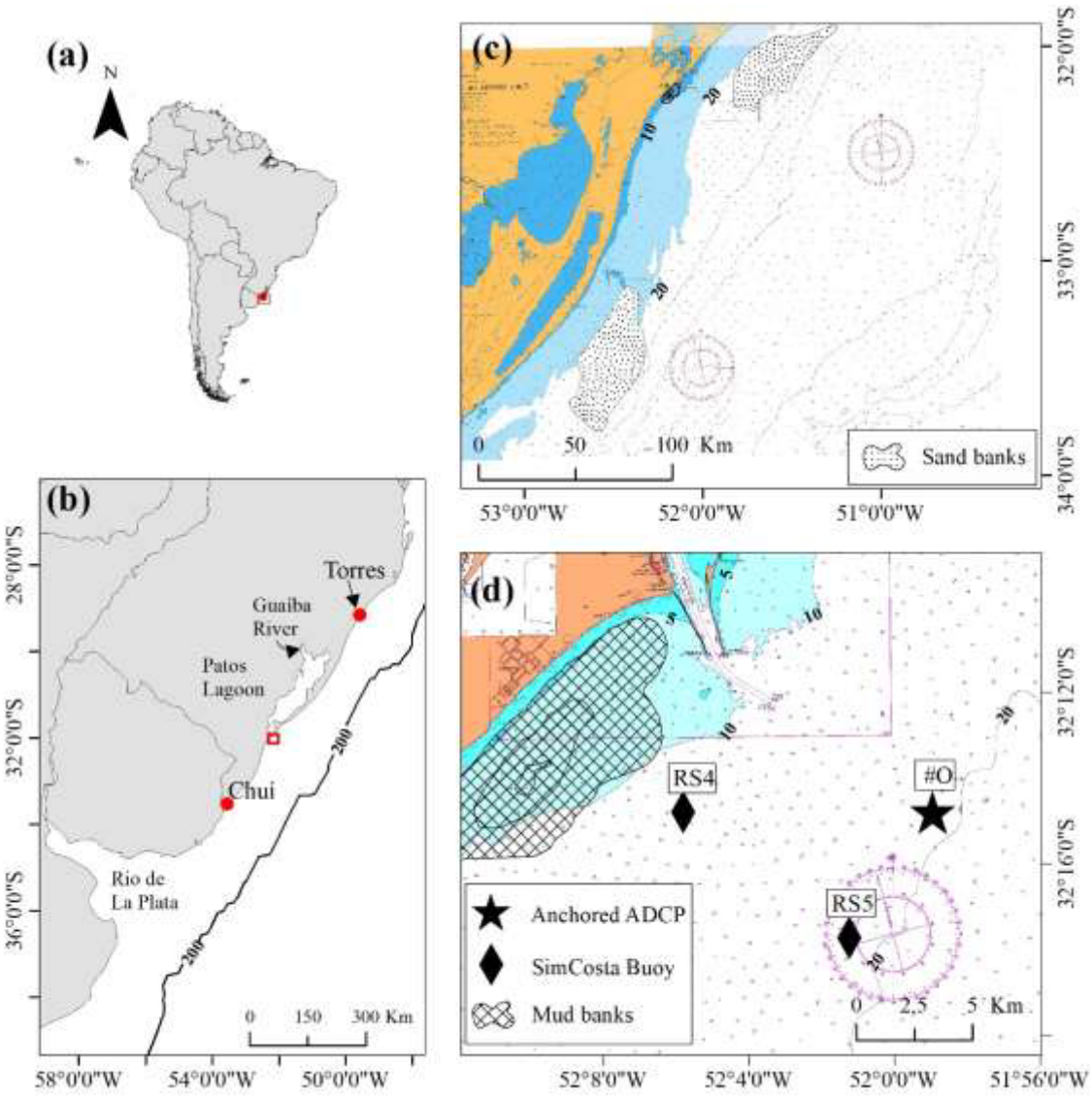


Figure 1 – Cap II. Location of the study area. The larger panel shows the situation of the continental shelf on a smaller scale with indication of bathymetric lines, and in detail presents the location of the ADCP mooring and buoys RS4 and RS5. The location of the mud bank was extracted from Calliari et al. (2007). The location of the sandy banks was obtained from navy nautical charts.

Most of the shelf is dominated by mud deposits sourced by the La Plata estuary and Patos lagoon (Martins et al., 2003; Campos et al., 2008; Corrêa et al., 2019; Toldo et al., 2006). The coast south of the the mouth of Patos Lagoon (Cassino beach) experiences cyclic events of mud deposition on the beach (Calliari et al., 2007). On the inner shelf off

the beach, pockets of unconsolidated mud occur, and after certain storms, this material is eroded and transported towards the shore (Calliari et al., 2001; Pereira et al., 2011), which indicate the shelf experiences high mud mobility.

The local climate is humid subtropical, with a strong seasonal signal. The monthly mean temperature ranges between 11 and 23°C (Reboita and Kruche, 2018). There is a predominance of winds from NE throughout the year, with higher intensity in spring (Reboita & Kruche, 2018; Saraiva et al., 2003). This wind pattern is cyclically disturbed by the passage of frontal systems occurring at intervals of 6 to 11 days (Stech and Lorenzetti, 1992). Figure 2 shows the frequency distribution of the wind and the monthly climatology of the along-shelf and cross-shelf wind.

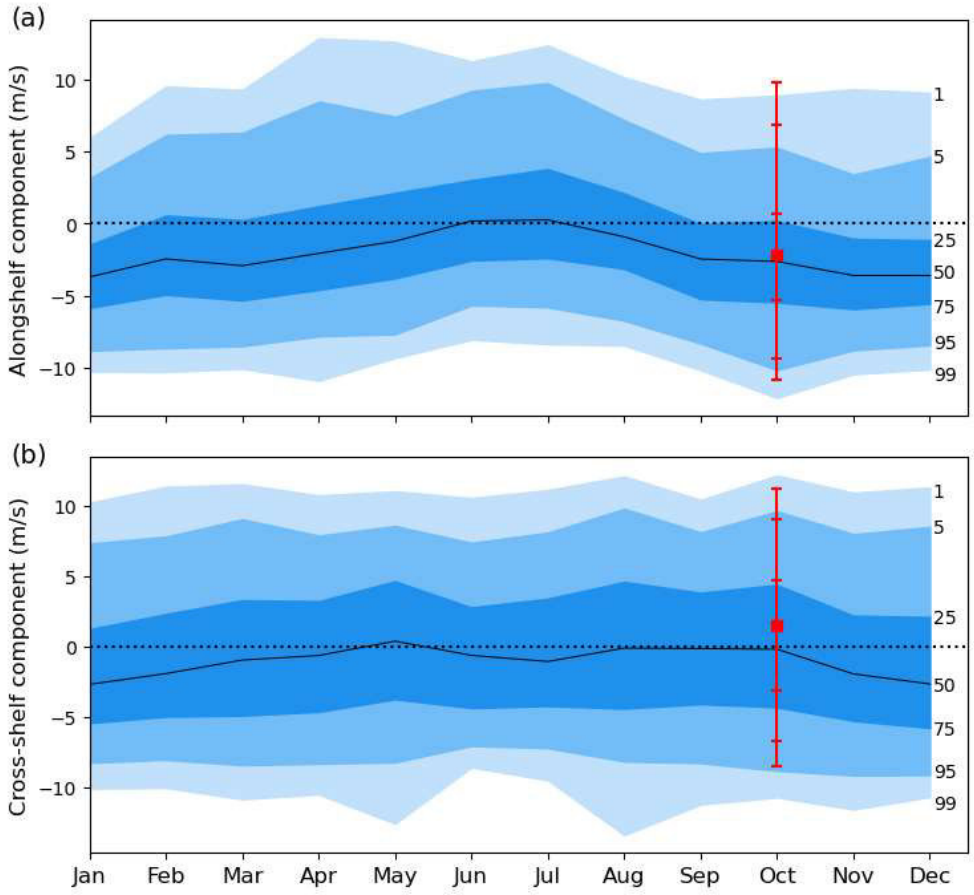


Figure 2 – Cap II. Monthly frequency distribution of wind velocity for the alongshelf and cross-shelf components based on observational data recorded at buoys RS4 (Feb/2019 to Apr/2021) and RS5 (Dec/2016 to Mar/2023). The median value is represented by the black line, and the shades of blue represent the range of percentiles 1-99, 5-95, and 25-75%. The vertical red line in the month of October represents the data observed during mooring from September 17th to November 2nd, 2020 (45 days).

Wave climatology of the region has been described using observational data (Motta, 1963; Strauch, 1997), and numerical models (Cuchiara et al., 2009; Cecilio et al. (2019). There are two main propagation directions: 110° (from the E) with significant wave height of 1.0 m and period of 8 s, and 160° (from the SSE) with significant wave height of 1.5 m, and average period of 12 s. However, during storms wave heights can reach up to 5 m.

There are relatively few observations of the currents. Zavialov et al. (2002), and Costa and Möller (2011), assessed the currents based on observations on the 50 m and 15 m isobaths, respectively. Their results indicate that currents are primarily forced by local wind, with little importance of astronomical tides. On the outer shelf the mean flow is southward, responding to mesoscale processes (Palma et al., 2008). Near the mouth of Patos Lagoon, circulation patterns are more complex, both due to the presence of the lagoon's mouth and the presence of jetties that extend approximately 4 km offshore. The lagoon produces predominant outflow of low salinity waters, which produces a pronounced buoyancy plume (Hartmann et al.,, 1990; Möller et al., 2001; Marques and Möller, 2008). However, the entire area is within the fluvial influence region of the Rio de la Plata, especially during periods of winds from the S-SE, which displaces the low salinity plume to lower latitudes (Piola et al., 2008).

The Rio de la Plata has an average discharge of 25.000 m^3/s (Urien, 1972), with suspended solid discharge on the order of 100 x 10^6 tons/year (Isupova and Mikhailov, 2018), and SSC values on the shelf of 200 mg/L (Moreira et al., 2013). The average discharge of Patos Lagoon is 2400 m^3/s (Vaz et al., 2006), and the average suspended solid discharge of the Rio Guaíba of 1.1 x 10^6 tons/year (Andrade Neto et al., 2012). SSC values observed near the mouth of Patos Lagoon vary between 5 and 200 mg/L (Hartmann et al., 1990).

6.1 Material and Methods

Pressure (depth), temperature, velocity, current direction, and acoustic intensity data were obtained using an ADCP anchored at a depth of 20 m approximately 15 km from the coastline and 10 km from the mouth of Patos Lagoon (32°14'48"S, 51°58'52.5"W, Figure 1d #O). The installation period was during the spring season, from September 17th to November 2nd, 2020 (45 days). A Nortek Aquadopp Profiler ADCP with a frequency of 1000 kHz was used, configured to record vertical profiles at 10-minute intervals, based on 120-second averages, with a vertical resolution of 0.5 m. When the ADCP is moored, data near the surface are often inaccurate due to turbulence generated by waves and the presence of bubbles, which distort the acoustic signal measurements. The selection of valid cells for analysis was based on the temporal mean profile of acoustic amplitude. The acoustic amplitude signal decreases with distance from the instrument, but near the surface, the signal increases, showing a peak that coincides with the air-water interface. We used only the data where the amplitude signal decreases, which in this case was up to approximately 14.5 meters above bottom (m.a.b). Considering that the local tidal range is microtidal (~0.5 m), we applied a constant cutoff level for the entire record of ~3 m. The valid measurement levels ranged from approximately 1 m above the seafloor to approximately 3 m below the surface, or ~78% of the water column.

Wind speed and direction data were obtained from buoys RS4 and RS5 (Figure 1), covering the period from December 2016 to April 2021. Synoptic data for the ADCP anchoring site, including surface salinity and wave parameters (direction, period, and height), were obtained from buoy RS4, located 10 km south of the ADCP installation site.

The current and wind data were decomposed into longshore and cross-shore components, considering the inclination of the maximum velocity variance relative to the north, which was 29 degrees.

Inversion of ABS to SSC:

The acoustic intensity data recorded by the ADCP were converted into acoustic backscatter strength (ABS) in decibels (dB) using the sonar equation (Urick, 1975).

$$ABS = RL + 2TL - TS \quad (2)$$

Where ABS is the relative acoustic backscatter strength (dB), RL is the reverberation level, given by $K_c(E - E_r)$, where E is the intensity recorded by the ADCP in counts, E_r is the intensity of the signal received by the ADCP when no signal is transmitted (reference level measured with the equipment out of water), and K_c is a scale factor used to convert counts to dB (0.43). 2TL is the transmission loss level, defined as:

$$2TL = 20log(R) + 2\alpha R \quad (3)$$

Where R is the range of the volume of water being sonified (m), α is the coefficient of absorption of seawater (dB/m), obtained through a function of acoustic frequency, salinity, temperature, and pressure (Schulkin et al., 1962).

TS is the target strength and represents the transmission loss by the source and depends on the frequency of the ADCP and the diameter of the particle. However, this term is not considered in general. The transmission attenuation by this term is significant only at low concentrations or when the diameter of the particle is small (<10 μm), which is typically not the case of flocculated material found in coastal waters (Eisma, 1986).

For example, an ADCP with a frequency of 1000 kHz and particles with a mean diameter of 20 μm would have a sensitivity peak (ka) of approximately 0.04, characterizing Rayleigh distribution (ka≪1). This means that sound waves interact with particles much smaller than their wavelength. According to Rayleigh distribution theory, the maximum TS value would be ~37 dB; however, this estimate applies to a single, spherical, incompressible particle with a smooth surface. In coastal regions, turbidity is typically high enough to prevent individual particle scattering from significantly attenuating the signal. As a result, acoustic backscatter becomes more dependent on the collective scattering of suspended particles rather than isolated interactions (Urick, 1975).

The inversion from ABS (dB) to SSC (g/L) was performed using the relationship:

$$SSC_{ABS} = 1.2 \times 10^{-4} + exp^{(0.126\,ABS)} \quad (4)$$

This relationship was obtained for the same brand, model, and frequency of ADCP used in the present study, based on a fitting between ABS and SSC with $r^2 = 0.78$, for a location nearly 20 km southwards from the mooring of the present study. This relationship was obtained using simultaneous ADCP data and turbidity data from optical backscatter sensors (OBS) at two measurement levels, with hourly intervals over a 30-day period. The OBS sensors were calibrated with local sediment, thereby allowing the relationship between ABS and SSC to be determined.

Bottom shear-stress:

The bottom shear stress (τ) is a measure of the frictional force exerted by the fluid per unit area of the bottom (Pa). It is also closely related to the level of turbulence, which controls the suspension of sediments. The bottom shear stress can be generated by currents (τ_C), waves (τ_W), and combined by currents and waves. We used the approach

described by Soulsby and Clark (2005) to calculated the bottom shear stress, where the latter can be calculated in two ways: the mean bottom shear stress for wave + current (τ_{mwc}), which considers the interactions of τ_c by τ_w during the wave orbital velocity incursion, and the maximum bottom shear stress for wave + current (τ_{maxwc}), which considers the interaction of τ_c by τ_w when the wave orbital velocity (U_w) is maximum.

The Soulsby and Clarke (2005), algorithm for determining the combined wave and current shear stress is based on the findings of Simons et al. (2000), where the wave-induced oscillatory stress component is nonlinearly added to the current stress. Soulsby et al. (1993) compared results obtained from various theoretical models with observational data and demonstrated that nonlinearity arises due to the difference in the angle of attack between waves and currents, which is corroborated by recent studies (Choi et al., 2009; Malarkey et al., 2012; Ribeiro et al., 2017; Wang et al., 2018). The additional turbulence generated by waves near the bed represents, for the current, the equivalent of an increase in apparent bed roughness. In sediment transport analyses, τ_{maxwc} is used to determine the threshold for sediment movement initiation or intrusion, while τ_{mwc} is used in the suspension sediment diffusion to upper layers (Soulsby et al., 1993).

The equations to estimate the different bottom shear stresses used are:

$$\left.\begin{array}{l} \tau_c = \rho C_D \overline{U}^2 \text{ , for } \overline{U} > 0 \; and \; U_w = 0 \\ \tau_w = \frac{1}{2}\rho f_w {U_w}^2, \text{for } \overline{U} = 0 \; and \; U_w > 0 \\ \tau_{mwc} = \rho C_{Dm} \overline{U}^2 \text{ or } \tau_{maxwc} = \rho C_{Dmax} \overline{\mathrm{U}}^2, \text{ for } \overline{U} > 0 \; and \; U_w > 0 \end{array}\right\} \quad (5)$$

where ρ is the water density; $\overline{U}$ is the depth averaged current velocity; C_D is the drag coefficient; f_w is the wave friction factor; U_w is the wave orbital velocity; C_{Dm} and C_{Dmax} are the drag coefficients when considering the combined current + wave mean and maximum effects, respectively. The approach of Soulsby and Clark (2005), distinguish flow conditions for rough and smooth bottoms, which affect how the drag and wave friction coefficients are calculated. In present case we used the formulation for smooth bottom. The implementation of the algorithm for calculation of bed shear stress implemented in Python is available at https://github.com/GuiCruz/SoundSSC.

Using the approach described in Soulsby (2006), the calculation of the wave orbital velocity (U_w) depends on ratio between the natural scaling period (T_n) to the wave period (T)

$$\frac{T_n}{T} = \left(\frac{h}{gT^2}\right)^{0.5}. \quad (6)$$

where h is the water depth, and g is the acceleration of gravity. If T_n/T is < 0.2, U_w is calculated by Nielsen's method by

$$U_w = 0.5H\left(\frac{g}{h}\right)^{0.5}\left[1 - \frac{1}{3}\frac{2\pi T_n}{T}^2\right] \quad (7)$$

where H is the wave height. Otherwise, it is used Soulsby's exponential approximation by

$$U_w = 0.5H(g/h)^{0.5} exp\left\{-\left[\frac{4.41}{T}\left(\frac{h}{g}\right)^{0.5}\right]^{2.45}\right\} \quad (8)$$

Rouse Model and Terminal Velocity:

The terminal settling velocity of suspended sediment (w_s), the mean suspended particle diameter (d_s), diffusion coefficient (ε_s), and SSC_{rouse} were estimated using the Rouse model, modified by Boudreau et al., (2020). The results were compared with SSC_{ABS} estimates obtained through ABS inversion, and the best-fitting profile was selected based on the mean squared error. The original formulation developed by Rouse (1939) predicts an infinite amount of sediment at the bottom (z = 0). To address this singularity issue at the sediment source, the authors considered the existence of residual turbulent diffusion (ε_0) near the bottom, defined as:

$$\varepsilon_0 = \varepsilon_s - \kappa u_* z \tag{9}$$

where ε_s is the turbulent diffusion coefficient, k is the von-Karman constant (0.41), u_* is the shear velocity ($= \sqrt{\tau/\rho}$), and z is the distance from the bottom. ε_s is estimated by

$$\varepsilon_s = \kappa u_* (z + z_r) \tag{10}$$

where z_r is the bottom roughness scale given by

$$z_r = \frac{26 d_b}{\kappa} \tag{11}$$

where d_b is the mean bottom sediment diameter. The vertical distribution of sediment concentration $C(z)$ (or SSC_{rouse}) can be modelled by

$$C(z) = C_{ref} \left(1 + \frac{\kappa u_* z}{\varepsilon_0}\right)^{-Ro} \tag{12}$$

where C_{ref} is the reference concentration at the bottom (z = 0), and Ro is the Rouse number ($= w_s/ku_*$).

The input variables used to solve the model are: u_*, calculated using the $\tau_c, \tau_w \; or \; \tau_{mwc}$ described above (Soulsby and Clarke, 2005); water density ρ was calculated based on the measured salinity from Buoy RS4 and the temperature obtained from the ADCP; bottom sediment diameter d_b was obtained from the literature ($\cong$ 130 μm; Martins et al., 2003; Corrêa et al., 2019), The iterable variables used in fitting the SSC_{rouse} profile are: the reference concentration, C_{ref}, varying from 0.01 to 100 kg/m^3; the mean suspended sediment diameter, d_s, varying from 20 μm to 250 μm, which was constrained based on values previously observed in nearby regions (Martins et al., 2003); and the particle density, ρ_{sed}, ranging from 2000 to 2650 kg/m^3, which was defined based on laboratory studies on the characteristics of mud flocs (Manning et al., 2010). With d_s and ρ_{sed} , the w_s in Ro was calculated using Stokes Law.

$$w_s = \frac{2}{9} \frac{(\rho_s - \rho)}{\mu} \; g \; d_s^2 \qquad (13)$$

where μ is the water dynamic viscosity (10^{-3} kg/(m.s))

The algorithm developed to analyze, process, and apply the mathematical models was implemented in Python, following these steps: (1) preprocessing of oceanographic data to remove outliers from the ADCP data near the surface and to estimate the longitudinal and transverse velocity components; (2) application of the Soulsby model to generate estimates of bottom shear stress (Equation 5); (3) application of the Rouse model to generate estimates of sediment characteristics, where the iterable variables provided various SSC_{rouse} profiles which were compared to the SSC_{ABS} profile using the root mean squared percentage error (RMSPE), with the best-fitted profile being selected; (4) post-

processing where basic statistics were applied and the data were reduced for graphical representation. Detailed information on the resolution of equations and the developed algorithms are available in https://github.com/GuiCruz/SoundSSC.

The RMSPE is calculated by

$$RMSPE = \sqrt{\frac{1}{m}\sum_{i=1}^{m}\left(\frac{y_i - \hat{y}_i}{y_i}\right)^2} \times 100 \quad (14)$$

where m is the sampling size, y_i is the reference value (SSC_{ABS}), and $\hat{y}_i$ is the modeled value (SSC_{rouse}).

Validation of the vertical SSC profile:

The vertical SSC profiles generated using the Rouse theory were validated considering two hierarchical criteria: (1) a minimum threshold of bottom shear stress for vertical sediment mobilization to occur; and (2) a condition of positive mean concentration gradient of the water column $\left(\overline{\frac{dC(z)}{dz}}\right)$, when Rouse theory does not apply. In the first step, we identified the profiles with τ_{mwc} values below 0.05, which is the critical shear stress for sediment mobilization (τ_{crit}). The threshold of 0.05 Pa was defined based on the available data on the average sediment size (Martins et al., 2003) combined with the critical shear stress data available in the literature (van Rijn, 2020, and Salehi et al., 2012). Below this value, there is not enough turbulent energy to mobilize bottom sediments.

The τ_{crit} is determined by the combination of sedimentary characteristics, hydrodynamic properties, and environmental conditions. Smaller, more cohesive flocs exhibit higher τ_{crit} compared to larger sediments with a greater proportion of sand and silt (Manning et al., 2010). Compacted sediments also require more energy to be eroded. Turbulence and hydrodynamic history affect their thixotropic properties: under high-energy conditions, the bonds between particles are broken, reducing the material's resistance to shear (Winterwerp and van Kesteren, 2004). Environmental conditions, such as salinity, influence flocculation and cohesion (Al Ani et al., 1991). The presence of organic matter can act as a binding agent, increasing cohesion and shear resistance. On the other hand, biological activity, such as that of benthic organisms, can destabilize the bed, facilitating erosion (Black et al., 2002). Although determining a specific τ_{crit} value is complex, given the numerous factors acting simultaneously, in the absence of a value for the region, a τ_{crit} of 0.05 Pa was established based on data available in the literature. For bottoms consisting mainly of mud (> 80%), a critical stress of 0.05 Pa is considered, and when the composition is muddy sand (diameter 150-250 μm), the stress increases to 0.15 Pa (van Rijn, 2020). Observational studies conducted by Salehi et al., (2012) obtained similar values, between 0.06 and 0.14 Pa, for beds composed of mud and sand, respectively.

Temporal Representativeness:

To assess the temporal representativeness of the data obtained during mooring and thus temporally validate the estimates obtained through the Soulsby and Rouse models, a comparative analysis of the meteorological and oceanographic conditions with the corresponding parameters from the historical series obtained by buoys RS4 and RS5 (Figure 1) was conducted. Wind parameters were compared with data from buoys RS4

and RS5 together, covering approximately 2293 days. Wave and current parameters were compared only with the historical series of buoy RS4, covering about 774 days. After a detailed review of each parameter, the temporal distribution of the variable was analyzed through persistence curves and the application of basic statistics.

7.1 Results

The time series of wind speed, depth-integrated currents, sea level oscillation, and wave height, period, and direction for the mooring period are shown in Figure 3. The persistence curves and frequency distributions for these variables, except for sea level, are presented in Figure 4, and the values for the median and percentiles of 1, 5, 25, 75, 95, and 99% are presented in Table 1. Figure 4 and Table 1 also present the results for the long-term monitoring from buoys RS4 and RS5.

The time series of wind components (Figure 3a and b) exhibited the expected oscillations of the wind regime for the region, with high variability in wind direction and intensity, including several events where the wind exceeded 10 m/s, interspersed with periods of low intensity. The response of the water level and currents to the wind regime were expected according to the previous assessments in the region (Costa and Moller, 2011; Santos and Garcia, 2023). The sea level oscillation (Figure 3c) followed the alongshore wind variation, with variations on the order of 1.5 m, and a much smaller astronomical signal compared to the low-frequency signal. The alongshore component of the depth-integrated water column mean current (Figure 3d) followed the wind variability pattern, varying with an amplitude of 0.7 m/s. The cross-shore component of the depth-

integrated water column mean current (Figure 3e) showed an amplitude of 0.15 m/s, with a greater presence of the astronomical tide component.

During the period, three events of higher wave energy occurred, with wave height exceeding 1 m (Figure 3f), but presenting distinct periods (Figure 3g). The first event showed swell conditions with a period of 10 s, while the other events showed sea conditions with a period of 6 s. In all cases, the wave orientation was from the southeast quadrant (Figure 3h). The maximum observed wave height and period were 1.6 m and 10 seconds, respectively, while the average was 0.7 m and 5.4 seconds, respectively.

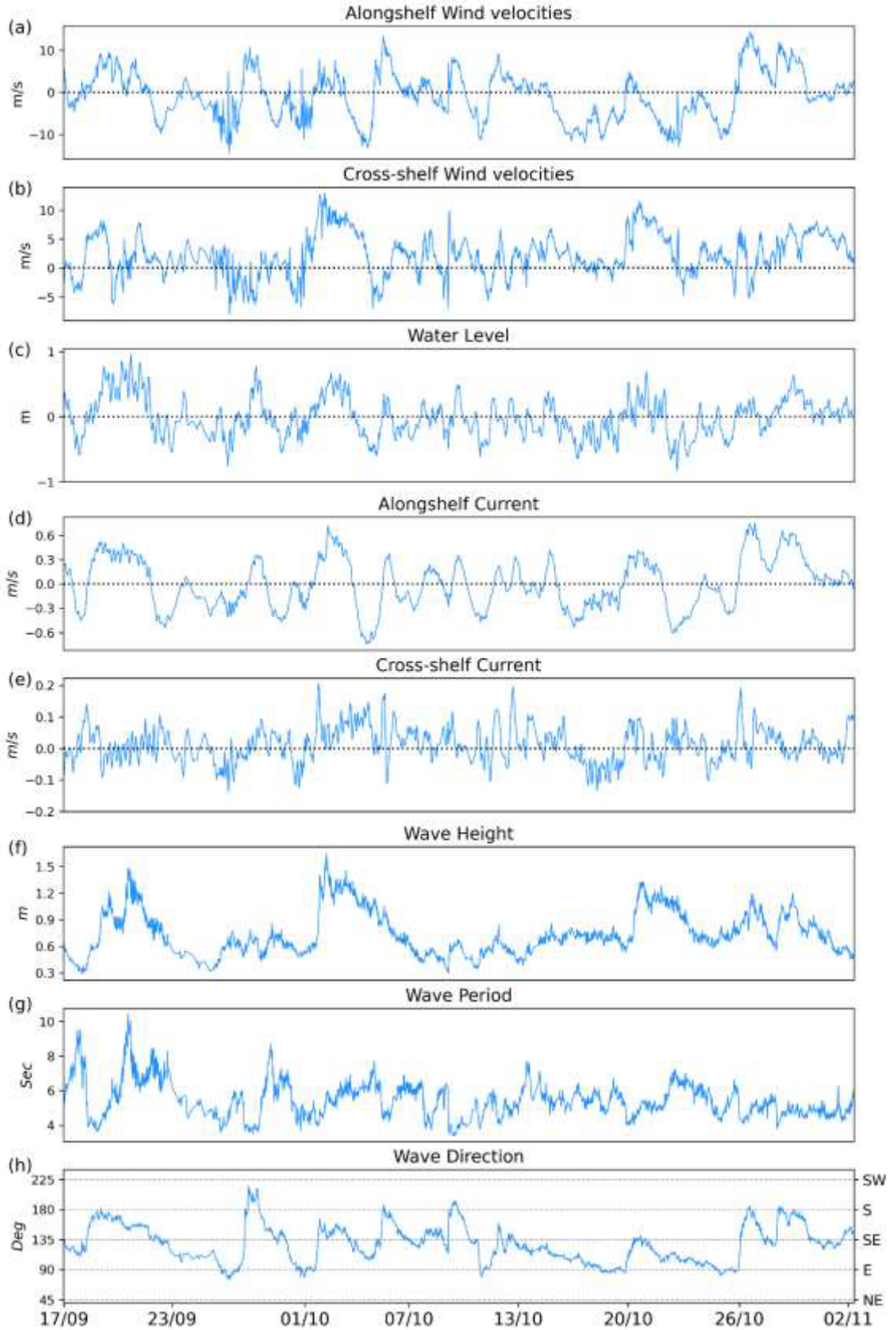

(a)
Alongshelf Wind velocities
m/s
10
0
−10
(b)
Cross-shelf Wind velocities
m/s
10
5
0
−5
(c)
Water Level
m
1
0
−1
(d)
Alongshelf Current
m/s
0.6
0.3
0.0
−0.3
−0.6
(e)
Cross-shelf Current
m/s
0.2
0.1
0.0
−0.1
−0.2
(f)
Wave Height
m
1.5
1.2
0.9
0.6
0.3
(g)
Wave Period
Sec
10
8
6
4
(h)
Wave Direction
Deg
225
180
135
90
45
SW
S
SE
E
NE
17/09
23/09
01/10
07/10
13/10
20/10
26/10
02/11

Figure 3 – Cap II. Time series of (a) longitudinal and (b) transverse wind velocities, (c) sea level oscillation, average water column velocity (d) longitudinal and (e) transverse, (f) wave height, (g) wave period, and (h) wave propagation direction.

During the observed period, the longitudinal and transverse wind speeds exceeded ±10 m/s for 8% and 2% of the time, respectively. There is also a higher frequency of negative longitudinal wind speeds and positive transverse wind speeds compared to the historical series. Approximately 59% of the observed wind speed data were negative for longitudinal winds, while in the historical series it was about 30%. On the other hand, observed transverse wind speeds were negative 34% of the time, while in the historical series it was 43% of the time. The greatest differences occurred at the 5th and 1st percentiles, where the transverse wind speed in the historical series reached -8 m/s and -11 m/s, while in the observed period, the transverse wind speeds were -3.8 m/s and -6.3 m/s, respectively (Figure 4 and Table 1).

The observed longitudinal current speed, although not showing significant average trends, exceeded 0.5 m/s for 6% of the time and -0.5 m/s for 4% of the time. The histograms estimate also demonstrate this slight tendency of positive velocities (> 0.5 m/s). There are no major variations between the observed and historical data, with a maximum difference of 0.1 m/s for the 1st percentile. The observed transverse current speed did not show significant average trends, and moreover, the variations of percentiles between the observed and historical data were less than 0.05 m/s. The greatest differences occurred at the 1st or 99th percentile, where historical transverse current speeds could be > 0.5 m/s, while the observed transverse current speeds were around 0.2 m/s.

The observed significant wave height exceeded 1 m for 20% of the time and was less than 0.5 m for 12% of the time. Duration curve shows that the greatest differences

between observed and historical data occur after the 1st percentile. The predominant observed wave direction is from the E-SE quadrant, with a median of 130° degrees, while for the historical series, the predominant wave direction is from the E-SE quadrant, with a median of 123° degrees. There is a difference of about 6° degrees between the percentiles of the observed and historical wave directions.

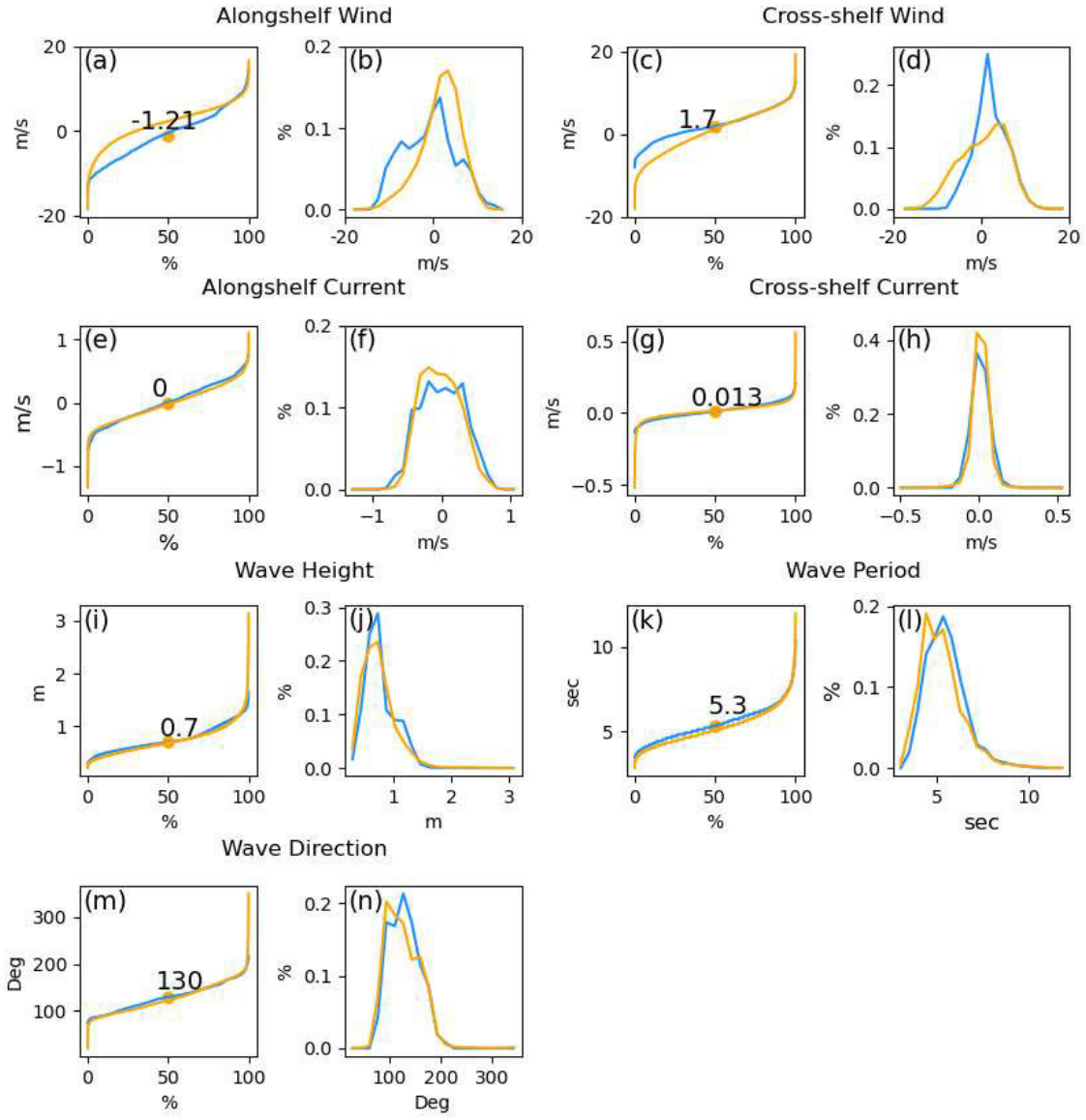


Figure 4 – Cap II. Duration curve and frequency distributions of the time series presented in Figure 3 for (a, b) longitudinal and (c, d) transverse wind speed, (e, f) longitudinal and (g, h) transverse current speed, (i, j) wave height, (k, l) wave period,

and (m, n) wave propagation direction. The blue lines represent the observed data during the ADCP mooring, and the orange lines represent the historical data series.

Table 1 – Cap II. Median and percentile values for the observed data during the ADCP mooring (M) and for the long-term records from the buoys (LT), for alongshore and cross-shore components of wind and currents, and wave parameters.

Parameter	Period	1th	5th	25th	50th	75th	95th	99th
Alongshore Wind (m/s)	M	-11.9	-10.25	-5.65	-1.21	2.3	8.38	11.84
	LT	-10.61	-6.8	-0.82	2.29	4.88	8.3	10.28
Cross-shore Wind (m/s)	M	-6.28	-3.83	-1.05	1.69	4.95	8.62	10.82
	LT	-11.25	-8.48	-3.21	1.26	4.82	8.37	10.76
Alongshore Current (m/s)	M	-0.66	-0.47	-0.23	0.0	0.26	0.52	0.66
	LT	-0.56	-0.43	-0.24	-0.03	0.19	0.45	0.63
Cross-shore Current (m/s)	M	-0.12	-0.08	-0.03	0.01	0.05	0.11	0.16
	LT	-0.15	-0.06	-0.01	0.01	0.04	0.08	0.14
Wave Height (m)	M	0.34	0.43	0.58	0.7	0.91	1.23	1.36
	LT	0.31	0.38	0.53	0.68	0.87	1.25	1.6
Wave Period (s)	M	3.59	3.95	4.7	5.31	6.07	7.37	8.68
	LT	3.4	3.7	4.4	5.0	5.8	7.3	8.9
Wave Direction (°)	M	81.42	87.15	106.96	129.76	149.9	176.9	198.23
	LT	75.07	84	101	122.8	151.3	180.1	204

Figure 5 presents the climatology of the hydrodynamic parameters recorded by the monitoring buoys in terms of monthly frequency distributions, represented by the median and the range of percentiles 1-99, 5-95, and 25-75%. The results from the monitoring period of the present study (Table 1) are indicated as a red bar for the month of October, with the indication of various percentiles. Overall, the hydrodynamic conditions observed in the experiment reasonably captured the expected variability throughout the year, especially for the longitudinal component of the current (Figure 5a), and to a lesser extent for the transverse components (Figure 5b), although for the latter only in April are there more significant occurrences of currents towards the coast. The

lowest climatological representativeness occurred with the significant wave height, for percentiles above 5%, especially when compared to the months of February, April, and July. The representativeness of the wave direction (Figure 5d) and period (Figure 5e) parameters was quite satisfactory, with only the months of May and June presenting differentiated extreme situations.

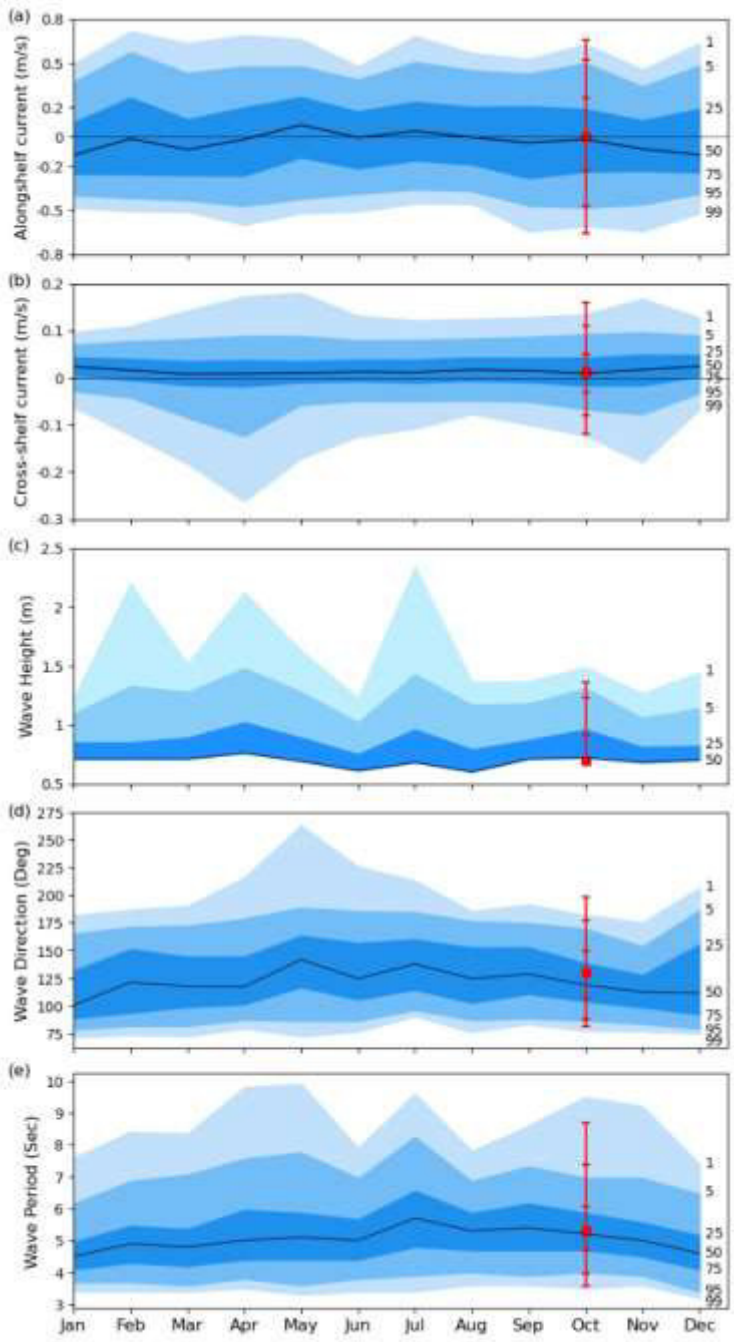


Figure 5 – Cap II. Monthly climatology of the alongshore (a) and cross-shore (b) components of the mean water column current, and of the wave height (c), direction (d), and period (e). The median value is represented by the black line, and the shades of blue represent the range of percentiles 1-99, 5-95, and 25-75%. The vertical red line in the month of October represents the data observed during mooring.

Figure 6 shows the result of the validation of the vertical SSC profiles generated by the Rouse theory, summarized in Table 2. Out of the total of 1765 profiles recorded during the study period, 55% were considered valid, 39% were rejected by the shear stress limit criterion, and 5% were rejected by the positive mean SSC gradient criterion, considering the hierarchical removal of the total profiles. This means, the first criteria selects the profiles when the environmental conditions are not favorable for sediment mobilization (low bed shear stress). The second criteria selects the profiles when the Rouse Theory does not apply, even under energetic conditions. Considering the overlap of criteria, out of the total profiles rejected by the shear stress criterion, 40% also had a positive mean SSC gradient. And considering the total profiles rejected by the positive mean SSC gradient criterion (370 profiles), 76% also had shear stress below the limit value.

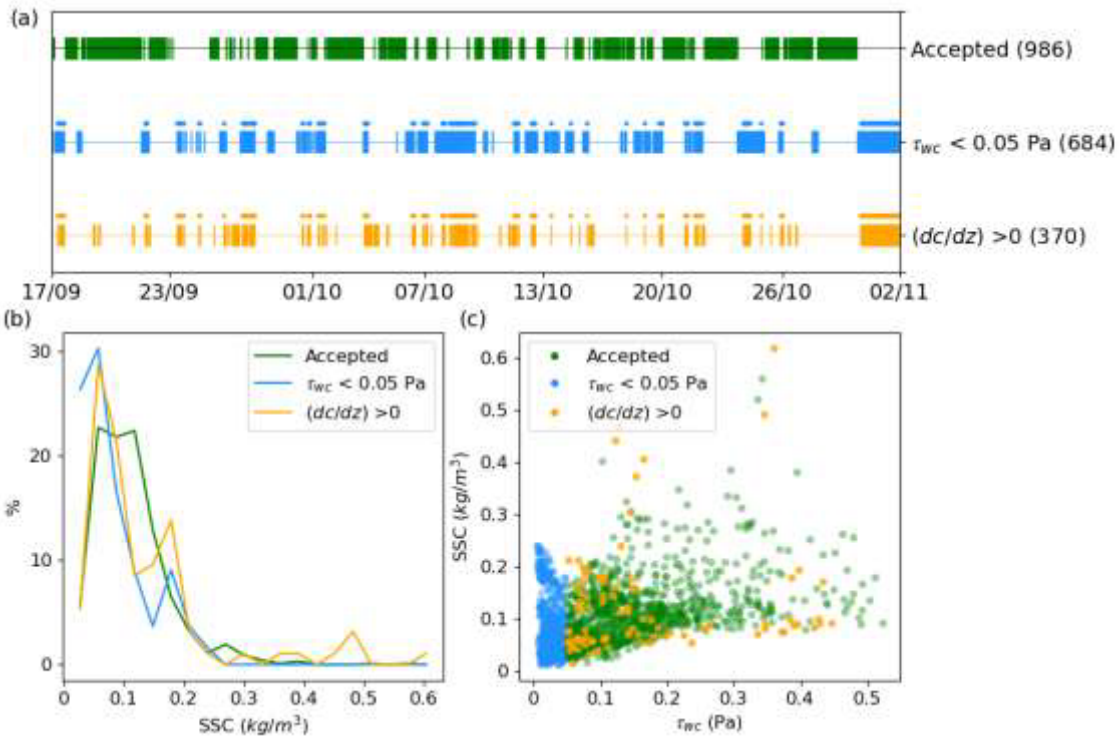


Figure 6 – Cap II. (a) Temporal indication of accepted and rejected vertical SSC profiles from the validation procedure. The profiles for each criterion are presented with

vertical bars, and the points on the bars for the exclusion criteria indicate the overlap with the other criterion. (b) Frequency distributions of mean SSC for each selection category, and (c) relationship between shear stress and mean SSC for each selection category.

Table 2 – Cap II: Summary of the validation results for vertical SSC profiles, including the total number of profiles and the remaining profiles after selection by the criteria of shear stress ($\tau_{mwc} < 0.05$) and positive vertical mean SSC gradient ($\left(\overline{\frac{dC(z)}{dz}}\right) > 0$), also indicating the percentage, mean, and maximum SSC for each subset (SSC and C(z) are in kg/m³ and τ_{mwc} is in Pa).

Condition	#	%	$\overline{SSC}$ (kg/m^3)	SSC_{max} (kg/m^3)
Total	1765			
$\tau_{mwc} < 0.05$	684	39	0.22	0.46
$\left(\overline{\frac{dC(z)}{dz}}\right) > 0$	95	5	0.3	0.85
Validated	986	55	0.27	0.8

The time series of the bottom shear stresses (by currents, τ_c, waves, τ_w, and combined current+waves, τ_{mwc} and τ_{maxwc}), turbulent diffusion coefficient (ε_s), RMSPE, suspended particle size (d_s), and particle terminal velocity (w_s) are presented in Figure 7, with their respective frequency distributions. The statistical parameters of these time series are summarized in Table 3.

The bottom shear stress by currents and waves presented a relatively similar values, with the ones due to currents being slightly more pronounced. However, the combined effect (τ_{mwc} and τ_{maxwc}), the effect of waves appears to have a minor role. The turbulent diffusion coefficient (e_s) followed the oscillations of the bottom shear stress, with a mean value of 0.92 cm²/s and a maximum of 1.77 cm²/s. The RMSPE of the

SSC_{rouse} estimates in relation to SSC_{ABS} showed a median of 5 %; furthermore, the highest RMSPE values showed a trend with the peaks of τ_{mwc}, while the lowest values were seen when τ_{mwc} is less than 0.1 - 0.2 Pa, approximately (Figure 7c). Estimates of the mean sediment size (d_s) had a median of 25 μm and a maximum value of 50 μm; the median particle terminal velocity (w_s) was 0.15 cm/s, with a maximum value of 0.7 cm/s.

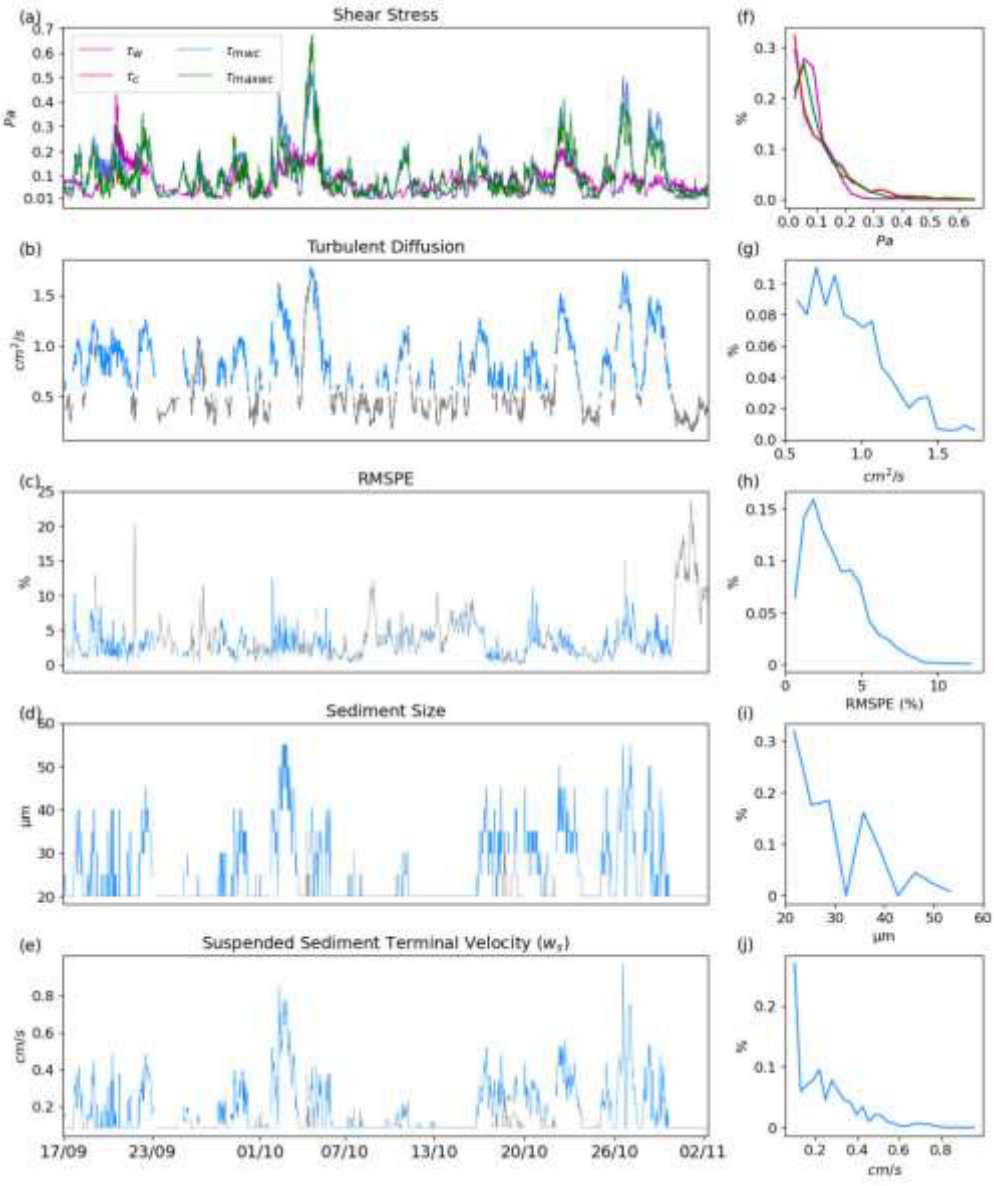


Figure 7 – Cap II. The left-hand side graphs display the time series of (a) bottom shear stress produced by waves (fuchsia), currents (red), mean wave-current combined (blue) and maximum wave-current combined (green), (b) turbulent diffusion coefficient,

(c) root mean square percentage error - RMSPE, (d) sediment size, and (e) particle terminal velocity in suspension. On the right-hand side of each panel, the respective (f, g, h, i, and j) frequency distributions for each parameter from the first column are presented. Valid profile data are shown in blue, and discarded profiles are shown in gray. The frequency distributions are only for valid data.

Table 3 – Cap II. Mean values, standard deviation (σ), and percentiles of shear stress data, turbulent diffusion, RMSPE, sediment size, and particle terminal velocity.

Parameter	Mean	σ	1th	5th	25th	50th	75th	95th	99th
Max Shear-stress wc (Pa)	0.1	0.09	0.01	0.02	0.04	0.07	0.13	0.26	0.44
Mean Shear-stress wc (Pa)	0.1	0.1	0.01	0.01	0.03	0.08	0.15	0.32	0.45
Shear-stress current (Pa)	0.1	0.1	0.01	0.01	0.03	0.07	0.14	0.31	0.44
Shear-stress wave (Pa)	0.08	0.05	0.01	0.02	0.04	0.07	0.11	0.18	0.23
Turbulent diffusion (cm^2/s)	0.92	0.26	0.56	0.58	0.72	0.88	1.07	1.43	1.68
RMSPE (%)	5.5	2.8	1.32	1.94	3.3	5.02	7.38	10.69	13.01
Sediment size (μm)	25	6.3	20.0	20.0	20.0	25.0	30.0	40.0	45.0
Settling velocity (cm/s)	0.18	0.11	0.09	0.09	0.09	0.15	0.23	0.38	0.52

The Figure 8 presents the time series of mean water column SSC obtained from the inversion of ADCP data and from the Rouse model, along with the respective Hovmöller diagrams showing SSC distributions over time and in the water column. For the most part, the equivalence of SSC values was excellent, with low RMSPE values. However, about 55% of the SSC_{ABS} time series was used in the Rouse model, while the rest of the series showed higher concentrations near the surface than at the bottom, making it impossible to apply the Rouse model.

The median of the SSC_{ABS} series near the bottom (0.9 m) showed concentrations of 0.31 kg/m^3, and near the surface (14.4 m), concentrations of 0.15 kg/m^3. At some moments, SSC_{ABS} measurements showed higher concentrations in the upper layers compared to the bottom, with maximum differences of up to 0.42 kg/m^3 on 01/11. On the

other hand, the maximum difference between the bottom and the surface was up to 0.73 kg/m³ on 03/10.

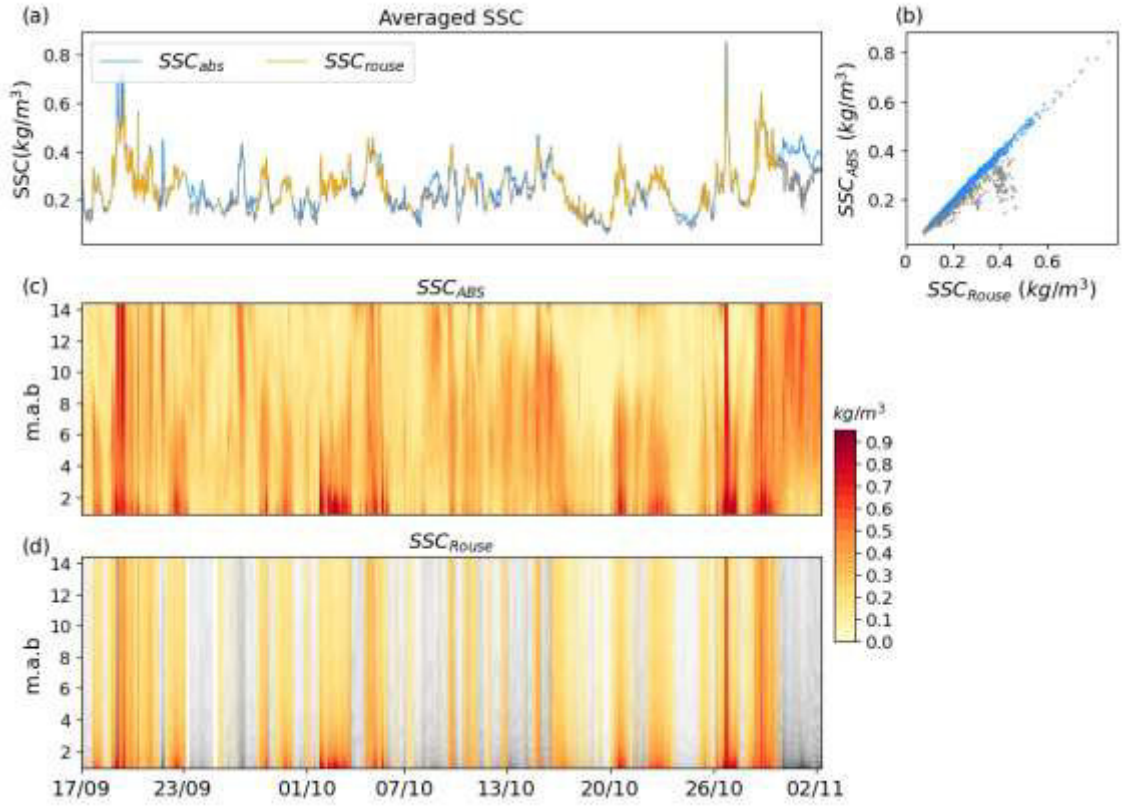


Figure 8 – Cap II. (a) Time series of mean water column SSC obtained from ABS and Rouse model, and (b) the respective relationship between them. (c) and (d) Hovmöller diagrams for SSC distributions derived from ABS and Rouse, respectively. The gray areas in (d) indicates the discarded profiles.

8.1 Discussion

Rivers are the main sources of sediment for continental shelves (Swift, 1974). Coarse sediments (sands) will be deposited near the sources and become involved in processes related to coastal dynamics, whereas fine sediments (muds) will be transported in suspension and their dispersion will be influenced by factors controlling shelf hydrodynamics (density gradients, wind and tidal currents, and waves) (Swift and Thorne, 1991; Walsh and Nittrouer, 2009). Once released onto the shelf, fine sediments enter a cycle of deposition/erosion/transport depending on the momentary environmental conditions (Wiseman and Garvine, 1995). Thus, although the sediment source is initially rivers, the presence of suspended sediments in the water column at a given location can be interpreted as either horizontal advective processes (transport) or exchange processes with the seafloor (deposition/erosion), with temporal variability ranging from hours to days (Traykovski et al., 2000), which is the scenario captured in our observations.

Our results demonstrated that the use of the inversion method of ABS to estimate the vertical distribution of the SSC, in conjunction with and the application of Rouse theory, are valuable tools for evaluating sediment characteristics and/or examining vertical SSC trends in coastal environments or continental shelves (Lynch et al., 1994; Lee et al. 2002; Shi et al., 2002; Yuan et al., 2008; Liu et al.,2014, Al-Ragum et al.,2014). Rouse theory assumes that vertical SSC profiles are in equilibrium between downward settling flux and upward turbulent diffusion flux, resulting in profiles with an exponential increase in SSC towards the bottom. However, observed SSC profiles can exhibit various shapes (Liu et al., 2014), in situations where the estimated Rouse profile does not reflect the observed profile. We observed profiles where SSC where higher in the upper layers

than near the bottom. These situations indicate that the main sediment source for the water column at the position of observation is not the bottom: it could be due to horizontal advection or aerial deposition, and Rouse theory does not apply. The present case, the vertical SSC distribution agreed with the Rouse theory in most of the time when the conditions were energetic enough to mobilize sediments. This supports the idea that the main sediment source for the water column is the seabed. The role of horizontal advection is secondary, even though the study area is relatively close (~10 km) to the mouth of Patos Lagoon and potentially influenced by it (Marques et al., 2010).

A key parameter to apply the Rouse theory is the vertical turbulent diffusion of suspended sediments, which results from the interaction between the fluid and the bottom, and is scaled based on the bottom shear stress. We used the approach proposed by Soulsby and Clarke (2005), to obtain the bottom shear stress, which allowed us to compute the combined effects of waves and currents, over rough or smooth beds. It employs an empirical approach based on the quadratic addition of shear stresses from waves and currents to estimate τ_{mwc}, also accounting for the directional difference between flow and wave action to determine τ_{maxwc}. On the other hand, the method of Grant and Madsen (1979) models the nonlinear interactions between waves and currents based on the fundamental laws of fluid mechanics, including the concept of apparent roughness and considering the angle between the flow and the wave propagation direction. Finally, Myrhaug et al. (1997) employs a probabilistic approach based on the Weibull distribution, where the directional difference between flow and wave action is indirectly accounted for. Long-term time series analyses are ideal for this approach as they include the natural variability of waves and currents. One way to determine the best stress value to use is simply to identify which one best explains the SSC near the bed. In this case, the coefficient of determination (r^2) of SSC with τ_{mwc} and τ_{maxwc} were 0.82 and 0.69,

respectively. In Figure 7a, it can be observed the low contribution of $\tau_w$to the estimates of τ_{mwc} and τ_{maxwc} even with relatively high values of τ_w compared to τ_c, the increment was low and without significant variations between τ_c, τ_{mwc}, and τ_{maxwc}. The greatest variations occurred between the maximum values of $\tau_c$and τ_{maxwc}, 0.64 Pa and 0.53 Pa, respectively.

During the observation period, there was a single short-lived occurrence (1 hour on October 27th) where the vertical profile showed indications of disqualification due to a positive vertical gradient, despite energetic environmental conditions (τ_{mwc} = 0.38 Pa). This situation was recorded in only 1% of the records. During this period, the SSC was ~ 0.9 kg/m^3 at the surface layer and ~ 0.72 kg/m^3 near the bed. The wind was blowing to the north (velocity = 12 m/s), and the longitudinal component of the current was also to the north (velocity = 0.5 m/s). These conditions, even if for a brief moment, indicate that the input of SSC by horizontal advection was as relevant as by vertical diffusion (Figure 8c). It is interesting to note that this event indicated transport parallel to the coast, rather than directly associated with an input from the Patos Lagoon plume.

During the period between October 30th and November 2nd, a period was recorded where the SSC_{ABS} near the surface was higher than SSC_{ABS} near the bed, with relatively low bottom shear stress values (~0.02 Pa), an E/NE wind direction (164°), average alongshelf and cross-shelf wind speeds of -0.8 m/s and 4.6 m/s, respectively, and depth averaged alongshelf current speed of 0.06 m/s. As it will be detailed in the next section, these conditions favor the cross-shelf circulation, with the upper layer moving offshore, along with the ebb flow from the Patos Lagoon (Moller et al., 2001), leading to the formation of a sediment rich buoyancy plume (Marques et al., 2010). These conditions suggest that during this particular period the presence of higher SSC at the upper layer

may be explained in terms of horizontal advection (Figure 8c). In the study by Yuan et al. (2008) in Jiaozhou Bay, China, it was reported that during periods of weak currents (< 0.15 m/s), the Rouse model used (Perlin et al., 2005) was not satisfactory and thus disregarded.

Although the data recording period was relatively short (45 days) and covered only the spring period, the estimates generated by the Rouse theory showed good temporal representativeness, as the frequency distributions of oceanographic parameters (waves & currents) were similar to those of long-term series, or even when compared to monthly climatology. Only extreme events where the frequency distribution is > 99% or < 1% were not observed. The greatest discrepancy concerning environmental conditions is related to wave height. However, as seen earlier, the contribution of τ_w to the estimates of τ_{mwc} was low, meaning that even under extreme wave conditions, the estimates of τ_{mwc} will not change significantly compared to the maximum values obtained in this study.

Even though it is relatively close to the mouth of Patos Lagoon, sediment dynamics and transport were dominated by processes of exchange with the seafloor. This allows inferring that most of the shelf in the depth range between 15 and 25 m responds similarly. As one approaches the coastline, other mechanisms start to influence the fluid force, such as wave action under storm or low-energy conditions, thus a model that combines diffusion-advection, or solely vertical advection, may provide more realistic estimates (Lee et al., 2002). The buoyant plume coming from the estuary mouth and interacting with shelf currents can be another source of sediment by horizontal advection (Swift and Thorne, 1991). Therefore, the estimates obtained in this study by the Rouse and Soulsby theories cannot be extrapolated to the region closer to the surf zone or the

mouth of Patos Lagoon, as the input of SSC by advection becomes increasingly notable. For deeper regions, the estimates of τ_{mwc} and τ_{maxwc} will gradually decrease since the amount of turbulent energy generated by waves and/or currents diminishes gradually with distance from the seafloor. Additionally, the shelf region is dominated by the fluvial influence of the Rio de la Plata and Patos Lagoon, with different quantities and periods, and according to oceanographic conditions (Moller et al., 2001; Piola et al., 2008). Thus, at latitudes greater or lesser than the two estuary mouths, the input of suspended material by horizontal advection becomes less or more noticeable in the surface layers.

Consequences for Sediment Transport:

Depending on the wind direction and coastline configuration, resultant currents may cause either stacking (water level rise) or subduction (water level decrease) near the coastline, creating a positive or negative pressure gradient favoring transport towards the sea or shore, near the seafloor (Niedoroda et al., 1989; Niedoroda et al., 1985; Austin et al., 2002). Three periods of data records were selected to assess these more energetic hydrodynamic conditions, which exhibited the highest bottom shear stress values, with τ_{mwc} above 0.2 Pa, and mean longitudinal current velocities above 0.5 m/s (Table 4). Period 1 (October 2nd and 3rd) showed the highest mean values of wave height and sea level oscillation. Period 2 (October 4th and 5th) displayed the highest mean and maximum longitudinal current velocities, and the mean and maximum τ_{mwc} were higher compared to periods 1 and 3. Period 3 (October 27th and 28th) exhibited the lowest mean values of sea level oscillation and wave height, and a mean and maximum τ_{mwc} similar to period 1 (Table 4).

Table 4 – Cap II. Oceanographic parameters for periods 1, 2, and 3 as indicated in Figure 10. WL represents the sea level oscillation in meters. U and V denote the mean or

maximum longitudinal and transverse velocities, respectively (m/s). τ represents the mean or maximum bottom shear stress produced by waves and currents (Pa). w_s is the terminal particle velocity (cm/s), and d_s is the mean particle size (μm).

	WL	U_{mean}	U_{max}	V_{mean}	V_{max}	τ_{mean}	τ_{max}	$Wave_{height}$	$Wave_{dir}$	w_s	d_s
	(m)	(m/s)	(m/s)	(m/s)	(m/s)	(Pa)	(Pa)	(m)	(deg)	(cm/s)	(μm)
1	0.44	0.5	0.72	0.03	0.08	0.24	0.44	1.31	145	0.5	41
2	-0.3	-0.55	-0.74	0.09	0.15	0.33	0.52	1.09	114	0.24	29
3	0.13	0.5	0.75	0.04	0.19	0.28	0.5	0.9	155	0.41	38

In period 1, when the wind is coming from the south, at around 9 m/s, the longitudinal current flows northward, and the transverse current in the upper layer moves towards the coast, while that in the lower layer moves towards the open ocean (Figure 9c). In period 2, when the wind originates from the northeast, at about 10 m/s, the longitudinal current flows southward, and the transverse current separates, with the upper layer flow heading towards the open ocean and the lower layer towards the coast (Figure 9d). In period 3, when the wind direction is south, at around 12 m/s, the longitudinal current flows northward, and the transverse current in the upper layer moves towards the coast, while that in the lower layer moves towards the open ocean (Figure 9e).

It was observed that near-bed flow (at 0.9 m depth) transports more suspended sediment material when the flow direction is northward; in periods 1 and 3, the median SSC_{ABS} near the bed was higher compared to period 2 when the flow had a southward direction (Figure 10c-h-m). Even when the mean τ_{mwc} is similar in periods 2 and 3, the mean integrated SSC_{ABS} depth-wise in period 2 was 0.29 kg/m^3, whereas in period 3, it was 0.34 kg/m3. The low values of w_s and $d_s$in period 2 may be related to the concentration and τ_{mwc}; even with similar turbulence forces, at low concentrations, the collision rate is low, preventing the formation of larger flocs, while at high concentrations, flocculation occurs due to the high collision rate. However, this shear stress force

promoting flocculation can also be responsible for breaking the flocs, as turbulence forces increase, flocs with lower binding force break apart. According to laboratory studies by Manning et al. (2010), for a mixture of 75% mud and 25% sand, the τ required for the initiation of micro-floc breakage is 0.6 Pa, and for macro-flocs, it is 0.35 Pa, with floc breakage facilitated at higher concentrations (5 g/l).

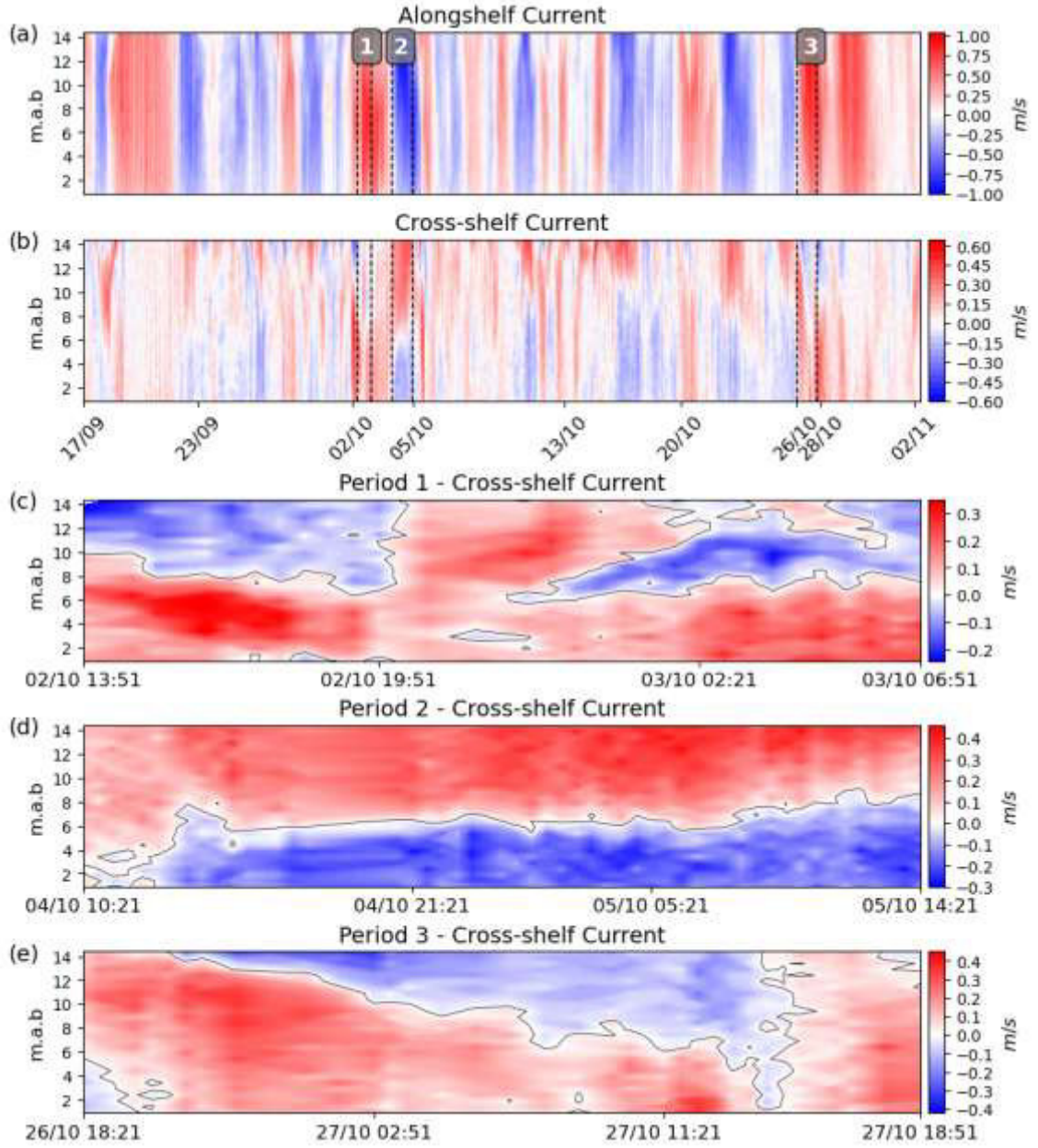


Figure 9 – Cap II. Hovmöller plot of longitudinal and transversal velocity along the water column. In (a), red colors indicate currents with northward direction, and blue

indicates southward direction. In (b) and (c), red colors indicate currents directed towards the coast, and blue indicates currents directed towards the open ocean.

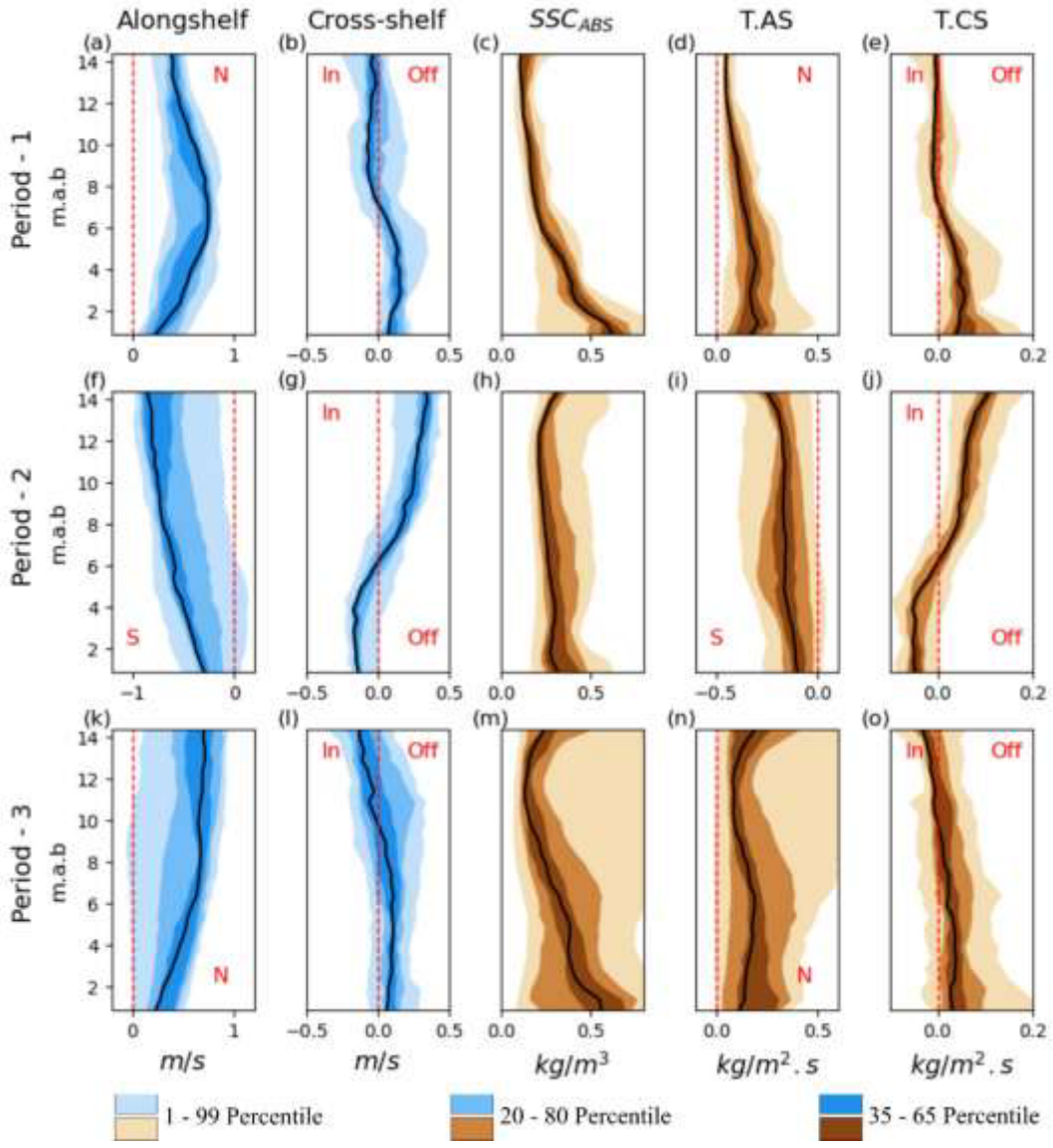


Figure 10 – Cap II. Plots (a, b, c, d, e) show the calculated duration curve for period 1, plots (f, g, h, i, j) for period 2, and plots (k, l, m, n, o) for period 3. In black, the median, and shades of brown and blue indicate the percentiles 1%, 20%, 35%, 65%, 80%, and 99%. T.AS represents alongshelf sediment transport and T.CS represents cross-shelf sediment transport.

Approach limitations:

The Rouse model assumes equilibrium between settling velocity and turbulent diffusion, and does not consider water stratification, which is a common feature on shelves and can affect considerably the vertical turbulent diffusion (Rippeth, 2005). Low-energy conditions (no turbulent diffusion) and horizontal advection also limits its application, as indicated by the exclusion of 45% of SSC_{rouse} profiles. The threshold value of bottom shear stress to separate 'high' and 'low' energy conditions can vary in time and space, in response to the bottom rheological properties (Winterwerp and van Kesteren, 2004).

The validation of the parameters obtained from the best fit (suspended particle size and settling velocity) can be verified through direct observations; however, their representation remains limited. Particle size can be measured in situ using laser scattering devices (e.g., LISST by Sequoia https://www.sequoiasci.com) and could be moored together with the ADCP, though not without technical challenges related to fouling. Measuring particle settling velocity in coastal waters remains a major challenge. It can be done using a settling tube (Owen tube) or more intricate optical devices operating under calm sea conditions (Dyer et al., 1996).

The interaction between the currents and waves on the bottom shear stress, which ultimately will give the vertical turbulent diffusion, is a complicate matter based on methodological assumptions rather than purely physical processes, differing from each author (Grant and Madsen, 1979; Myrhaug et al., 1997; Soulsby and Clarke, 2005). The SSC_{rouse} estimates obtained from acoustic backscatter SSC_{ABS} might be limited to regions with relatively high SSC (> 10 mg/L), and it will depend on how satisfactory is the calibration achieved. At low concentrations, estimated SSC_{ABS} may have higher error due

to echo attenuation or the equipment limitation to detect smaller particles in clear waters. Furthermore, the empirical relationship used to convert acoustic backscatter to SSC may not fully account for in sediment, flocculation dynamics, or acoustic scattering properties.

9.1 Conclusion

The approach of coupling the SSC profiles estimated from ADCP records with SSC profiles predicted by Rouse theory provided valuable insights on the continental shelf off the state of Rio Grande do Sul in Brazil. The results indicate that when the environmental conditions are energetic, sediment resuspension and transport were primarily controlled by bottom shear stress generated mainly by currents. The Rouse profile explain satisfactorily the observations, what indicates the balance between settling velocity and turbulent diffusion. Although horizontal advection played a secondary role under most conditions, it became relevant during periods of weak currents and low bottom shear stress.

Periods of high-energy conditions revealed distinct transport patterns associated with upwelling and downwelling. When the longitudinal current was northward, bottom SSC was higher, enhancing sediment transport along the seabed. Conversely, southward currents corresponded to lower bottom SSC and a more vertically uniform distribution, suggesting reduced resuspension and greater mixing throughout the water column (Figure 10). These findings align with downwelling conditions enhancing near-bed transport, while upwelling conditions favor a more homogeneous SSC profile.

The study also provided insights into sediment characteristics. The median grain size was 25 μm, with a maximum of 50 μm, and the median settling velocity was 0.15 cm/s, reaching up to 0.7 cm/s. These values are consistent with previously reported sediment characteristics for coastal waters and reinforce the validity of the Rouse-based estimates.

The combination of ADCP-derived SSC estimates and Rouse theory proved to be an effective framework for assessing suspended sediment dynamics in the inner shelf, providing a valuable tool for future studies.

10.1 Acknowledgements

We would like to express our gratitude to all the individuals who provided assistance during the intensive field experiment. We are also thankful for the support from the Office of Naval Research (ONR Grant N62909-19-1-2145), Brazilian National Science Council (CNPq, #316037/2021-4), through INCT-COI and PELD Estuário da Patos Lagoon. To the Coordenação de Aperfeiçoamento de Pessoal de Nível Superior – Brasil (CAPES) for GC's scholarship.

Capítulo III: HYDRODYNAMICS OF AN INNER SHELF SHELTERED BY LONG JETTIES

1.1 Abstract

This study investigated the hydrodynamics of the inner shelf in the sheltered area created by the 4-km long jetties at the Patos Lagoon mouth. A field experiment was designed to capture the horizontal and vertical hydrodynamic patterns at the southwestern side of the jetties during an intense northeast wind event. Despite the experiment lasted for a short period of time, the analysis of temporal representativity, in relation to a long-term time series, demonstrated robust coverage that validates the applicability of the obtained results. Two vortices were observed: one near the coast with counterclockwise rotation and another in the outer portion of the jetties with clockwise rotation. Additionally, the jetties are permeable, allowing the flow of low-salinity water through

them, highlighting the importance of baroclinicity in understanding the local hydrodynamics. This stratification, marked by the presence of a pycnocline, results in the decoupling of the upper and lower layers, accumulating wind-driven momentum in the upper layer and consequently intensifying the vertical gradient of longitudinal and cross-shelf velocity. The jetties permeability allowing the flow of low density waters, creating stratification in the sheltered area, extends the southwestwards the effect of the jetties on the inner shelf farther away.

Keywords: circulation, stratification, Patos Lagoon mouth.

2.1 Introduction

The continental shelf is the region connecting the coast to the open ocean and plays a crucial role in the exchange of water masses and material transport between these environments. This region is considered a key area for interdisciplinary research due to its significance in water mass exchanges between the ocean and the coast, and for material transport such as sediments, nutrients, larvae, phytoplankton, and contaminants, which originate from various sources, including river discharge, outfalls, coastal erosion processes, or atmospheric deposition (Austin et al., 2002; Lentz et al., 2012; Moulton et al., 2023).

The continental shelf is divided into the outer and inner shelf. The inner shelf refers to the coastal sector with higher influence of continental influence, such as the freshwater inflow. In dynamic terms, it differs from the outer shelf in the sense that the

turbulent boundary layers of the surface and bottom occupy the entire water column (Lentz, 1995). The main mechanisms driving hydrodynamic circulation on the inner shelf are the coast line morphology, bathymetry, wind shear stress, tides, and river discharge. The processes occurring on the inner shelf play an important role in the hydrodynamics of the entire shelf, as it is the region where the flow adjusts to the coastline and frictional effects are more intense. Although the along shelf current component is more energetic and dominant in the flow, the cross-shelf circulation exerts significant impacts, particularly on material transfer processes across the shelf (Brink, 2016). The cross-shelf divergence of Ekman transport on the inner shelf drives both upwelling and coastal downwelling, affecting sediment transport, dissolved nutrient supply to the shelf, regulating residence time, redistributing heat and salinity, determining biogeochemical balances, transporting planktonic organisms, and removing contaminants from the coastal region (Gill and Clarke, 1973; Simpson and Sharples, 2012; Brink, 2016; Moulton et al., 2023).

One of the major challenges in coastal hydrodynamics lies in understanding the processes controlling cross-shelf exchange processes. Although significant advances have been made recently in understanding cross-shelf material exchange, the problem of cross-shelf circulation greatly depends on the specific conditions of each area (Brink, 2023). Various phenomena occur simultaneously with varying intensities across different spatial and temporal scales, such as tidal forcing, bottom stress, wave or current stress, Stokes drift, Earth's rotation effects, and baroclinicity due to continental drainage (Brink, 2016; Moulton et al., 2023).

Due to the pressure of economic and port growth, coastal protection measures, jetties, and groins perpendicular to the coastline are constructed to stabilize estuarine mouths, ensure navigation safety, and minimize coastal erosion. However, these

interventions create obstructions to the longitudinal flows of the inner shelf and consequently also affect the cross-shelf circulation, impacting material transport across the shelf (Rosa-Santos et al., 2009; Kudale, 2010; Dias et al., 2011; Dugan et al., 2012; Ostrowski et al., 2012; Peixoto et al., 2016; Guimarães et al., 2016; Franzen et al., 2021; Filho et al., 2023). The jetties at Patos Lagoon mouth were constructed in the 1910s and are among the largest coastal engineering works of their time (Motta, 1969; Bicalho, 1983). The motivation for this construction was to stabilize the lagoon bar, ensure navigation safety, and provide access to the Port of Rio Grande. Construction began in 1911, and in its final configuration, the jetties extended 4 km offshore from the coastline (Bicalho, 1983; Motta, 1969; Cunha et al., 2009). The construction material used was loose stones, and in 2010, the jetties were modified with tetrapod blocks (Migliorini et al., 2008), resulting in a permeable structure, with the final portion located in an area of 15 m depth. The jetties represent the only obstruction, almost perpendicular to the coastline, in an extensive beach stretching between Chuí, 215 km to the south, and Torres, 390 km to the north (Fig. 1).

Under N-NE wind conditions, currents on the inner shelf flow southward (Cruz and Schettini, 2023). The presence of the jetties creates a sheltered area southwestward. In this sheltered area, a clockwise vortex forms, which, according to Vinzon et al. (2009) and Franzen et al. (2023), favors the deposition of fine sediments on the inner shelf offshore of Cassino beach. These studies were based on numerical simulations. Although the horizontal flow of currents is well represented, the limitations imposed by boundary conditions and numerical schemes do not allow for the reproduction of the hydrodynamic complexity of this region. This process of cross-shelf sediment transport is thought to be related to mud deposition events on the beach (Pereira et al., 2011), which remains an unresolved phenomenon.

This study aims to investigate the hydrodynamics in the sheltered area formed by the presence of the jetties at the mouth of the Patos Lagoon. In a broader sense, the effects of a nearly orthogonal to the coast line obstruction on the long shelf flow, and its impacts on the cross-shelf flows, and their consequences for material transport dynamics around these obstructions. For this purpose, the jetties at Patos Lagoon mouth present an excellent case study due to their dimensions. This study is based on climatological analyses of long-term meteorological model data and oceanographic observations (current velocity, salinity, density, and turbidity). Vertical and horizontal hydrodynamic patterns in the shadow zone created by the jetty were observed through a short-term experiment, and the results illustrate the local hydrodynamic complexity. The intensity and patterns of cross-shelf and longitudinal circulation were compared with areas unaffected by the obstruction.

3.1 Study Area

The continental shelf of the state of Rio Grande do Sul extends approximately along a northeast-southwest axis between Arroio Chuí (34° S) and Torres (29° S), with a coastline characterized by a long sandy beach interrupted by the Patos Lagoon mouth (Figure 1). The continental shelf width varies between 100 and 180 km, with the shelf break depth at around 180 m and a gentle bottom slope. In the vicinity of the Patos Lagoon mouth, the shelf is relatively flat, featuring extensive sandy banks to the north and south of the mouth (Fachin, 1998; Corrêa et al., 2019).

Southwestward of the Patos Lagoon mouth is the Cassino Beach, where occurs unconsolidated mud deposits on the inner shelf. During certain high-energy events, these

deposits can be remobilized and transported towards the coast, potentially resulting in mud deposition on the beach with various economic, ecological, and geomorphological impacts (Calliari et al., 2001; Calliari et al., 2007; Calliari et al., 2009; Holland et al., 2009; Pereira, 2011). The areas with the highest mud concentrations are found in the Rio Grande Cone, consisting of relic mud deposited under past conditions when sea levels were lower than current levels, and at the mouth of Patos Lagoon with contemporary contributions (Martins et al., 2003). Non-mud sediment (NMS) showed the lowest concentrations between 31ºS and 33ºS, accounting for approximately 30% of the total. Between the mouth of the Rio de la Plata and 33ºS, NMS concentration ranges from 60% to 70%, while north of 31ºS, the concentration is approximately 40% to 50% (Campos et al., 2008). The sediment material drained into the Patos Lagoon system is lithologically composed of sedimentary, volcanic, and plutonic rocks, primarily transported by the Guaíba River. Coarser sediments are retained in the depositional bay of the Guaíba River (~500 km²), while finer sediments, which do not find favorable deposition conditions, are transported to the mouth of Patos Lagoon and subsequently deposited on the inner continental shelf (Corrêa et al., 2019; Toldo et al., 2006).

The climate of the region is classified as humid temperate with hot summers (Cfa) according to the Köppen-Geiger classification and as humid subtropical according to the Strahler classification. There is a significant thermal amplitude between summer and winter (11°C), with the highest temperature in January (23°C) and the lowest in July (12°C), with an annual average of 19°C (Reboita and Kruche, 2018). The wind regime is controlled by two high-pressure systems: in summer, the South Atlantic Subtropical Anticyclone (ASAS) is more intense, and in winter, the mobile polar anticyclone increases its influence. In spring, the center of ASAS moves eastward, and in winter, ASAS moves to lower latitudes with its western sector affecting the coast of Rio Grande

do Sul. Consequently, there is a predominance of NE winds throughout the year, with higher intensity in spring (Reboita & Kruche, 2018; Saraiva et al., 2003). This pattern is cyclically disturbed by the passage of frontal systems occurring at intervals of 6 to 11 days (Stech and Lorenzetti, 1992). In the region around the Patos Lagoon mouth, the predominant wind throughout the year is from the N-NE quadrant, with a decrease in frequency during winter (Cruz and Schettini, 2023).

The local tide is mixed with a diurnal predominance, with an average amplitude of 0.3 m, and does not play a significant role in the hydrodynamics (Moller et al., 2007). The flow is primarily driven by local wind (Soares et al., 2001; Zavialov et al., 2002; Costa et al., 2011; Cruz and Schettini, 2024). Current regime have been investigated with observational data at a depth of 48 m, approximately 125 km from the mouth. Current measurements with two anchored current meters showed a barotropic response of the longitudinal current to the longitudinal wind forcing. Contrary to theoretical expectations (Brink et al., 2023), favorable downwelling winds exhibited a near-bottom flow towards the coast, while favorable upwelling winds displayed a bottom current directed offshore (Soares et al., 2001). At a depth of 15 m, current patterns were consistent with Ekman force balance, where southward longitudinal currents showed a return flow in the deeper layers of the water column (Costa et al., 2011). At a depth of 20 m, 11 km from the jetty, cross-shelf circulation gradients were also observed during upwelling or downwelling wind events (Cruz and Schettini, 2024).

Exchange patterns between the lagoon and the coastal region have been investigated by Hartmann and Schettini (1991), Moller et al. (2001), Marques and Moller (2008) and Santa-Rosa and Schettini (2024). The combined action of wind and river discharge is the main factor controlling the exchange processes. During periods of high rainfall, river discharge predominates and drives ebb flow. During low rainfall periods,

wind becomes the primary control of exchange processes. Winds from the southern quadrant increase coastal water levels, driving flood flow at the estuary mouth. Winds from the northern quadrant produce the opposite effect. During ebb events, a buoyant plume is formed, intensifying baroclinic processes in the coastal region. However, the entire area is influenced by the fluvial discharge of the Rio de la Plata, especially during periods of higher occurrence of winds from the S-SE quadrant, which displaces the low salinity plume to lower latitudes (Piola et al., 2008).

The Rio de la Plata has an average discharge of 23,000 to 28,000 m^3/s (Urien, 1972), with suspended solid discharge on the order of 100 x 10^6 tons/year (Isupova and Mikhailov, 2018), making it the main regional source of sediment for the shelf. Suspended sediment concentration (SSC) values on the shelf off the Plata estuary can reach 200 mg/L (Moreira et al., 2013). The average discharge of Patos Lagoon is approximately 2,400 m^3/s (Vaz et al., 2006). The average suspended solid discharge of the Rio Guaíba, the main tributary of Patos Lagoon, is 1.1 x 10^6 tons/year (Andrade et al., 2012). SSC values observed near the mouth of Patos Lagoon range between 5 and 200 mg/L (Hartmann et al., 1990). Avila et al. (2021), observed an average SSC of up to 300 mg/L, with an estimated sediment discharge of 5.38 x 10^6 tons/year to the ocean.

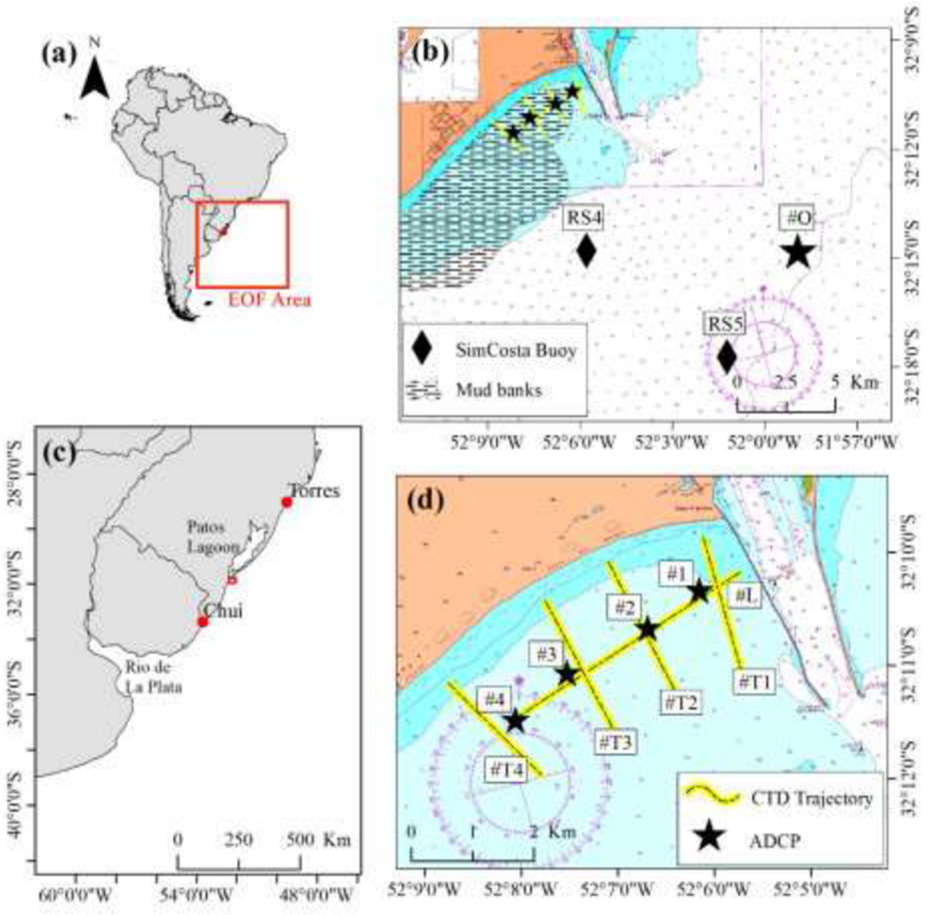


Figure 1 – Cap III. Location of the anchored ADCPs (#1, #2, #3, #4, and #O), CTD profile collection trajectories (#T1, #T2, #T3, #T4, and #L), the size of the analyzed EOF area, and the location of the cities of Torres, Chuí, and Patos Lagoon. The bathymetric contours were obtained from the Brazilian Navy nautical charts.

4.1 Materials and Methods

A field experiment was designed to capture the hydrodynamic patterns in the sheltered area at the southwest side of the jetties during a period of strong northeast wind. Based on climatological data, such conditions are expected particularly at the end of spring and the beginning of summer (Cruz and Schettini, 2024). The logistics of the

experiment were organized, and a waiting period was established starting from October 2023. The experiment was conducted on November 28, 2023. Considering that the hydrodynamic regime is primarily wind-driven and that astronomical tides are not significant, the experiment involved data recording for approximately 10 hours. Water level, current speed, and direction data were recorded simultaneously at four points along the inner shelf (Figure 1), and water properties (salinity, temperature, and turbidity) were recorded along four cross-shore sections and one parallel to the coast (Figure 1). The meteorological conditions during the experiment were compared with a long-term time series (20 years) to assess temporal significance, both in terms of intensity and duration.

Data collection:

Pressure (water level), current speed and direction data were recorded using Doppler Acoustic Current Profilers (ADCPs) mounted on the seafloor. The ADCPs were positioned along the inner shelf, approximately 1/3 of the total length of the jetties from the shore (~1.5 km), with a 1 km spacing between them (Figure 1). Four Nortek Aquadopp Profilers were used, with one operating at 2 MHz and three at 1 MHz. The 2 MHz ADCP was deployed at point #1, at a depth of 6.5 m. The depths at the other points were: point #2, 7.4 m; point #3, 8.5 m; and point #4, 7.2 m. The ADCP data recording started at 06:20 and ended at 16:30. The 2 MHz ADCP was configured to record 0.1 m cells, while the 1 MHz ADCPs recorded 0.3 m cells. Speed data were recorded with 120 s averaging, at 5-minute intervals.

Data from a fifth ADCP (#O) were used to investigate processes in an area away from the sheltered area. This data was recorded approximately 10 km offshore from the Patos Lagoon mouth (32° 15' S, 51° 59' W), at a depth of 20 m (#O in Fig. 1). These data cover the period from September 17 to November 2, 2021, recorded at 10-minute intervals

with a vertical resolution of 0.5 m. Furgher details about these data are presented in Cruz and Schettini (2024).

Salinity, temperature, and turbidity data were recorded using a CTD probe JFE RINKO profiler. The data were obtained from vertical profiles at points along four cross-shore sections (#T1, #T2, #T3, and #T4) and along one along shelf section relative to the coastline (#L) (Figure 1). The locations of the sampling paths and the ADCP points were constantly acquired with a GARMIN GPS and interpolated with the time series from the multiparameter sensor to obtain the location of each profile.

Velocity data were rotated using principal component analysis (PCA) to obtain the longitudinal and cross-shelf current components based on maximum variance and to determine the angle between these vectors and true north..

Turbidity data were obtained through an optical backscatter sensor (OBS) on the CTD, providing data in NTU. To convert the data to SSC (mg/L) it was used the equation

$$SSC_{obs} = 8.215 + 0.455OBS_{NTU} \qquad : r^2 = 0.79 \tag{1}$$

which was obtained for the local conditions (Santa-Rosa and Schettini, 2024).

Stratification stability:

Stratification occurs when layers of different densities form due to variations in temperature and salinity, with the potential effect of preventing the transfer of properties through the pycnocline (Simpson and Sharples, 2012). The Richardson number (Ri) is a dimensionless measure of stratification stability. Above the critical value of 0.25, the stabilizing force of the flow prevents current shear from vertically mixing the fluid, while

below this value, the flow is considered unstable, forming vortices and turbulence that mix the fluid vertically. Ri is obtained by:

$$Ri = \frac{N^2}{(\partial u/\partial z)^2}, \qquad N = \sqrt{-\frac{g}{\rho}\frac{\partial \rho}{\partial z}} \tag{2}$$

where N is the Brunt-Väisälä buoyancy frequency, which is a measure of the fluid's stability to vertical movement, given by the density gradient (ρ), and is divided by the term representing the shear force ∂u/∂z.

Shear estimates:

Shear stress is a measure of the frictional force exerted by a fluid per unit area (Pa) and is related to the level of turbulence that controls the vertical diffusion of suspended sediments. Bottom shear stress (τ_0) was calculated using the mean water density (ρ), below the pycnocline, and the bottom shear velocity (u_*):

$$\tau_0 = \rho {u_*}^2 \tag{3}$$

The near-bottom shear velocity was determined using the Law of the Wall (Heinz, 2024), applied up to the water column below the pycnocline

$$u(z) = \frac{u_*}{k} \ln\left(\frac{z}{z_0}\right) \tag{4}$$

where k is the von Kármán constant (0.4), and z_0 is the bottom roughness, determined by the Nikuradse roughness scale, defined as $d_{50}/12$, where d_{50} is the median sediment diameter.

Potential Lagrangian Displacement:

The potential Lagrangian displacement (L) of water parcels near the bottom and surface layers was calculated. For ADCPs #1, #2, #3 and #4, velocity data was corrected for the local magnetic declination of 16º. For ADCP #O, L was calculated for the longitudinal and cross-shelf velocity components to quantify cross-shelf displacement during southward current periods (negative values). The along shelf and cross-shelf components of the ADCP #O current were filtered with a Butterworth filter (Roberts and Roberts, 1978), using a 1-hour passband to remove high-frequency disturbances and isolate periods when the flow was directed southward and toward the coast. After rotating the components relative to true north and identifying periods using the filtered components, L was estimated from the raw velocity data in the deepest layer.

For ADCPs #1, #2, #3, and #4, L was calculated using the along shelf and cross-shelf current components rotated relative to true north and the raw velocity data for both the deepest and upper measured layers. The L estimates were normalized by the duration of each event ($\hat{L}$) to compare the variation in intensity of $\hat{L}$ for the bottom layer along the E/W or N/S axes at each ADCP measurement point.

Cross-shore Circulation:

To evaluate the response of cross-shore currents under different wind conditions, a cross-shore current intensity index (I_{cs}) was established. This index is determined by the difference between the cross-shore current velocities in the lower and upper layers ($|V_s - V_b|$), multiplied by the along shelf wind component (U_w). The I_{cs} index allows for analyzing the influence of wind on cross-shore current exchanges and the time lag between the maximum longitudinal wind velocity and the intensity of the cross-shore current.

$$I_{cs} = U_w * (|V_s - V_b|) \quad (5)$$

Temporal Representativity and Analysis:

The temporal representativity of the data obtained during the field experiment, and the estimation of the significance of the observed oceanographic conditions, were achieved by a comparative analysis with wind conditions from a long-term time series. Reanalysis data from the Copernicus ERA5 numerical model were used to create a 20-year time series (2003–2023). Observational wind data from the SimCosta project buoys RS4 and RS5 (Figure 1), covering a 7-year period (2017–2024), were used to validate the error between simulated and observed data. The error was estimated using the root mean square error (RMSE). These data were then concatenated into a single time series, interpolated to a 1-hour temporal resolution, and compared with the nearest ERA5 numerical grid point to the buoy locations, also with a 1-hour temporal resolution. It is worth noting that ERA5 data are provided for 10 m above sea level, while the RS4 and RS5 buoy sensors are located at 3 m above sea level.

The spatiotemporal variability of wind patterns was assessed using Empirical Orthogonal Function (EOF) analysis. EOF reduces the dimensionality and complexity of climate variations and identifies the main patterns explaining their variability (Hannachi, 2004). The EOF was performed on model data for daily averaged wind values at 10 m above the sea surface. The model data are represented on a non-uniform numerical grid, with higher density towards the poles, and to satisfy the orthogonality constraints required by the EOF in space and time, the data were weighted by their location before analysis. Thus, each point on the numerical grid was weighted by the cosine of its latitude. The EOF was performed on wind data by combining the Cartesian components in complex

form (e.g., u + vi). A relatively large area was chosen for analysis (Figure 1) compared to the study area, as the EOF structure tends to be dependent on domain size, which can complicate its physical interpretation (Richman, 1986).

The evaluation of the representativity of wind conditions observed during the experiment was performed by identifying continuous wind events with similar direction in the long-term hourly time series. The average wind direction during the experiment was 242º, and events with directions within ±20° were considered, distinguishing between all wind speeds and those above 8 m/s, which was the average wind speed during the experiment.

Numerical Modelling:

To obtain a broader spatial view of the circulation around the jetties, the FLOW module of the Delft3D modeling software was used. Simulations were conducted with a 30-second time step for a duration of 30 days. The model domain was defined between 32°22'S - 32°0'S and 52°14'W - 51°49'W, with 10 sigma layers set at constant 10% intervals. The Coriolis coefficient for latitude 32ºS was applied, along with a constant bottom roughness coefficient of 0.02, following the Manning formula. The computational curvilinear grid resolution was approximately 200 m towards the open ocean and around 50 m near the jetties, totaling 22,784 cells. Bathymetry was implemented from the digitization of nautical charts. The chosen turbulence model was K-epsilon, with horizontal and vertical turbulent viscosity coefficients of 1 N/m² and 0.0001 N/m², respectively.

The model was implemented to analyze the hydrodynamic circulation south of the jetty under wind conditions from the N/NE quadrant. The effect of the jetty on hydrodynamic circulation was considered as a fixed impermeable barrier. Sea-level

oscillation and outflow from the river mouth were set to zero, with a constant salinity of 31 g/kg. The wind direction was set as constant (242º). Two scenarios were simulated, with wind speeds of 5 and 10 m/s. The final simulated moment was extracted for interpretation.

5.1 Results

For the sake of clarity, the presentation sequence of the results is organized as follows: (1) spatial analysis of wind patterns (EOF), (2) temporal representativity of the experiment compared to similar events, (3) cross-shore transport on the outer shelf (without jetty influence), (4) evaluation of the jetty sheltered area based on numerical simulation, (5) current patterns observed during the experiment, (6) distribution of physical properties, and (7) characterization of the flow.

Spatial wind patterns (EOF)

The results of the EOF analysis are presented in Figure 2. EOFs 1 and 7 (Figure 2a,g) highlight winds from the N/NE quadrant, with an average direction of 209º and an average speed of 1.47 m/s, explaining 42.4% of the variance. EOFs 2, 3, and 4 (Figure 2b,c,d) represent wind conditions from the S/SE quadrant, with an average direction of 25º and an average speed of 2.74 m/s, accounting for 37.3% of the variance. EOFs 5, 6, and 8, in turn, present weak wind conditions, with an average speed of 0.66 m/s from the W or E quadrants, representing 10.3% of the variance. It was found that the largest fraction of variation corresponds to winds from the N quadrant, reaching 40%, with an

average speed of 1.65 m/s. Meanwhile, winds from the S quadrant have a variation fraction of 12.8%, but with higher average speeds, around 3.1 m/s.

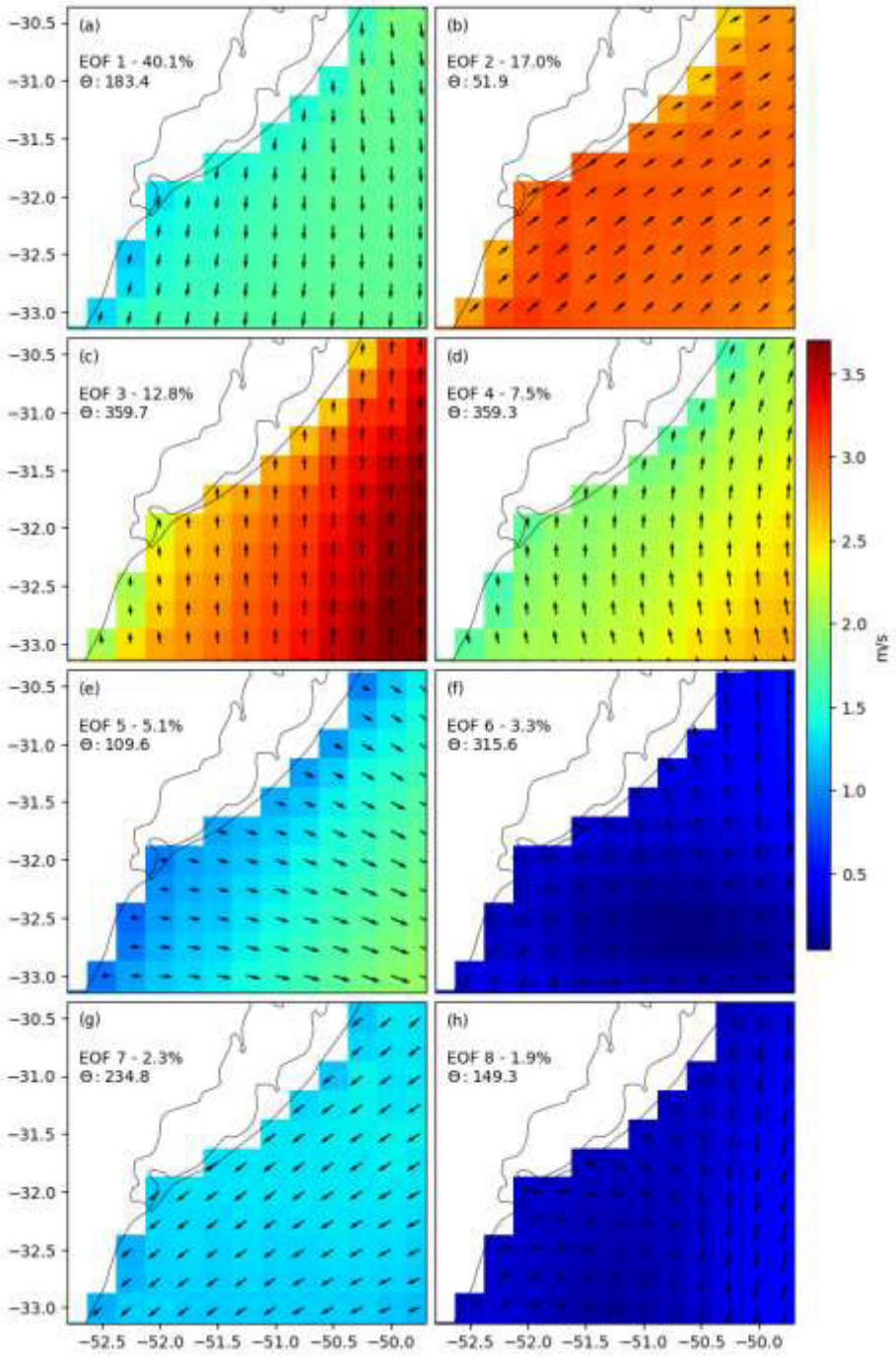


Figure 2 – Cap III. Results of the empirical orthogonal functions (EOFs) analysis. The variance of each EOF is displayed in each graph, along with the average wind direction. The color shades represent the wind magnitude.

Temporal representativity of the experiment

Figure 3 presents the monthly climatology for wind magnitude and the duration of continuous periods of northeast wind events, based on the long-term time series extracted from ERA5 model data. The months from September to April exhibit the longest event durations, both in scenarios with wind speeds above 0 m/s and in scenarios with speeds exceeding 8 m/s (Fig. 3a, 3c). Notably, although the months of June, July, and August show the lowest percentage of duration, wind speed during these events matches that observed in September, October, and November, in scenarios where wind speeds exceed 0 m/s. In contrast, for scenarios with speeds above 8 m/s, wind speed during May to August is equal to or higher than that observed from September to April, which shows the highest percentage duration values. Considering the proximity to the sampling period (28/11/2023), the duration of the event, when the wind direction was between 222º and 262º and speed exceeded 0 m/s, was 103 hours, with an average speed of 8.5 m/s. For speeds above 8 m/s in the same direction range, the duration was 25 hours, with an average speed of 9.6 m/s (Figure 3).

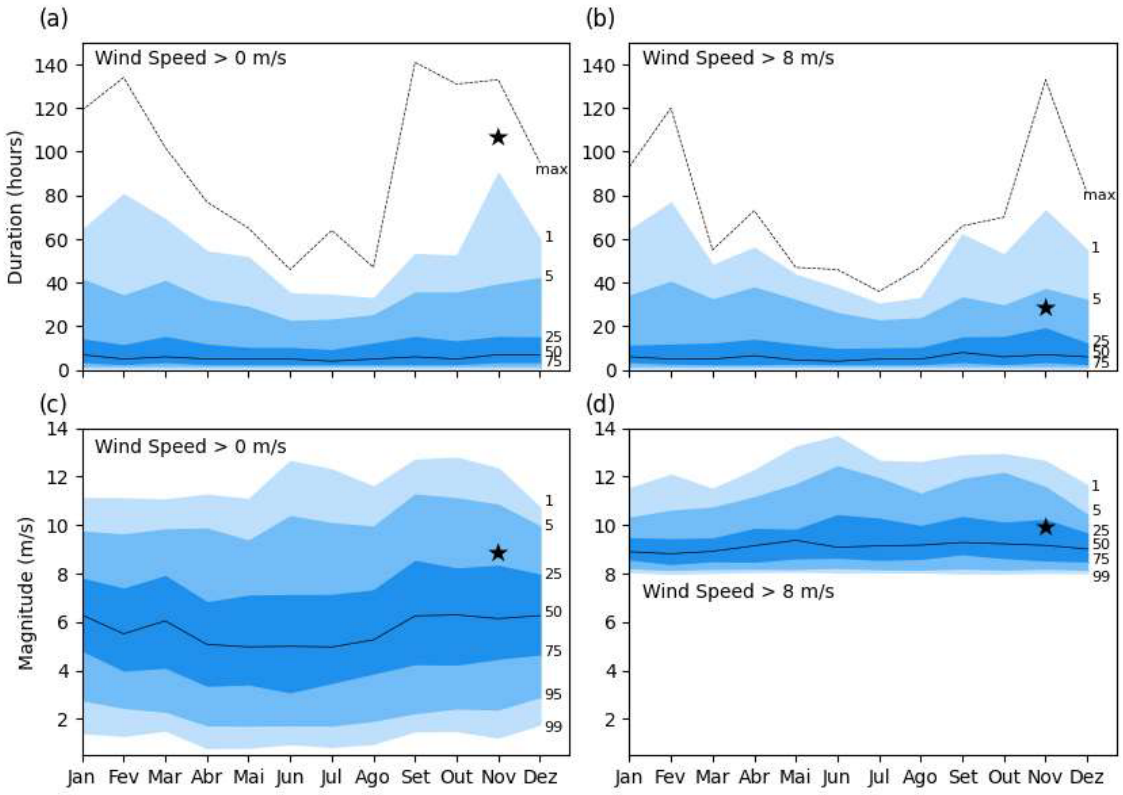


Figure 3 – Cap III. Monthly frequency distribution of periods of continuous NE wind events, with the median in black and the 1st, 5th, 25th, 50th, 75th, 95th, and 99th percentiles in blue. In (a) and (c), the duration and magnitude of NE wind events when the wind speed exceeds 0 m/s. In (b) and (d), the duration and magnitude of NE wind events when the wind speed exceeds 8 m/s.

Cross-shore transport away from the jetties

From the ADCP #O data, twelve continuous southward current events were identified (Figures 4 and 5). The average duration of the events, characterized by negative longitudinal and cross-shelf velocities, is 1 day and 19 hours, with a maximum duration of 3 days and 19 hours, and a minimum duration of 10 hours and 40 minutes. The average distance along the East/West axis is 18.3 km, and along the North/South axis is 38.2 km. The average total distance from the mooring point is 43 km. The average values of $\bar{L}$ in the N/S axis were 0.23 m/s, and in the E/W axis, 0.12 m/s (Table 1).

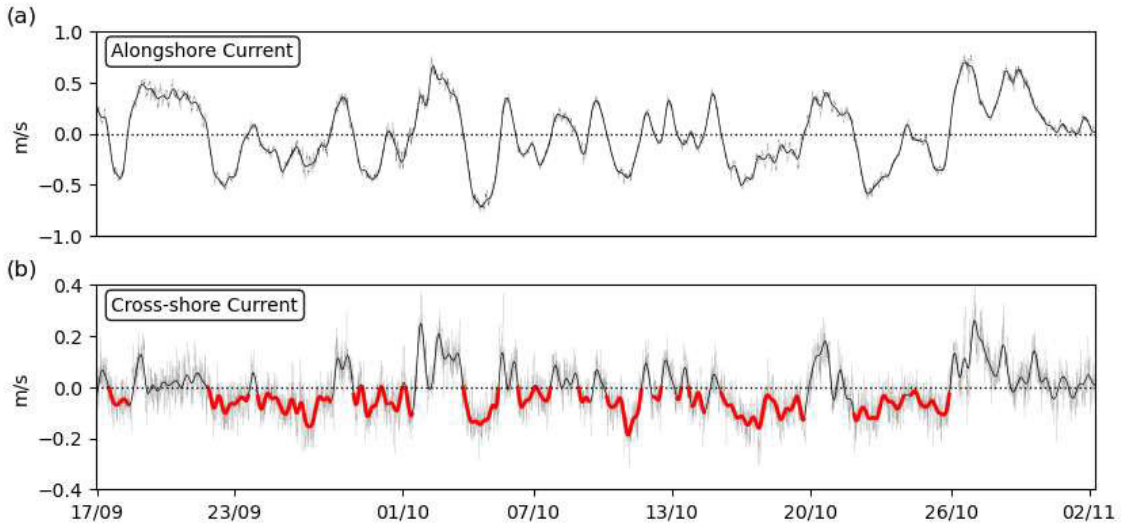


Figure 4 – Cap III. Time series of average along shelf (a) and cross-shelf current velocities (b) estimated from ADCP data moored at a depth of 20 m. The red lines in (b) indicate the events where the average longitudinal and cross-shelf velocities were negative (onshore).

Table 1 – Cap III. Selected periods from the time series obtained by the ADCP at point #O, with the respective displacement values (L) along the E/W or N/S axis, and the normalized potential Lagrangian displacement ($\bar{L}$) by the event duration. Units are in m/s.

Trajeto	Início	Duração	L (E/W)	L (N/S)	$\bar{L}$ (E/W)	$\bar{L}$ (N/S)
1	09-18 01:40	0 d - 20:50	15.6	15.1	0.21	0.20
2	09-24 11:50	1 d - 20:30	26.5	35.5	0.17	0.22
3	09-28 06:20	3 d - 8:00	21.4	31.7	0.07	0.11
4	09-30 21:00	1 d - 12:40	15.8	36.3	0.12	0.28
5	10-02 00:50	0 d - 23:10	12.3	9.6	0.15	0.12
6	10-06 00:20	1 d - 14:50	33.7	73.8	0.24	0.53
7	10-08 09:50	1 d - 11:50	8	21	0.06	0.16

8	10-10 03:50	0 d - 10:40	-2.4	6.5	-	-
9	10-12 14:10	1 d - 14:00	4.8	41.6	0.04	0.30
10	10-20 01:50	3 d - 19:20	43.4	93	0.13	0.28
11	10-24 16:10	2 d - 6:40	32.2	65.8	0.16	0.33
12	10-26 18:40	1 d - 18:00	7.8	28.6	0.05	0.19

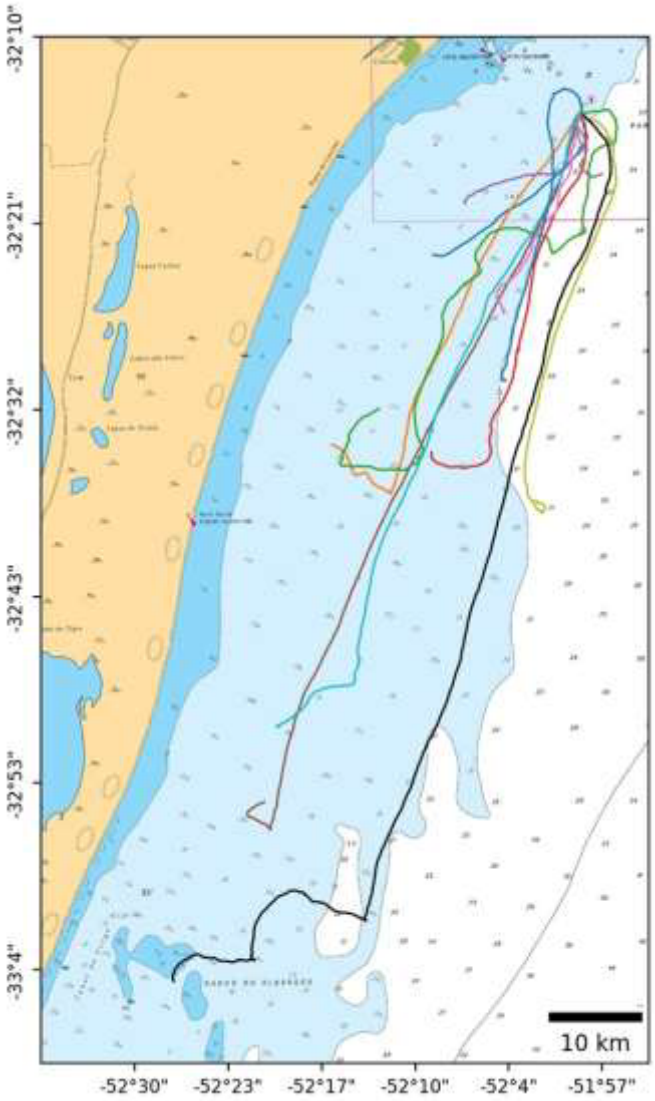


Figure 5 – Cap III. Potential lagrangean displacement of the bottom water layer located 0.9 m above the seabed, with a cell size of 50 cm. Estimated from ADCP data moored at a depth of 20 m and during events where the average longitudinal and cross-shelf velocities were negative.

A difference is observed between the along shelf wind time series, with northward and southward directions, and the cross-shelf current intensity index (Figure 6). When the longitudinal wind direction is positive, i.e., northward, there is a delay in reaching the

maximum value of the index during two periods: from 10/04/2020 to 10/05/2020 and from 10/15/2020 to 10/20/2020, with delays of 9 and 6 hours, respectively. In contrast, when the along-shelf wind direction is negative, i.e., southward, the maximum values of the index are reached more quickly, from 10/05/2020 to 10/06/2020 and from 10/26/2020 to 10/28/2020, with delays of 4 and 5 hours (Figure 6).

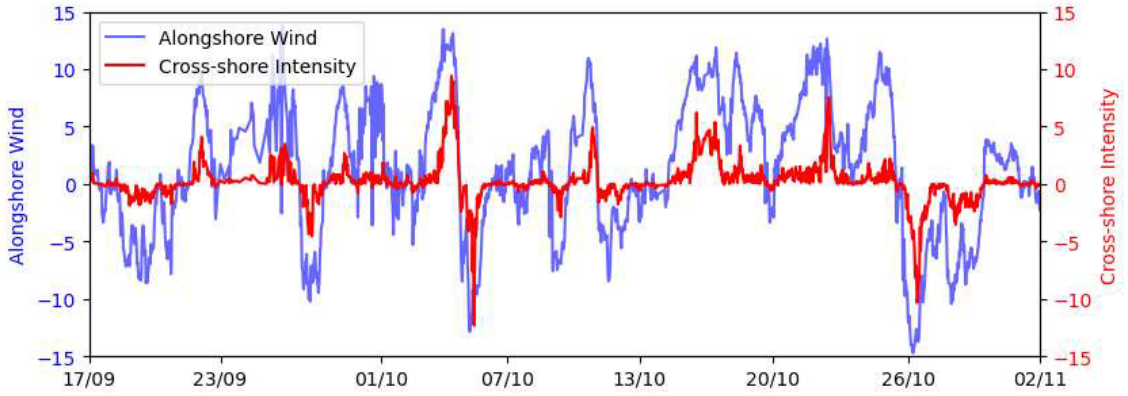


Figure 6 – Cap III. The alongshelf wind component obtained from the RS5 buoy (in blue) and the cross-shelf current intensity index (in red) estimated from ADCP data moored at a depth of 20 m and the longitudinal wind obtained from the RS5 buoy.

Spatial scale of the sheltered area (numerical model)

Figure 7 shows the results of numerical simulations, illustrating the spatial variability of streamlines on the inner shelf adjacent to the jetties. The shadow effect is characterized by the formation of a clockwise vortex extending from the jetties westward and toward the coast, reaching about ¼ of the jetties' length. Near the coast, a new current reversal occurs, flowing westward along the shore. In the scenario with a wind speed of 10 m/s, the streamlines are closer to the coast and the jetty compared to the scenario with a wind speed of 5 m/s (Figure 7). The distance between the longitudinal velocity contours and the coastline and the middle of the southern jetty is 1.1 km and 3.7 km, respectively, in the 5 m/s wind scenario (Figure 7a). In contrast, in the 10 m/s wind scenario, the

distance between the longitudinal velocity contours and the coastline and the southern jetty is 0.95 km and 3.45 km, respectively (Figure 7b).

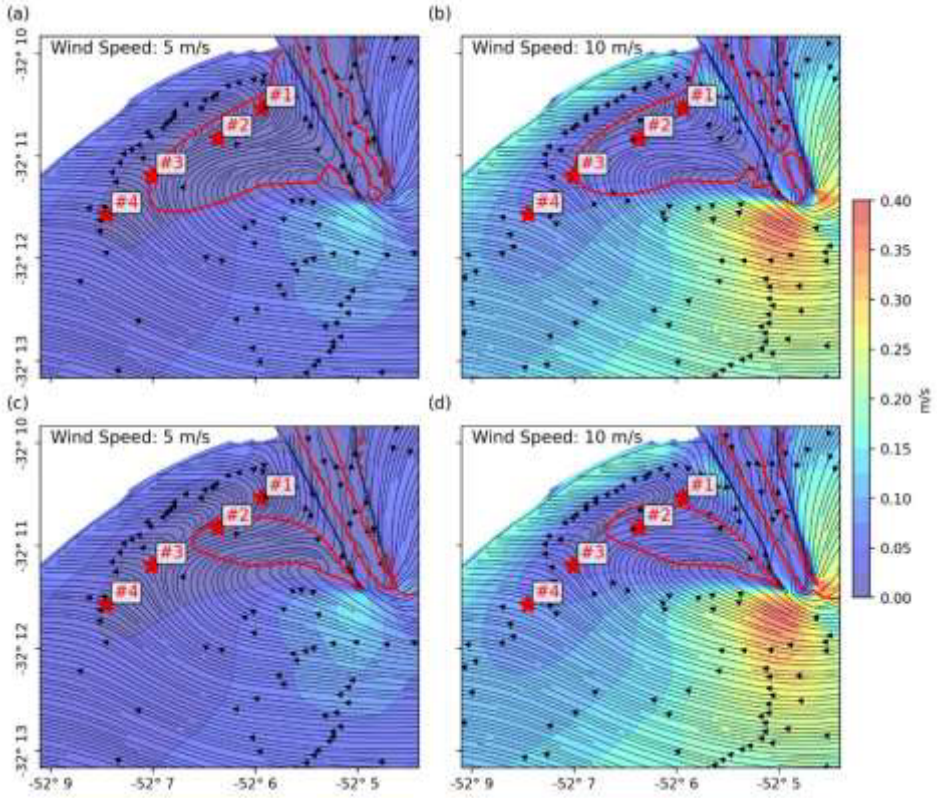


Figure 7 – Cap III. Results numerical simulation with constant wind speeds of 5 and 10 m/s at 243º, respectively. The black lines represent streamlines and colors indicate current magnitude. The red line shows the average alongshelf velocity of 0 m/s in (a) and (b), and cross-shelf velocity of 0 m/s in (c) and (d).

Observed current patterns during the experiment

Figure 8a presents the results of the potential Lagrangian displacement from current data at points #1, #2, #3, and #4, for surface and bottom currents. Figures 8b and 8c show the same results but represented in polar diagrams for surface and bottom currents, respectively. A clear distinction can be seen between the flow patterns in the upper layer compared to the deeper layer. Near the bottom, displacement occurs parallel to the coast and toward the jetty, or obliquely toward the coast. In the upper layer, the

displacement is parallel to the coastline, moving southward of the jetty, with brief moments where displacement shifts toward the jetty. The current magnitude in the deeper layer is predominantly distributed in the N/NE quadrant. In the upper layer, the distribution is mostly in the SE quadrant at points #1, #3, and #4, while at point #2, the distribution occurs in both the SE and NE quadrants. The average ∇L for the points in the E/W axis was 2.9 km, and in the N/S axis, it was 3.2 km. The average values of $\hat{L}$ in the N/S axis were 0.09 m/s, and in the E/W axis, they were 0.09 m/s (Table 2).

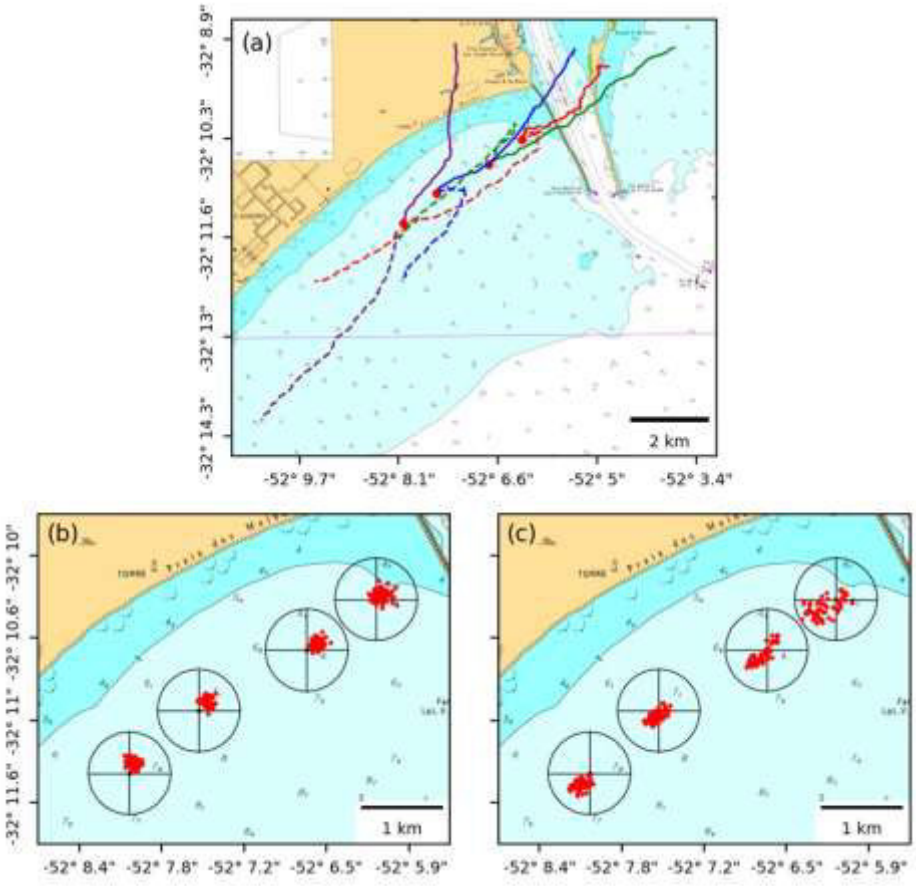


Figure 8 – Cap III. (a) potential Lagrangian displacement of the near bottom (solid lines) and the near surface (dashed lines). (b) and (c) distributions of current vectors of near bottom (b) and near-surface (c). The circles representing a scale of 0.5 m/s.

Table 2 – Cap III. Potential Lagrangian displacement (L) in the E/W or N/S axis, and the potential Lagrangian displacement normalized by the duration of the event ($\bar{L}$) for ADCPs #1, #2, #3, and #4. Units are in m/s.

ADCP	Duração	L (E/W)	L (N/S)	$\bar{L}$ (E/W)	$\bar{L}$ (N/S)
#1	9.8	2.2	1.8	0.06	0.05
#2	9.7	4.7	2.9	0.13	0.08
#3	9.2	3.5	3.6	0.11	0.11
#4	9.5	1.3	4.5	0.04	0.13

Physical Properties of Water

Figure 9 shows the distributions of salinity and SSC for the longitudinal section #L and the cross-shelf sections #T1-4. All sections exhibited salinity stratification, with salinity ranging from 20 to >30 g/kg. The salinity in the longitudinal section #L shows a deepening of the halocline with increasing distance from the jetty. Near the jetty, at a distance of 220 m, the halocline is located at a depth of 1.25 m, increasing to nearly 5 m at a distance of 4.8 km (Fig. 9a). In the cross-shelf sections, stratification is more pronounced in the deeper regions. In sections #T1, #T2, #T3, and #T4, the halocline becomes more pronounced up to distances of 160 m, 450 m, 500 m, and 1000 m, respectively. Salinity profiles become more homogeneous closer to the coast, with salinity values below 30 g/kg throughout the water column (Fig. 9b, c, d, e).

In section #L, the SSC distribution showed maximum values both in the near-surface layer and in the deeper layers, with the SSC peak at a distance of ~1 km from the jetty. This pattern suggests that the material transported by the flow accumulates in this region (Fig. 9f). In the cross-shelf sections, it is observed that the near-surface SSC values

display a distinct gradient. In the central portion of section #T4, SSC values are lower and increase towards the coast or ocean, indicating a tendency for accumulation near the margins (Fig. 9j). This trend is also seen in sections #T3 and #T2, where near-surface SSC values are higher near the coast and in the outer portion (Fig. 9h, i). In section #T1, the near-surface SSC values remain uniform throughout the cross-shelf section, which may indicate a different sedimentary dynamic in this region (Fig. 9g).

When integrated over the water column, SSC values in the cross-shelf sections reveal two peaks. The first occurs near the coast, suggesting the influence of surf zone processes. The second peak, located about 1 km to 1.5 km from the coast, likely reflects the center of accumulation of vortices formed in the shadow zone (Fig. 9g, h, i, j).

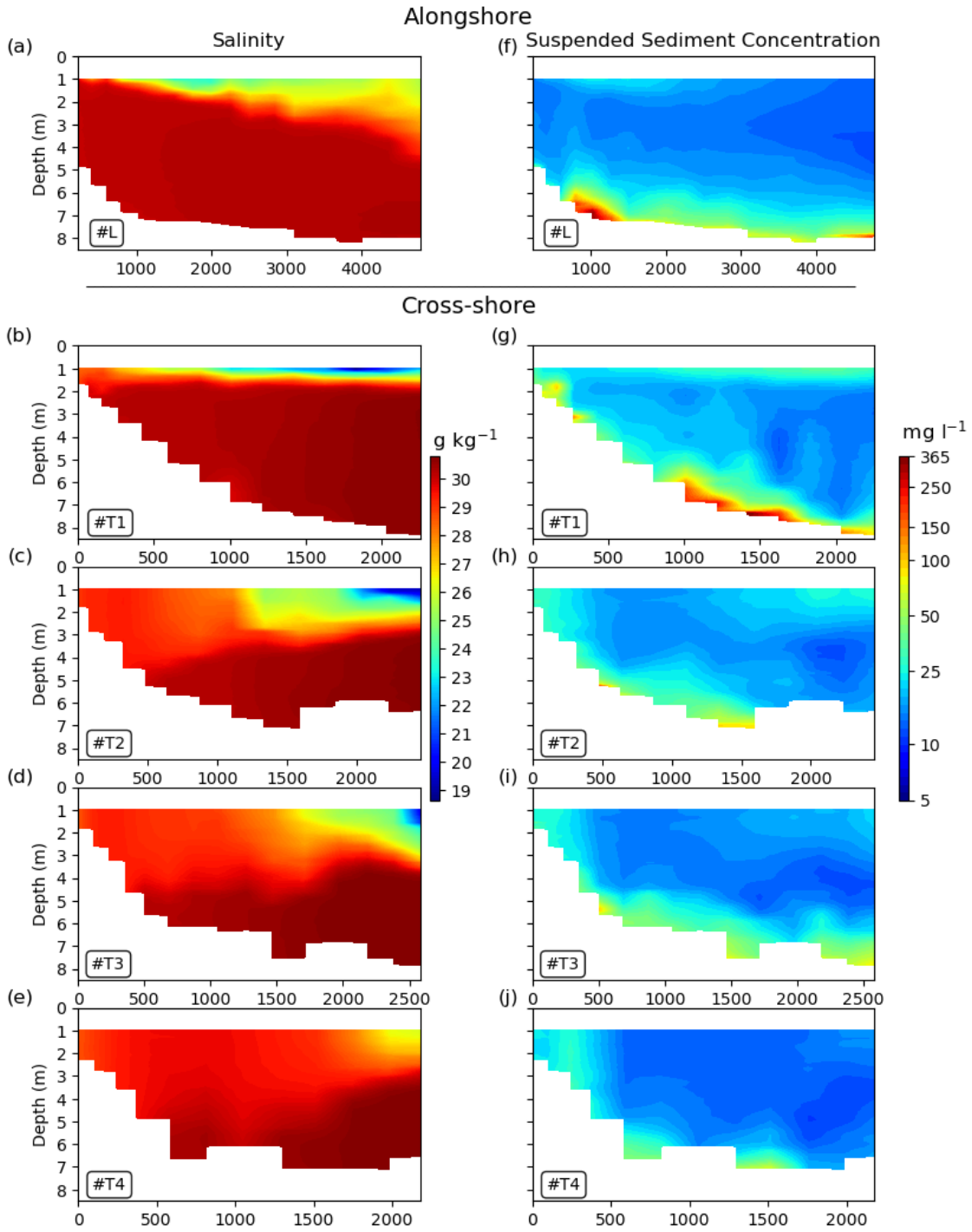


Figure 9 – Cap III. Panels (a) and (f) present the salinity and SSC distribution graphs for the longitudinal section (#L, Figure 1). Panels (b), (c), (d), and (e) show the salinity distributions, while panels (g), (h), (i), and (j) show the SSC distributions for the cross-shelf sections #T1, #T2, #T3, and #T4, respectively.

Flow Characterization

Figure 10 presents the Hovmoller diagrams for the long-shelf and cross-shelf current components at the four observation points, and Figure 11 presents the median vertical profile for both components, with the respective occurrence percentiles, as well as the vertical density profiles and the Richardson number.

The longitudinal current components exhibited stratified flow, with surface layers flowing westward and bottom layers flowing northward (Figure 10b,c,d,e). During the observation period, the longitudinal wind intensity increased from 9 m/s to 10 m/s (Figure 10a), and there was also an apparent increase in the thickness of the surface layer moving southward. At the beginning of the time series, there are moments when the entire observed water column moves in the opposite direction to the wind, northward, although the layer not measured by the ADCP might still show southward flow.

The cross-shelf current component showed much more complex patterns than the longitudinal component at all points (Figure 10g, h, i, j). The highest variability was recorded at #1, with a broader distribution of the median and percentiles towards the coast (Figure 10g and Figure 11e). At points #2 and #3, the percentiles and median distribution are predominantly oceanward (Figure 11f,g), while at ADCP #4, the distribution is oriented towards the coast (Figure 11h). It is observed that when the longitudinal wind component is 10 m/s and the cross-shelf component is less than 1 m/s (Figure 10a,f), there is a greater tendency for currents to move towards the coast at all four ADCPs (Figure 10g,h,i,j).

At all points, the vertical profile of the Richardson number showed values greater than 0.25, indicating the stability of the stratification presented in the salinity distribution

data. At points #1, #2, #3, and #4, the depth at which the 0.25 threshold is exceeded is 2.1 m, 4.1 m, 5.1 m, and 5.5 m, respectively (Figure 11m,n,o,p).

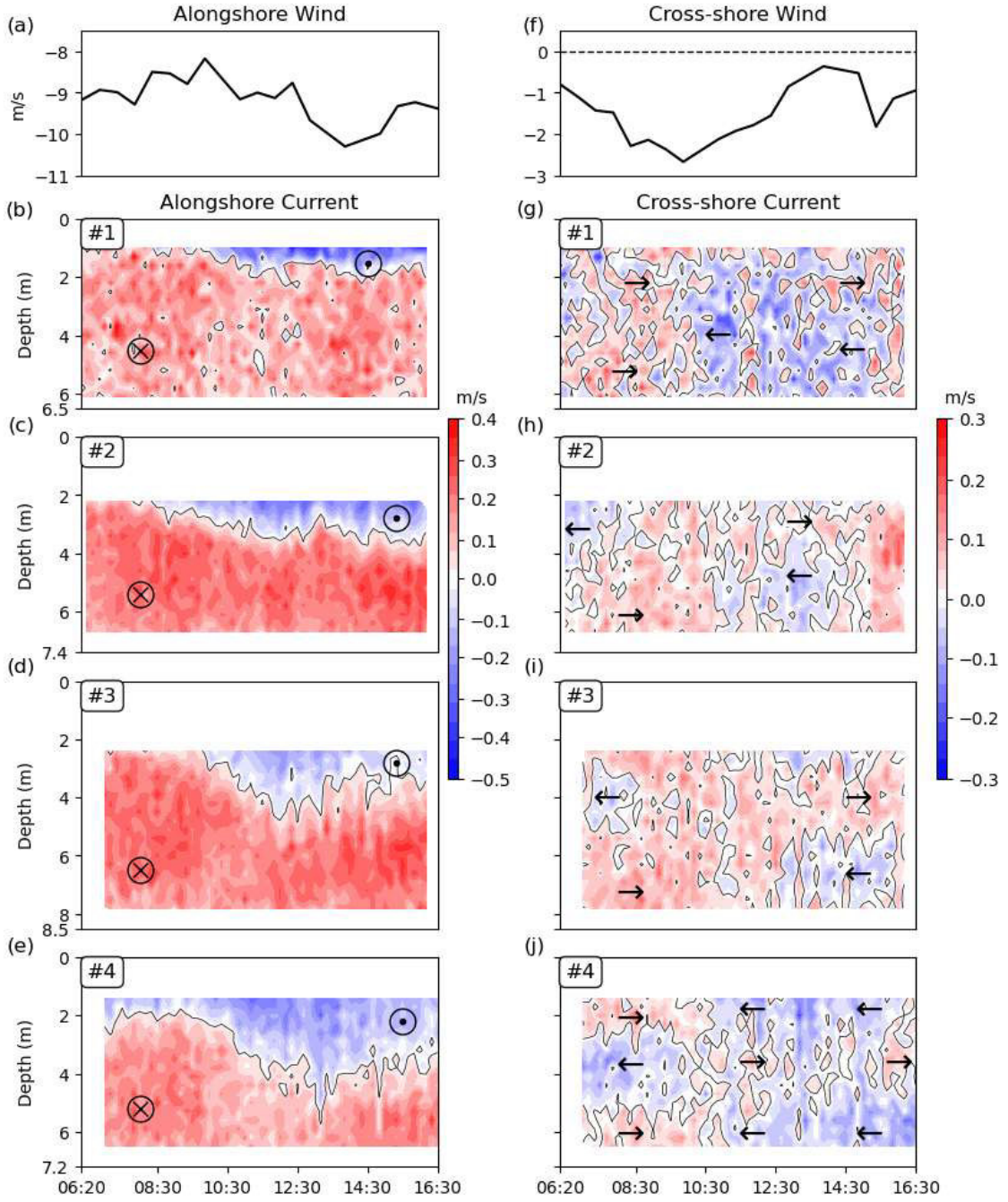


Figure 10 – Cap III. Top panels (a) and (f) show the alongshelf and cross-shelf wind speeds, respectively. Panels (b), (c), (d), and (e) present the Hovmoller diagrams of alongshelf current speed, with red colors indicating westwards currents (away from the jetties) and blue colors indicating eastwards currents. Panels (g), (h), (i), and (j) present

the Hovmoller diagrams of cross-shelf current speed. Red colors indicating seawards currents and blue colors indicating landwards currents.

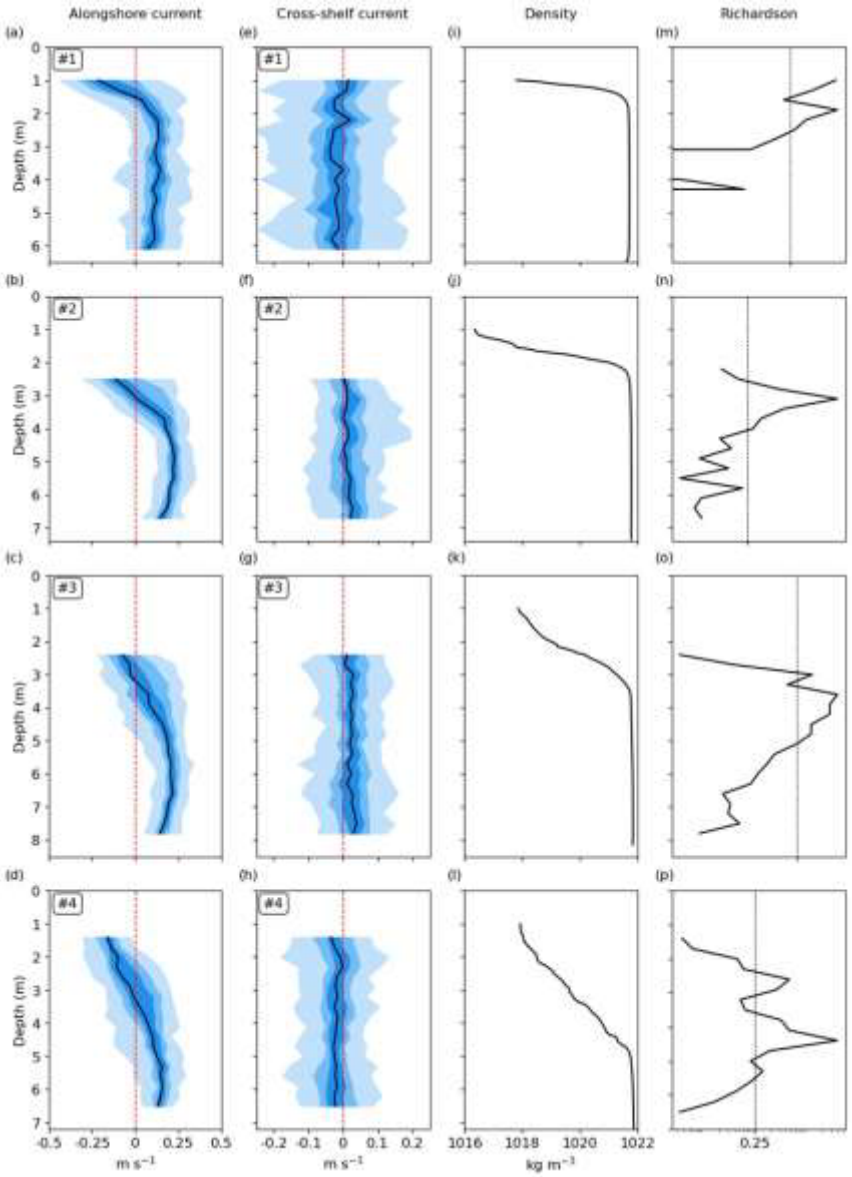


Figure 11 – Cap III. Vertical variation of the alongshelf (panels (a), (b), (c), and (d)) and cross-shelf (panels (e), (f), (g), and (h)) current speed. The median is shown in black, and the percentiles of 1, 5, 25, 50, 75, 95, and 99% are shown in blue shades. Panels (i), (j), (k), and (l) present the density profiles closest to the mooring sites, and panels (m), (n), (o), and (p) show the Richardson number, with the dashed line indicating the 0.25 Ri threshold.

6.1 Discussion

The inner shelf near river mouths and estuaries, as in the present case, is a region characterized by great complexity in oceanographic features that evolve on small temporal (~hours) and spatial (~100s of meters horizontally, 0.1 m vertically) scales (e.g., Moum et al., 2008). The use of numerical models, given the simplifications and constraints imposed by boundary conditions and numerical schemes, does not allow for the inclusion of all environmental factors. Consequently, numerical simulation results do not capture all the complexities of reality but provide an overall picture, both spatially and temporally, at relatively low cost. The spatial characterization of the vortex in the sheltered area southwestwards from the Patos Lagoon jetties was initially identified and quantified through studies based on hydrodynamic numerical modeling (Vinzon et al., 2009; Franzen et al., 2022). These previous studies observed the recirculation zone forming near the jetty and analyzed its potential effect on fine sediment deposition on the inner shelf off Cassino Beach. This process is believed to be related to mud deposition events on the beach during storms (Pereira et al., 2011), though the dynamics of the process are not yet fully understood.

The observational results of the present study, although spatially and temporally limited compared to the space-time extent allowed by numerical models, provided a more accurate picture of the complexity of hydrodynamic patterns and the water column structure, offering a more complete diagnosis of the main local forcing factors. The presence of an intense pycnocline produced by freshwater percolation through the jetties was particularly surprising and suggests that the baroclinic component cannot be disregarded in the local dynamics.

In conditions without vertical density variation, or well mixed, vertical momentum transfer and turbulent diffusion follow a predictable pattern throughout the water column. On the other hand, the presence of a pycnocline creates a physical barrier to property transfer vertically, with turbulence/mixing confined to one of the layers, limiting momentum transfer. Turbulence parameterization in numerical models is a way to adjust the turbulent diffusion coefficient to adequately represent stratified or homogeneous areas (Burchard et al., 2008). Numerical models also require appropriate boundary condition setup. Domain boundaries can be defined as closed, open to allow free entry or exit of flow, or dissipative to minimize reflections. However, permeable boundaries, which would allow partial flow exchange, are not considered. This can result in artificial reflections, flow confinement, and physical property restriction, limiting the applicability and accuracy of numerical simulations. The horizontal and vertical resolution needed to reproduce stratification, physical and oceanographic processes in numerical models varies across different spatial scales and must be appropriately adjusted for the study's objectives (Greenberg et al., 2007).

The model results of the present study showed the formation of two vortices in the sheltered area: one near the coast rotating counterclockwise and another further out from the jetties rotating clockwise (Figures 7). Observational data, however, do not corroborate the model results. Near the observation points furthest from the jetties (#3 and #4), the model indicates a pronounced cross-shelf component (Figure 7), however, observations show the dominance of the alongshelf component relative to the cross-shelf component (Figures 10 and 11). This difference may be attributed to the presence of stratification generated by the influx of low-salinity water through the jetties. Periods of N/NE quadrant winds favor the outflow from the lagoon, leading to the formation of an upwelling plume from the river mouth on the inner shelf (Moller et al., 2001; Austin et al., 2002; Marques

et al., 2010). However, our observations demonstrate that the flow of low-salinity water through the jetties is significant enough to influence the hydrodynamics on the adjacent inner shelf. This flow through the jetties is analogous to the process of a diffuser from a submarine outfall, occurring along the entire length of the jetties (~4 km). It can be stated that this flow is considerably smaller than the flow through the river mouth but becomes significant considering the shallow depth and confined position.

Ignoring the effect of stratification presence, the barotropic response for the leeward region of the jetty to wind shear stress is analogous to a lake. The upper layer is forced away from the structure, resulting in a return flow in the lower layer in the opposite direction to conserve volume (Figure 12a). With the entry of low-salinity water through the jetties, a less dense surface layer forms. The currents are not strong enough to produce mixing, with stratification remaining stable, resulting in the decoupling of the upper and lower layers (Figure 11m,n,o,p). This implies that wind-driven momentum accumulates in the upper layer, consequently intensifying the along-shelf speed outward, and thereby the bottom layer speed for volume replacement. As this upper layer moves away from the jetty, available kinetic energy decreases, reducing the ability to sustain turbulent mixing. With this reduction, potential energy associated with layers of different densities begins to dominate, promoting mixing between these layers of different densities (Figure 12a). This intensification of longitudinal flow gradients due to baroclinicity extends the vortex boundaries southward and explains the discrepancy observed between field data and the barotropic model results.

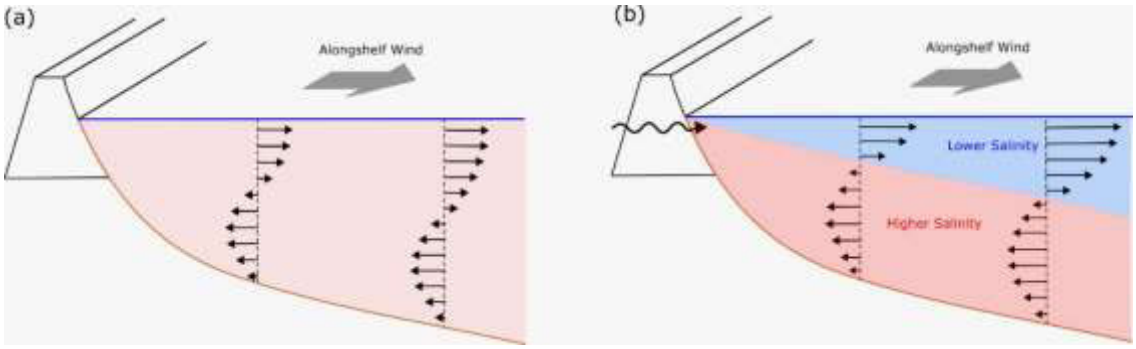


Figure 12 – Cap III. Cartoons of alongshelf flow at the sheltered area of the Patos Lagoon jetties, driven by a constant alongshelf wind, (a) without and (b) with low salinity water flow through the jetties. Black arrows represent the longitudinal current gradient. The wavy black arrow represents the permeability of the jetties allowing the inflow of brackish water south of the jetty.

In the outer shelf, beyond the influence of the jetties, at depths between 15 and 20 meters, cross-shelf circulation patterns are consistent with Ekman dynamics (remote wind effects), with a well-defined separation of cross-shelf circulation between the upper and bottom layers (Costa et al., 2011; Cruz and Schettini, 2023). However, in the shadow zone of the jetty, the cross-shelf current circulation becomes more complex, with multiple reversals in direction and no clear patterns. Near the middle of the jetty, the flow divides, with part heading towards the coast and the other part towards the ocean, explaining the greater variability of cross-shelf current observed at point #1 (Figure 10g, Figure 11e, and Figure 13). Despite the slope of the seabed, reduction in depth, and consequent increase in frictional forces, the intensity of bottom cross-shelf circulation (E/W), as evidenced by $\bar{L}$, was similar between observation point #O and points #2 and #3 (Tables 1 and 2), highlighting the intensification of vertical velocity gradients due to baroclinicity observed around the jetty.

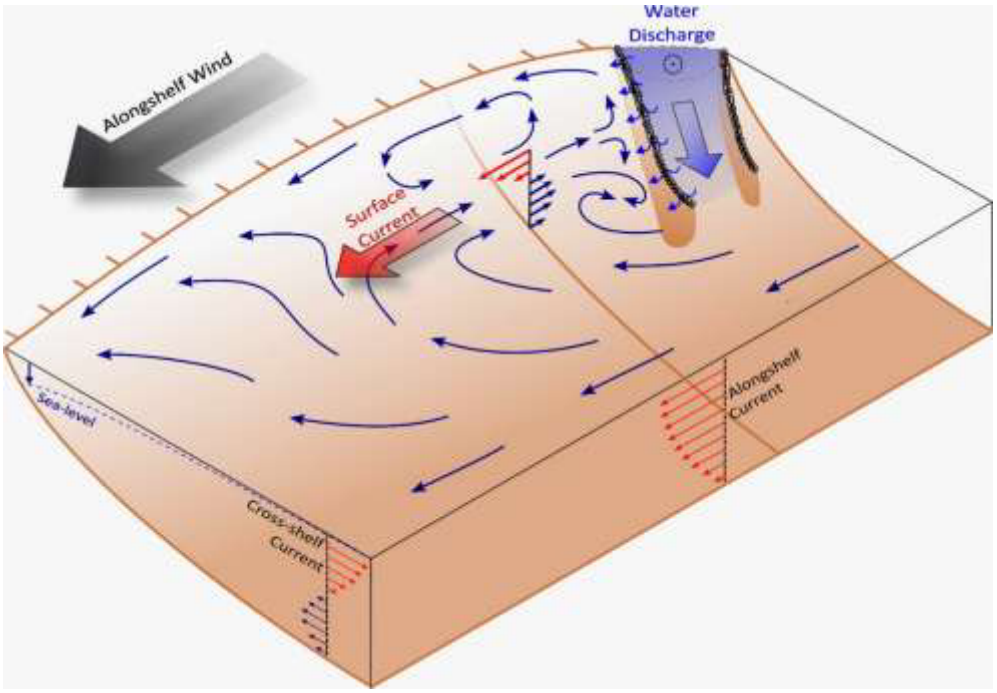


Figure 13 – Cap III. Diagram illustrating the spatial variability of vortices formed in the shadow zone of the jetty at Patos Lagoon. The longitudinal component along the water column, both inside and outside the jetty's influence zone, is represented by blue and red arrows, which also indicate the cross-shelf current component. The thick red arrow represents the surface current moving southward.

Along Cassino beach, between 5 and 10 km from the jetties, events of mud deposition on the beach occur following some storm events (Calliari et al., 2007). The mud deposited on the beach is remobilized from unconsolidated mud packets on the inner shelf. The thickness of this packet increases both south of the jetty and towards the coast (Figure 1). This mud accumulation area appears to be stable over the years (Calliari et al., 2009). The northern limit of the mud bank, where it is thinner, is located near the observed coastal vortex (Figure 7) and the region where the highest SSC values occurred, between 1 and 1.5 km from the coast (Figure 9). The zone of highest SSC suggests a convergence process, and the vortex near the coast is possibly a preferential deposition zone. The deposition center of this mud bank is located about 5.5 km from the nearest observation

point (#4) and indicates a potential interaction with the southern boundary of the vortices formed in the jetty's shadow zone, which cannot be fully captured by the four observation points. New measurements are needed to accurately define the vortex boundaries and their potential interaction with this deposition center.

For fine sediment deposition to occur, the bottom shear stress must be below the critical deposition level. The critical deposition stress is relatively difficult to estimate but is lower than the critical stress for erosion, which is more effectively quantified experimentally. Critical erosion shear stress values vary widely depending on sediment type. For erosion of surface particles, shear stress values range from 0.05 to 0.15 Pa (Dyer, 1995; Salehi et al., 2012; van Rijn, 2020). In shallow areas near the coastline, wave-induced shear stress also plays a role, but this relationship is complex, as there is remobilization but not necessarily transport due to its oscillatory nature (Sahin et al., 2012; Lentz et al., 2012). The bottom shear stress due to currents observed during the experiment ranged from 0.11 to 0.24 Pa, which are in the same order of magnitude as the critical values for erosion. Considering the observed conditions of intense wind, it can be assumed that weaker wind conditions might create favorable conditions for deposition.

7.1 Conclusion

The interference of the jetties on longitudinal and cross-shelf flows during a NE wind event was evidenced by both field observations and idealized numerical simulations. The temporal representativeness of the experiment was robust, validating the applicability of the results obtained in different temporal scenarios. The presence of a well-defined pycnocline, produced by the percolation of fresh water through the jetties, highlights the

importance of the baroclinic response in understanding the hydrodynamic circulation of the region. This process resulted in the decoupling between the upper layer and the intermediate and deep layers of the flow, with the thinnest upper layer near the jetty, and the thickest layer as it moves away from the jetties. This decoupling accumulates the momentum transferred by the wind in the upper layer, consequently intensifying the vertical gradient of both longitudinal and cross-shelf velocities.

The formation of vortices and the intensification of the vertical velocity gradient due to baroclinicity indicate that the jetty's shadow zone plays a crucial role in sediment transport and the spatial variability of the mud bank. The vortex center closest to the coast suggests a convergence zone with conditions favorable to deposition. However, further measurements are necessary to precisely delineate the vortex boundaries and their interaction with the mud bank deposition center, as the experiment conducted in this study could not capture the full extent of the vortices formed.

8.1 Acknowledgments

We would like to express our gratitude to all the individuals who helped during the intensive field experiment. We are also thankful for the support from the Brazilian National Science Council (CNPq, #316037/2021-4 & #404847/2021-8), through INCT-COI and PELD Estuário da Lagoa dos Patos. To the Coordenação de Aperfeiçoamento de Pessoal de Nível Superior – Brasil (CAPES) for GC's scholarship.

Capítulo IV: Circulation and water properties in the leeward of long jetties: the Rio Grande bar, RS, Brazil

1.1 Abstract

This study investigated the spatial variability of the vortex formed in the leeward of the jetties at the mouth of Patos Lagoon, and its impacts on the distribution of physical and biological properties in the adjacent coastal region. We employed an integrated approach combining remote sensing data (Sentinel-2), ERA5 wind data reanalysis, and field campaigns with Acoutic Doppler Current Profiler, oceanographic parameters (T/S), and indirect estimates of particulate matter. Results revealed that vortex formation occurs under both NE and W/NW winds, with its spatial extent and core position being modulated by wind intensity and relative angle to the jetties. We further demonstrated

that bottom interactions constitute the primary sediment accumulation mechanism in the shadow zone, while stratification actively controls vertical oxygen and nutrient distribution. Subsurface chlorophyll maxima (SCM) associated with this stratification were identified, along with development of hypoxic conditions (~45% DO saturation) below the mixed layer. Collectively, these processes highlight the vortex's critical role in modulating coastal biogeochemical gradients.

2.1 Introduction

The continental shelf is the region connecting the continent shores to the open ocean and plays a crucial role in the transfer of materials from continents to the world oceans, what will ultimately affect the marine ecology, biological productivity and the fate of organic matter (Mann and Lazier, 2005). This region is a key area for interdisciplinary research due to its environmental significance, which is highly affected by cross-shelf exchanges of sediments, nutrients, larvae, phytoplankton, and contaminants. These materials originate from various sources, including river discharge, outfalls, coastal erosion processes, or atmospheric deposition (Austin et al., 2002; Lentz et al., 2012; Moulton et al., 2023).

The continental shelf is divided into the outer and inner shelf, with the latter referring to the coastal sector where turbulent boundary layers from the surface and bottom occupy the entire water column, and where the strongest water property gradients are observed (Lentz, 1995). The synergistic interactions among physical processes occurring on the inner shelf play a fundamental role in determining the fertility of the region and sustaining primary production by regulating nutrient availability, turbulence,

and vertical mixing of the water column (Simpson and Sharples, 2012; Brink, 2016; Moulton et al., 2023).

Shelf hydrodynamics are driven by the combined action of wind, tides, river discharge, and surface waves, interacting with coastal bathymetry and shoreline geometry (Brink, 2023). The flow regime is typically stratified due to the proximity of continental inputs and the seasonal radiative balance (Simpson and Sharples, 2012). The balance between buoyancy-driven stratification and turbulence-induced mixing directly influences nutrient distribution, biological production, and the oxygenation of deeper layers. Stratified conditions limit vertical exchanges, promoting the formation of subsurface chlorophyll-a maxima (SCM) and enhancing oxygen depletion processes in the layers below, potentially leading to hypoxia (Simpson and Sharples, 2012).

The along-shelf component of flow on the inner continental shelf is typically more energetic and dominant in terms of water column transport, often exhibiting a unidirectional pattern. In contrast, the cross-shelf component, although less energetic, is more complex due to the influence of the coastal boundary and cross-shelf forcing mechanisms. For instance, remotely driven Ekman transport can induce local coastal upwelling or downwelling. The processes that modulate cross-shelf transport of materials also affect nutrient availability, regulate water residence time, redistribute heat and salinity, influence the transport of planktonic organisms, and determine the region's biogeochemical balances (Gill and Clarke, 1973; Simpson and Sharples, 2012; Brink, 2016; Moulton et al., 2023). The presence of a promontory enhances cross-shelf mixing processes on the inner shelf (Russel and Vernell, 2017).

The coast of the state of Rio Grande do Sul is characterized by an extensive coastal plain, with a sandy shoreline stretching for approximately 600 km. The only prominent

and rigid feature along this coastline is the Rio Grande jetties, located between Chuí, 215 km to the south, and Torres, 390 km to the north (Fig. 1). The jetties extend nearly perpendicular to the shoreline, reaching approximately 4 km offshore and intersecting the 15 m isobath at their seaward end. Under N–NE wind conditions, inner shelf currents flow southward (Cruz et al., 2023), and a clockwise coastal eddy forms on the leeward side of the jetties (Vinzon et al., 2009; Franzen et al., 2023). Additionally, because the jetties are permeable, low-salinity water flows through them, enhancing the stratification of the adjacent inner shelf (Cruz and Schettini, 2025b).

This study aims to investigate the effects of the vortex formed in the shadow zone of the western jetty on the circulation and distribution of water properties, with a particular focus on its influence on the transport of suspended particulate matter. Remote sensing data and *in situ* measurements of oceanographic and meteorological variables were analyzed, enabling the description of the distribution of physical and biological properties during northeasterly wind conditions, as well as the spatial configuration of the vortex under different synoptic scenarios.

3.1 Study Area

The continental shelf of the state of Rio Grande do Sul extends approximately along a northeast-southwest axis between Arroio Chuí (34°S) and Torres (29°S), with a coastline characterized by a sandy coastal plain and few prominent features, except for the mouth of Patos Lagoon (Fig. 1). The shelf width varies between 100 and 180 km, with the shelf break depth at around 180 m and a gentle bottom slope. In the vicinity of the

Patos Lagoon mouth, the shelf is relatively flat, featuring extensive sandy banks to the north and south of the mouth (Fachin, 1998; Corrêa et al., 2019).

The jetties at Rio Grande Bar, at the mouth of Patos Lagoon, were constructed in the 1910s and are among the largest coastal engineering works of their time (Motta, 1969; Bicalho, 1983). The motivation for this construction was to stabilize the lagoon bar, ensure navigation safety, and provide access to the Port of Rio Grande. Construction began in 1911, and in its final configuration, the jetties extended 4 km from the coastline (Bicalho, 1983; Motta, 1969; Cunha et al., 2009). The construction material used was loose stones, and in 2010, the jetties were modified with tetrapod blocks (Migliorini et al., 2008), resulting in a permeable structure, with the final portion located in an area of 15 m depth.

The climate of the region is classified as humid temperate with hot summers (Cfa) according to the Köppen-Geiger classification. The monthly mean air temperature ranges between 11° C (July) and 23°C (January), with an annual average of 19°C (Reboita and Kruche, 2018). There is a predominance of NE winds throughout the year, which blows nearly parallel to the coastline, with higher intensity in spring (Reboita & Kruche, 2018; Saraiva et al., 2003; Cruz and Schettini, 2025). The wind regime is disturbed cyclically by the passage of frontal systems occurring at intervals of 6 to 11 days (Stech and Lorenzetti, 1992).

The local tide is mixed with a diurnal predominance, with an average amplitude of 0.3 m, and does not play a significant role in the hydrodynamics (Moller et al., 2007). The flow is primarily driven by local wind (Soares et al., 2001; Zavialov et al., 2002; Costa et al., 2011; Cruz et al., 2023). Currents on the continental shelf responds mainly to the wind regime (Soares et al., 2001). Currents in the inner shelf (20 and 15 m)

displayed patterns consistent with Ekman force balance, where southward longitudinal currents showed a return flow in the deeper layers of the water column (Costa et al., 2011; Cruz et al., 2023).

Exchange patterns between the lagoon and the coastal region have been investigated by Hartmann and Schettini (1991), Moller et al. (2001), and Marques and Moller (2008), Santa-Rosa and Schettini (2024). During periods of high rainfall, river discharge predominates and drives ebb flow. During low rainfall periods, wind becomes the primary control of exchange processes, acting both locally as remotely due to Ekman mechanism. Winds from the northern quadrant forces dominant ebb flow, producing a buoyant plume on the shelf. The coastal water quality is also influenced by the fluvial discharge of the Rio de la Plata (Piola et al., 2008; Muelbert et al., 2008).

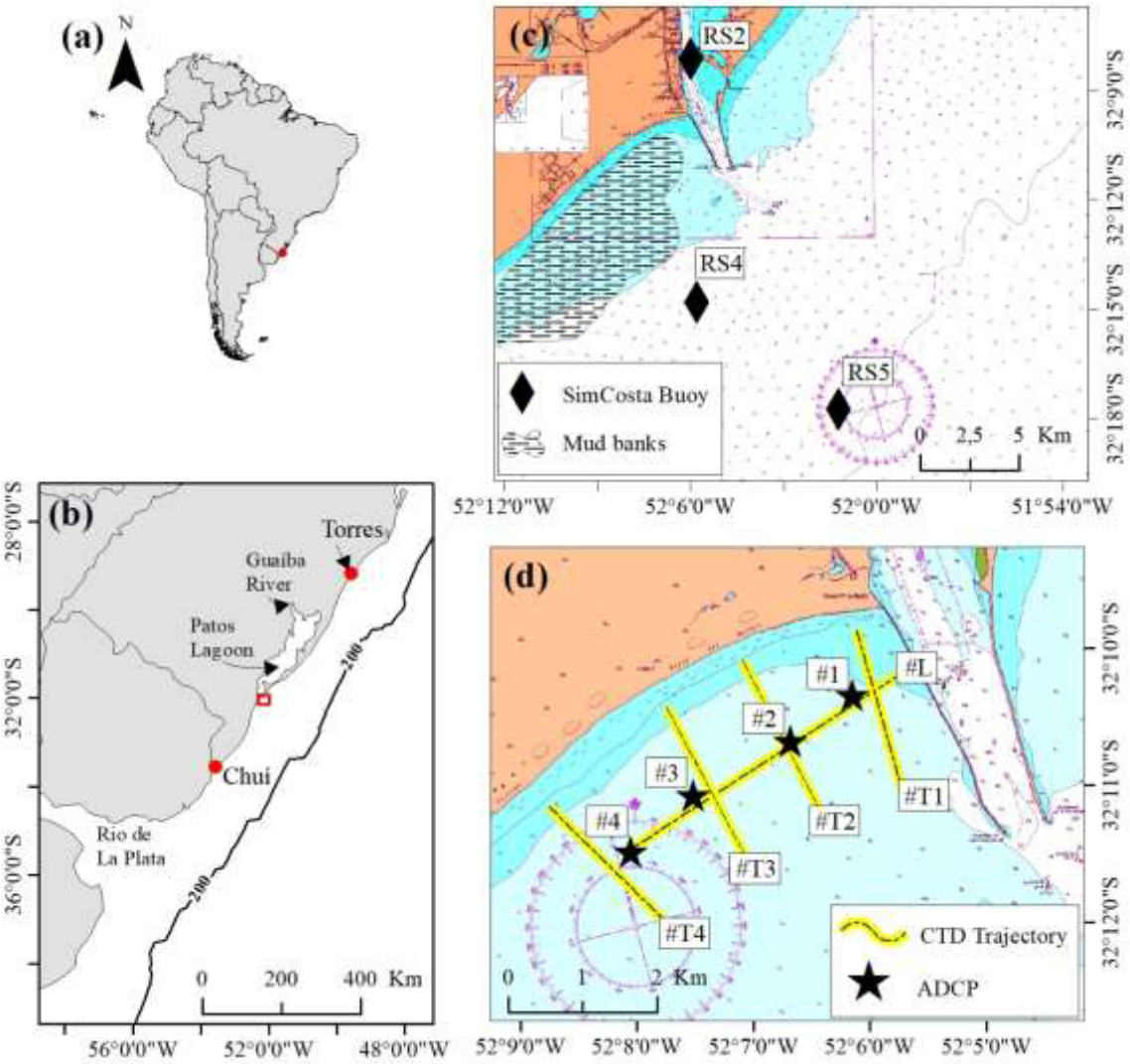


Figure 1 – Cap IV. Location of the anchored ADCPs (#1, #2, #3, #4), CTD profile collection trajectories (#T1, #T2, #T3, #T4, and #L), and SimCosta Buoys (RS2, RS4 and RS5). The bathymetric contours were obtained from the Brazilian Navy nautical charts.

4.1 Materials and Methods

Field Data:

A field experiment was designed to capture the hydrodynamic patterns in the leeward of the jetties during a period of strong northeast wind. Based on climatological data, such conditions are expected particularly at the end of spring and the beginning of summer (Cruz and Schettini, 2025). The logistics of the experiment were organized, and a waiting period was established starting from Octobe 2023. The experiment was conducted on November 28, 2023. Considering that the hydrodynamic regime is primarily wind-driven and that astronomical tides are not significant, the experiment involved data recording for approximately 10 hours. Water, current speed, and direction data were recorded simultaneously at four points along the inner shelf (Figure 1), and water properties (salinity, temperature, and turbidity) were recorded along four cross-shore sections and one parallel to the coast (Figure 1).

Vertical profiles of temperature, salinity, turbidity, chlorophyll-a, and dissolved oxygen were collected using a JFE RINKO multiparameter profiler. Several sampling points were distributed along four cross-shore transects (#T1, #T2, #T3, and #T4) and one alongshore transect (#L) relative to the coastline (Figure 1). The sampling track locations were recorded using a GARMIN GPS device.

Sea level, current velocity, and direction data were recorded using Acoustic Doppler Current Profilers (ADCPs) deployed at four locations along the alongshore transect (#L), approximately 1.5 km from the coastline, with 1 km spacing between sites. Nortek Aquadopp Profilers were used—one operating at 2 MHz and three at 1 MHz. The 2 MHz ADCP was deployed at point #1, at a depth of 6.5 m. The depths at the other points

were: point #2, 7.4 m; point #3, 8.5 m; and point #4, 7.2 m. ADCP data acquisition started at 06:20 and ended at 16:30. The 2 MHz ADCP was configured to record velocity profiles in 0.1 m cells, while the 1 MHz profilers used 0.3 m cells. Current speed data were averaged over 120-second intervals, with measurements recorded every 5 minutes.

Current data from the Rio Grande Channel were obtained from the RS2 oceanographic buoy of the SimCosta project (https://simcosta.furg.br), located approximately 8 km upstream of the jetty outlet (Figure 1). The RS2 buoy is equipped with a downward-facing 600 kHz ADCP, positioned at a depth of 0.7 m, with a blanking distance of 0.5 m and a cell size of 1 m. The bottommost cells were removed to eliminate outliers caused by acoustic side-lobe interference with the seafloor. The data were then depth-averaged to obtain the mean current direction and velocity. Observed wind data were obtained from the SimCosta project's RS4 and RS5 buoys (Figure 1), located near the study area, covering the period from 2019 to 2024.

Data Processing:

Current velocity data were rotated using principal component analysis (PCA) to obtain the longitudinal and transverse current components based on maximum variance and to determine the angle between these vectors and true north. The rotation angles at points #1, #2, #3, and #4 were 74.2°, 64.9°, 48°, and 40°, respectively. The current velocity data were used in this study to investigate the transfer of physical and biological properties in the region and to calculate the Richardson number. The study by Cruz and Schettini (2024) conducted a more detailed investigation using these current data and provided a more robust foundation regarding property transfer processes.

A key factor influencing this transfer of physical and biological properties is water column stratification, which occurs due to variations in temperature and salinity and can

inhibit vertical mixing of water masses and property exchange (Simpson and Sharples, 2012). To assess stratification stability, we employed the Richardson number (Ri), a dimensionless parameter that indicates the flow's tendency toward stratification. Ri values below 0.25 suggest unstable flow where generated turbulence is sufficient to promote vertical fluid mixing. Conversely, values above 0.25 indicate that stabilizing forces dominate over current shear, preventing vertical mixing. The Richardson number is given by:

$$Ri = \frac{N^2}{(\partial u/\partial z)^2}, \qquad N = \sqrt{-\frac{g}{\rho}\frac{\partial \rho}{\partial z}} \tag{1}$$

where N is the Brunt-Väisälä buoyancy frequency, which represents a measure of vertical motion stability determined by the density gradient (ρ), divided by the term representing shear force ∂u/∂z.

Turbidity data obtained from the optical backscatter sensor (OBS) of the multiparameter probe were converted to suspended sediment concentration (SSC) using the calibration curve:

$$SSC_{obs} = 8.215 + 0.455 OBS_{NTU} \qquad : r^2 = 0.79 \tag{2}$$

Remote sensing and reanalysis wind field:

We used Sentinel-2 satellite imagery (https://www.esa.int/Applications/Observing_the_Earth/Copernicus/Sentinel-2) to analyze vortex patterns under different environmental conditions. The images contain four spectral bands with 10 m spatial resolution, a 290 km orbital swath width, available data from 2016 to present, and a revisit frequency of ~5 days. All available images for the study area were visually inspected, selecting those with minimal cloud cover and clearly

visible vortex structures. From 1304 available images of the study region, 22 were selected for analysis.

The raw satellite data were downloaded as individual spectral bands (e.g., red, green, and blue) and processed using Python algorithms. Each band was handled separately and then combined into RGB composites. To enhance visual interpretation, a percentile stretching method (2–98%) was applied to each spectral band. This technique adjusts pixel values based on the lower and upper percentiles of their distribution, thereby enhancing contrast and emphasizing relevant oceanographic structures. Importantly, this approach improves the distinction between patterns without altering the original color balance of the image.

For the dates of the selected images, we used wind reanalysis data from the ERA5 numerical model, provided by the Copernicus Climate Change Service (C3S). ERA5 offers global atmospheric reanalysis data with a spatial resolution of ~31 km and hourly temporal resolution, generated by the European Centre for Medium-Range Weather Forecasts (ECMWF) prediction model.

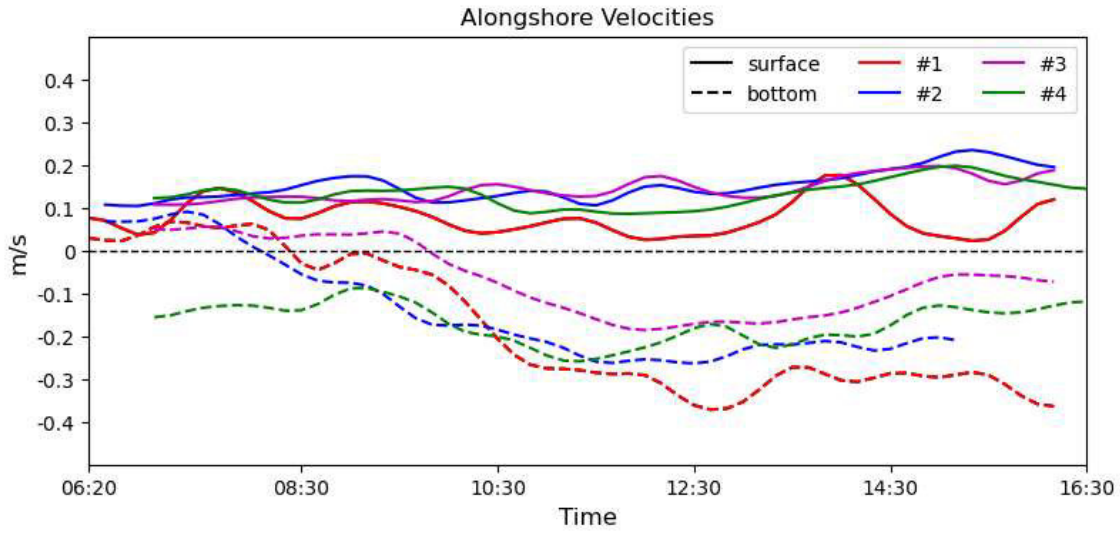
Wind speed and direction variables at 10 m above sea level were extracted to ensure adequate synoptic representation, since observational data from meteorological buoys contained temporal gaps that prevented climatological analysis of all images. Nevertheless, the buoy observational data were used to calculate the root mean square error (RMSE) between observed and modeled values to assess the reanalysis data accuracy. Additionally, ERA5 data were interpolated to a new grid with ~3 km resolution to improve data visibility.

5.1 Results

The presentation sequence was organized as follows: (1) flow characterization, (2) water properties, and (3) satellite imagery. Representative images showing distinct synoptic conditions are presented in the main text, while all selected images are provided in the Supplementary Material.

Flow Characterization

Figure 2 shows the time series of current velocity for the along-shelf component at both surface and near-bottom levels. Positive values indicate flow direction toward the jetties, while negative values indicate flow away from the jetties. All four instruments showed similar patterns. The surface layer flows away from the jetties, while the bottom layer flows in the opposite direction, toward the jetties. At the beginning of the period (before 08:00), except for point #4, the flow at all other points was unidirectional toward the jetties. It is important to note that the surface data were actually collected approximately 1-2 m below the water surface.



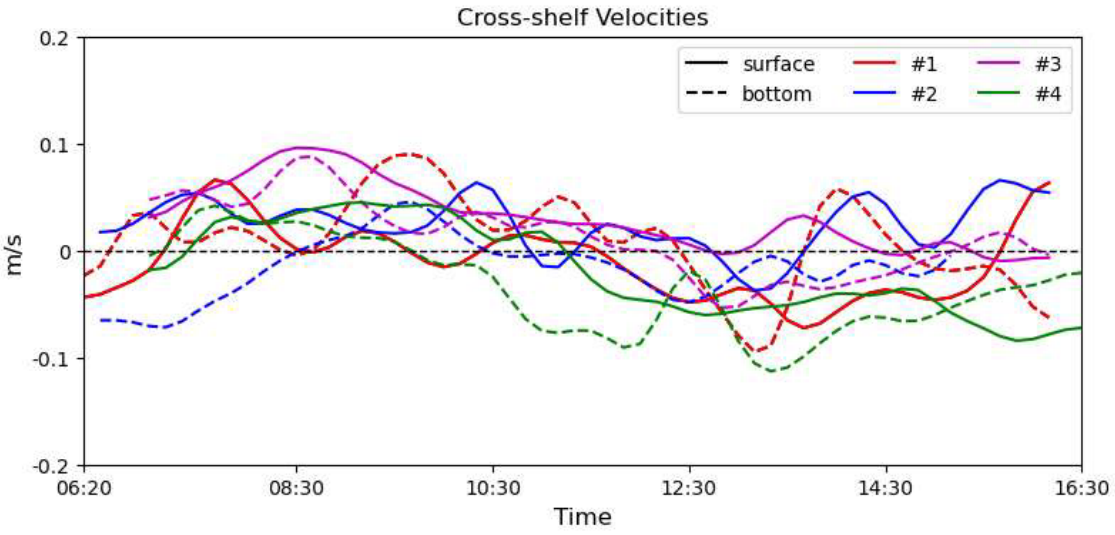


Figure 2 – Cap IV. Time series of alongshore current velocity for the four ADCP measurement points (#1, #2, #3, #4). The solid lines represent the uppermost layer measured by the ADCP, while the dashed lines indicate the bottommost layer.

Figures 3a and 3b display the vertical profiles of the alongshore and cross-shore current components, respectively. These profiles represent the temporal median values with their corresponding occurrence percentile intervals for each measurement level. The alongshore flow exhibits vertical direction reversal, with the surface layer thickness increasing with distance from the jetties (Figure 3a). The cross-shore component showed vertically unidirectional patterns in terms of median values, but with significantly greater variance (Figure 3b). The highest variability was recorded at point #1, featuring a broader distribution of both median and percentiles toward the coast. At points #2 and #3, the percentiles and median distribution were predominantly oriented seaward, while at ADCP #4 the distribution was directed landward.

Figure 3c presents the vertical profiles of density and Richardson number values. In all profiles there is water column stratification, and coinciding with the pycnocline occur Ri values > 0.25, indicating stratification stability. At points #1, #2, #3 and #4, the depth where the 0.25 threshold is exceeded ranges from 1.3–1.9 m, 2.5–4 m, 2.7–5.1 m,

and 2.3–5 m, respectively. It is observed that the abrupt pycnocline boundary seen at #1 becomes smoother as the distance from the jetty increases (#2, #3 and #4), with the thickness of the layer where depth exceeds the 0.25 Ri threshold matching the range of pycnocline boundary smoothing.

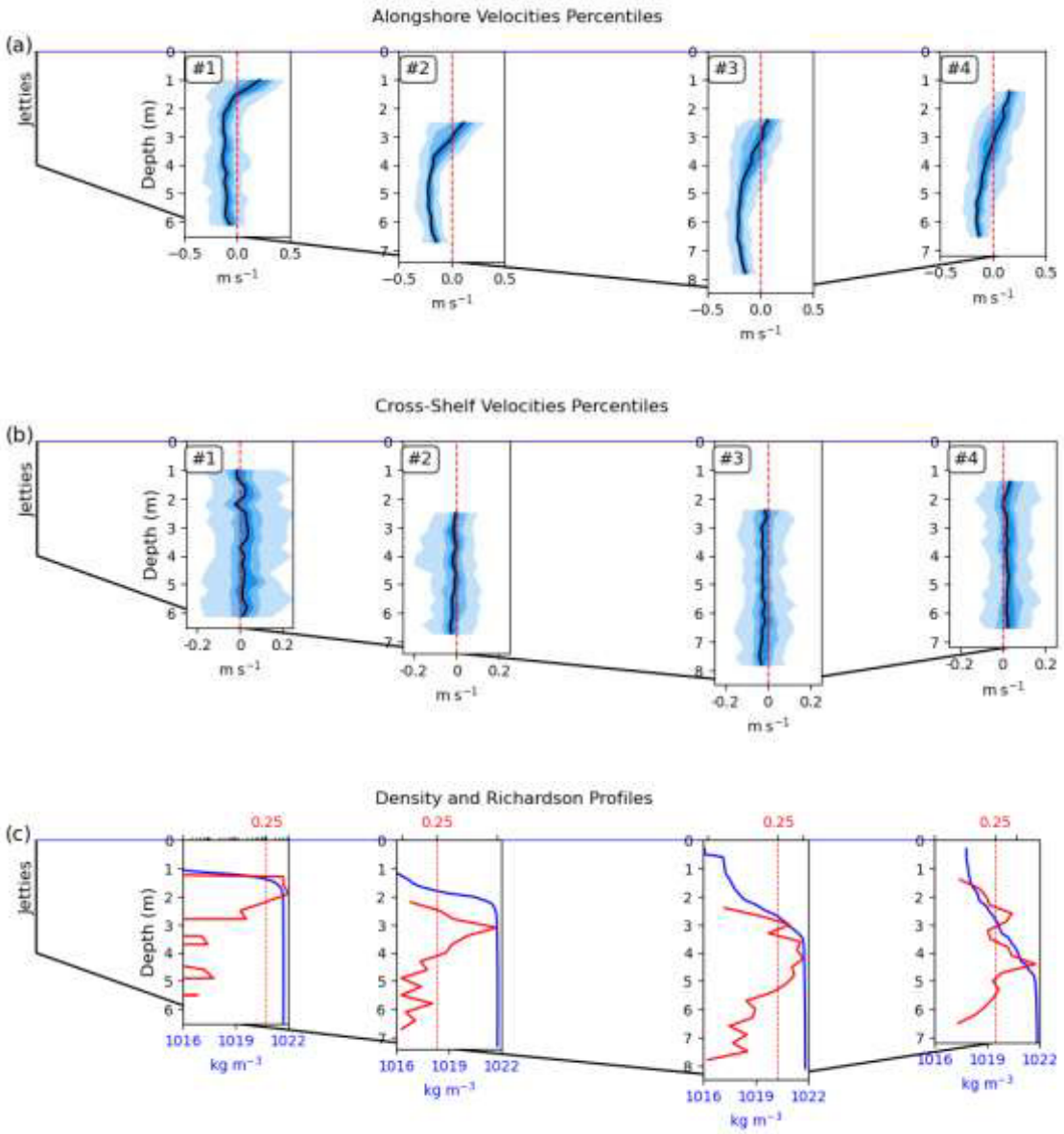


Figure 3 – Cap IV. (a) and (b): vertical profiles of alongshore and cross-shore current components, respectively. The median value is shown by the black line, while the 1st, 5th, 25th, 75th, 95th, and 99th percentiles are displayed through blue shades. The depth at each point and the distance between them are proportional to actual field

measurements. (c) Vertical profiles of density (blue) and Richardson number (red) calculated for the same period as the density profile. The red dashed line indicates the 0.25 Ri threshold.

Water Properties:

Figure 4 presents the distributions of temperature, salinity, SSC, chlorophyll-a, and dissolved oxygen for the longitudinal section (#L) and transverse sections (#T1-T4). The sections exhibited water column stratification for salinity and temperature, with salinity ranging from 14 g/kg at the surface to >30 g/kg at the bottom layer, and temperature varying from >20°C at the surface to 17°C at the bottom layer. In section #L, the thermocline and halocline coincide and deepen with increasing distance from the jetties. Near the jetties (~220 m), the thermocline occurs at ~1 m depth, increasing to ~2 m at a distance of 4.8 km (Figure 4a1). Similarly, the halocline boundary near the jetties is at ~1 m depth, deepening to ~4 m at 4.8 km distance (Figure 4b1).

In transverse sections #T1-T4, the thermocline and halocline are more pronounced in deeper regions (Figure 4b2-5). Near the coast, salinity and temperature profiles are more homogeneous. The halocline and thermocline boundaries in sections #T1, #T2, #T3, and #T4 are most clearly defined at distances of approximately 200 m, 750 m, 1000 m, and 1500 m from the coast, respectively (Figures 4a1-5, 4b1-5).

The SSC distribution in the longitudinal section (#L) showed maximum values near the surface within 1 km of the jetty, while maximum bottom values occurred between 2 and 3 km from the jetties (Figure 5c1). In section #T1, near-surface SSC values remained nearly homogeneous throughout the entire section (Figure 4c2). In contrast, sections #T2 and #T3 exhibited higher near-surface SSC values both near the coast and in the offshore region (Figure 4c3-4). Section #T4 showed elevated SSC profiles only

near the margins, with relatively lower values toward the open ocean. Near the bottom, two distinct high-SSC regions were observed: one located close to the beach, influenced by surf zone processes, and another between 1 km and 1.5 km from the coast (Figure 4c1-5).

The chlorophyll-a distribution in section #L exhibited maximum values both near the surface and near the bottom. Surface values showed a gradual decrease with increasing distance from the jetty (Figure 4d1). In the transverse sections, higher values occurred near the coast and close to the bottom. In sections #T1, #T3, and #T4, an intermediate layer with elevated chlorophyll-a concentrations was observed, showing reasonable alignment with the pycnocline position (Figure 5d1-5).

The dissolved oxygen saturation distribution in section #L exhibited stratification throughout the entire section, with near-saturation values at the surface decreasing to below 40% in the bottom layer, following the distribution patterns of salinity and temperature (Figure 4e1-5). In all transverse sections, the highest dissolved oxygen saturation values occurred at the surface and near the coast throughout the water column. At depth, all sections showed a zone of minimum saturation approximately 1-1.5 km from the coast. The low-saturation area was most extensive in section #T1 and progressively decreased across sections through to #T4.

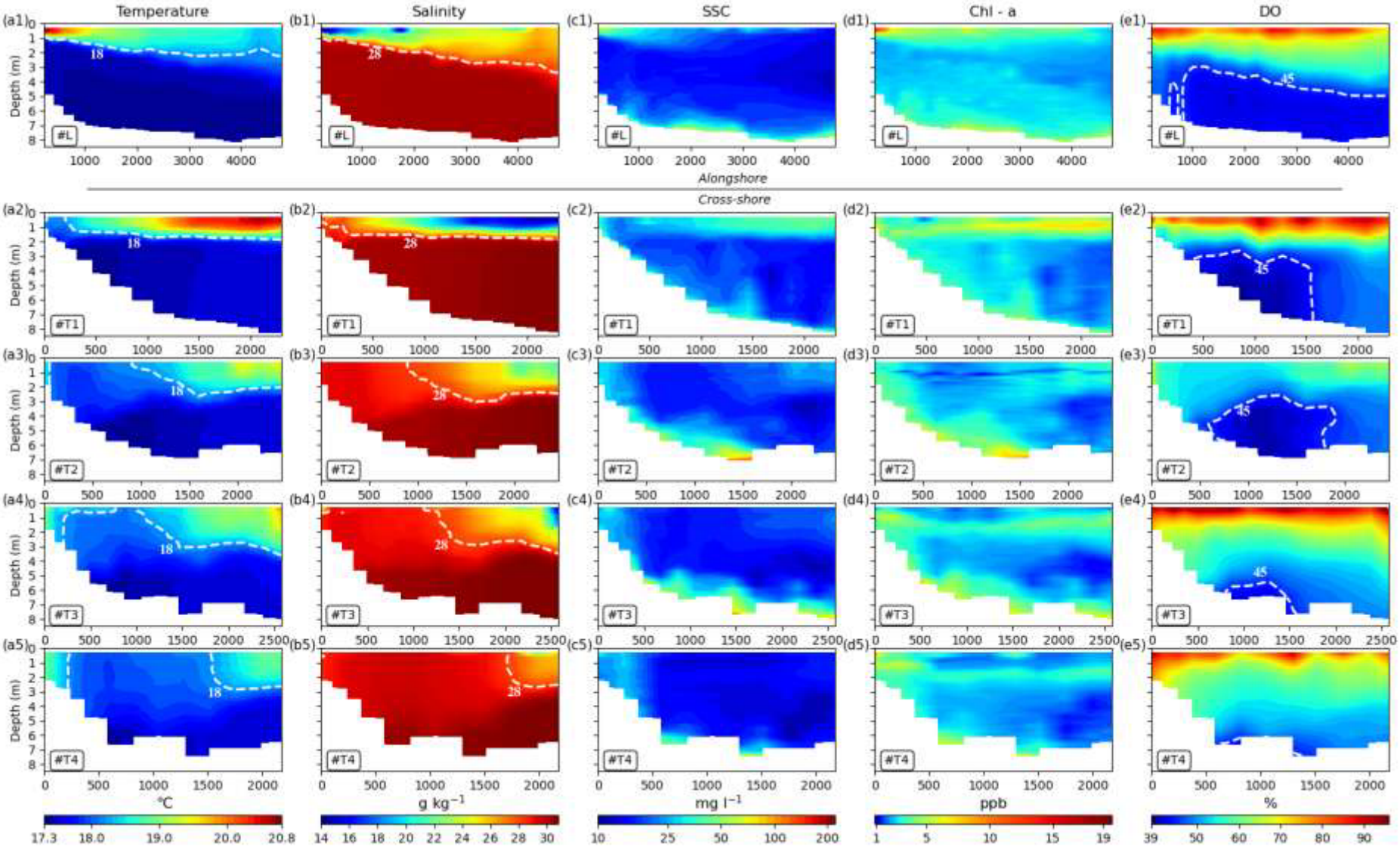

(a1)
Temperature
(b1)
Salinity
(c1)
SSC
(d1)
Chl - a
(e1)
DO
Depth (m)
#L
Alongshore
Cross-shore
(a2)
(b2)
(c2)
(d2)
(e2)
#T1
(a3)
(b3)
(c3)
(d3)
(e3)
#T2
(a4)
(b4)
(c4)
(d4)
(e4)
#T3
(a5)
(b5)
(c5)
(d5)
(e5)
#T4
°C
g kg⁻¹
mg l⁻¹
ppb
%

Figure 4 – Cap IV. Longitudinal (#L) and transverse (#T1, #T2, #T3, and #T4) sectional distributions of temperature, salinity, suspended sediment concentration (SSC), chlorophyll-a (Chl), and dissolved oxygen (DO) saturation. In the first column plots, the white dashed contour (18°C) indicates the approximate thermocline boundary. In the second column plots, the white contour (28 g kg^{-1}) marks the approximate halocline boundary. In the fifth column plots, the white dashed contour (45%) delineates regions where hypoxic conditions are favorable.

The horizontal spatial distributions for the surface layer (up to 1 m depth) and bottom layer (up to 1 m above the seabed) are shown in Figure 5. Note that the color scales used for the same variable differ between depth levels to enhance gradient visualization.

The surface distributions of temperature and salinity (Figures 5a and b) indicate upwelling is occurring near the coast, where temperatures are lower and salinity is higher. Moving away from the coast toward the jetty, temperature increases while salinity decreases, reflecting the gradient formed by estuarine water outflow through the jetties and lagoon mouth. In the bottom layer, temperature and salinity gradients are less pronounced, with warmer temperatures near the coast (shallower areas) and further from the jetties. Notably, the lowest temperatures occur not in the deepest offshore zone but in an intermediate band (Figure 5f), a pattern also evident in the sectional distributions (Figure 4a1-a4).

The surface distribution of Chl-a and SSC follows the salinity pattern, though Chl-a shows elevated values along the coast (Figure 5c-d). Near the bottom, the highest Chl-a and SSC values occur in the central region, with chlorophyll generally decreasing seaward (Figure 5h-i). Surface DO saturation (Figure 5e) shows near-saturation levels across most of the area, with lower values (~60%) near the coast where surface temperatures are coldest (Figure 5a). Bottom DO saturation (Figure 5j) displays a zone of lower saturation (<40%) along the central portion, mirroring the bottom temperature distribution (Figure 5f). The highest values occur toward the coast and SW direction.

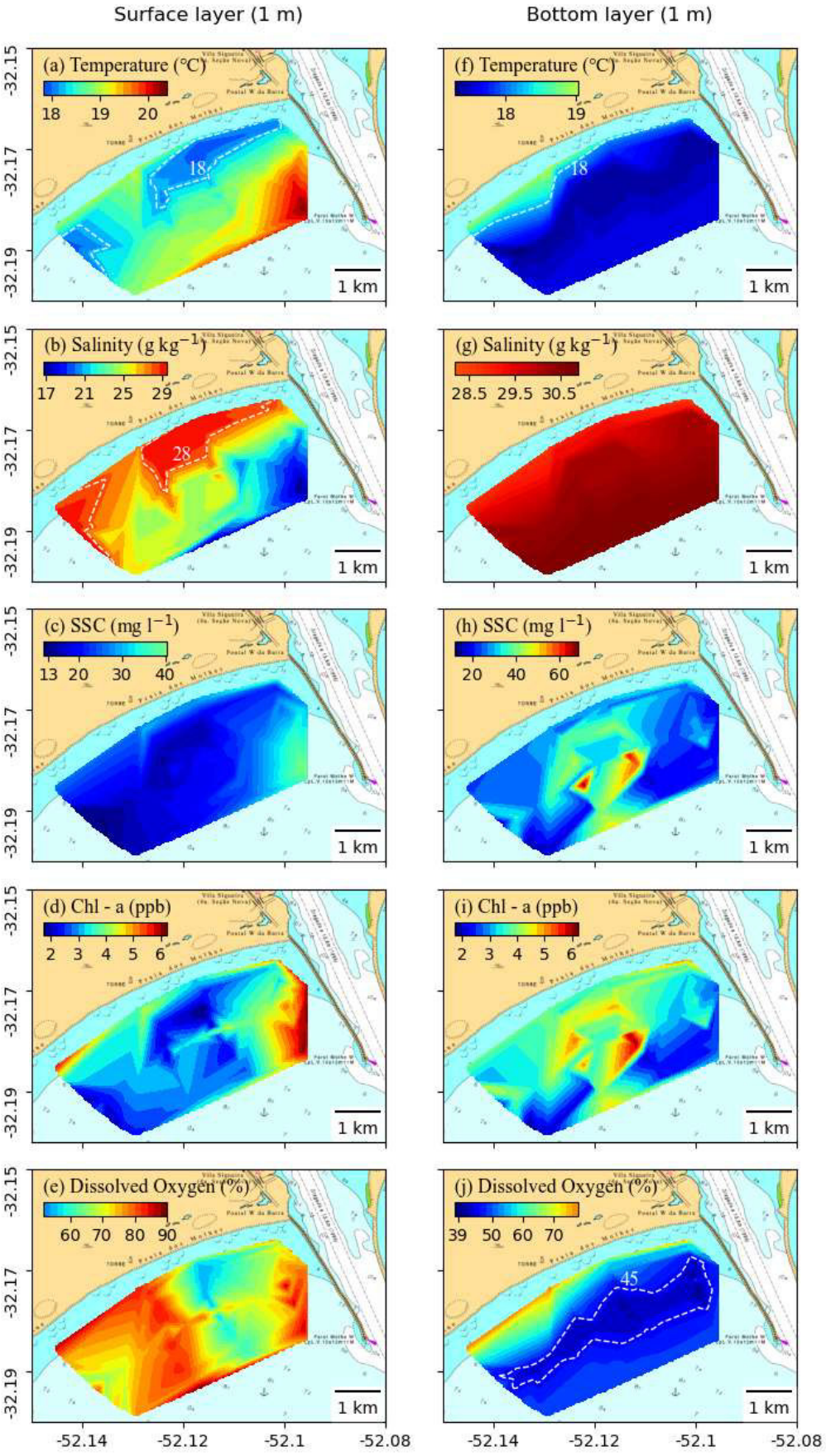

Surface layer (1 m)
Bottom layer (1 m)
(a) Temperature (°C)
18 19 20
18
(f) Temperature (°C)
18 19
18
(b) Salinity (g kg^{-1})
17 21 25 29
28
(g) Salinity (g kg^{-1})
28.5 29.5 30.5
(c) SSC (mg l^{-1})
13 20 30 40
(h) SSC (mg l^{-1})
20 40 60
(d) Chl - a (ppb)
2 3 4 5 6
(i) Chl - a (ppb)
2 3 4 5 6
(e) Dissolved Oxygen (%)
60 70 80 90
(j) Dissolved Oxygen (%)
39 50 60 70
45
1 km
-32.15
-32.17
-32.19
-52.14
-52.12
-52.1
-52.08

Figure 5 – Cap IV. Spatial distribution of temperature, salinity, suspended sediment concentration (SSC), chlorophyll-a (Chl-a), and dissolved oxygen (DO), calculated from data collected in the transverse and longitudinal sections. The first column plots (a-e) show the mean distribution for the upper 2 m water column, while the second column plots (f-j) display the mean distribution from 1 m above the seabed. The white 18°C contour in (a) and 28 g kg^{-1} contour in (b) mark the approximate thermocline and halocline positions, respectively. The white 45% contour in (j) identifies the region prone to hypoxic conditions.

Sattelite Images:

No satellite imagery was available for the exact date of the field surveys. Therefore, images acquired under relatively similar meteorological conditions were analyzed to provide a larger-scale synoptic perspective. A total of 22 Sentinel-2 satellite images were selected and combined with atmospheric conditions simulated by the ERA5 reanalysis model at the time of image acquisition. These images were obtained under wind conditions with a mean direction of 222° (SW) and average speed of 3.8 m/s. Of the 22 images, 18 were acquired with winds between 201°-282° (W-SW), while 3 showed a mean wind direction of 172° (S).

Due to varying atmospheric conditions in each image, the duration of each event was defined considering periods when wind direction fell within the E-N quadrant (180°-270°), either starting at or spanning the satellite image acquisition time. The average event duration was 2 days and 9 hours, with a maximum of 5 days and 3 hours recorded on January 9, 2022. Table 1 summarizes the dates of selected satellite images, atmospheric conditions, and current velocity/direction recorded at the RS-2 buoy in the Rio Grande Channel. All current directions indicate ebb tide conditions.

Table 1 – Cap IV. Summary of selected periods from Sentinel-2 satellite imagery, with corresponding atmospheric conditions obtained from the ERA5 reanalysis model and RS4-5 buoys of the SimCosta (SC) project. Current conditions were derived from ADCP data of the SimCosta project's RS2 buoy. Satellite image acquisition time was 13:20 for all dates.

Date	Wind						Current	
	Direction		Magnitude		Event duration		Magnitude	Direction
	ERA5	SC	ERA5	SC	ERA5	SC	SC	
2017-01-28	245	12	0.8	1.9	4.7	4.7	-	-
2019-04-13	205	206	4.1	3.6	1.7	1.7	0.8	183
2019-06-27	254	262	6.5	5.6	1.8	1.1	0.7	180
2020-02-12	188	200	6.9	8.9	2.6	2.8	0.1	232
2020-02-24	237	213	7.2	6.5	1.5	1.4	0.4	188
2020-03-23	209	202	7.4	7.2	3.7	3.5	0.1	211
2020-05-19	248	235	8.7	7.5	2.5	2.5	0.8	188
2020-11-20	153	231	5.1	6.3	3.3	3.2	0.1	179
2021-01-29	239	204	5.6	5.8	1	1	0.1	213
2021-03-20	239	232	11.6	11.9	1.5	1.2	1.4	175
2021-04-19	175	170	6.8	5.9	4	4.3	0.6	180
2021-05-09	227	233	8.4	4.6	1.7	1.1	0.7	182
2022-01-09	210	221	9.2	9.6	5.1	5.4	-	-
2022-01-14	244	-	6.5	-	2.1	-	-	-
2022-02-03	232	221	7.1	7.3	2.4	2.2	-	-
2022-04-24	267	262	7.5	8.2	1	1.1	-	-
2022-12-08	243	223	7.0	6.0	2.9	2.7	0.5	180
2023-02-08	250	-	6.9	-	1.6	-	0.5	160
2023-03-28	240	237	8.0	9.4	1.5	1.9	0.7	204
2023-04-22	282	274	4.0	3.8	0.9	0.7	0.5	175
2023-04-24	220	209	6.5	6.6	2.4	2.3	0.9	172
2024-03-07	201	-	3.8	-	2.2	-	-	-

On the field survey date (2023-11-28), the duration of the east-north (E-N) wind event was approximately 6 days, from 2023-11-25 to 2023-12-02. During this period, the mean wind speed and direction were 9.2 m/s and 199°, respectively, with a maximum wind speed of 10.3 m/s. Although no satellite images were available near the field survey

date, the synoptic conditions recorded on 2020-02-12 (Figure 6) were similar, according to SimCosta buoy data (Table 1). On this date, the vortex center location is visible approximately 3 to 4 km from the midpoint of the west jetty. Near the margins, between 1 and 2 km from the coast, two small counter-rotating vortices are observed opposite to the main vortex, forming a complex structure in the jetty's shadow zone.

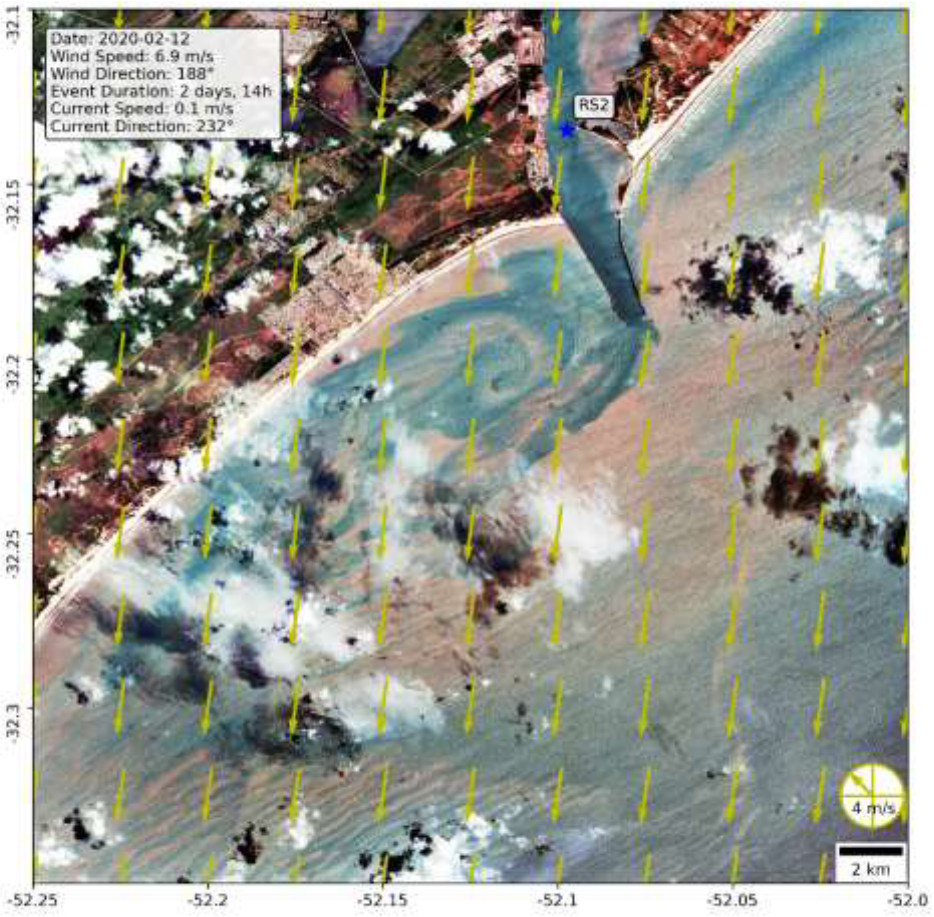


Figure 6 – Cap IV. Sentinel-2 satellite image acquired on 2 of November of 2023. The yellow vectors indicate wind direction and intensity. The scale in the lower right corner represents 2 km (spatial reference) and 4 m/s (wind intensity reference).

In Figure 7, the synoptic conditions showed wind directions with more oblique or perpendicular angles relative to the jetty (approximately 153°), indicating that even without direct influence from the physical barrier created by the jetties, the vortex structure remained well-defined. On 2020-02-12 and 2021-04-19, the mean wind direction was similar to that observed on 2020-11-20 (Figure 7), approximately 188° and 174° respectively, and on all these dates, the presence of the vortex in the shadow zone was easily identified.

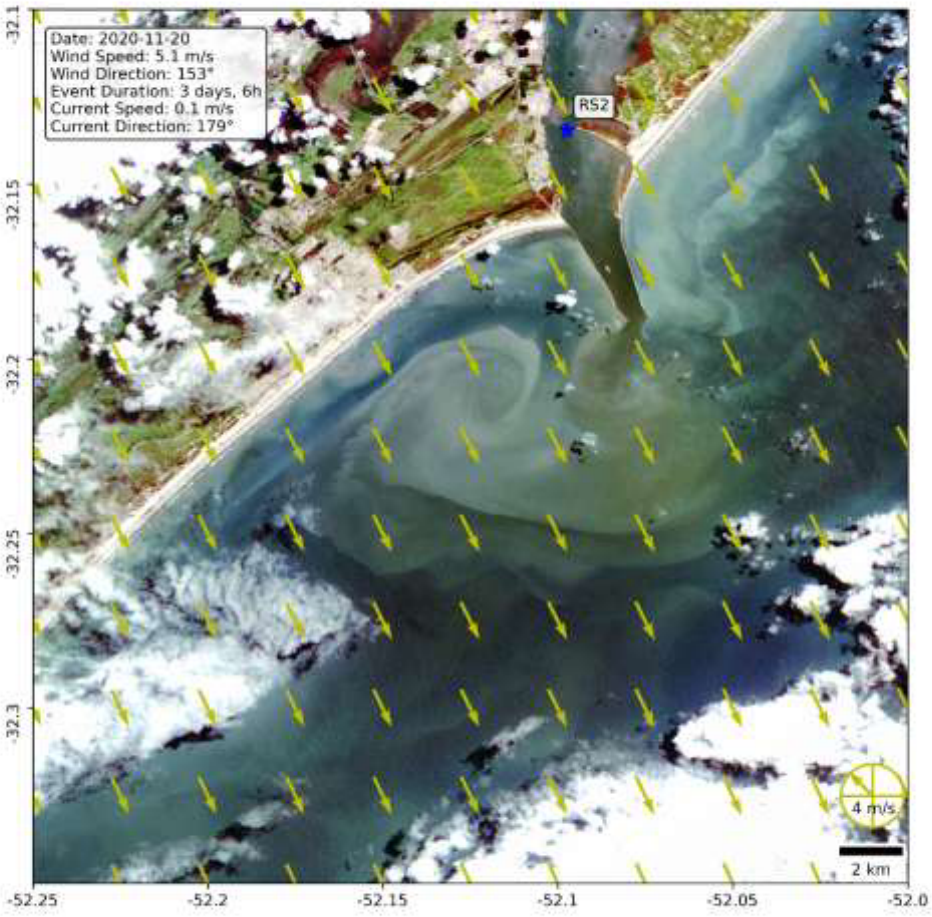


Figure 7 – Cap IV. Sentinel-2 satellite image acquired on 20 of November of 2020. The yellow vectors indicate wind direction and intensity. The scale in the lower right corner represents 2 km (spatial reference) and 4 m/s (wind intensity reference).

On 2021-03-20, the most intense wind conditions of the image dataset were observed, with speeds reaching 11.6 m/s and direction nearly parallel to the jetty axis. Currents within the lagoon also recorded their highest values at approximately 1.4 m/s. Although cloud cover hindered precise estimation of the vortex extent, its boundaries can be inferred to have reached at least 12 km from the western jetty (Figure 8).

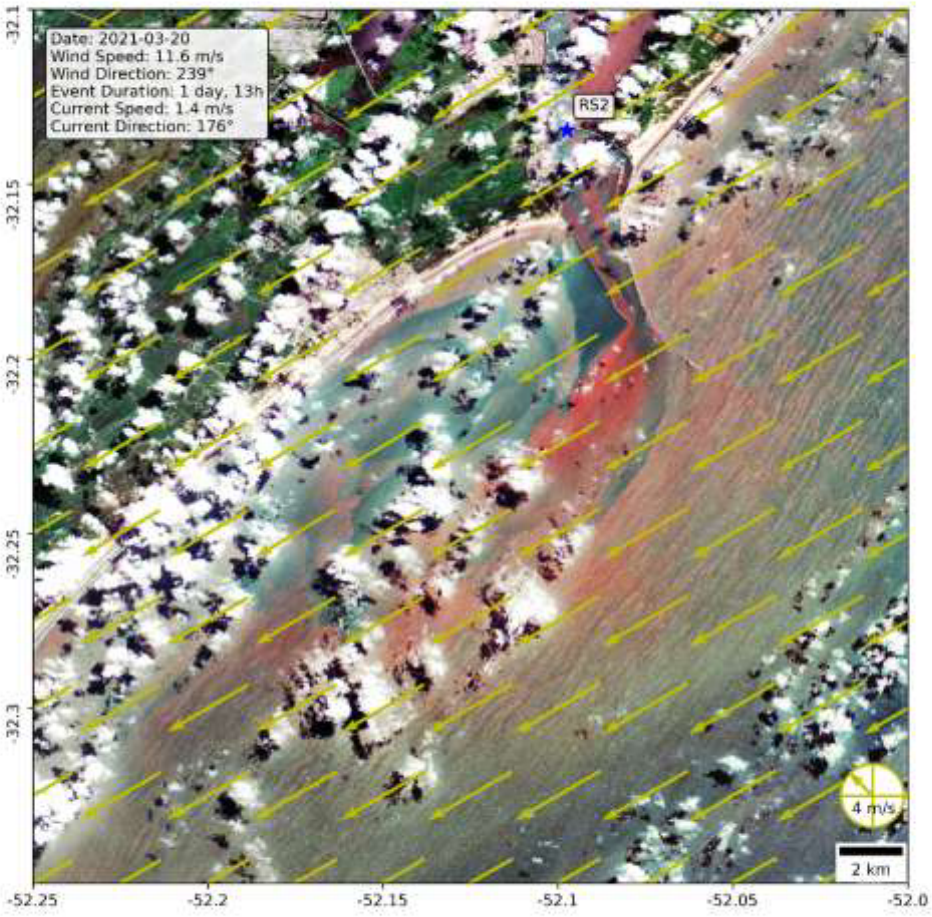


Figure 8 – Cap IV. Sentinel-2 satellite image acquired on 20 of March of 2021. The yellow vectors indicate wind direction and intensity. The scale in the lower right corner represents 2 km (spatial reference) and 4 m/s (wind intensity reference).

A wind direction near the E quadrant (270°) also leads to vortex formation, though with typically reduced spatial extent. On 2022-04-24, with wind speeds of 7.5 m/s and direction of 266°, the vortex boundaries extended approximately 4 km from the western jetty (Figure 9).

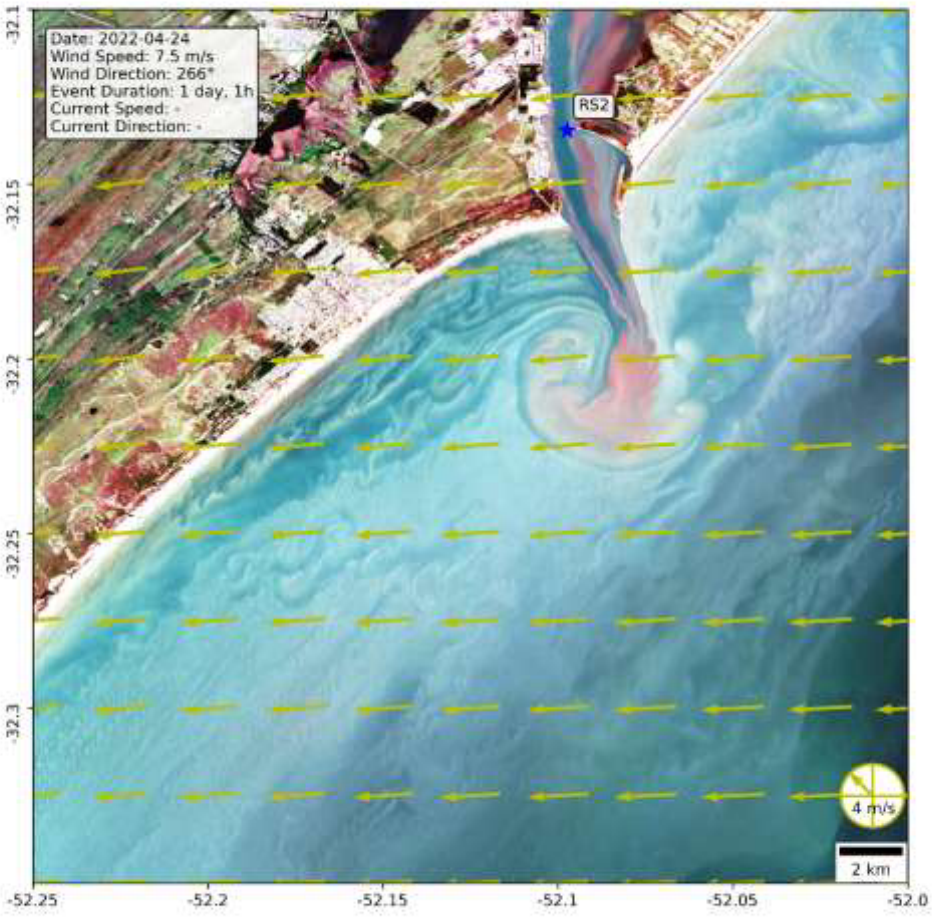


Figure 9 – Cap IV. Sentinel-2 satellite image acquired on 24 of April of 2022. The yellow vectors show wind direction and intensity. The scale in the lower right corner represents 2 km (spatial reference) and 4 m/s (wind intensity reference).

Figure 10 shows the vortex structure was less defined compared to other analyzed dates. This occurred because the wind direction on this date (2023-04-22) - approximately 288° - did not favor vortex maintenance, initiating its dissipation.

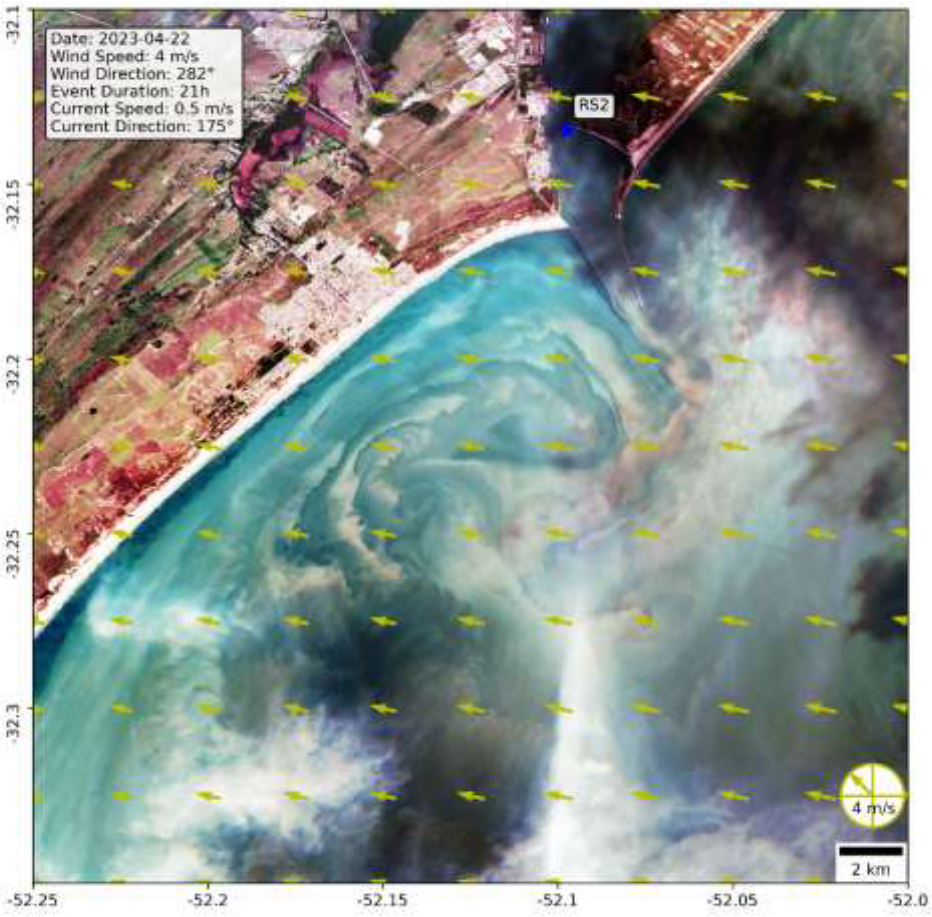


Figure 10 – Cap IV. Sentinel-2 satellite image acquired on 22 of April of 2023. The yellow vectors display wind direction and intensity. The scale in the lower right corner represents 2 km (spatial reference) and 4 m/s (wind intensity reference).

During certain periods (2019-04-13, 2020-11-20, 2021-04-19, 2024-03-07), water percolation from inside the jetties to the western jetty's shadow zone is visible, as demonstrated by Cruz and Schettini (2025b). Figure 11 illustrates this water inflow through the jetties on 2024-03-07.

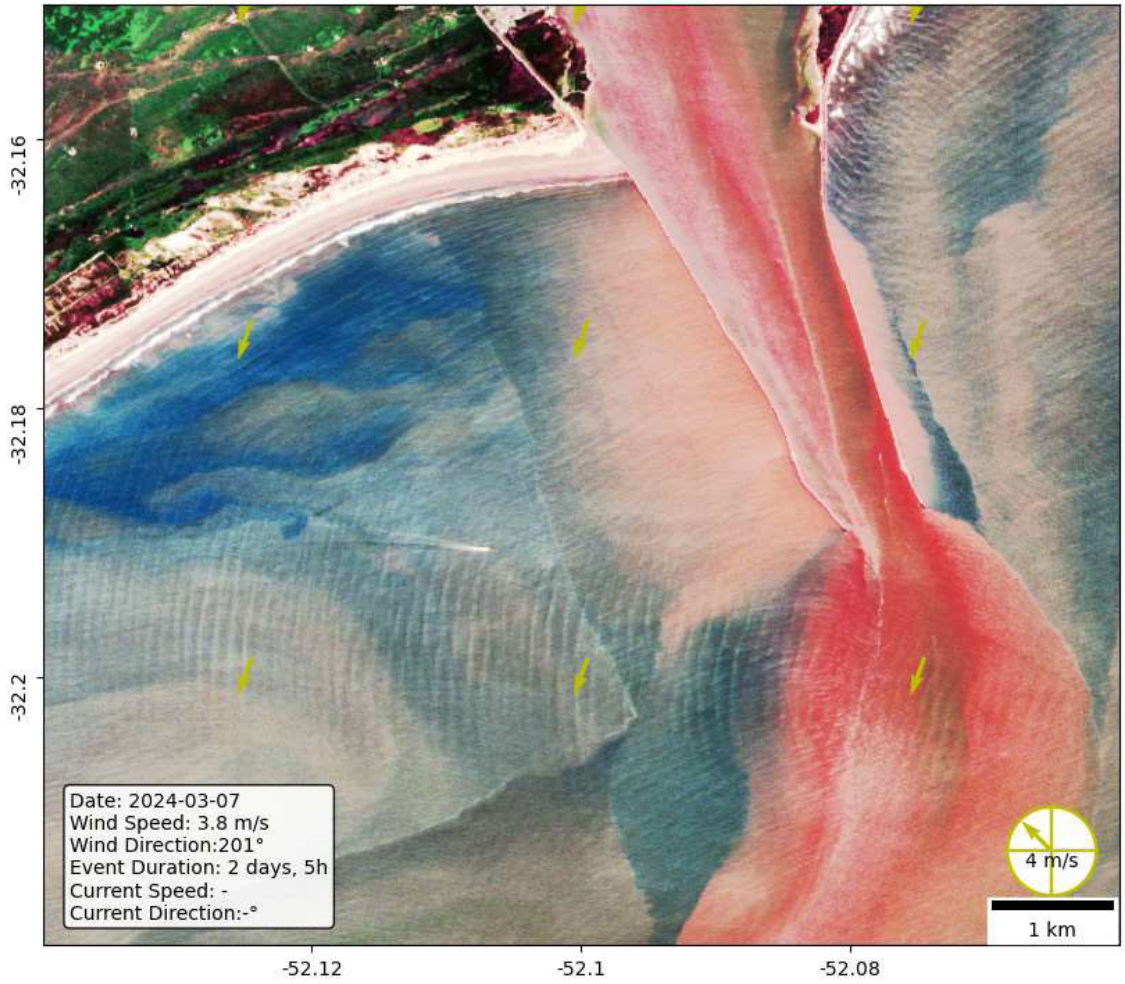


Figure 11 – Cap IV. Sentinel-2 satellite image acquired on 7 of March of 2024, showing water percolation through the jetties into the western jetty's shadow zone. The scale in the lower right corner represents 2 km (spatial reference) and 4 m/s (wind intensity reference).

6.1 Discussion

The coast south of the mouth of Patos Lagoon (Cassino beach) experiences cyclic events of mud deposition on the beach (Calliari et al., 2007). On the inner shelf off the beach, pockets of unconsolidated mud occur, and after certain storms, this material is eroded and transported shoreward (Calliari et al., 2001; Pereira et al., 2011), indicating high mud mobility on the shelf. However, the factors controlling these beach deposition events or high turbidity periods are not yet fully understood. This process is highly relevant for primary production, as it can either enhance or inhibit high production rates. Elevated turbidity may reduce light intensity in the photic zone, or conversely, fertilize the upper water column layers. Bacteria and organic matter production also alter the biogeochemical conditions of the environment and may act as binding agents, indirectly affecting mud floc formation (Black et al., 2002).

The characterization of the vortex in the jetty's shadow zone was initially identified and quantified through hydrodynamic numerical models (Vinzon et al., 2009; Franzen et al., 2023), which analyzed its potential effect on sediment deposition on Cassino Beach's inner shelf. However, these models suggest that the sediment accumulated in the jetty's shadow zone originates from the Patos Lagoon plume. In contrast, the field-based study by Cruz and Schettini (2025), using data collected from the inner shelf (20 m depth), demonstrated that bottom interactions represent the main factor responsible for temporal SSC variability.

Our results support the hypothesis that bottom interaction is the primary source of mud accumulation in the jetty's shadow zone. Cross-shore current data, along with salinity and temperature measurements, reveal a bottom flow toward the coast (Figure 2b), albeit

with lower intensity and high variability. We also observed the intrusion of colder, saltier waters mixing with Patos Lagoon outflow and advancing coastward (Figure 4a-b). This mechanism helps explain sediment accumulation in the jetty's shadow zone, where resuspension of bottom material - progressively transported by the shoreward flow - results in a concentration peak at the vortex center, as seen in section #T2 (Figure 4c3).

When light and nutrient availability are sufficient, photosynthetic organisms use sunlight to fix carbon and convert it into organic compounds, releasing oxygen as a byproduct of this process (Muelbert et al., 2008; Calliari et al., 2009). Dissolved oxygen (DO) concentration in seawater can therefore serve as an indicator of primary production (Braga et al., 2008). In this study, chlorophyll-a and SSC concentrations showed strong correlation with surface salinity, suggesting that low-salinity water rich in particles and nutrients originates from the Patos Lagoon channel. However, as demonstrated by Cruz and Schettini (2025b), this export occurs through percolation within the jetties, promoting more efficient nutrient distribution across the surface layer and explaining the high primary production rates observed near the jetty (Figure 4d1).

The balance between light and nutrient availability, combined with the presence of a pycnocline—which acts as a physical barrier trapping phytoplankton in the surface layer—promotes the formation of a subsurface chlorophyll maximum (SCM), as observed in cross-sections #T1, #T3, and #T4 (Figures 4d2, 4d4, and 4d5). Just below the pycnocline, restricted vertical diffusion leads to a rapid decline in dissolved oxygen (DO) levels, creating favorable conditions for hypoxia development (~30% saturation) (Figure 4e5) (Rabalais et al., 2010). This pattern results from the interaction of three coupled processes: (i) DO consumption by bacterial respiration and organic matter decomposition; (ii) advection of oxygen-poor water masses by bottom currents toward the coast; and (iii) restricted atmospheric ventilation or SCM oxygenation due to the pycnocline barrier. In

section #T2, where the vortex center increases water residence time, this mechanism is intensified, causing subsurface nutrient and DO depletion (Figures 4d3 and 4e3).

Similar hypoxia-favoring mechanisms are observed in the Louisiana Dead Zone, where excess nutrients from rivers lead to increased primary production but also decrease dissolved oxygen (DO) in bottom waters (Rabalais et al., 2003). Upwelling regions exhibit analogous behavior, as the upwelled deep waters from beyond the shelf break can introduce low-DO waters, either through natural oxygen depletion or via organic matter decay stimulated by upwelled nutrients (Connolly et al., 2010). These hypoxic conditions may cause mortality, reduced physiological capacity in aerobic organisms and macrofauna, biodiversity loss, and a shift toward more hypoxia-resistant species (Diaz and Rosenberg, 1995; Rabalais et al., 2010; Brauko et al., 2020).

In sections #T3 and #T4, the stratified layers occur at greater depths with more intense vertical mixing, enabling more efficient redistribution of dissolved oxygen (DO) throughout the water column. This mechanism promotes both DO level recovery and subsurface chlorophyll maximum (SCM) reestablishment, indicating enhanced renewal of water masses and physical-biogeochemical properties in these areas farther from the jetty (Figures 4e4 and 4e5).

Additionally, the settling of organic matter produced by high subsurface primary productivity may facilitate mud floc formation and growth, acting as a binding agent between flocs. While physical forcing plays a dominant role in mud floc formation and size, organic matter presence can increase floc cohesion and adhesion, contributing to the stabilization of larger flocs (Black et al., 2002).

Existing studies of the jetty-shadow vortex have focused exclusively on NE quadrant winds, but as shown in Figure X, NW winds also favor vortex formation. A more

parallel angle between wind direction and jetty orientation enhances vortex extension (Figure 3), while wind intensity and angle relative to the jetties control the vortex core position (Figures 4 and 5). Consequently, this displaces and potentially expands the low-DO zone, increasing its susceptibility to hypoxic conditions depending on event duration.

7.1 Conclusion

This study investigated the spatial variability of the vortex formed west of the jetties at the mouth of Patos Lagoon and how this phenomenon affects the distribution of physical and biological properties in the area. The combination of remote sensing data with ERA5 numerical model wind data allowed characterization of the vortex's spatial structure, revealing the necessary conditions for its formation and spatial variability. Field-collected data enabled a more detailed assessment of the vortex's impacts on water quality.

The characteristics of water masses and particulate matter in this region directly influence dissolved oxygen (DO) availability, chlorophyll-a concentration, and suspended sediment (SSC) distribution. Additionally, the pycnocline acts as a barrier to vertical diffusion, restricting oxygen and nutrient exchange between water column layers while trapping phytoplankton in the subsurface layer, promoting the formation of subsurface chlorophyll maxima (SCM). These findings highlight the importance of considering small-scale circulation features when assessing coastal ecosystem dynamics near engineered structures.

Capítulo V: Síntese das Conclusões

Este capítulo apresenta uma síntese das conclusões derivadas dos três estudos que compõem esta tese, focando na dinâmica hidro-sedimentar da plataforma interna, tendo como área de observação a plataforma continental do Rio Grande do Sul, adjacente à desembocadura da Lagoa dos Patos. Além das limitações de cada metodologia e perspectivas para trabalhos futuros.

A hipótese inicial deste estudo propunha que a presença dos molhes da desembocadura da Lagoa dos Patos altera os fluxos hidrodinâmicos e a dinâmica de sedimentos na plataforma interna adjacente. A análise dos resultados, contudo, mostra que essa influência não ocorre de forma uniforme em toda a área estudada.

No primeiro trabalho, realizado a aproximadamente 10 km da desembocadura, não foram observadas evidências consistentes de que os processos hidrodinâmicos e sedimentares registrados fossem diretamente influenciados pelos molhes. Que está de

acordo com os resultados de simulações numéricas feita para a mesma região, antes e após a construção dos molhes (Franzen et al, 2023). Os padrões identificados respondem principalmente a forçantes como o vento, ondas e plumas fluviais, e não às alterações estruturais impostas pelos molhes. Nota-se a importância da tensão de cisalhamento de fundo, principalmente por correntes, sob a ressuspensão de sedimentos, especialmente sob condições de alta energia. As correntes longitudinais para norte resultaram em uma maior SSC no fundo, enquanto correntes para sul levaram a umas menor SSC no fundo e uma distribuição mais homogênea na coluna d'água, sugerindo menor ressuspensão e maior mistura. Com a advecção horizontal tendo um papel secundário na distribuição vertical de SSC, sua relevância aumenta em períodos de correntes fracas e baixa tensão de cisalhamento.

Por outro lado, os resultados do segundo e do terceiro trabalhos evidenciam que, nas proximidades imediatas dos molhes, há uma influência significativa nos fluxos longitudinais e transversais e na distribuição espacial de sedimentos. A presença de uma picnoclina bem definida, resultante da percolação de água doce através dos molhes, ressaltq a importância da resposta baroclínica na circulação hidrodinâmica regional e na transferência de propriedades de qualidade da água. Este processo induz um desacoplamento entre a camada superior e as camadas intermediárias/profundas do fluxo, com a camada superior mais fina próxima ao molhe e mais espessa à medida que se afasta. Este desacoplamento concentra o momento transferido pelo vento na camada superior, intensificando o gradiente vertical das velocidades longitudinais e transversais. As medições de SSC sugerem zonas de convergência favorável à deposição

Ademais, a picnoclina atua como uma barreira à difusão vertical, restringindo a troca de oxigênio entre as camadas da coluna d'água, ao mesmo tempo em que retém o

fitoplâncton na camada subsuperficial, promovendo a formação de máximos de clorofila-a de subsuperfície (SCM).

Dessa forma, conclui-se que a hipótese inicial foi parcialmente confirmada. A influência dos molhes é clara nas áreas próximas às estruturas, mas não se estende de forma significativa para regiões mais afastadas, onde predominam outros mecanismos de controle.

Limitações da Metodologia e Perspectivas Futuras

A aplicação do modelo de Rouse possui limitações, como a não consideração da estratificação da coluna d'água (Rippeth, 20050 e restrições a condições de baixa energia e advecção horizontal, resultando na exclusão de perfis de SSC. A validação de parâmetros como tamanho e velocidade de decantação é desafiadora devido às dificuldades de medição in situ e à complexidade da interação onda-corrente na tensão de cisalhamento no fundo (Grant e Madsen, 1979; Myrhaug et al., 1997; Soulsby e Clarke, 2005). A estimativa de SSC por retroespalhamento acústico é limitada a altas concentrações (> 10 mg/L), com precisão dependente da calibração, frequência, e com um maior erro em baixas concentrações. Apesar dessas ressalvas, a combinação de estimativas de SSC derivadas de ADCP com a teoria de Rouse provou ser uma estrutura eficaz para avaliar a dinâmica de sedimentos em suspensão na plataforma interna, sendo uma ferramenta valiosa para estudos futuros.

Além disso, os dados de sensoriamento remoto em conjuntos com os de vento do ERA5 mostraram que a formação do vórtice ocorre sobre diferentes direções de vento. Futuros trabalhos com coletas de dados de campo, nessas condições de vento, podem ajudar a esclarecer ou elucidar as condições favoráveis ao acúmulo de material sedimentar em suspensão. Os processos hidro-morfodinâmicos relacionados à zona de surf e ação de

ondas nessa região também podem beneficiar a compreensão dos eventos de deposição de lama na praia

Capítulo VI: Referências

Al Ani, S., Dyer, K. R., & Huntley, D. A., 1991. Measurement of the influence of salinity on floc density and strength. Geo-Marine Letters, 11(3–4), 154–158. https://doi.org/10.1007/BF02431002.

Al-Ragum, A., Monge-Ganuzas, M., Amos, C.L., Cearreta, A., Townend, I., Manca, E., 2014. An evaluation of the Rouse theory for sand transport in the Oka estuary, Spain. Continental Shelf Research, 39-50, 78. https://doi.org/10.1016/j.csr.2014.01.018.

Andrade, J., Rigon, L., Toldo, E., & Schettini, C., 2012. Descarga sólida em suspensão do sistema fluvial do Guaíba, RS, e sua variabilidade temporal. Pesquisas Em Geociências, 39(2), 161. https://doi.org/10.22456/1807-9806.35910.

Austin, A.J., Lentz, S.J., 2002. The Inner Shelf Response to Wind-Driven Upwelling and Downwelling. Journal of Physical Oceanography, 2171-2193, 32(7). https://doi.org/10.1175/1520-0485(2002)032<2171:TISRTW>2.0.CO;2

Ávila, R.A., Orozco, P.M.S., Andrade, M.M., Möller, O. O., 2021. Temporal Variability of Suspended-Solids Concentration in the Estuarine Channel of Patos Lagoon, Southern Brazil. Water, 13(5), 646. https://doi.org/10.3390/w13050646.

Azam, F., Fenchel, T., Field, J. G., Gray, J. S., Meyer-Reil, L. A. and Thingstad, F., 2022. The Ecological Role of Water-Column Microbes in the Sea. In Foundations of Ecology II: Classic Papers. Chicago: University of Chicago Press. https://doi.org/10.7208/chicago/9780226125534-024

Barlow, R.G., Mantoura, R.F.C., Gough, M.A., Fileman, T.W., 1993. Pigment signatures of the phytoplankton composition in the northeastern Atlantic during the 1990 spring bloom. Deep Sea Research Part II: Topical Studies in Oceanography, 40, 459-477. https://doi.org/10.1016/0967-0645(93)90027-K.

Bicalho, H., 1983. Ministério dos Negócios da Agricultura: In: Comércio e Obras Públicas – Província do Rio Grande do Sul – Melhoramento da Barra e da Navegação Interior da Província – Relatório apresentado ao governo imperial. Tipografia Nacional, Rio de Janeiro.

Black, K. S., Tolhurst, T. J., Paterson, D. M., & Hagerthey, S. E., 2002. Working with Natural Cohesive Sediments. Journal of Hydraulic Engineering, 128(1), 2–8. https://doi.org/10.1061/(ASCE)0733-9429(2002)128:1(2).

Boudreau, B. P., & Hill, P. S., 2020. Rouse revisited: The bottom boundary condition for suspended sediment profiles. Marine Geology, 419, 106066. https://doi.org/10.1016/j.margeo.2019.106066.

Braga, E.S., Chiozzini, V.C., Berbel, G.B.B., Maluf, J.C.C., Aguiar, V.M.C., Charo, M., Molina, D., Romero, S.I., 2008. Nutrient distributions over the Southwestern South

Atlantic continental shelf from Mar del Plata (Argentina) to Itajaí (Brazil): Winter–summer aspects. Continental Shelf Research, 28, 1649-1661. https://doi.org/10.1016/j.csr.2007.06.018.

Brauko, K. M., Cabral, A., Costa, N. V., Hayden, J., Dias, C. E. P., Leite, E. S., Westphal, R. D., Mueller, C. M., Hall-Spencer, J. M., Rodrigues, R. R., Rörig, L. R., Pagliosa, P. R., Fonseca, A. L., Alarcon, O. E., & Horta, P. A. (2020). Marine Heatwaves, Sewage and Eutrophication Combine to Trigger Deoxygenation and Biodiversity Loss: A SW Atlantic Case Study. Frontiers in Marine Science, 7, 590258. https://doi.org/10.3389/fmars.2020.590258.

Brink, K.H., 2016. Cross-Shelf Exchange. Annual Review of Marine Science, 8(1), 59-78. https://doi.org/10.1146/annurev-marine-010814-015717.

Brink, K.H., 2023. Physical Oceanography of Continental Shelves. Princeton University Press.

Burchard, H., Craig, P.D., Gemmrich, J.R., van Haren, H., Mathieu, Pierre-Philippe, Meier, H.E.M., Smith, A.M.N., Prandke, H., Rippeth, T.P., Skyllingstad, E.D., Smyth, W.D., Welsh, D.J.S, Wijesekera, H.W., 2008. Observational and numerical modeling methods for quantifying coastal ocean turbulence and mixing. Progress in Oceanography, 76(4), 399-442. https://doi.org/10.1016/j.pocean.2007.09.005.

Calliari, L. J., Holland, K. T., Pereira, P. S., Guedes, R. M. C., Santo, R. E., 2007. The Influence of Mud on the Inner Shelf, Shoreface, Beach, and Surf Zone Morphodynamics — Cassino, Southern Brazil. Coastal Sediments, pp 1455-1465. https://doi.org/10.1061/40926(239)112.

Calliari, L. J., Speranski, N. S., Torronteguy, M., & Oliveira, M. B., 2001. The Mud Banks of Cassino Beach, Southern Brazil: Characteristics, Processes and Effects. Source: Journal of Coastal Research, pp 318-325. https://www.jstor.org/stable/25736298.

Calliari, L.J., Brugnoli, E., Ferrari, G., Vizziano, D., 2009. Phytoplankton distribution and production along a wide environmental gradient in the South-West Atlantic off Uruguay. Hydrobiologia, 620, 47-61. https://doi.org/10.1007/s10750-008-9614-7.

Calliari, L.J., Speranski, N.S., Torronteguy, M., & Oliveira, M.B., 2001. The Mud Banks of Cassino Beach, Southern Brazil: Characteristics, Processes and Effects. Source: Journal of Coastal Research, 318-325. https://www.jstor.org/stable/25736298.

Calliari, L.J., Winterwerp, J.C., Fernandes, E., Cuchiara, D., Vinzon, S.B., Sperle, M., Holland, K.T., 2009. Fine grain sediment transport and deposition in the Patos Lagoon-Cassino beach sedimentary system. Continental Shelf Research, 29(3), 515-529. https://doi.org/ 10.1016/j.csr.2008.09.019.

Campos, E. J. D., Mulkherjee, S., Piola, A. R., & de Carvalho, F. M. S., 2008. A note on a mineralogical analysis of the sediments associated with the Plata River and Patos Lagoon outflows. Continental Shelf Research, 28(13), 1687–1691. https://doi.org/10.1016/j.csr.2008.03.014.

Castelo, W.F.L., Martins, M.V.A., de Lima Ferreira, P.A., et al, 2021. Long-term eutrophication and contamination of the central area of Sepetiba Bay (SW Brazil). Environmental Monitoring and Assessment, 193, 100. https://doi.org/10.1007/s10661-021-08861-1.

Cecilio, R.O., Dillenburg, S.R., 2019. An ocean wind-wave climatology for the Southern Brazilian Shelf. Part II: Variability in space and time. Dynamics of Atmospheres and Oceans, 88: 101103. https://doi.org/10.1016/j.dynatmoce.2019.101103.

Choi, W., 2009. Nonlinear surface waves interacting with a linear shear current. 29-36, 80(1). https://doi.org/10.1016/j.matcom.2009.06.021.

Connolly, T.P., Hickey, B.M., Geier, S.L., Cochlan, W.P., 2010. Processes influencing seasonal hypoxia in the northern California Current System. Journal of Geophysical Research: Oceans, 115, C03021. https://doi.org/10.1029/2009JC005283.

Corrêa, I., Weschenfelder, J., Calliari, L., Toldo, E., Carlos Nunes, J., & Baitelli, R., 2019. Plataforma Continental do Rio Grande do Sul. PGGM – RJ, 74-158.

Costa, R. L., Möller, O., 2011. Estudo da estrutura e da variabilidade das correntes na área da plataforma interna ao largo de Rio Grande (RS, Brasil), no sudoeste do Atlântico Sul, durante a primavera-verão de 2006-2007. Revista de Gestão Costeira Integrada, 11(3):273-281. https://doi.org/10.5894/rgci258.

Couceiro, M. A., Schettini, C. A., 2010. Estudo da dinâmica dos sedimentos em suspensão do estuário do Rio Araranguá (SC): possíveis efeitos da drenagem ácida da atividade de mineração de carvão. Geociências, UNESP, SP – BR, 26(2):251-266.

Cruz, G.O., Schettini, C.A.F., 2025. The dynamics of the inner-shelf suspended sediments based on ADCP records and Rouse theory. Continental Shelf Research. 289, 105467. https://doi.org/10.1016/j.csr.2025.105467

Cruz, G.O., Schettini, C.A.F., 2025b. Hydrodynamics of the Inner Shelf in the Shadow Zone of a Jetty: Rio Grande, Brazil. Continental Shelf Research. IN REVIEW

Cuchiara, D., Fernandes, E., Strauch, J. C., Winterwerp, J., Calliari, L., 2009. Determination of the wave climate for the southern Brazilian shelf. Continental Shelf Research, 29(3):545-555. https://doi.org/10.1016/j.csr.2008.09.025.

Cunha, R.M.P., Calliari, L.J., 2009. Natural and Antropic Geomorphological Changes in the Inlet of PAtos Lagoon Before and After its Fixation. Journal of Coastal Research, 708-712. http://www.jstor.org/stable/25737670.

Dias, J.M., Mariano, S.C., 2011. Numerical Modelling of Hydrodynamic Changes Induced by a Jetty Extension-the Case of Ria de Aveiro (Portugal). Journal of Coastal Research, 64, 1008-1012. https://www.jstor.org/stable/26482325.

Downing, J. P., Sternberg, R. W., & Lister, C. R. B., 1981. New Instrumentation for the Investigation of Sediment Suspension Processes in the Shallow Marine Environment. Marine Geology, 42, pp, 19–34. https://doi.org/10.1016/S0070-4571(08)70292-9.

Drake, C.L., and Burk, C.A., 1974. Geological significance of continental margins. The geology of continental margins, pp 3-10. https://doi.org/10.1007/978-3-662-01141-6_1.

Dugan, J.E., Airoldi, L., Chapman, M.G., Walker, S.J., Schlacher, T., 2012. Estuarine and Coastal Structures: Environmental Effects, A Focus on Shore and Nearshore Structures. Treatise on Estuarine and Coastal Science, 8, 17-41. https://doi.org/10.1016/B978-0-12-374711-2.00802-0.

Dyer, K. R., & Manning, A. J., 1999. Observation of the size, settling velocity and effective density of flocs, and their fractal dimensions. Journal of Sea Research, 41(1–2), 87–95. https://doi.org/10.1016/S1385-1101(98)00036-7.

Dyer, K.J., Cornelisse, J., Dearnaley, M.P., Fennessy, M.J., Jones, S.E., Kappenberg, J., McCave, I.N., Pejrup, M., Puls, W., Van Leussen, W., Wolfstein, K., 1996. A comparison of in situ techniques for estuarine floc settling velocity measurements. J. Sea Res. 36 (1–2), 15–29. doi:10.1016/S1385-1101(96)90766-2.

Dyer, K.R., 1995. Chapter 14 Sediment Transport Processes in Estuaries. Geomorphology and Sedimentology of Estuaries. Developments in Sedimentology, 53, 423-449. https://doi.org/10.1016/S0070-4571(05)80034-2.

Díaz, R.J., Rosenberg, R., 1995. Marine benthic hypoxia: A review of its ecological effects and the behavioural response of benthic macrofauna. Oceanography and Marine Biology , An Annual Review, 33, 245-303.

Eisma, D., 1986. Flocculation and de-flocculation of suspended matter in estuaries. Netherlandas Journal of Sea-Research, 20(2-3):183-199. https://doi.org/10.1016/0077-7579(86)90041-4.

Fachin, S., 1998. Caracterização do perfil de equilíbrio da ante-praia na costa do Rio Grande do Sul. Porto Alegre, UFRGS, Master Thesis, 88p.

Filho, M.L., Roebeling, P., Coelho, C., 2023. Influence of Local Factors on Coastal Erosion: The Case of Vagueira Beach in Portugal. Environments, 10(2):24. https://doi.org/10.3390/environments10020024.

Franzen, M.O., Fernandes, E.H.L, Siegle, E., 2021. Impacts of coastal structures on hydro-morphodynamic patterns and guidelines towards sustainable coastal development: A case studies review. Regional Studies in Marine Science, 44, 101800. https://doi.org/10.1016/j.rsma.2021.101800

Franzen, M.O., Silva, P., Siegle, E., Fernandes, E.H.L, 2023. Influence of long jetties on estuarine and coastal hydrodynamics in a microtidal estuary. Regional Studies in Marine Science, 59, 102809. https://doi.org/10.1016/j.rsma.2022.102809.

Gartner, J. W., 2004. Estimating suspended solids concentrations from backscatter intensity measured by acoustic Doppler current profiler in San Francisco Bay, California. Marine Geology, 211(3–4), 169–187. https://doi.org/10.1016/j.margeo.2004.07.001.

Gill, A.E., Clarke, A.J., 1974. Wind-induced upwelling, coastal currents and sea-level changes. Deep Sea Research and Oceanographic Abstracts, 21(5), 325-345. https://doi.org/10.1016/0011-7471(74)90038-2

Grant, D.W., 1979. Combined Wave and Current Interaction With a Rough Bottom. Journal of Geophysical Research, 84(C4):1797-1808. https://doi.org/10.1029/JC084iC04p01797.

Greenberg, D.A., Dupont, F., Lyard, F.H., Lynch, D.R., Werner, F.E., 2007. Resolution issues in numerical models of oceanic and coastal circulation. Continental Shelf Research, 27(9), 1317-1343. https://doi.org/10.1016/j.csr.2007.01.023.

Guillén, J., Bourrin, F., Palanques, A., Durrieu de Madron, X., Puig, P. Buscail, R., 2006. Sediment dynamics during wet and dry storm events on the Têt inner shelf (SW Gulf of Lions). Marine Geology, 234(1-4):129-142. https://doi.org/10.1016/j.margeo.2006.09.018.

Guimarães, A., Lima, M., Coelho, C., Silva, R., Veloso-Gomes, F., 2016. Groin impacts on updrift morphology: Physical and numerical study. Coastal Engineering, 109, 63-75. https://doi.org/10.1016/j.coastaleng.2015.12.003.

Hannachi, A., 2004. A primer for EOF analysis of climate data. Department of meteorology, University of Reading, UK.

Hartmann, C., Galliari, L., & Moller, O., 1990. Material em suspenção no estuário da Laguna dos Patos (RS) Fase I - Observações preliminares - Abril/1979 a Março/1980. Sociedade & Natureza, 2(4). https://doi.org/10.14393/SN-v2-1990-60757.

Hartmann, C., Schettini, C.A.F., 1991. Aspectos Hidrológicos na Desembocadura da Laguna dos Patos, RS. Revista Brasileira de Geociências, 21(4):371-377.

Heinz, S., 2024. The Law of the Wall and von Kármán Constant: An Ongoing Controversial Debate. Fluids, 9(3), 63. https://doi.org/10.3390/fluids9030063.

Holland, K.T., Vinzon, S.B., Calliari, L.J., 2009. A field study of coastal dynamics on a muddy coast offshore of Cassino beach, Brazil. Continental Shelf Research, 29(3), 503-514. https://doi.org/10.1016/j.csr.2008.09.023.

Isupova, M. V., & Mikhailov, V. N., 2018. Long-Term Variations of Water Runoff and Suspended Sediment Yield in the Parana and Uruguay Rivers. Water Resources, 45(6), 846–860. https://doi.org/10.1134/S0097807818060088.

Kirk, J.T.O., 2010. Light and Photosynthesis in Aquatic Ecosystems. Cambridge University Press. https://doi.org/10.1017/CBO9780511623370

Kudale, M.D., 2010. Impact of port development on the coastline and the need for protection. Indian Journal of Geo-Marine Sciences, 36(4), 597-604.

Lee, G., Friedrichs, C.T., Vincente, C.E., 2002. Examination of diffusion versus advection dominated sediment suspension on the inner shelf under storm and swell conditions,

Duck, North Carolina. Journal of Geophysical Research: Oceans, 107(C7). https://doi.org/10.1029/2001JC000918.

Lentz, S.J., 1995. Sensitivity of the Inner-Shelf Circulation to the Form of the Eddy Viscosity Profile. Journal of Physical Oceanography, 25(1), 19-28. https://doi.org/10.1175/1520-0485(1995)025<0019:SOTISC>2.0.CO;2

Lentz, S.J., Fewings, M.R., 2012. The wind- and wave-driven inner-shelf circulation. Annual Review of Marine Science, 4, 317-343. https://doi.org/10.1146/annurev-marine-120709-142745.

Liu, J.H., Yang, S.L., Zhu, Q., Zhang, J., 2014. Controls on suspended sediment concentration profiles in the shallow and turbid Yangtze Estuary. Continental Shelf Research, 96-108, 90. https://doi.org/10.1016/j.csr.2014.01.021.

Lohrenz, S.E., Carroll, C.L., Weidemann, A.D., Tuel, M., 2003. Variations in phytoplankton pigments, size structure and community composition related to wind forcing and water mass properties on the North Carolina inner shelf. Continental Shelf Research, 27, 1447-1464. https://doi.org/10.1016/S0278-4343(03)00131-6.

Lukawska-Matuszewsda, K., Broclawik, O., Brodecka-Goluck, A., Rzepa, G., Manecki, M., Bolalek, J., 2022. Biogeochemical and mineralogical effects of Fe-P-S dynamics in sediments of continental shelf sea: impact of salinity, oxygen conditions, and catchment area characteristics. Science of Total Environment, 807:151035. https://doi.org/10.1016/j.scitotenv.2021.151035.

Lynch, J.F., Irish, J.D., Sherwood, C.R., Agrawal, Y.C., 1994. Determining suspended sediment particle size information from acoustical and optical backscatter measurements.

Continental Shelf Research, 1139-1165, 14(10-11). https://doi.org/10.1016/0278-4343(94)90032-9.

Malarkey, J., Davies, A., 2012. A simple procedure for calculating the mean and maximum bed stress under wave and current conditions for rough turbulent flow based on Soulsby and Clarke's (2005) method. Computers and Geosciences, 101-107, 43. https://doi.org/10.1016/j.cageo.2012.02.020.

Mann, K.H., Lazier, J.R.N., 2005. Dynamics of Marine Ecosystems. Blackwell Publishing. https://doi.org/10.1002/9781118687901.

Manning, A. J., Baugh, J. V., Spearman, J. R., & Whitehouse, R. J. S., 2010. Flocculation settling characteristics of mud: sand mixtures. Ocean Dynamics, 60(2), 237–253. https://doi.org/10.1007/s10236-009-0251-0.

Marmin, S., Lesueur, P., Dauvin, J.C., Samson, S., Tournier, P., Lavanne, A.G., Dubrulle-Brunaud, C., Thouroude, C., 2016. An experimental study on dredge spoil of estuarine sediments in the bay of seine (France): a morphosedimentary assessment. Continental Shelf Research, 116:89-102. https://doi.org/10.1016/j.csr.2016.01.010.

Marques, W. C., & Möller, O. O., 2008. Variabilidade Temporal em Longo Período da Descarga Fluvial e Níveis de Água da Lagoa dos Patos, Rio Grande do Sul, Brasil. Revista Brasileira de Recursos Hídricos, 13(3), 155–163. https://doi.org/10.21168/rbrh.v13n3.p155-163.

Marques, W.C., Fernandes, E.H.L., Moraes, B.C., Moller Jr., O.O., Malcherek, A. 2010. Dynamics of the Patos Lagoon coastal plume and its contribution to the deposition pattern of the southern Brazilian inner shelf. Journal of Geophysical Research, https://doi.org/10.1029/2010JC006190.

Martins, L. R., Martins, I. R., & Urien, C. M., 2003. Aspectos Sedimentares da Plataforma Continental na Área de Influência do Rio de La Plata. Gravel, 68–80.

Migliorini, A.V., Guimarães, A.T.C., 2008. Tipos de blocos de concreto para estrutura hidráulica de proteção às ondas marinhas e análise visual dos Tetrápodes da Barra de Rio Grande. Universidade Federal de Rio Grande – FURG.

Moller, O. O., Castaing, P., Fernandes, E.H.L., Lazure, P., 2007. Tidal frequency dynamics of a Southern Brazil coastal lagoon: Choking and short period forced oscillations. Estuaries and Coasts, 30, 311-320. https://doi.org/10.1007/BF02700173.

Moller, O. O., Castaing, P., Salomon, J.-C., & Lazure, P., 2001. The Influence of Local and Non-Local Forcing Effects on the Subtidal Circulation of Patos Lagoon. Estuaries, 24(2), 297. https://doi.org/10.2307/1352953.

Moreira, D., Simionato, C. G., Gohin, F., Cayocca, F., & Luz Clara Tejedor, M., 2013. Suspended matter mean distribution and seasonal cycle in the Río de La Plata estuary and the adjacent shelf from ocean color satellite (MODIS) and in-situ observations. Continental Shelf Research, 68, 51–66. https://doi.org/10.1016/j.csr.2013.08.015.

Motta, V., 1963. Análise e previsão das alturas de onda em Tramandaí. Instituto de Pesquisas Hidráulicas, IPH, pp 18.

Motta, V.F., 1969. Relatório-Diagnóstico sobre a melhoria e o aprofundamento do acesso pela barra de Rio Grande. Instituto de Pesquisas Hidráulicas, UFRGS.

Moulton, M., Suanda, S.H., Garwood, J.C., Kumar, N., Fewings, M.R., Pringle, J.M., 2023. Exchange of Plankton, Pollutants, and Particles Across the Nearshore Region.

Annual Review of Marine Science, 15(1), 167-202. https://doi.org/10.1146/annurev-marine-032122-115057.

Moum, J.N., Nash, J.D., Klymak, J.M., 2008. Small-scale processes in the coastal oceano. Oceanography, 21(4):22-33.

Muelbert, J. H., Acha, M., Mianzan, H., Guerrero, R., Reta, R., Braga, E.S., Garcia, V.M.T., Berasategui, A., 2008. Biological, physical and chemical properties at the Subtropical Shelf Front Zone in the SW Atlantic Continental Shelf. Continental Shelf Research, 28, 1662-1673. https://doi.org/10.1016/j.csr.2007.08.011

Myrhaug, D., Hansen, H.E., 1997. Long-term distribution of seabed shear stresses beneath random waves. Coastal Engineering, 31(1997), 327-337. https://doi.org/10.1016/S0378-3839(97)00018-5.

Niedoroda, A.W., Swift, D.J.P., Figueiredo, A.G., Freeland, G.L., 1989. Modeling shelf storm beds: controls of bed thickness and bedding sequence. Shelf Sandstones, Shelf Depositional Sequences and Petroleum Accumulation: a Symposium, pp 15-39. https://doi.org/10.5724/gcs.89.07.0015.

Ostrowski, R., Pruszak, Z., Babakov, A., Chubarenko, B., 2012. Anthropogenic Effects on Coastal Sediment Fluxes in a Nontidal Gulf System. Journal of Waterway, Port, Coastal, and Ocean Engineering, 138(6), 491-500. https://doi.org/10.1061/(ASCE)WW.1943-5460.0000156.

Palanques, A. and Diaz, J.I., 1994. Anthropogenic heavy metal pollution in the sediments of the Barcelona continental shelf (Northwestern Mediterranean). Marine Environmental Research, 38(1):17-31. https://doi.org/10.1016/0141-1136(94)90043-4.

Palma, E., Matano, R., Piola, A., 2008. A numerical study of the Southwestern Atlantic Shelf circulation: Stratified ocean response to local and offshore forcing. Journal of Geophysical Research, 113(c11). https://doi.org/10.1029/2007JC004720

Park, H.-B., & Lee, G., 2016. Evaluation of ADCP backscatter inversion to suspended sediment concentration in estuarine environments. Ocean Science Journal, 51(1), 109–125. https://doi.org/10.1007/s12601-016-0010-3.

Peixoto, R., Iglesias, I., Avilez-Valente, P., 2016. Efeito dos molhes do Douro em diferentes cenários de cheia na cidade do Porto, Portugal. 31-43.

Pereira, P.S., Calliari, L.J., Holman, R., Holland, K.T., Guedes, R.M.C., Amorin, C.K., Cavalcanti, P.G., 2011. Video and field observations of wave attenuation in a muddy surf zone. Marine Geology, 279(1-4):210-221.

Perlin, A., Moum, J., Klymak, J., Levine, M., Boyd, T., Kosro, P., 2005. A modified law-of-the-wall applied to oceanic bottom boundary layers. Journal of Geophysical Research: Oceans, 110(c10):1-9. https://doi.org/10.1029/2004JC002310

Piola, A. R., Romero, S. I., & Zajaczkovski, U., 2008. Space-time variability of the Plata plume inferred from ocean color. Continental Shelf Research, 28(13), 1556–1567. https://doi.org/10.1016/j.csr.2007.02.013.

Pomeroy, L.R., P.J. leB. Williams, F. Azam, and J.E. Hobbie. 2007. The microbial loop. Oceanography 20(2):28–33, https://doi.org/10.5670/oceanog.2007.45.

Qian, Y., Jochens, A.E., Kennicutt II, M.C., Biggs, D.C., 2003. Spatial and temporal variability of phytoplankton biomass and community structure over the continental

margin of the northeast Gulf of Mexico based on pigment analysis. Continental Shelf Research, 23, 1-17. https://doi.org/10.1016/S0278-4343(02)00173-5.

Rabalais, N.N., Díaz, R.J., Levin, L.A., Turner, R.E., Gilbert, D., Zhang, J., 2010. Dynamics and distribution of natural and human-caused hypoxia. Biogeosciences, https://doi.org/7, 585-619. 10.5194/bg-7-585-2010.

Rabalais, N.N., Turner, R.E., 2003. Gulf of Mexico hypoxia, A.K.A. “the dead zone”. Annual Review of Ecology and Systematics, 33(1):235-263. https://doi.org/10.1146/annurev.ecolsys.33.010802.150513.

Reboita, M. S., & Kruche, N., 2018. Normais Climatológicas Provisórias de 1991 a 2010 para Rio Grande, RS. Revista Brasileira de Meteorologia, 33(1), 165–179. https://doi.org/10.1590/0102-7786331010.

Ribeiro, R., Milewski, P., Nachbin, A., 2017. Flow structure beneath rotational water waves with stagnation points. Journal of Fluid Mechanics, 792-814, 812. https://doi.org/10.1017/jfm.2016.820.

Richardson, L.F., 1920. The Supply of Energy from and to Atmospheric Eddies. Proceedings of the Royal Society of London. Series A, Containing Papers of a Mathematical and Physical Character. https://www.jstor.org/stable/93887.

Richman, M.B., 1986. Rotation of principal components. Journal of Climatology, 6(3), 293-33. https://doi.org/10.1002/joc.3370060305.

Rippeth, T.P., 2005. Mixing in seasonally stratified shelf seas: a shifting paradigm. Philosophical Transactions of the Royal Society A. https://doi.org/10.1098/rsta.2005.1662.

Roberts, J., Roberts D.F., 1978. Use of the Butterworth low-pass filter for oceanographic data. Journal of Geophysical Research: Oceans, 83(C11), 5510-5514. https://doi.org/10.1029/JC083iC11p05510.

Rosa-Santos, P., Veloso-Gomes, F., Taveira-Pinto, F., Silva, R., Pais-Barbosa, J., 2009. Evolution of Coastal Works in Portugal and their Interference with Local Morphodynamics. Journal of Coastal Research, 757-761. https://www.jstor.org/stable/25737680.

Rouse, H., 1939. An analysis of sediment transportation in the light of fluid turbulence. Sedimentation Division SCS-TP-25California Institute of Technology, Sedimentation Division, p. 38 SCS-TP-25 https://authors.library.caltech.edu/records/9we10-nep55.

Russell, P., Vennell, R., 2017. High-resolution observations of secondary circulation and tidally synchronized upwelling around a coastal headland. Journal of Geophysical Research: Oceans, 122(2):890-913.

Sahin, C., Safak, I. Scheremet, A., Mehta, A., 2012. Observations on cohesive bed reworking by waves: Atchafalaya shelf, Lousiana. Journal of Geophysical Research, v117(c9). https://doi.org/10.1029/2011JC007821.

Salehi, M., Strom, K., 2012. Measurement of critical shear stress for mud mixtures in the San Jacinto estuary under different wave and current combinations. Continental Shelf Research, 78-92,47. https://doi.org/10.1016/j.csr.2012.07.004.

Santa-Rosa, P.R.A., Schettini, C.A.F., 2024. Daily variability of estuary-shelf exchange at the Lagoa dos Patos´ Mouth. Regional Studies in Marine Science, 77:103633.

Santa-Rosa, P.R.A., Schettini, C.A.F., 2024. Daily variability of estuary-shelf exchange at the Lagoa dos Patos's mouth. Regional Studies in Marine Science, 77(2024)103633.

Santos, J.G. and Garcia, C.A.E., 2023. Vertical structure and variability of currents on the southern Brazilian inner shelf at 32oS. Ocean and Coastal Research, 71:e23027.

Saraiva, J. M. B., Bedran, C., & Carneiro, C., 2003. Monitoring of Storm Surges on Cassino Beach, RS, Brazil. Proceedings of the brazilian symposium on sandy beaches: morphodynamics, ecology, 35(35), 323–331. https://www.jstor.org/stable/40928778.

Schettini, C.A.F., 2022. Dredging, mud, and Dunning-Kruger. Arquivos de Ciências Do Mar, 55(Especial), 485–491. https://doi.org/10.32360/acmar.v55iEspecial.78212.

Schettini, C.A.F., Duarte Pereira, M., Siegle, E., de Miranda, L. B., & Silva, M. P., 2013. Residual fluxes of suspended sediment in a tidally dominated tropical estuary. Continental Shelf Research, 70, 27–35. https://doi.org/10.1016/j.csr.2013.03.006.

Schulkin, M., Marsh, H. W., 1962. Sound Absorption in Sea Water. The Journal of the Acoustical Society of America, 34(6):864-865. https://doi.org/10.1121/1.1918213.

Shi, Z., Zhou, H.J., 2004. Controls on effective settling velocities of mud flocs in the Changjiang Estuary, China. Hydrological Processes, 18(15). https://doi.org/ 10.1002/hyp.1500.

Simons, R., Myrhaug, D., Thais, L., Chapalain, G., Holmedal, L., MacIver, R., 2000. Bed Friction in Combined Wave-Current Flows. Coastal Engineering, 216-226. https://doi.org/10.1061/40549(276)17.

Simpson, J. H., Sharples, J., 2012. Introduction to the Physical and Biological Oceanography of Shelf Seas. Cambridge University Press. https://doi.org/10.1017/CBO9781139034098.

Soares, I. Möller, O., 2001. Low-frequency currents and water mass spatial distribution on the southern Brazilian shelf. Continental Shelf Research, 21(16-17), 1785-1814. https://doi.org/10.1016/S0278-4343(01)00024-3.

Soulsby, R. L., & Clarke, S., 2005. Bed Shear-stresses Under Combined Waves and Currents on Smooth and Rough Beds (TR137). Estuary Processes Research Project. HR Wallingford. https://eprints.hrwallingford.com/558/.

Soulsby, R., 2006. Simplified calculation of wave orbital velocities (TR155). Sand Transport in Oscillatory Flow Project. HR Wallingford, 28p.

Soulsby, R., Hamm, L., Klopman, G., Myrhaug, D., Simons, R., Thomas, G., 1993. Wave-current interaction within and outside the bottom boundary layer. Coastal Engineering, 41-69, 21(1-3). https://doi.org/10.1016/0378-3839(93)90045-A

Stech, J. L., Lorenzzetti, J., 1992. The response of the South Brazil Bight to the passage of wintertime cold fronts. Journal of Geophysical Research: Oceans, 97(c6):9507-9520. https://doi.org/10.1029/92JC00486.

Strauch, J. C., 1997. Aquisição e análise de dados de onda em Rio Grande, XII Simpósio Brasileiro de Recursos Hídricos, 4:385-391.

Swift, D.J.P. 1974. Continental shelf sedimentation. In: Burk, C.A. and Drake, C.L. (Eds) The geology of continental margins. New York, Springer, pp 117-135.

Swift, D.J.P., 1974. Continental shelf sedimentation. The geology of continental margins, pp 117-135. https://doi.org/10.1007/978-3-662-01141-6_10.

Swift, D.J.P., Niederoda, A.W., Vincent, C.E., Hopkins, T.S., 1985. Barrier island evolution, middle Atlantic shelf, U.S.A. Part I: Shoreface dynamics. Marine Geology, 331-361, 63(1-4). https://doi.org/10.1016/0025-3227(85)90089-1.

Swift, D.J.P., Oertel, G.F., Tillman, R.W., Thorne, J.A., 1991. Shelf Sand and Sandstone Bodies: Geometry Facies and Sequence Stratigraphy;. International Association of Sedimentologists, p.544.

Toldo, E., Dillenburg, S., Dorrêa, I., Almeida, L., Weschenfelder, J., & Gruber, N., 2006. Sedimentação de Longo e Curto Período na Lagoa dos Patos, Sul do Brasil. Pesquisas Em Geociências, 33(2), 79. https://doi.org/10.22456/1807-9806.19516.

Traykovski, P., Geyer, W.R., Irish, J.D., Lynch, J.F. 2000. The role of wave-induced density-driven fluid mud flows for cross-shelf transport on the Eel River continental shelf. Continental Shelf Research, 20(16):2113-2140.

Urick, R. J., 1975. Principles of underwater sound. Second Edition, McGraw-Hill.

Urien, C. M., 1972. Rio de la Plata Estuary Environments.Memoir of the Geological Society of America 133, pp. 213–234. https://doi.org/10.1130/MEM133-p213.

Van Rijn, L. C., 2020. Note: Critical bed-shear stress for mud-sand beds - Literature review of critical bed-shear stresses for mud-sand mixtures.

Vaz, A. C., Möller jr, O. O., & de Almeida., T. L., 2006. Análise quantitativa da descarga dos rios afluentes da Lagoa dos Patos. Atlântica, 28(1), 13–23. https://doi.org/https://doi.org/10.5088/atlântica.v28i1.1724.

Vaz, A. C., Möller jr, O. O., & de Almeida., T. L., 2006. Análise quantitativa da descarga dos rios afluentes da Patos Lagoon. Atlântica, 28(1), 13–23. https://doi.org/https://doi.org/10.5088/atlântica.v28i1.1724.

Vinzon, S.B., Winterwerp, J.C., Nogueira, R., de Boer, G.J., 2009. Mud deposit formation on the open coast of the larger Patos Lagoon-Cassino Beach system. Continental Shelf Research, 29(3), 572-588. https://doi.org/10.1016/j.csr.2008.09.021.

Walsh, J.P. and Nittrouer, C.A., 2009. Understanding fine-grained river-sediment dispersal on continental margins. Marine Geology, 263(2009):34-45.

Wang, J., Ma, Q., Yan, S., 2018. A fully nonlinear numerical method for modeling wave–current interactions. Journal of Computational Physics, 173-190, 369. https://doi.org/10.1016/j.jcp.2018.04.057.

Williams, A. and Bax, N.J., 2001. Delineating fish-habitat associations for spatially based management: an example from the south-eastern Australian continental shelf. Marine & Freshwater Research, 52(4):513. https://doi.org/10.1071/MF00017.

Winterwerp, J.C., van Kesteren, W.G.M., 2004. Introduction to the physics of cohesive sediment dynamics in the marine environment. Elsevier, 576p.

Wiseman, W.J., Garvine, R.W., 1995. Plumes and coastal currents near large river mouths. Estuaries, 18:509-517.

Yu, J., Jiang, J., Gong, D., Li, S., Xu, Y., 2011. Determining suspended sediment concentration and settling velocity from PC-ADP measurements in the Beibu Gulf, China. Chinese Journal of Oceanology and Limnology, 29(3):691-701. https://doi.org/10.1007/s00343-011-0164-x.

Yuan, Y., Wei, H., Zhao, L., & Jiang, W., 2008. Observations of sediment resuspension and settling off the mouth of Jiaozhou Bay, Yellow Sea. Continental Shelf Research, 28(19), 2630–2643. https://doi.org/10.1016/j.csr.2008.08.005.

Zavialov, P., Möller, O., & Campos, E., 2002. First direct measurements of currents on the continental shelf of Southern Brazil. Continental Shelf Research, 22(14), 1975–1986. https://doi.org/10.1016/S0278-4343(02)00049-3.

Algoritmos e Dados Utilizados

Os dados utilizados no Capítulo II, bem como os algoritmos implementados para o pré-processamento, o cálculo da tensão de cisalhamento por onda e/ou corrente pelo método de Soulsby e Clark (2005) e o cálculo do perfil teórico de SSC pelo método de Boudreau e Hill (2020), estão disponibilizados através do link: https://github.com/GuiCruz/SoundSSC. Já para o capítulo III estão disponibilizados através do link: https://github.com/GuiCruz/Jetties_Shadow_Zone. A seguir o algoritmo implementado para o cálculo da tensão de cisalhamento e perfil teórico de SSC.

In [1]:
```
import numpy as np
import matplotlib.pyplot as plt
import datetime
import time
import csv
import pickle
import matplotlib.dates as mdates
from scipy import stats
from matplotlib import animation, rc
from IPython.display import HTML
import seawater as sw
```

In [2]:
```
# Define the root directory and file name prefix
roots = "C:/Users/guioc/Documents/Art1/SoundSSC/Output_Data/"
file_names = ['U_fft.pkl', 'V_fft.pkl', 'U_raw.pkl', 'V_raw.pkl', 'Time_fft.pkl',
              'Time_II_fft.pkl', 'REA.pkl', 'SSC_rea.pkl', 'depth.pkl', 'wave_T_fft
              'wave_H_fft.pkl','wave_dir_SC.pkl','wave_dt_stamp.pkl','wave_dt.pkl',
# Dictionary to store the processed velocity data and others
data = {}
# Loop through the file names and load the data using pickle
for file_name in file_names:
    with open(roots+file_name, 'rb') as file:
        data[file_name.replace('.pkl', '')] = pickle.load(file)
```

In [3]:
```
#Loading salinity data from RS4 buoy
sal_SC = np.genfromtxt('C:/Users/guioc/Documents/Art1/SoundSSC/Raw_Data/SIMCOSTA_RS
time_sal = []

sal_SC[0,0] = 2020.0
for i in range(len(sal_SC[:,0])):
    tsh_tempo = datetime.datetime.timestamp(datetime.datetime(int(sal_SC[i,0]),int(
    time_sal.append(tsh_tempo)
```

In [4]:
```
z = np.array([0.90,1.40,1.90,2.40,2.90,3.40,3.90,4.40,4.90,5.40,5.90,6.40,6.90,7.40
M = np.sqrt(data['U_raw']**2+data['V_raw']**2)
UV_dir = np.arctan2(data['U_raw']/M, data['V_raw']/M)
UV_dir_degrees = np.rad2deg(UV_dir)
#inteporlando os dados de Vel., SSC_rea, e profundidade para o tempo do simcosta.
M_intp = np.stack([np.interp(data['wave_dt_stamp'], data['Time_II_fft'], M[:, j]) f
M_dir_intp = np.stack([np.interp(data['wave_dt_stamp'], data['Time_II_fft'], UV_dir
ssc_intp = np.stack([np.interp(data['wave_dt_stamp'], data['Time_II_fft'], data['SS
niveis_intp = np.interp(data['wave_dt_stamp'], data['Time_II_fft'], data['depth'])
temp_intp = np.interp(data['wave_dt_stamp'], data['Time_II_fft'], data['temp_ADCP']
sal_intp = np.interp(data['wave_dt_stamp'],time_sal,sal_SC[:,6])
pressure_intp = np.interp(data['wave_dt_stamp'], data['Time_II_fft'],data['pressure

gv = 9.80665
```

```
C:\Users\guioc\AppData\Local\Temp\ipykernel_97992\2414745597.py:3: RuntimeWarning: i
nvalid value encountered in divide
  UV_dir = np.arctan2(data['U_raw']/M, data['V_raw']/M)
```

In [5]:
```
def orbital_velocity(wave_T_fft, wave_H_fft, niveis_intp):
    lengths = len(wave_T_fft)
```

```
    wv_array = []
    for i in range(lengths):
        # Calcular a vel. orbital de onda
        TN_T = np.sqrt(niveis_intp[i] / (gv * (wave_T_fft[i] ** 2)))  # (A1)
        if TN_T < 0.2:
            #(A2)
            wv = (0.5*data['wave_H_fft'][i]*np.sqrt(gv/niveis_intp[i])*(1-(1/3*(( 2
        elif TN_T >= 0.2:  #
            #(A3)
            wv = (wave_H_fft[i] / 2) * np.sqrt(gv / niveis_intp[i]) * np.exp((((4.4
        wv_array.append(wv)
    return wv_array
```

```
dens = sw.dens(sal_intp,temp_intp,pressure_intp)#1025 #water density (kg/m3)
sed_size = 0

def shear_wc(velocity, vel_dir, density, nivel, wv, wave_dir, wave_t, sed_size):
    t_m_array = []
    t_mc_array = []
    t_mw_array = []
    t_max_array = []
    ucr = []
    lengths = len(nivel)
    for i in range(lengths):

        visc_k = 0.000001 #kinematic viscosity (m2/s)1e-06
        vel_m =  velocity[i] #Depth-averaged velocity  (m/s)
        dir_WV = np.abs((wave_dir[i]) - vel_dir[i])#Angular difference between wave
        dir_WV_rad = np.deg2rad(dir_WV) #converting to radians
        #Calculating basic parameters
        if sed_size>0:
            ks = sed_size/12 #rough bottom - (A4)
        re_v = (vel_m*nivel[i])/visc_k #Reynolds number for current (A7)
        A_wv = wv[i]*wave_t[i]/6.283185307179586 #wave semi-orbital excursion (A8)
        re_w = (wv[i]*A_wv)/visc_k #Reynolds number for wave (A9)
        cds = 0.0001615*(np.exp(6*(re_v**-0.08))) #drag coefficient for current for
        fws = 0.0521*(re_w**-0.187)#wave friction factor for smooth turbulent flow
        u_xe = ((cds**2)*(vel_m**4)+(fws/2)**2*(wv[i]**4))**0.25 # (A6)
        if sed_size==0:
            ks = visc_k/(9*u_xe)#smooth bottom - #(A5)
        cdr = (0.4/(np.log(nivel[i]/ks)-1))**2 #drag coefficient for current for ro
        fwr = 1.39*(A_wv/ks)**-0.52 #wave frictionn factor for rought turbulent flo
        #Parte 1 - Shear stress for Current only
        if re_v <= 2000: #laminar flow
            t_c = (3*density[i]*visc_k*vel_m)/nivel[i]# (A14)
            t_mc_array.append(t_c)
        elif re_v > 2000:  #turbulent flow
            t_cs = density[i]*cds*(vel_m**2)# (A15)
            t_cr = density[i]*cdr*(vel_m**2)# (A16)
            if t_cs > t_cr:
                t_c = t_cs
            if t_cr > t_cs:
                t_c = t_cr
            t_mc_array.append(t_c)
        #Parte 2 - Shear stress for Wave only
        if re_w <= 150000: #Laminar flow
```

```
            t_w = density[i]*(re_w**-0.5)*(wv[i]**2)# (A18)
            t_mw_array.append(t_w)
        elif re_w > 150000: #rough flow
            t_ws = (density[i]*fws*(wv[i]**2))/2# (A19)
            t_wr = (density[i]*fwr*(wv[i]**2))/2# (A20)
            if t_ws < t_wr:
                t_w = t_wr
            elif t_wr < t_ws:
                t_w = t_ws
            t_mw_array.append(t_w)
        #Parte 3 - Shear stress for combined wave and current flow
        if vel_m>0 and wv[i]>0:
            Cre_v = 2000+(592000*re_w)**0.35
            Cre_w = 150000
            if re_v > Cre_v or re_w>Cre_w:
                #rough turbulent wave-plus-current shear-stress
                ar = 0.24
                T_I = [0,12]# (A22)
                T_I[0] = ar*((fwr/2)**0.5)*(A_wv/ks)# (A22)
                T_I = np.max(T_I)# (A22)
                T_II = nivel[i]/(T_I*ks)# (A23)
                T_III = ((cdr**2)+((fwr/2)**2)*((wv[i]/vel_m)**4))**0.25# (A24)
                A_I = (T_III*(np.log(T_II)-1))/(2*np.log(T_I))# (A25)
                A_II = 0.4*T_III/np.log(T_I)# (A26)
                Cdm = ((np.sqrt(A_I**2+A_II) - A_I)**2)# (A27)
                #(A28)
                Cdm_max = np.sqrt((Cdm+(T_III*(wv[i]/vel_m)*np.sqrt(fwr/2)*np.cos(d
                t_mc = density[i]*Cdm*(vel_m**2)# (A32)
                t_maxc = density[i]*Cdm_max*(vel_m**2)# (A33)
                #smooth turbulent wave-plus-current shear-stress
                T_I = 9*ar*re_w*np.sqrt(fws/2)*(((cds**2)*(vel_m/wv[i])**4+(fws/2)*
                T_II = (re_v/re_w)*(wv[i]/vel_m)*(1/ar)*np.sqrt(2/fws)# (A30)
                T_III = ((cds**2)+(fws/2)**2*(wv[i]/vel_m)**4)**0.25# (A31)
                A_I = (T_III*(np.log(T_II)-1))/(2*np.log(T_I))# (A25)
                A_II = 0.4*T_III/np.log(T_I)# (A26)
                Cdm = ((np.sqrt(A_I**2+A_II) - A_I)**2)# (A27)
                #(A28)
                Cdm_max = np.sqrt((Cdm+(T_III*(wv[i]/vel_m)*np.sqrt(fws/2)*np.cos(d
                t_mw = density[i]*Cdm*(vel_m**2)# (A32)
                t_maxw = density[i]*Cdm_max*(vel_m**2)# (A33)
                if t_maxc > t_maxw:
                    t_m = t_mc
                    t_max = t_maxc
                elif t_maxc < t_maxw:
                    t_m = t_mw
                    t_max = t_maxw
                ucr.append(np.sqrt(t_m/density[i]))# (A34)
                t_m_array.append(t_m)
                t_max_array.append(t_max)
            elif re_v <Cre_v and re_w<Cre_w:
                print('Laminar flow - not implemented')
        else:
            print("erro")
    return t_mc_array, t_mw_array, t_m_array, t_max_array, ucr
```

In [7]:
```
#TESTING THE ALGORITHM ACCORDING TO SOULSBY PAPER
```

Inputs: $h = 5m$, $\rho = 1000kgm^{-3}$, $\nu = 1.0 \times 10^{-6}m^2s^{-1}$, $d_{50} = 0.001m$, $U_w = 0.7ms^{-1}$, $T = 8s$, $\overline{U} = 0.5ms^{-1}$, $\phi_d = 90^0$

Outputs: $(\tau_c, \tau_w, \tau_m, \tau_{max}, \tau_{rms}) = (0.3998, 2.7353, 0.7236, 2.8434, 2.0651)\ Nm^{-2}$

In [8]:
```
velocity2 = np.array([0.5])
vel_dir2 = np.array([0])
density2 = np.array([1000])
nivel2 = np.array([5])
wv2 = np.array([0.7])
wave_dir2 = np.array([90])
wave_t2 = np.array([8])
sed_size2 = 0.001


print(np.round(shear_wc(velocity2, vel_dir2, density2, nivel2, wv2, wave_dir2, wave
```

```
[[0.3998]
 [2.7353]
 [0.7236]
 [2.8434]
 [0.0269]]
```

In [9]:
```
#Applying the functions with the data gathered

M_vel = np.nanmean(M_intp[:, :], 1)
M_dir = np.nanmean(M_dir_intp[:,:], 1)

wv_s = orbital_velocity(data['wave_T_fft'][:], data['wave_H_fft'][:], niveis_intp)
tc, tw, tmw, tmax, ucr = shear_wc(M_vel, M_dir, dens, niveis_intp, wv_s, data['wave
```

In [10]:
```
visc = 1e-3
C_test = np.zeros((len(data['wave_dt']), len(z)))
C_eo_test = np.zeros((len(data['wave_dt']), len(z)))
C_R = np.zeros(len(data['wave_dt']))+1
C_sed = np.zeros(len(data['wave_dt']))
C_dens = np.zeros(len(data['wave_dt']))
C_con = np.zeros(len(data['wave_dt']))
C = np.zeros((len(data['wave_dt']), len(z)))
C_eo = np.zeros((len(data['wave_dt']), len(z)))
C_ws = np.zeros(len(data['wave_dt']))

sed_range = np.arange(0.02,0.065, 0.005)
#Density values from this articles: https://link.springer.com/article/10.1007/s1023
dens_range = np.array([2600,2500,2400,2300,2200,2100,2000])
aa = np.arange(0.01,1.01, 0.01)
bb = np.arange(0.2,10.1, 0.1)
```

```
cc = np.arange(11,61, 1)
conc_range = np.concatenate((aa,bb,cc))
del aa,bb,cc
# Note that to calculate z_r, the sediment size used to estimate Ks is not the same
# The D50 value was defined based on the article: 10.5088/atl.2011.33.2.123

value = 0
k = 0.41
B = 1
for i in range(len(data['wave_dt'])):
        for cc in range(len(conc_range)):
            for ss in range(len(sed_range)):
                for dd in range(len(dens_range)):
                    sed_size = sed_range[ss]/1000  #median grain diamenter (m)
                    #Particle fall velocity
                    ws = 2/9*(dens_range[dd]-dens[i])/visc*gv*sed_size**2# (A38)
                    c_ref = conc_range[cc]
                    RO = B*ws/(k*ucr[i])# (A39)
                    z_r = (26*(2*0.150/1000))/k# (A37) - 0.150 is the sediment size
                    C_eo_test[i,:] = k*ucr[i]*z_r# (A36)
                    C_test[i,:] = c_ref*(1 + (k*ucr[i]*z/C_eo_test[i,:]))**-RO# (A4
                    cod1 =(np.sum((C_test[i,:] - ssc_intp[i,:]/1000)**2)/28)**0.5 #
                    if cod1 < C_R[i]:
                        C_R[i] = cod1
                        C_eo[i,:] = C_eo_test[i,:]
                        C_sed[i] = sed_range[ss]
                        C_con[i] = conc_range[cc]
                        C_ws[i] = ws
                        C[i,:] = C_test[i,:]
                        C_dens[i] = dens_range[dd]-dens[i]
        print('time: '+str(i)+'/'+str(len(data['wave_dt']))+' RMSE: '+str(round(C_R
```

```
time: 1764/1765 RMSE: 8.89 eo: 0.41 sed_size: 0.02 Co: 1.400
```

```
#roots = "C:/Users/guioc/Documents/Art1/SoundSSC/Output_Data/"

with open(roots+'t_mc_fft.pkl', 'wb') as file: # Shear stress for current
    pickle.dump(tc, file)

with open(roots+'t_m_fft.pkl', 'wb') as file: # Mean shear stress for current+wave
    pickle.dump(tmw, file)

with open(roots+'t_max_fft.pkl', 'wb') as file: # Maximun shear stress for current+
    pickle.dump(tmax, file)

with open(roots+'t_mw_array.pkl', 'wb') as file: # Shear stress for wave
    pickle.dump(tw, file)

with open(roots+'ucr_fft.pkl', 'wb') as file: # Shear velocity of flow
    pickle.dump(ucr, file)

with open(roots+'C_R.pkl', 'wb') as file: # RMSE for SSC_rouse X SSC_abs
    pickle.dump(C_R, file)

with open(roots+'C_eo.pkl', 'wb') as file: # Residual Turbulent diffusion coefficie
    pickle.dump(C_eo, file)
```

```
with open(roots+'C_sed.pkl', 'wb') as file: # Sediment size obtained from rouse pro
    pickle.dump(C_sed, file)

with open(roots+'C_con.pkl', 'wb') as file: # Sediment concentration at z = 0
    pickle.dump(C_con, file)

with open(roots+'C_ws.pkl', 'wb') as file: # Particle fall velocity
    pickle.dump(C_ws, file)

with open(roots+'C_dens.pkl', 'wb') as file: # Sediment density obtained from rouse
    pickle.dump(C_dens, file)

with open(roots+'ssc_rouse.pkl', 'wb') as file: # Sediment concentration by depth
    pickle.dump(C, file)

with open(roots+'Sal_SC.pkl', 'wb') as file: # Salinity from RS4 Buoy
    pickle.dump(sal_intp, file)
```

Parte 1. Estimar a tensão de cisalhamento médio, para corrente, onda e onda+corrente.

Calculando a vel. Orbital de onda:

$$\frac{\mathrm{T}_n}{\mathrm{T}} = \left(\frac{h}{\mathrm{gT}^2}\right)^{0.5} \tag{A1}$$

Método de Nielsen's:

$$\mathrm{U}_w = 0.5\mathrm{H}(\mathrm{g}/h)^{0.5}\left[1 - \frac{1}{3}\frac{2\pi\mathrm{T}_n}{\mathrm{T}}^2\right] se\, \frac{\mathrm{T}_n}{\mathrm{T}} < 0.2 \tag{A2}$$

Soulsby aproximação exponencial:

$$\mathrm{U}_w = 0.5\mathrm{H}(\mathrm{g}/h)^{0.5} exp\left\{-\left[\frac{4.41}{\mathrm{T}}\left(\frac{h}{\mathrm{g}}\right)^{0.5}\right]^{2.45}\right\} se\, \frac{\mathrm{T}_n}{\mathrm{T}} \geq 0.2 \tag{A3}$$

Calculando os parâmetros básicos:

$z_0 = d_{50}/12$ (fundo rugoso) (A4)

$z_0 = \nu/(9\mathrm{u}_{*e})$ (fundo liso) (A5)

$$\mathrm{u}_{*e} = \left(C_{Ds}^2 \overline{\mathrm{U}}^4 + \left(\frac{f_{ws}}{2}\right)^2 \mathrm{U}_w{}^4\right)^{0.25} \tag{A6}$$

$$Re_c = \frac{\overline{\mathrm{U}}h}{\nu} \tag{A7}$$

$$A = \frac{U_w \mathrm{T}}{2\pi} \tag{A8}$$

$$Re_w = \frac{\mathrm{U}_w A}{\nu} \tag{A9}$$

$$C_{Ds} = 0.0001615\exp\left[6(Re_c)^{-0.08}\right] \quad \text{(A10)}$$

$$f_{ws} = 0.0521 {Re_w}^{-0.187} \quad \text{(A11)}$$

$$C_{Dr} = \left[\frac{0.40}{\ln(h/z_0)-1}\right]^2 \quad \text{(A12)}$$

$$f_{wr} = 1.39\left(\frac{A}{z_0}\right)^{-0.52} \quad \text{(A13)}$$

Para corrente somente:

Se $Re_c < 2000$

$$\tau_{mc} = \tau_{max} = \frac{3\rho\nu\overline{\mathrm{U}}}{h} \quad \text{(A14)}$$

Se $Re_c > 2000$

$$\tau_{cr} = \rho C_{Dr}\overline{\mathrm{U}}^2 \quad \text{(A15)}$$

$$\tau_{cs} = \rho C_{Ds}\overline{\mathrm{U}}^2 \quad \text{(A16)}$$

$$\tau_{mc} = \tau_{cmax} = max(\tau_{cr}, \tau_{cs}) \quad \text{(A17)}$$

Para onda somente:

Se $Re_w < 1.5x10^5$

$$\tau_{mw} = 0, \tau_{max} = \rho Re_w^{-0.5} {\mathrm{U}_w}^2 \quad \text{(A18)}$$

Se $Re_w > 1.5x10^5$

$$\tau_{wr} = \frac{1}{2}\rho f_{wr} {\mathrm{U}_w}^2 \quad \text{(A19)}$$

$$\tau_{ws} = \frac{1}{2}\rho f_{ws} {\mathrm{U}_w}^2 \quad \text{(A20)}$$

$$\tau_{mw} = 0, \tau_{max} = max(\tau_{wr}, \tau_{ws}) \quad \text{(A21)}$$

Para onda+corrente:

$Re_{c,cr} = 2000 + (5.92\ x\ 10^5\ x\ Re_w)^{0.35}$

$Re_{w,cr} = 1.5x10^5$

Se $Re_c < Re_{c,cr}$ **e** $Re_w < Re_{w,cr}$ **então:**

Não implementado. Os dados são maiores que o valor crítico para toda a série

Se $Re_c > Re_{c,cr}$ **ou** $Re_w > Re_{w,cr}$ **então:**

Tensão de cisalhamento onda+corrente turbulento e rugoso:

$a_r = 0.24$

$$\mathrm{T}_1 = \frac{\delta}{z_0} = max\left\{a_r\left(\frac{f_{wr}}{2}\right)^{0.5}\left(\frac{A}{z_0}\right), 12\right\} \quad \text{(A22)}$$

$$\mathrm{T}_2 = \frac{h}{\delta} = \frac{h}{\mathrm{T}_1 z_0} \quad \text{(A23)}$$

$$\mathrm{T}_3 = \frac{u_{*e}}{\overline{\mathrm{U}}} = \left[C_{Dr}^2 + \left(\frac{f_{wr}}{2}\right)^2\left(\frac{\mathrm{U}_w}{\overline{\mathrm{U}}}\right)^4\right]^{0.25} \quad \text{(A24)}$$

$$A_1 = \frac{\mathrm{T_3[ln(T_2)-1]}}{2\ln(\mathrm{T_1})} \quad \text{(A25)}$$

$$A_2 = \frac{0.4\mathrm{T_3}}{\ln(\mathrm{T_1})} \quad \text{(A26)}$$

$$C_{Dm} = \left[(A_1{}^2 + A_2)^{0.5} - A_1\right]^2 \quad \text{(A27)}$$

$$C_{Dmax} = \left[\left(C_{Dm} + \mathrm{T_3}.\frac{\mathrm{U_w}}{\overline{\mathrm{U}}}\left(\frac{f_{wr}}{2}\right)^{0.5}.|\cos\phi|\right)^2 + \left(\mathrm{T_3}.\frac{\mathrm{U_w}}{\overline{\mathrm{U}}}\left(\frac{f_{wr}}{2}\right)^{0.5}|\sin\phi|\right)^2\right]^{0.5} \quad \text{(A28)}$$

Tensão de cisalhamento onda+corrente turbulento e suave:

$$a_s = 0.24$$

$$\mathrm{T_1} = 9a_s Re_w \left(\frac{f_{ws}}{2}\right)^{0.5}\left[C_{Ds}^2\left(\frac{\overline{\mathrm{U}}}{\mathrm{U_w}}\right)^4 + \left(\frac{f_{ws}}{2}\right)^2\right]^{0.25} \quad \text{(A29)}$$

$$\mathrm{T_2} = \left(\frac{Re_c}{Re_w}\right)\left(\frac{\mathrm{U_w}}{\overline{\mathrm{U}}}\right)\frac{1}{a_s}\left(\frac{2}{f_{ws}}\right)^{0.5} \quad \text{(A30)}$$

$$\mathrm{T_3} = \left[C_{Ds}^2 + \left(\frac{f_{ws}}{2}\right)^2\left(\frac{\mathrm{U_w}}{\overline{\mathrm{U}}}\right)^4\right]^{0.25} \quad \text{(A31)}$$

CalculeA_1e A_2com as equações A25,A26. C_{Dm}com a equação A27, C_{Dmax}com a equação A28 substituindo f_{wr}por f_{ws}.

$$\tau_m = \rho C_{Dm}\overline{\mathrm{U}}^2 \quad \text{(A32)}$$

$$\tau_{max} = \rho C_{Dmax}\overline{\mathrm{U}}^2 \quad \text{(A33)}$$

Se $\tau_{max} > \tau_m$ então o fluxo é turbulento rugoso

$\tau_m = \tau_{m,r}$, $\tau_{max} = \tau_{max,r}$

Se $\tau_{max} \leq \tau_m$ então o fluxo é turbulento suave

$\tau_m = \tau_{m,s}$, $\tau_{max} = \tau_{max,s}$

Parte 2. Calcular o Perfil de Rouse

$$\mathrm{u_*} = (\tau_m/\rho)^{0.5} \quad \text{(A34)}$$

$$\varepsilon_s = \kappa \mathrm{u_*}(z + z_r) \quad \text{(A35)}$$

$$\varepsilon_s = \kappa \mathrm{u_*} z + \varepsilon_0$$

$$\varepsilon_0 = \varepsilon_s - \kappa \mathrm{u_*} z$$

$$\varepsilon_0 = \kappa \mathrm{u_*} z_r \quad \text{(A36)}$$

$$z_r = \frac{26 d_s}{\kappa} \quad \text{(A37)}$$

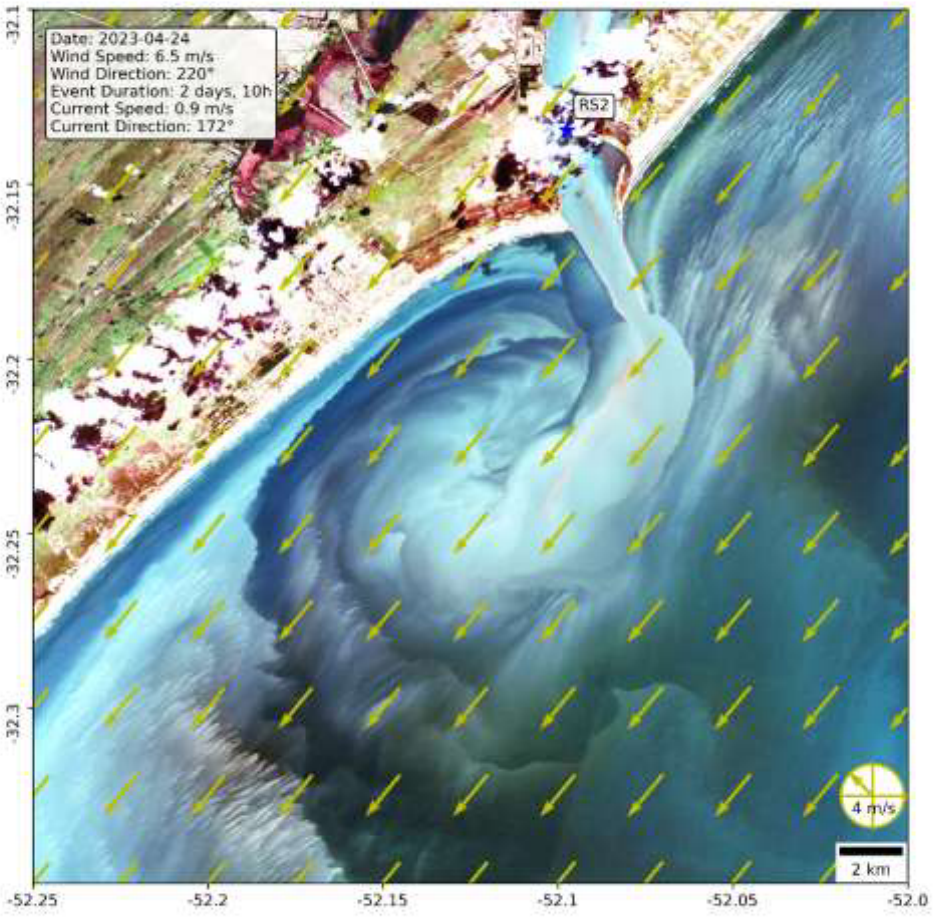
$$W_s = \frac{2}{9}\frac{(\rho_{sed}-\rho_{water})}{\nu}\mathrm{g}d_{50}{}^2 \quad \text{(A38)}$$

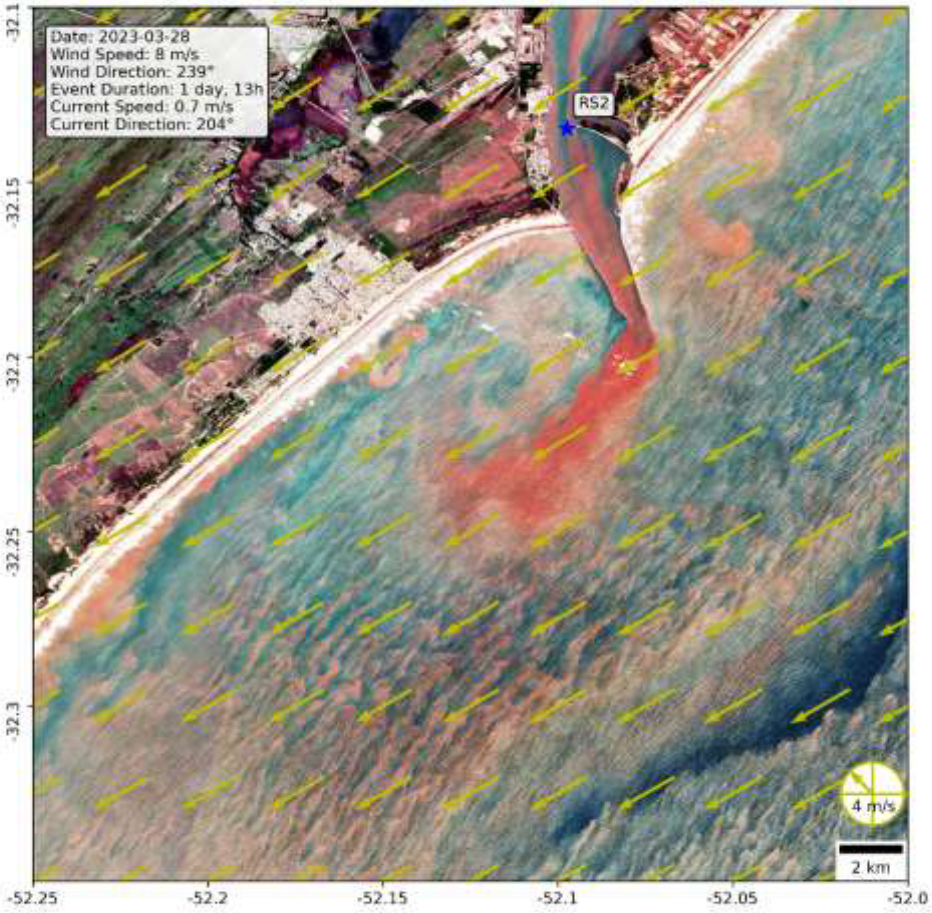
$$Ro = \frac{\beta W_s}{\kappa \mathrm{u_*}} \quad \text{(A39)}$$

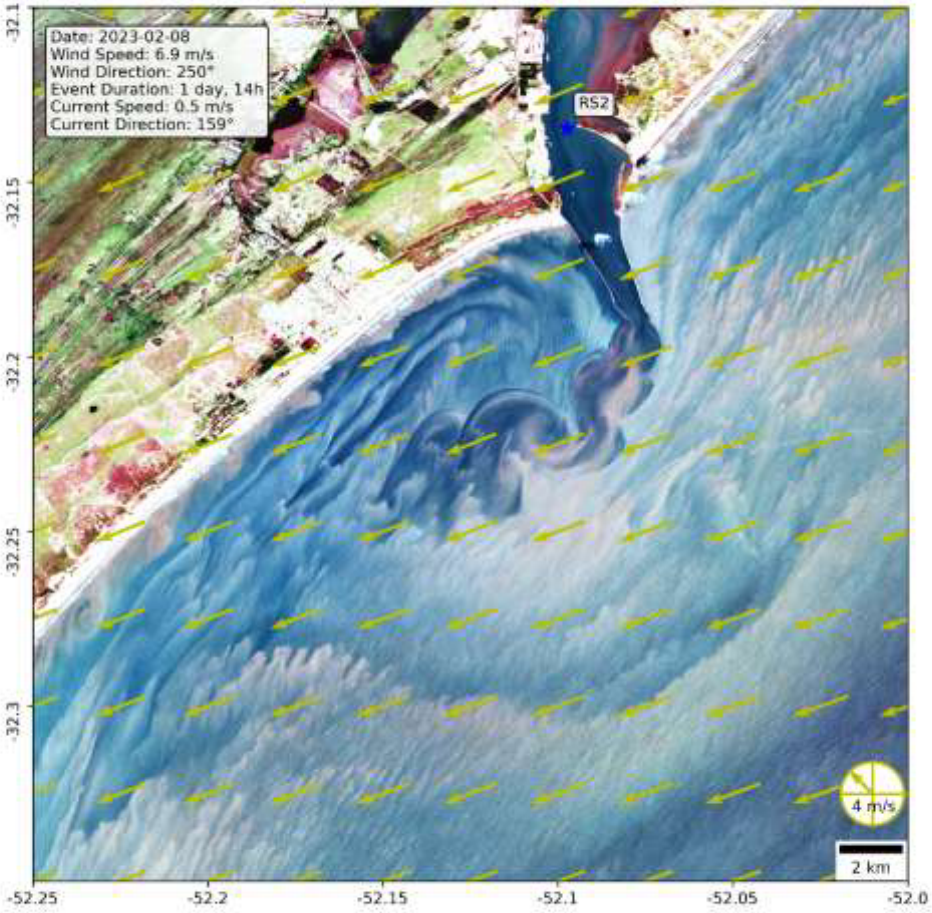
$$C(z) = C_{ref}\left(1 + \frac{\kappa \mathrm{u_*} z}{\varepsilon_0}\right)^{-Ro} \quad \text{(A40)}$$

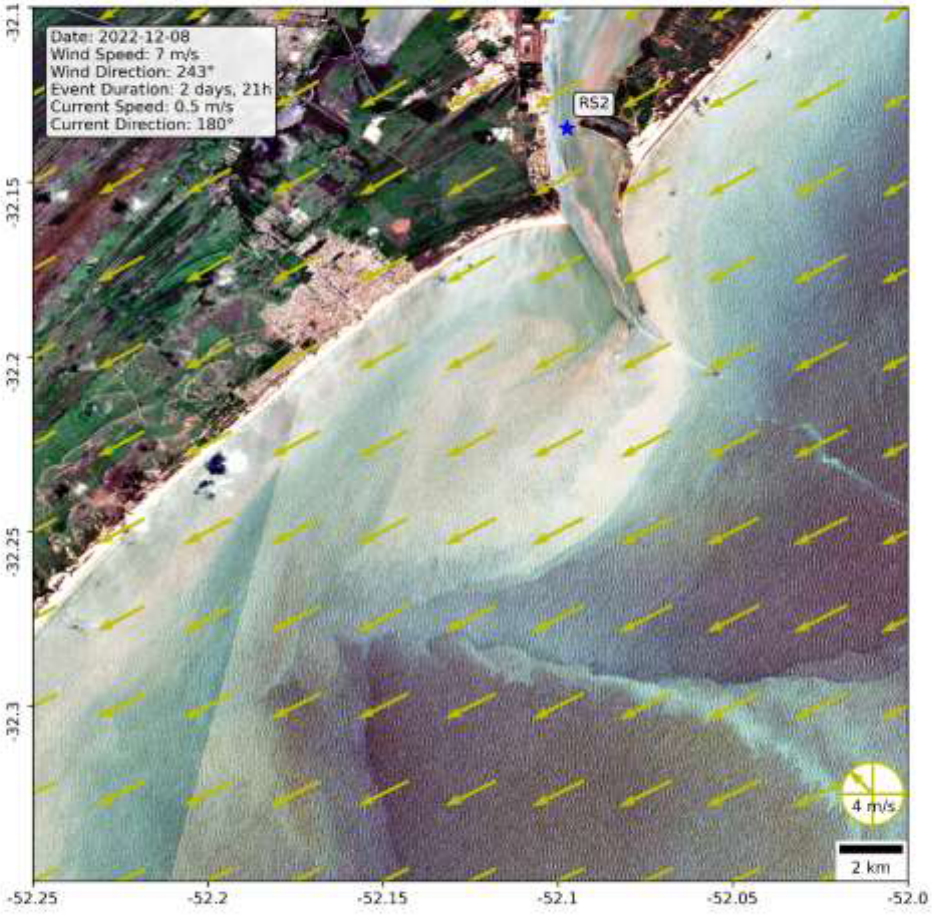
Apêndice A

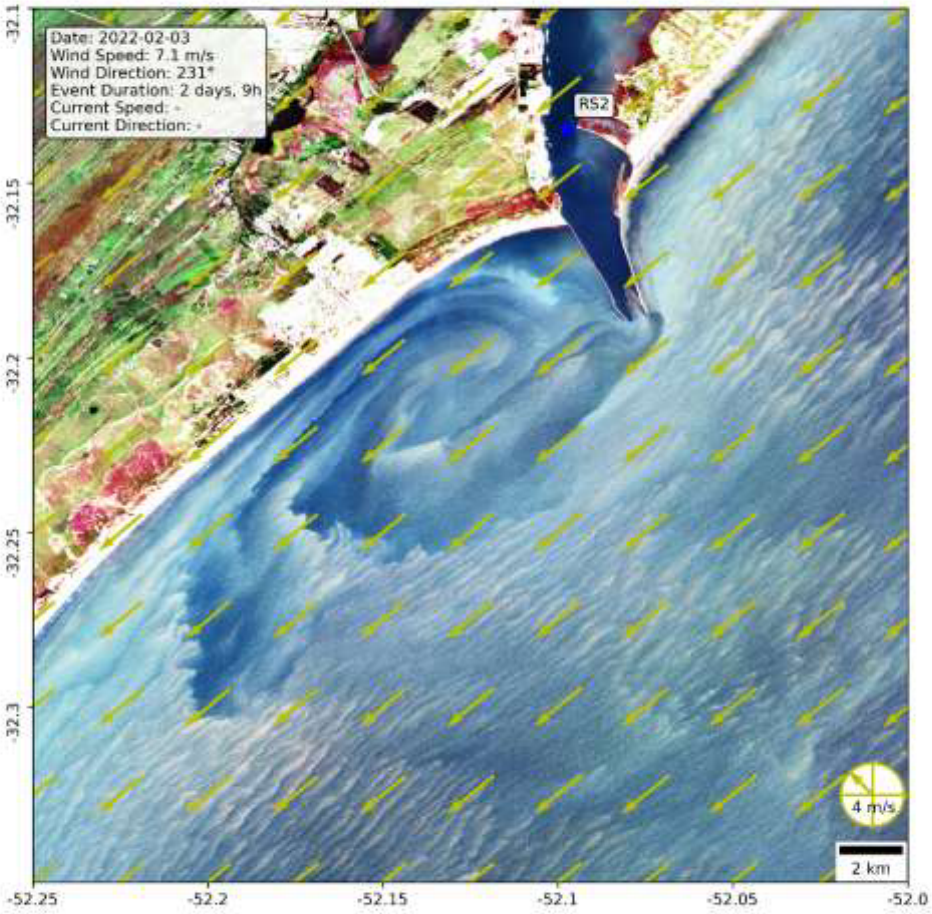
Imagens de satélite do sentinel 2 composta com os dados de vento do modelo numérico ERA5 referentes ao Capítulo IV.

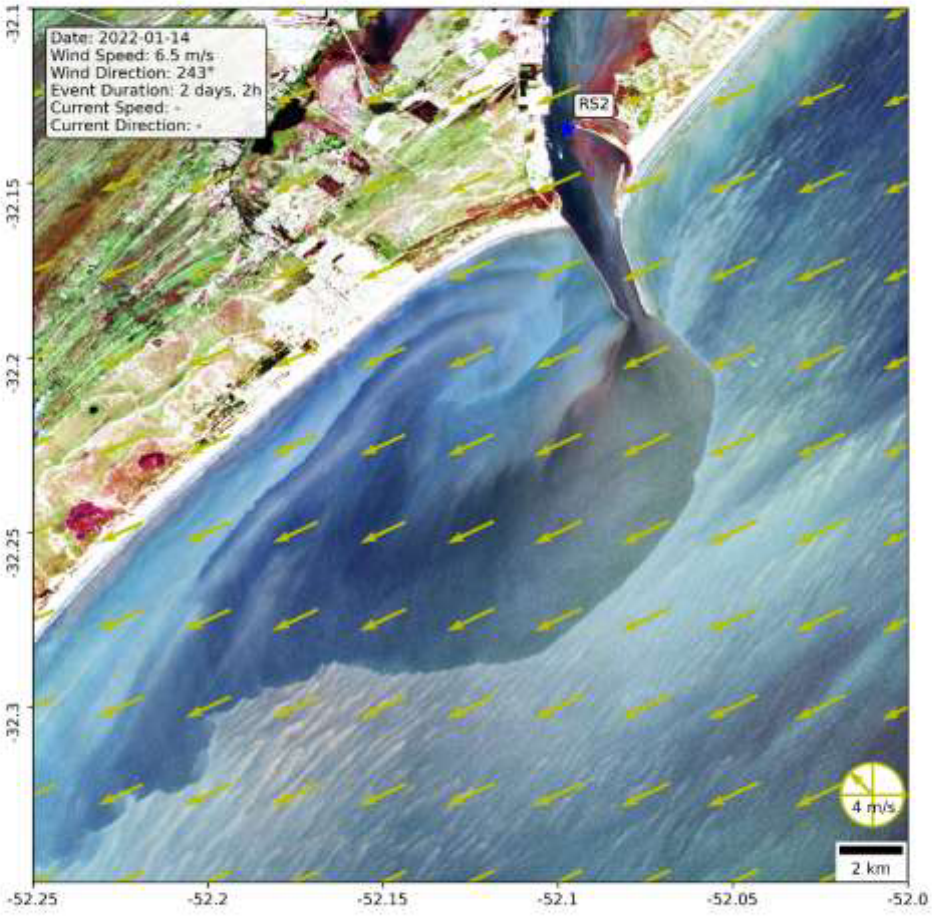


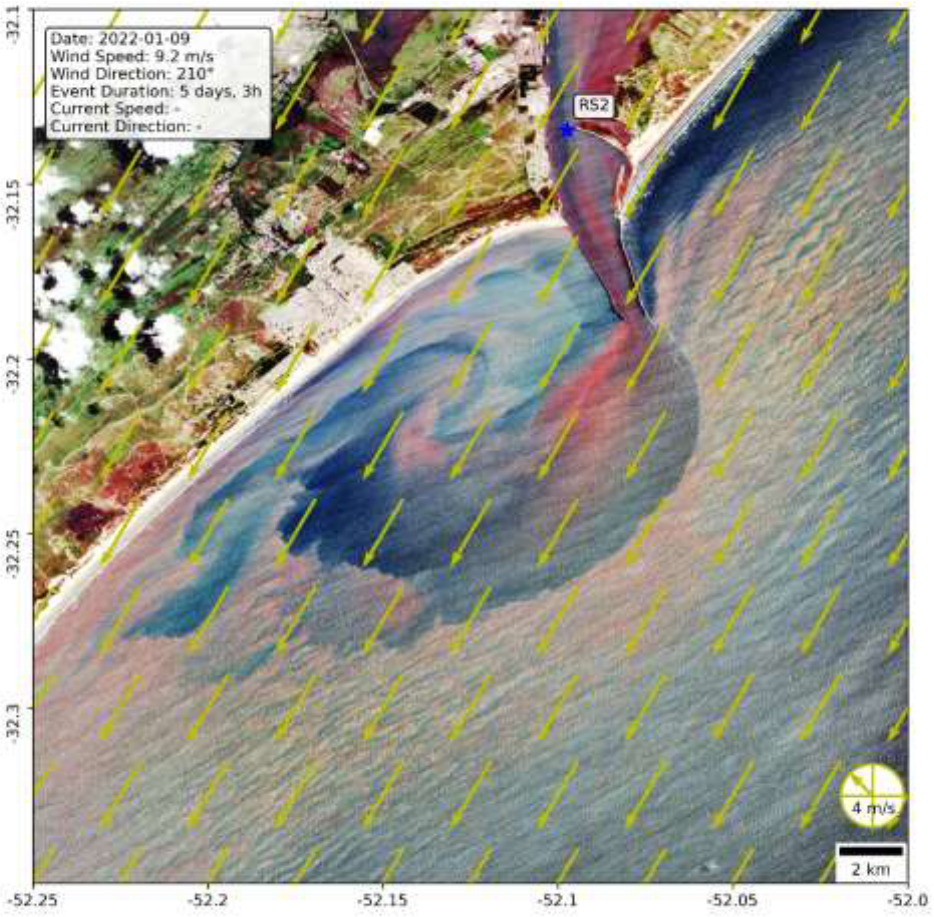

Date: 2023-03-28
Wind Speed: 8 m/s
Wind Direction: 239°
Event Duration: 1 day, 13h
Current Speed: 0.7 m/s
Current Direction: 204°
RS2
4 m/s
2 km
-32.1
-32.15
-32.2
-32.25
-32.3
-52.25
-52.2
-52.15
-52.1
-52.05
-52.0

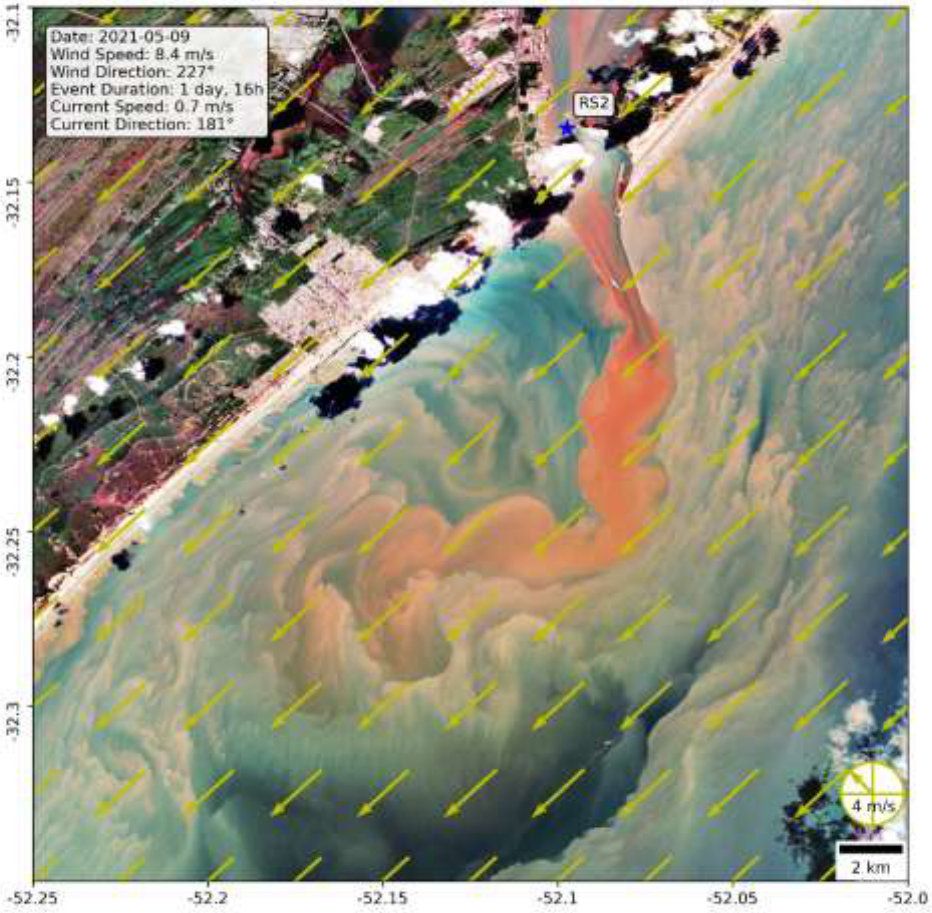

Date: 2023-02-08
Wind Speed: 6.9 m/s
Wind Direction: 250°
Event Duration: 1 day, 14h
Current Speed: 0.5 m/s
Current Direction: 159°
RS2
4 m/s
2 km
-32.1
-32.15
-32.2
-32.25
-32.3
-52.25
-52.2
-52.15
-52.1
-52.05
-52.0

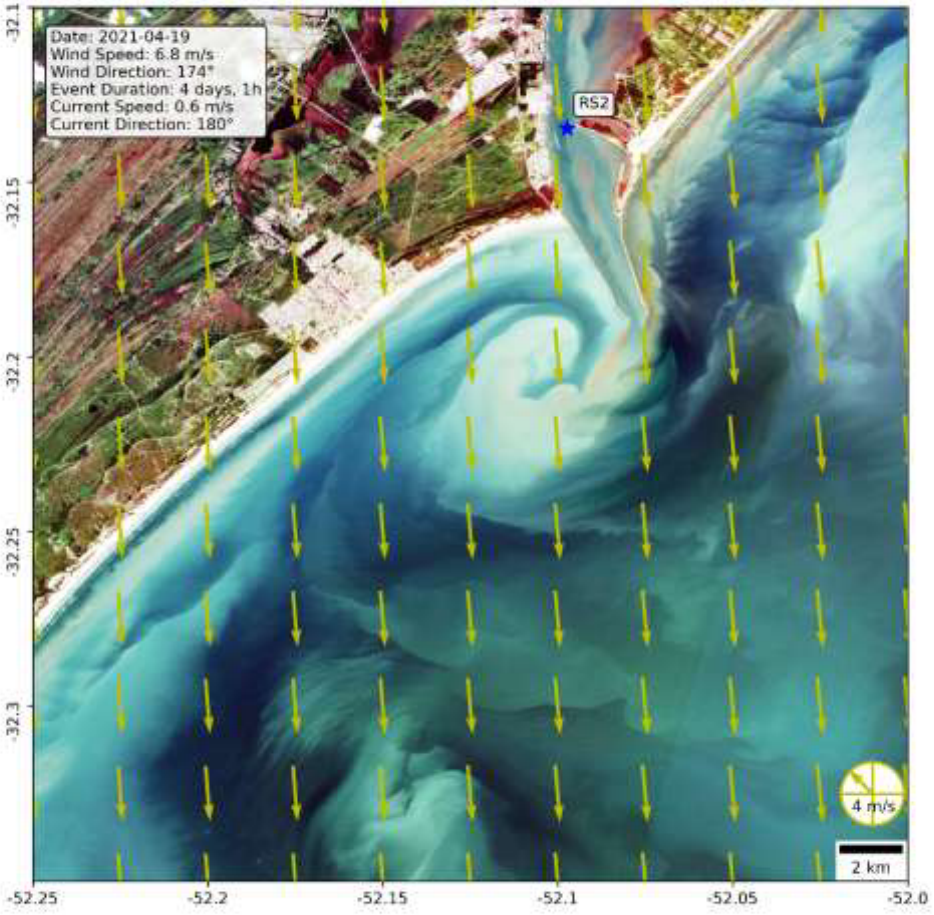

Date: 2022-12-08
Wind Speed: 7 m/s
Wind Direction: 243°
Event Duration: 2 days, 21h
Current Speed: 0.5 m/s
Current Direction: 180°
RS2
4 m/s
2 km
-32.1
-32.15
-32.2
-32.25
-32.3
-52.25
-52.2
-52.15
-52.1
-52.05
-52.0

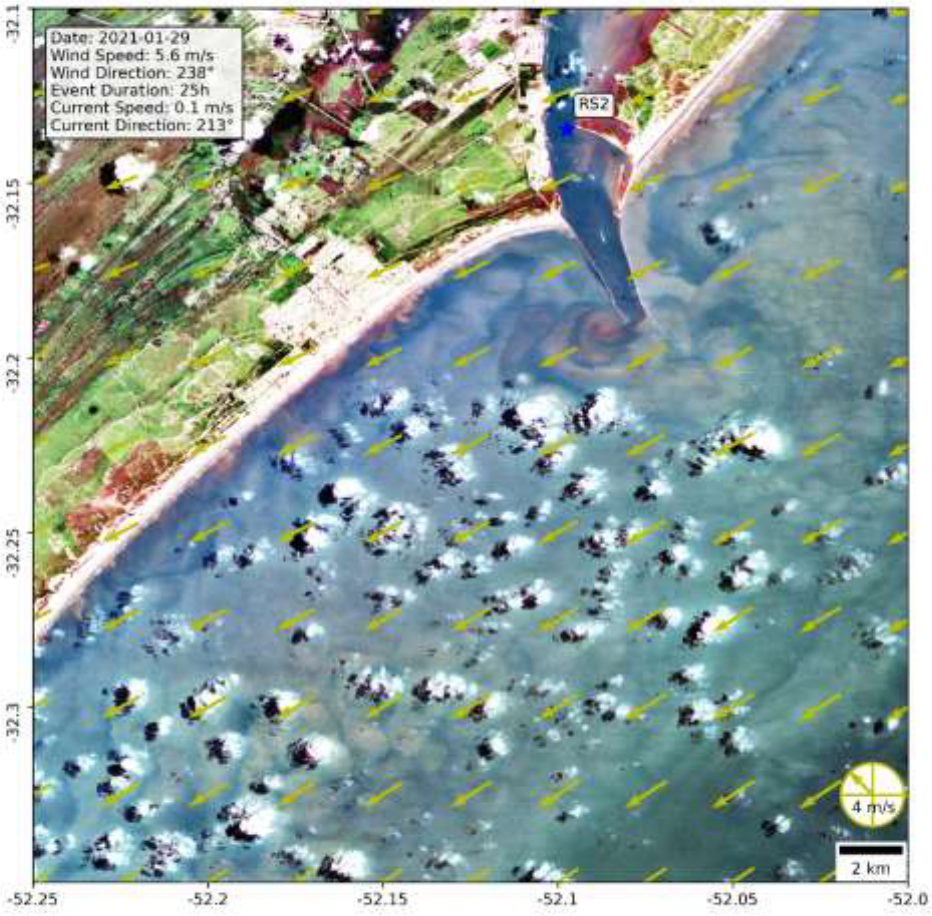

Date: 2022-02-03
Wind Speed: 7.1 m/s
Wind Direction: 231°
Event Duration: 2 days, 9h
Current Speed: -
Current Direction: -
RS2
4 m/s
2 km
-32.1
-32.15
-32.2
-32.25
-32.3
-52.25
-52.2
-52.15
-52.1
-52.05
-52.0

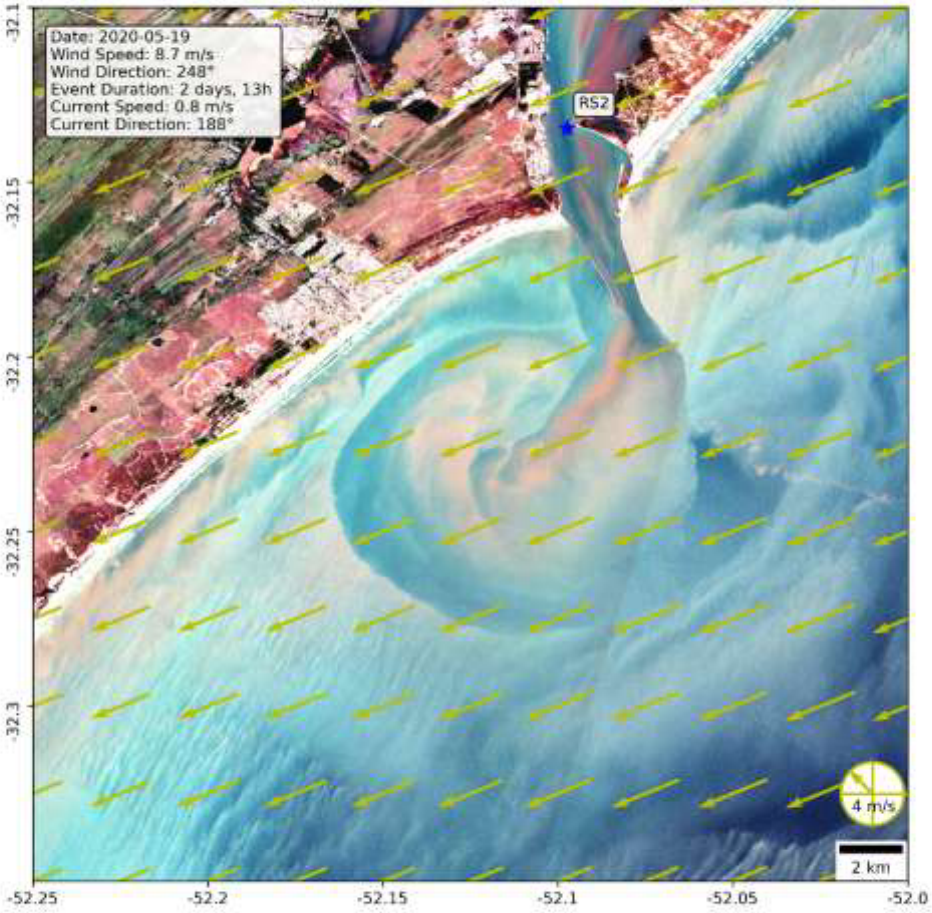

Date: 2022-01-14
Wind Speed: 6.5 m/s
Wind Direction: 243°
Event Duration: 2 days, 2h
Current Speed: -
Current Direction: -
RS2
4 m/s
2 km
-32.1
-32.15
-32.2
-32.25
-32.3
-52.25
-52.2
-52.15
-52.1
-52.05
-52.0

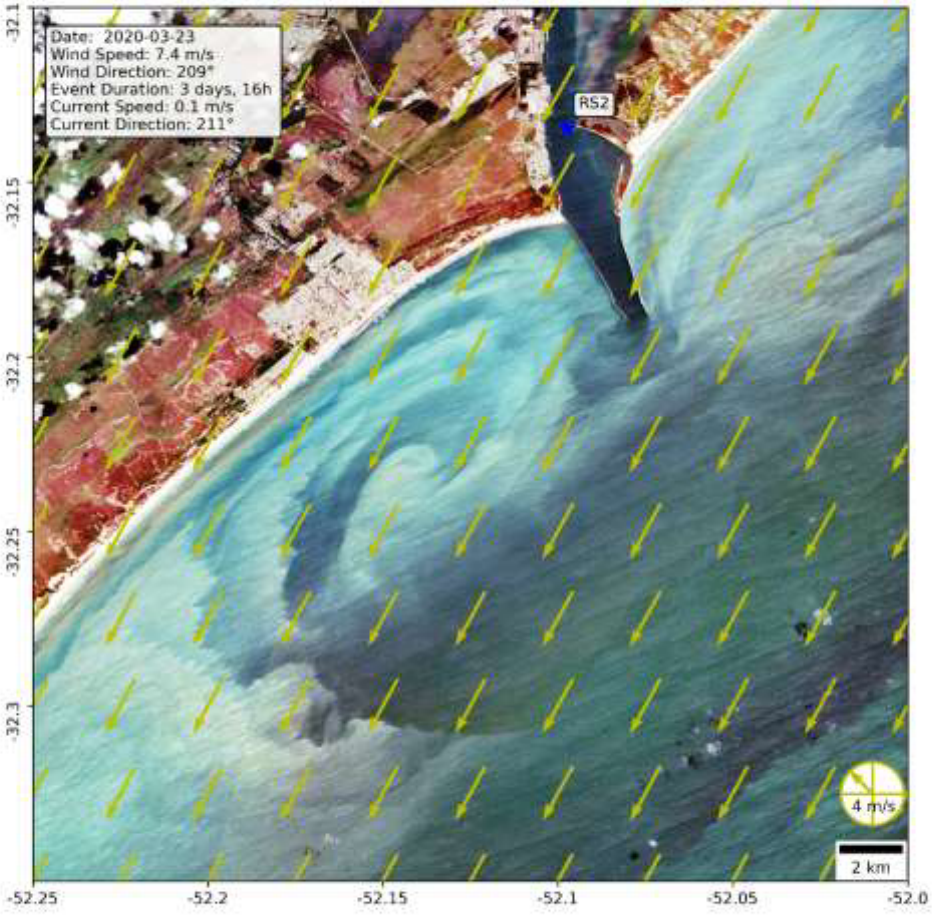

Date: 2022-01-09
Wind Speed: 9.2 m/s
Wind Direction: 210°
Event Duration: 5 days, 3h
Current Speed: -
Current Direction: -
RS2
4 m/s
2 km
-32.1
-32.15
-32.2
-32.25
-32.3
-52.25
-52.2
-52.15
-52.1
-52.05
-52.0

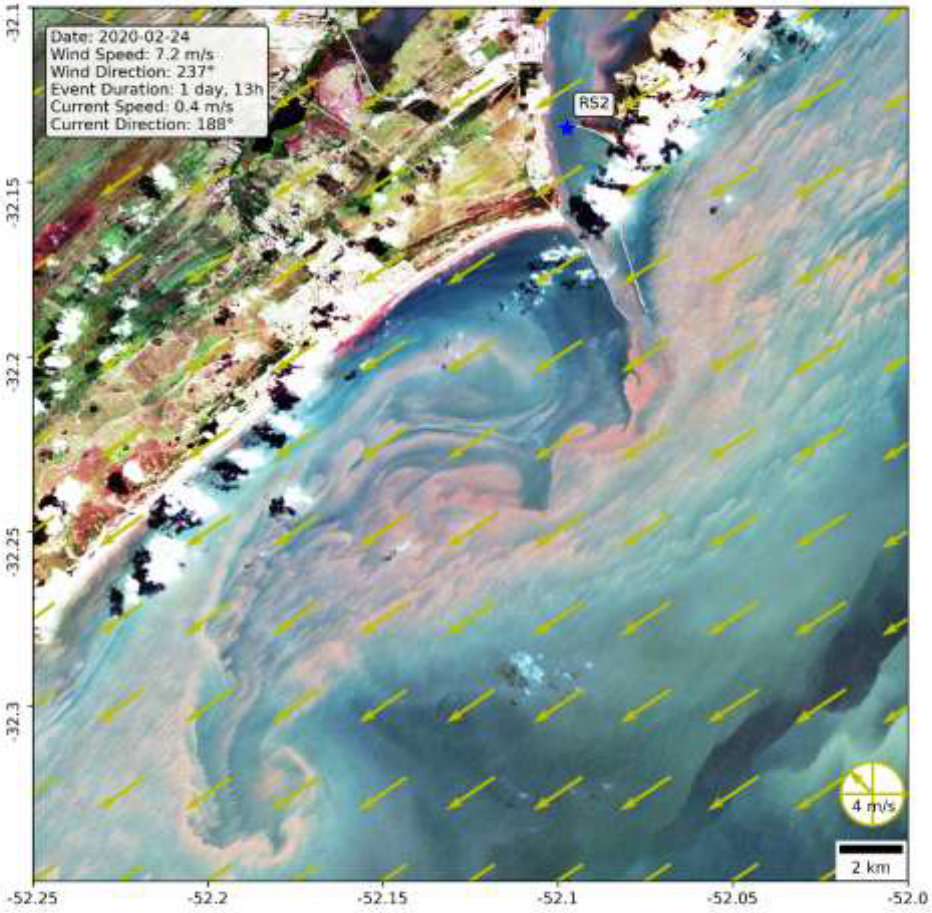

Date: 2021-05-09
Wind Speed: 8.4 m/s
Wind Direction: 227°
Event Duration: 1 day, 16h
Current Speed: 0.7 m/s
Current Direction: 181°
RS2
4 m/s
2 km
-32.1
-32.15
-32.2
-32.25
-32.3
-52.25
-52.2
-52.15
-52.1
-52.05
-52.0

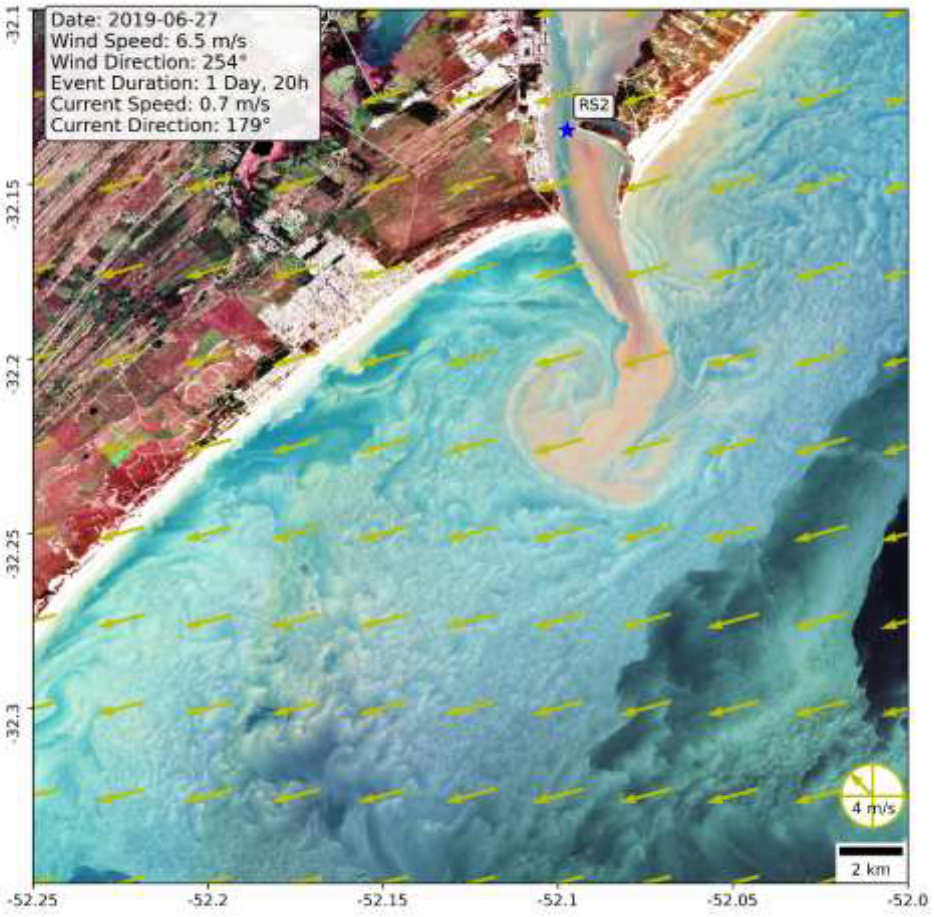

Date: 2021-04-19
Wind Speed: 6.8 m/s
Wind Direction: 174°
Event Duration: 4 days, 1h
Current Speed: 0.6 m/s
Current Direction: 180°
RS2
4 m/s
2 km
-32.1
-32.15
-32.2
-32.25
-32.3
-52.25
-52.2
-52.15
-52.1
-52.05
-52.0

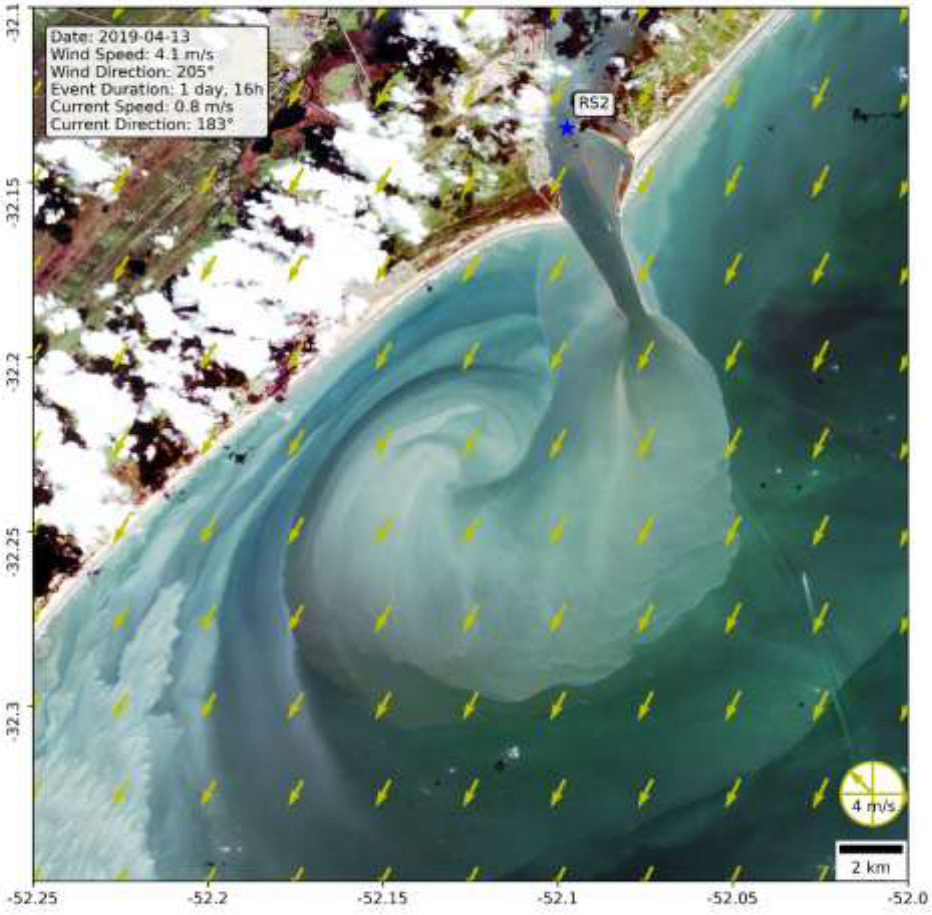

Date: 2021-01-29
Wind Speed: 5.6 m/s
Wind Direction: 238°
Event Duration: 25h
Current Speed: 0.1 m/s
Current Direction: 213°
RS2
4 m/s
2 km
-32.1
-32.15
-32.2
-32.25
-32.3
-52.25
-52.2
-52.15
-52.1
-52.05
-52.0

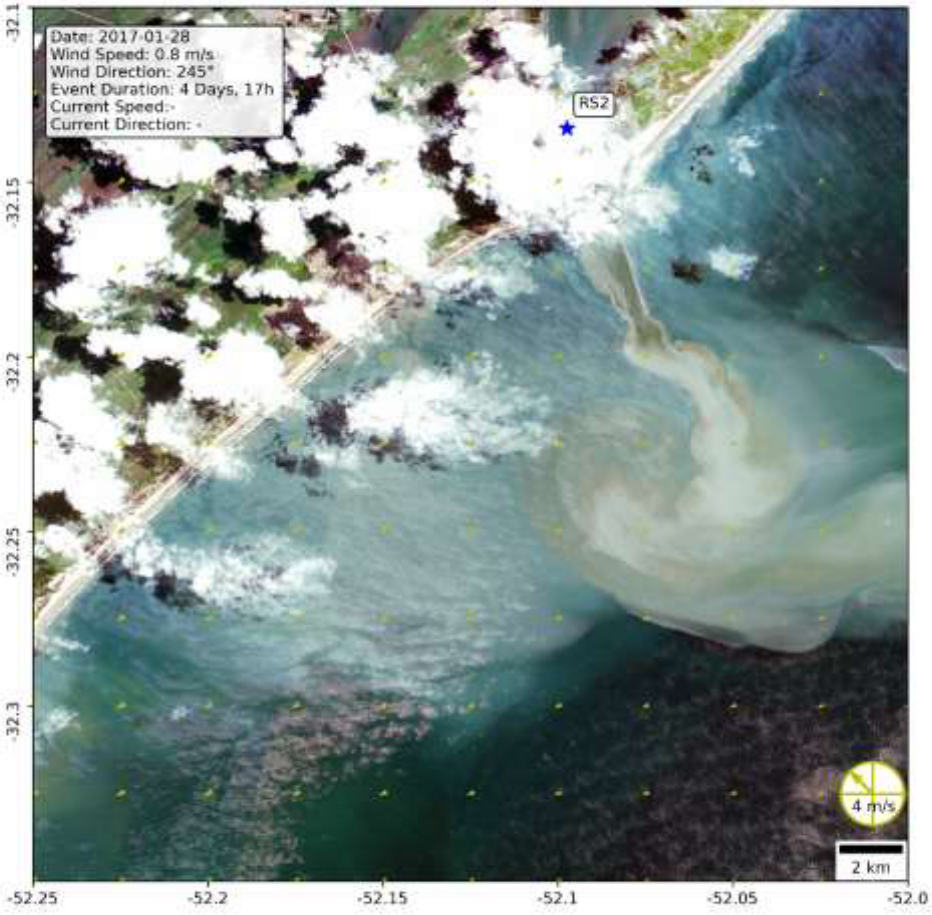

Date: 2020-05-19
Wind Speed: 8.7 m/s
Wind Direction: 248°
Event Duration: 2 days, 13h
Current Speed: 0.8 m/s
Current Direction: 188°
RS2
4 m/s
2 km
-32.1
-32.15
-32.2
-32.25
-32.3
-52.25
-52.2
-52.15
-52.1
-52.05
-52.0

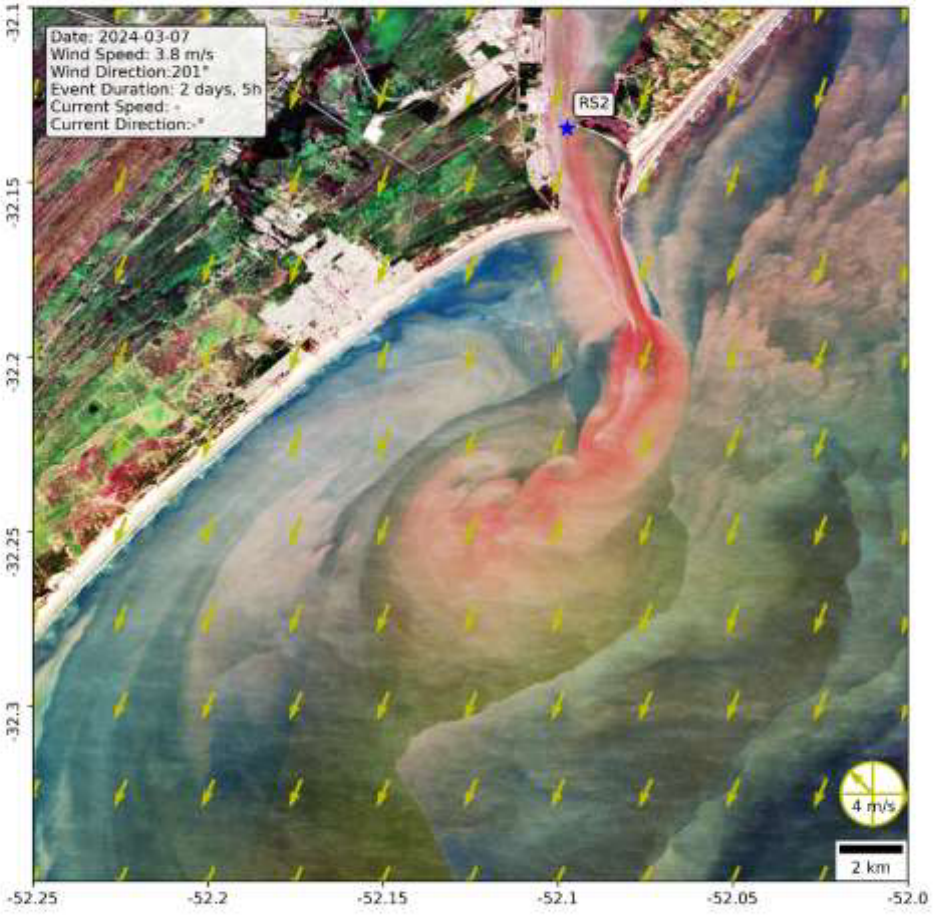

Date: 2020-03-23
Wind Speed: 7.4 m/s
Wind Direction: 209°
Event Duration: 3 days, 16h
Current Speed: 0.1 m/s
Current Direction: 211°
RS2
4 m/s
2 km
-32.1
-32.15
-32.2
-32.25
-32.3
-52.25
-52.2
-52.15
-52.1
-52.05
-52.0


Date: 2020-02-24
Wind Speed: 7.2 m/s
Wind Direction: 237°
Event Duration: 1 day, 13h
Current Speed: 0.4 m/s
Current Direction: 188°
RS2
4 m/s
2 km
-32.1
-32.15
-32.2
-32.25
-32.3
-52.25
-52.2
-52.15
-52.1
-52.05
-52.0


Date: 2019-06-27
Wind Speed: 6.5 m/s
Wind Direction: 254°
Event Duration: 1 Day, 20h
Current Speed: 0.7 m/s
Current Direction: 179°
RS2
4 m/s
2 km
-32.1
-32.15
-32.2
-32.25
-32.3
-52.25
-52.2
-52.15
-52.1
-52.05
-52.0


Date: 2019-04-13
Wind Speed: 4.1 m/s
Wind Direction: 205°
Event Duration: 1 day, 16h
Current Speed: 0.8 m/s
Current Direction: 183°
RS2
4 m/s
2 km
-32.1
-32.15
-32.2
-32.25
-32.3
-52.25
-52.2
-52.15
-52.1
-52.05
-52.0


Date: 2017-01-28
Wind Speed: 0.8 m/s
Wind Direction: 245°
Event Duration: 4 Days, 17h
Current Speed:-
Current Direction: -
RS2
4 m/s
2 km
-32.1
-32.15
-32.2
-32.25
-32.3
-52.25
-52.2
-52.15
-52.1
-52.05
-52.0


Date: 2024-03-07
Wind Speed: 3.8 m/s
Wind Direction:201°
Event Duration: 2 days, 5h
Current Speed: -
Current Direction:-°
RS2
4 m/s
2 km
-32.1
-32.15
-32.2
-32.25
-32.3
-52.25
-52.2
-52.15
-52.1
-52.05
-52.0

Apêndice B

Continental Shelf Research 289 (2025) 105467

Contents lists available at ScienceDirect

Continental Shelf Research

journal homepage: www.elsevier.com/locate/csr

The dynamics of the inner-shelf suspended sediments based on ADCP records and Rouse theory

Guilherme O. Cruz, Carlos A.F. Schettini *

Institute of Oceanography, Universidade Federal do Rio Grande (FURG), Brazil

ARTICLE INFO

Keywords:
Fine sediments
Bed exchanges
Hydrodynamics
Inner shelf

ABSTRACT

The present study investigates the suspended sediment dynamics on the southern Brazilian continental shelf in the fluvial influence region of the Rio de la Plata and Patos Lagoon. Estimates of suspended sediment concentration (SSC) in the water column were obtained using data from a Doppler-effect acoustic Doppler current profiler (ADCP) and were compared with theoretical profiles obtained using Rouse's theory. To construct the theoretical profile, sediment settling velocity and shear velocity are necessary. The former was iteratively estimated to minimize the error between observed and modeled profiles. The latter was obtained from ADCP measurements. The comparison between observed and modeled profiles underwent a validation process considering the shape of the observed profile and environmental energy conditions. For the period of analyzed data, there was agreement between observed and modeled profiles 56 % of the time. When energy conditions were low (39 % of the time), and the gradient profile of SSC had higher concentrations near the surface than bottom (5 %), Rouse's theory did not apply. These results indicate that the main source of sediment in the water column is due to exchanges with the bottom. Although the study area is near the mouth of Patos Lagoon, the role of horizontal advection was negligible. By indirect inference, it was obtained that the median sediment size was 25 μm, with maximum values around 60 μm, which coincides with values suggested in the literature for coastal waters, with a median settling velocity of 0.14 cm/s. During periods of more energetic hydrodynamic conditions, downwelling events were associated with northward longitudinal currents, while upwelling occurred with southward currents. When the flow was directed northward, more material was transported near the bottom compared to southward flow.

1. Introduction

Understanding sediment dynamics on the continental shelf is fundamental for comprehending the functioning and evolution of continental margins (Drake and Burk, 1974; Swift, 1974). Sediment transport plays a crucial role in distributing materials arriving from continental drainage, resulting in morphological changes on the seabed (Guillén et al., 2006), creating new habitats for benthic organisms (Williams and Bax, 2001), altering biogeochemical relationships at the sediment-water interface (Lukawska-Matuszewska et al., 2022), or even releasing toxic materials associated with sedimentary particles (Palanques and Diaz, 1994). Additionally, economic development requires the expansion of port infrastructure, such as enlarging docking berths to accommodate more and larger vessels. Such transformations necessitate sediment dredging, with the dredged materials being disposed of on the continental shelf (Marmin et al., 2016; Schettini, 2022). In this context, studying these regions and improving available techniques for quantifying sediment transport are necessary to predict and mitigate disturbances and ensure the environmental and economic sustainability of these areas.

Suspended sediments in coastal areas, excluding the surf zone on beaches, are essentially cohesive fine sediments (Winterwerp and van Kesteren, 2004), which exhibit complex relationships with hydrodynamics (Sahin et al., 2012), as well as biological activities (Black et al., 2002). One of the main characteristics of cohesive sediments in coastal areas is that they consist of very small particles (<2 μm); however, due to their cohesive nature, they occur as aggregates or flocs of much larger size (>50 μm) (Eisma, 1986). Nevertheless, flocs, as sedimentary units, are composed of sediment particles, water, and adsorbed organic matter, and thus, have a lower density of ~1650 kg/m^3 for flocs with size ~100

This article is part of a special issue entitled: Latin American Coastal Oceans published in Continental Shelf Research.

* Corresponding author.
E-mail addresses: guru.schettini@furg.br, guru.schettini@gmail.com (C.A.F. Schettini).

https://doi.org/10.1016/j.csr.2025.105467
Received 5 April 2024; Received in revised form 20 March 2025; Accepted 28 March 2025
Available online 29 March 2025
0278-4343/© 2025 Published by Elsevier Ltd.

μm, and only the microflocs with size lower than 30 μm approach the effective density of quartz, ~2650 kg/m³ (Black et al., 2002).

The formation of these flocs is influenced by various factors, such as the composition and concentration of these sediments, ion concentration in the water (salinity), pH, turbulence, and the presence of bacteria and other organisms (Black et al., 2002). The composition of sediments can affect the formation and stability of these flocs, as the bonding strength between flocs decreases exponentially as the proportion of non-cohesive sediment increases. Flocs formed from a higher concentration of silt are more susceptible to breakage, resulting in a lower terminal particle velocity (Manning et al., 2010). Sediment concentration influences flocculation, as higher concentrations increase the likelihood of particle encounters. The encounter of particles also depends on the turbulence of the medium, but this has a complex relationship with flocculation. Turbulence can increase the rate of floc formation by increasing the probability of collisions, but when turbulence exceeds a threshold, it can also break already formed flocs or even prevent their formation (Dyer and Manning, 1999; Manning et al., 2010). The presence of ions (salinity) in the water can affect the electric charge of cohesive particles, facilitating or inhibiting floc formation depending on the assembly of clay minerals constituting the sediment (Al Ani et al., 1991). In environments with acidic pH (<7), particles tend to acquire more positive charges, which can favor flocculation (Contreiro and Schettini, 2010). Bacteria and other organisms can act as binding agents and alter environmental conditions, such as pH, indirectly affecting floc formation (Black et al., 2002).

The shear stress of flow with the bed generated by waves and/or currents is the main source of energy to entrain or maintain sediment particles denser than water in suspension, through the conversion of kinetic energy into turbulent kinetic energy, creating turbulent diffusion. The work required to lift and keep these particles in suspension is directly related to the weight, shape, size, and viscosity of the fluid, as well as thixotropic properties in muddy bottoms (Winterwerp and van Kesteren, 2004). The amount of turbulent energy decreases with distance from the bed, resulting in fewer suspended particles and a vertical sediment concentration profile with an exponential shape (Rouse, 1939).

The vertical profile of suspended sediment concentration (SSC) can be represented by the Rouse model (1939). The equation describing the model represents the balance between the settling velocity of the sediment, which moves the particle towards the bottom, the turbulent diffusion coefficient, which is a measure of the vertical mixing rate, with the sediment concentration rate for each level (z).

$$w_s C(z) + \varepsilon_s \frac{dC(z)}{dz} = 0 \quad (1)$$

where z is the height above the water/sediment interface (m), w_s is the settling velocity of sediment particles (m/s), C is the suspended sediment concentration (kg/m³) at a given level, and ε_s is the vertical turbulent diffusion coefficient for suspended sediments (m²/s).

The use of Acoustic Doppler Current Profilers (ADCP) allows for precise observations of the vertical profile of SSC, providing the $C(z)$ in Eq. (1), as they record acoustic backscatter information (ABS), which has a direct and nonlinear relationship with SSC. ADCP's have proven to be efficient for this purpose in coastal regions (Gartner, 2004; Park and Lee, 2016; Schettini et al., 2013; Yu et al., 2011). This approach has the advantage of enabling data acquisition for long periods with high temporal and spatial resolution (in the vertical) compared to other methods for obtaining SSC, such as water sampling or the use of optical turbidimeters (Downing et al., 1981), at a relatively low cost. However, the use of these other methods for calibration and validation purposes is still necessary.

In the present study, we investigated the dynamics and transport of suspended sediments on the inner continental shelf of Rio Grande – RS, Brazil. Estimates of the vertical and temporal distribution of SSC were obtained using acoustic backscatter data recorded by an ADCP (Acoustic Doppler Current Profiler) and compared with vertical profiles derived from the Rouse model (Bourdreau and Hill, 2020). While the ADCP approach provides SSC estimates, the Rouse theory approach enables the assessment of settling velocity and vertical diffusion. The comparison of results allows us to diagnose the relationship between bottom exchange processes and advection. The study area exhibits a complex sedimentary dynamic, influenced by both the freshwater outflows of the Rio de la Plata and the Patos Lagoon. Thus, the SSC estimates and sedimentary characteristics obtained in this study contribute to a better understanding of transport processes and sedimentary dynamics in the region. Furthermore, the methods and algorithms used in this study can be applied to other continental shelves for the analysis of sediment dynamics.

2. Study area

The state of Rio Grande do Sul continental shelf extends approximately in a north-south axis between Arroio Chuí (34°S) and Torres (29°S), with a coastline dominated by a sandy coastal plain without prominent features except for the mouth of Patos Lagoon. The width of the shelf varies between 100 and 180 km, with a shelf break depth at ~180 m, and a low bottom slope. Near the mouth of Patos Lagoon, the shelf is relatively flat, with the presence of extensive sandy banks to the north and south of the mouth (Fachin, 1998; Corrêa et al., 2019).

Most of the shelf is dominated by mud deposits sourced by the La Plata estuary and Patos lagoon (Martins et al., 2003; Campos et al., 2008; Corrêa et al., 2019; Toldo et al., 2006). The coast south of the mouth of Patos Lagoon (Cassino beach) experiences cyclic events of mud deposition on the beach (Calliari et al., 2007). On the inner shelf off the beach, pockets of unconsolidated mud occur, and after certain storms, this material is eroded and transported towards the shore (Calliari et al., 2001; Pereira et al., 2011), which indicate the shelf experiences high mud mobility.

The local climate is humid subtropical, with a strong seasonal signal. The monthly mean temperature ranges between 11 and 23 °C (Reboita and Kruche, 2018). There is a predominance of winds from NE throughout the year, with higher intensity in spring (Reboita and Kruche, 2018; Saraiva et al., 2003). This wind pattern is cyclically disturbed by the passage of frontal systems occurring at intervals of 6–11 days (Stech and Lorenzzetti, 1992). Fig. 2 shows the frequency distribution of the wind and the monthly climatology of the along-shelf and cross-shelf wind.

Wave climatology of the region has been described using observational data (Motta, 1963; Strauch, 1997), and numerical models Cuchiara et al. (2009); Cecilio and Dillenburg (2019). There are two main propagation directions: 110° (from the E) with significant wave height of 1.0 m and period of 8 s, and 160° (from the SSE) with significant wave height of 1.5 m, and average period of 12 s. However, during storms wave heights can reach up to 5 m.

There are relatively few observations of the currents. Zavialov et al. (2002), and Costa and Möller (2011), assessed the currents based on observations on the 50 m and 15 m isobaths, respectively. Their results indicate that currents are primarily forced by local wind, with little importance of astronomical tides. On the outer shelf the mean flow is southward, responding to mesoscale processes (Palma et al., 2008). Near the mouth of Patos Lagoon, circulation patterns are more complex, both due to the presence of the lagoon's mouth and the presence of jetties that extend approximately 4 km offshore. The lagoon produces predominant outflow of low salinity waters, which produces a pronounced buoyancy plume (Hartmann et al., 1996; Möller et al., 2001; Marques and Möller, 2008). However, the entire area is within the fluvial influence region of the Rio de la Plata, especially during periods of winds from the S-SE, which displaces the low salinity plume to lower latitudes (Piola et al., 2008).

The Rio de la Plata has an average discharge of 25.000 m³/s (Ibler,

1972), with suspended solid discharge on the order of 100 × 10^6 tons/year (Ianpova and Mikhailov, 2019), and SSC values on the shelf of 200 mg/L (Moreira et al., 2013). The average discharge of Patos Lagoon is 2400 m^3/s (Vaz et al., 2006), and the average suspended solid discharge of the Rio Guaíba of 1.1 × 10^6 tons/year (Andrade Neto et al., 2012). SSC values observed near the mouth of Patos Lagoon vary between 5 and 200 mg/L (Hartmann et al., 1990).

3. Material and methods

Pressure (depth), temperature, velocity, current direction, and acoustic intensity data were obtained using an ADCP anchored at a depth of 20 m approximately 15 km from the coastline and 10 km from the mouth of Patos Lagoon (32°14'48"S, 51°58'52.5"W, Fig. 1d #O). The installation period was during the spring season, from September 17th to November 2nd, 2020 (45 days). A Nortek Aquadopp Profiler ADCP with a frequency of 1000 kHz was used, configured to record vertical profiles at 10-min intervals, based on 120-s averages, with a vertical resolution of 0.5 m. When the ADCP is moored, data near the surface are often inaccurate due to turbulence generated by waves and the presence of bubbles, which distort the acoustic signal measurements. The selection of valid cells for analysis was based on the temporal mean profile of acoustic amplitude. The acoustic amplitude signal decreases with distance from the instrument, but near the surface, the signal increases, showing a peak that coincides with the air-water interface. We used only the data where the amplitude signal decreases, which in this case was up to approximately 14.5 m above bottom (mab). Considering that the local tidal range is microtidal (~0.5 m), we applied a constant cutoff level for the entire record of ~3 m. The valid measurement levels ranged from approximately 1 m above the seafloor to approximately 3 m below the surface, or ~78 % of the water column.

Wind speed and direction data were obtained from buoys RS4 and RS5 (Fig. 1), covering the period from December 2016 to April 2021. Synoptic data for the ADCP anchoring site, including surface salinity and wave parameters (direction, period, and height), were obtained from buoy RS4, located 10 km south of the ADCP installation site. The current and wind data were decomposed into longshore and cross-shore components, considering the inclination of the maximum velocity variance relative to the north, which was 29°.

3.1. Inversion of ABS to SSC

The acoustic intensity data recorded by the ADCP were converted into acoustic backscatter strength (ABS) in decibels (dB) using the sonar equation (Urick, 1975).

$$ABS = RL + 2TL - TS \quad (2)$$

Where ABS is the relative acoustic backscatter strength (dB), RL is the reverberation level, given by $K_c(E - E_r)$, where E is the intensity recorded by the ADCP in counts, E_r is the intensity of the signal received by the ADCP when no signal is transmitted (reference level measured with the equipment out of water), and K_c is a scale factor used to convert counts to dB (0.43). 2 TL is the transmission loss level, defined as:

$$2TL = 20\log(R) + 2\alpha R \quad (3)$$

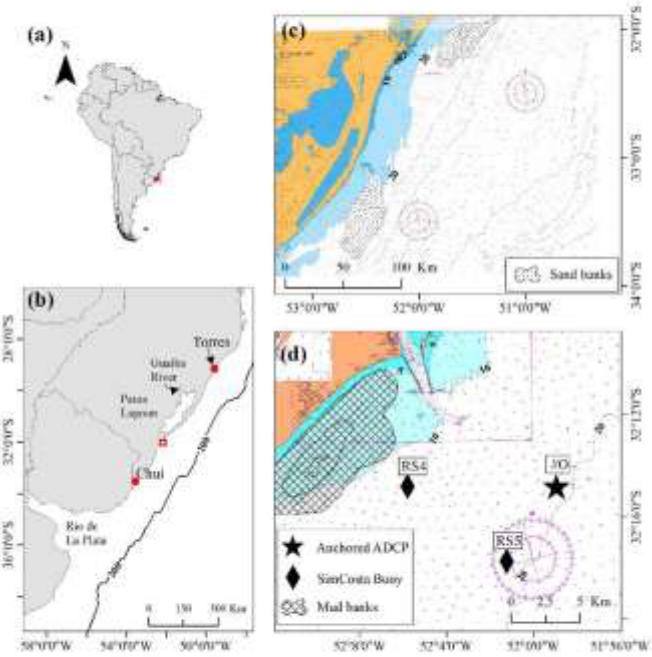


Fig. 1. Location of the study area. The larger panel shows the situation of the continental shelf on a smaller scale with indication of bathymetric lines, and in detail presents the location of the ADCP mooring and buoys RS4 and RS5. The location of the mud bank was extracted from Calliari et al. (2007). The location of the sandy banks was obtained from navy nautical charts.

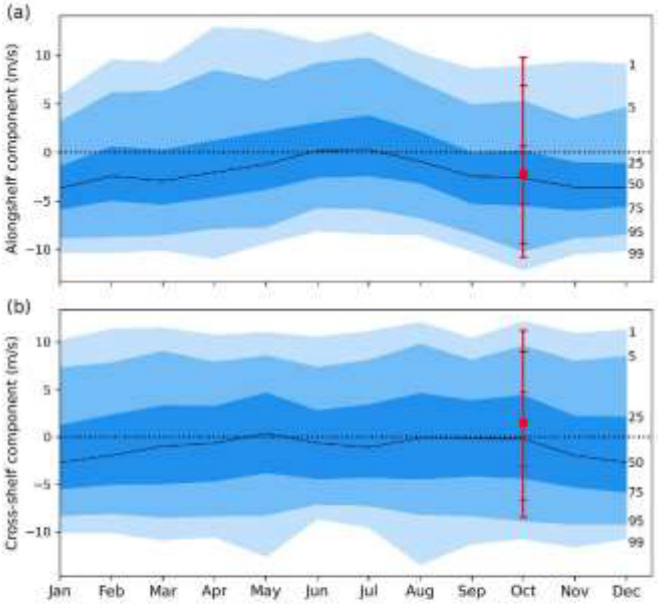


Fig. 2. Monthly frequency distribution of wind velocity for the alongshelf and cross-shelf components based on observational data recorded at buoys B34 (Feb/2019 to Apr/2021) and B35 (Dec/2016 to Mar/2023). The median value is represented by the black line, and the shades of blue represent the range of percentiles 1–99, 5–95, and 25–75 %. The vertical red line in the month of October represents the data observed during mooring from September 17th to November 2nd, 2020 (45 days).

Where R is the range of the volume of water being sonified (m), a is the coefficient of absorption of seawater (dB/m), obtained through a function of acoustic frequency, salinity, temperature, and pressure (Schulkin et al., 1962).

TS is the target strength and represents the transmission loss by the source and depends on the frequency of the ADCP and the diameter of the particle. However, this term is not considered in general. The transmission attenuation by this term is significant only at low concentrations or when the diameter of the particle is small (<10 μm), which is typically not the case of flocculated material found in coastal waters (Ebma, 1986). For example, an ADCP with a frequency of 1000 kHz and particles with a mean diameter of 20 μm would have a sensitivity peak (ka) of approximately 0.04, characterizing Rayleigh distribution (ka≪1). This means that sound waves interact with particles much smaller than their wavelength. According to Rayleigh distribution theory, the maximum TS value would be −37 dB; however, this estimate applies to a single, spherical, incompressible particle with a smooth surface. In coastal regions, turbidity is typically high enough to prevent individual particle scattering from significantly attenuating the signal. As a result, acoustic backscatter becomes more dependent on the collective scattering of suspended particles rather than isolated interactions (Urick, 1975).

The inversion from ABS (dB) to SSC (g/L) was performed using the relationship:

$$SSC_{ABS} = 1.2 \times 10^{-4} + \exp^{(0.126\ ABS)} \quad (4)$$

This relationship was obtained for the same brand, model, and frequency of ADCP used in the present study, based on a fitting between ABS and SSC with $r^2 = 0.78$, for a location nearly 20 km southwards from the mooring of the present study. This relationship was obtained using simultaneous ADCP data and turbidity data from optical backscatter sensors (OBS) at two measurement levels, with hourly intervals over a 30-day period. The OBS sensors were calibrated with local sediment, thereby allowing the relationship between ABS and SSC to be determined.

3.2. Bottom shear stress

The bottom shear stress (τ) is a measure of the frictional force exerted by the fluid per unit area of the bottom (Pa). It is also closely related to the level of turbulence, which controls the suspension of sediments. The bottom shear stress can be generated by currents (τ_C), waves (τ_W), and combined by currents and waves. We used the approach described by Soulsby and Clarke (2005) to calculated the bottom shear stress, where the latter can be calculated in two ways: the mean bottom shear stress for wave +current (τ_{mean}), which considers the interactions of τ_c by τ_w during the wave orbital velocity incursion, and the maximum bottom shear stress for wave +current (τ_{maxmc}), which considers the interaction of τ_c by τ_w when the wave orbital velocity (U_w) is maximum.

The Soulsby and Clarke (2005), algorithm for determining the combined wave and current shear stress is based on the findings of Simons et al. (2000), where the wave-induced oscillatory stress component is nonlinearly added to the current stress. Soulsby et al. (1993) compared results obtained from various theoretical models with observational data and demonstrated that nonlinearity arises due to the difference in the angle of attack between waves and currents, which is corroborated by recent studies (Choi, 2009; Malarkey and Davies, 2012; Ribeiro et al., 2017; Wang et al., 2018). The additional turbulence generated by waves near the bed represents, for the current, the equivalent of an increase in apparent bed roughness. In sediment

transport analyses, $\tau_{max,wc}$ is used to determine the threshold for sediment movement initiation or intrusion, while τ_{max} is used in the suspension sediment diffusion to upper layers (Soulsby et al., 1993).

The equations to estimate the different bottom shear stresses used are:

$$\left.\begin{array}{l} \tau_c = \rho C_D \overline{U}^2, \text{for } \overline{U} > 0 \text{ and } U_w = 0 \\ \tau_w = \frac{1}{2}\rho f_w U_w^2, \text{for } \overline{U} = 0 \text{ and } U_w > 0 \\ \tau_{max} = \rho C_{Dm}\overline{U}^2 \text{ or } \tau_{cmax} = \rho C_{Dmax}\overline{U}^2, \text{for } \overline{U} > 0 \text{ and } U_w > 0 \end{array}\right\} \quad (5)$$

where ρ is the water density; $\overline{U}$ is the depth averaged current velocity; C_D is the drag coefficient; f_w is the wave friction factor; U_w is the wave orbital velocity; C_{Dm} and C_{Dmax} are the drag coefficients when considering the combined current + wave mean and maximum effects, respectively. The approach of Soulsby and Clarke (2005), distinguish flow conditions for rough and smooth bottoms, which affect how the drag and wave friction coefficients are calculated. In present case we used the formulation for smooth bottom. The implementation of the algorithm for calculation of bed shear stress implemented in Python is available at https://github.com/GuiCruz/SoundSSC.

Using the approach described in Soulsby (2006), the calculation of the wave orbital velocity (U_w) depends on ratio between the natural scaling period (T_n) to the wave period (T)

$$\frac{T_n}{T} = \left(\frac{h}{gT^2}\right)^{0.5} \quad (6)$$

where h is the water depth, and g is the acceleration of gravity. If T_n/T is < 0.2, U_w is calculated by Nielsen's method by

$$U_w = 0.5H\left(\frac{\pi}{h}\right)^{0.5}\left[1 - \frac{1.2\pi T_n}{T}^2\right] \quad (7)$$

where H is the wave height. Otherwise, it is used Soulsby's exponential approximation by

$$U_w = 0.5H(g/h)^{0.5}\, exp\left\{-\left[\frac{4.41}{T}\left(\frac{h}{g}\right)^{0.5}\right]^{2.45}\right\} \quad (8)$$

3.3. Rouse model and terminal velocity

The terminal settling velocity of suspended sediment (w_s), the mean suspended particle diameter (d_s), diffusion coefficient (ε_s), and SSC_{rouse} were estimated using the Rouse model, modified by Boudreau and Hill (2020). The results were compared with SSC_{ABS} estimates obtained through ABS inversion, and the best-fitting profile was selected based on the mean squared error. The original formulation developed by Rouse (1939) predicts an infinite amount of sediment at the bottom ($z = 0$). To address this singularity issue at the sediment source, the authors considered the existence of residual turbulent diffusion (ε_0) near the bottom, defined as:

$$\varepsilon_0 = \varepsilon_z - \kappa u_* z \quad (9)$$

where ε_z is the turbulent diffusion coefficient, k is the von Karman constant (0.41), u_* is the shear velocity ($= \sqrt{\tau/\rho}$), and z is the distance from the bottom. ε_z is estimated by

$$\varepsilon_z = \kappa u_* (z + z_r) \quad (10)$$

where z_r is the bottom roughness scale given by

$$z_r = \frac{26 d_b}{\varepsilon} \quad (11)$$

where d_b is the mean bottom sediment diameter. The vertical distribution of sediment concentration C(z) (or SSC_{rouse}) can be modeled by

$$C(z) = C_{ref}\left(1 + \frac{\kappa u_* z}{\varepsilon_0}\right)^{-Ro} \quad (12)$$

where C_{ref} is the reference concentration at the bottom ($z = 0$), and Ro is the Rouse number ($= w_s/\kappa u_*$).

The input variables used to solve the model are: u_*, calculated using the τ_c, τ_w or τ_{max} described above (Soulsby and Clarke, 2005); water density ρ was calculated based on the measured salinity from Buoy RS4 and the temperature obtained from the ADCP; bottom sediment diameter d_b was obtained from the literature ($\approx$ 130 μm; Martins et al., 2003; Correa et al., 2019). The iterable variables used in fitting the SSC_{rouse} profile are: the reference concentration, C_{ref}, varying from 0.01 to 100 kg/m^3; the mean suspended sediment diameter, d_s, varying from 20 μm to 250 μm, which was constrained based on values previously observed in nearby regions (Martins et al., 2003); and the particle density, ρ_{sed}, ranging from 2000 to 2650 kg/m^3, which was defined based on laboratory studies on the characteristics of mud flocs (Manning et al., 2010). With d_s and ρ_{sed}, the w_s in Ro was calculated using Stokes Law

$$w_s = \frac{2}{9}\frac{(\rho_s - \rho)}{\mu} g\, d_s^2 \quad (13)$$

where μ is the water dynamic viscosity (10^{-3} Pa s).

The algorithm developed to analyze, process, and apply the mathematical models was implemented in Python, following these steps: (1) preprocessing of oceanographic data to remove outliers from the ADCP data near the surface and to estimate the longitudinal and transverse velocity components; (2) application of the Soulsby model to generate estimates of bottom shear stress (Equation (5)); (3) application of the Rouse model to generate estimates of sediment characteristics, where the iterable variables provided various SSC_{rouse} profiles which were compared to the SSC_{ABS} profile using the root mean squared percentage error (RMSPE), with the best-fitted profile being selected; (4) post-processing where basic statistics were applied and the data were reduced for graphical representation. Detailed information on the resolution of equations and the developed algorithms are available in https://github.com/GuiCruz/SoundSSC.

The RMSPE is calculated by

$$RMSPE = \sqrt{\frac{1}{m}\sum_{i=1}^{m}\left(\frac{y_i - \hat{y}_i}{y_i}\right)^2} \times 100 \quad (14)$$

where m is the sampling size, y_i is the reference value (SSC_{ABS}), and $\hat{y}_i$ is the modeled value (SSC_{rouse}).

3.4. Validation of the vertical SSC profile

The vertical SSC profiles generated using the Rouse theory were validated considering two hierarchical criteria: (1) a minimum threshold of bottom shear stress for vertical sediment mobilization to occur; and (2) a condition of positive mean concentration gradient of the water column $\left(\frac{\partial C(z)}{\partial z}\right)$, when Rouse theory does not apply. In the first step, we identified the profiles with τ_{max} values below 0.05, which is the critical shear stress for sediment mobilization (τ_{crit}). The threshold of 0.05 Pa was defined based on the available data on the average sediment size (Martins et al., 2003) combined with the critical shear stress data available in the literature (van Rijn, 2020; Salehi and Strom, 2012). Below this value, there is not enough turbulent energy to mobilize bottom sediments.

The τ_{crit} is determined by the combination of sedimentary characteristics, hydrodynamic properties, and environmental conditions. Smaller, more cohesive flocs exhibit higher τ_{crit} compared to larger sediments with a greater proportion of sand and silt (Manning et al., 2010). Compacted sediments also require more energy to be eroded.

Turbulence and hydrodynamic history affect their thixotropic properties: under high-energy conditions, the bonds between particles are broken, reducing the material's resistance to shear (Winterwerp and van Kesteren, 2004). Environmental conditions, such as salinity, influence flocculation and cohesion (Al Ani et al., 1991). The presence of organic matter can act as a binding agent, increasing cohesion and shear resistance. On the other hand, biological activity, such as that of benthic organisms, can destabilize the bed, facilitating erosion (Black et al., 2002). Although determining a specific τ_{cri} value is complex, given the numerous factors acting simultaneously, in the absence of a value for the region, a τ_{cri} of 0.05 Pa was established based on data available in the literature. For bottoms consisting mainly of mud (>80 %), a critical stress of 0.05 Pa is considered, and when the composition is muddy sand (diameter 150–250 μm), the stress increases to 0.15 Pa (van Rijn, 2020). Observational studies conducted by Salehi and Strum (2012) obtained similar values, between 0.06 and 0.14 Pa, for beds composed of mud and sand, respectively.

3.5. Temporal representativeness

To assess the temporal representativeness of the data obtained during mooring and thus temporally validate the estimates obtained through the Soulsby and Rouse models, a comparative analysis of the meteorological and oceanographic conditions with the corresponding parameters from the historical series obtained by buoys RS4 and RS5 (Fig. 1) was conducted. Wind parameters were compared with data from

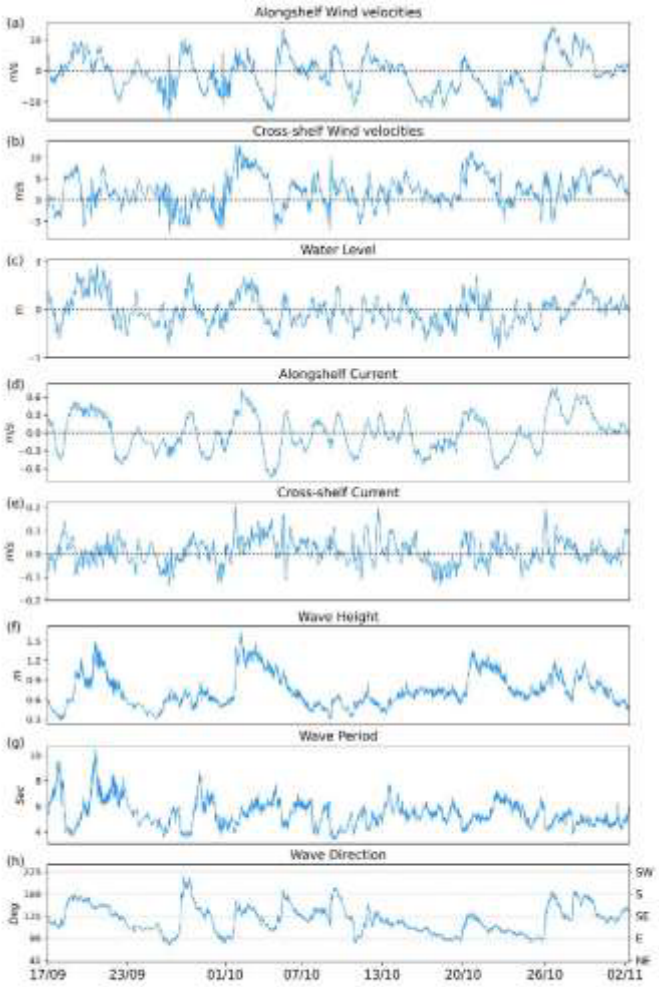


Fig. 3. Time series of (a) longitudinal and (b) transverse wind velocities, (c) sea level oscillation, average water column velocity (d) longitudinal and (e) transverse, (f) wave height, (g) wave period, and (h) wave propagation direction.

buoys RS4 and RS5 together, covering approximately 2293 days. Wave and current parameters were compared only with the historical series of buoy RS4, covering about 774 days. After a detailed review of each parameter, the temporal distribution of the variable was analyzed through persistence curves and the application of basic statistics.

4. Results

The time series of wind speed, depth-integrated currents, sea level oscillation, and wave height, period, and direction for the mooring period are shown in Fig. 3. The persistence curves and frequency distributions for these variables, except for sea level, are presented in Fig. 4, and the values for the median and percentiles of 1, 5, 25, 75, 95, and 99 % are presented in Table 1. Fig. 4 and Table 1 also present the results for the long-term monitoring from buoys RS4 and RS5.

The time series of wind components (Fig. 3a and b) exhibited the expected oscillations of the wind regime for the region, with high variability in wind direction and intensity, including several events where the wind exceeded 10 m/s, interspersed with periods of low intensity. The response of the water level and currents to the wind regime were expected according to the previous assessments in the region (Costa and Möller, 2011; Santos and Garcia, 2023). The sea level oscillation (Fig. 3c) followed the alongshore wind variation, with variations on the order of 1.5 m, and a much smaller astronomical signal compared to the low-frequency signal. The alongshore component of the depth-integrated water column mean current (Fig. 3d) followed the wind variability pattern, varying with an amplitude of 0.7 m/s. The cross-shore component of the depth-integrated water column mean current (Fig. 3e) showed an amplitude of 0.15 m/s, with a greater presence of the astronomical tide component.

During the period, three events of higher wave energy occurred, with wave height exceeding 1 m (Fig. 3f), but presenting distinct periods (Fig. 3g). The first event showed swell conditions with a period of 10 s, while the other events showed sea conditions with a period of 6 s. In all

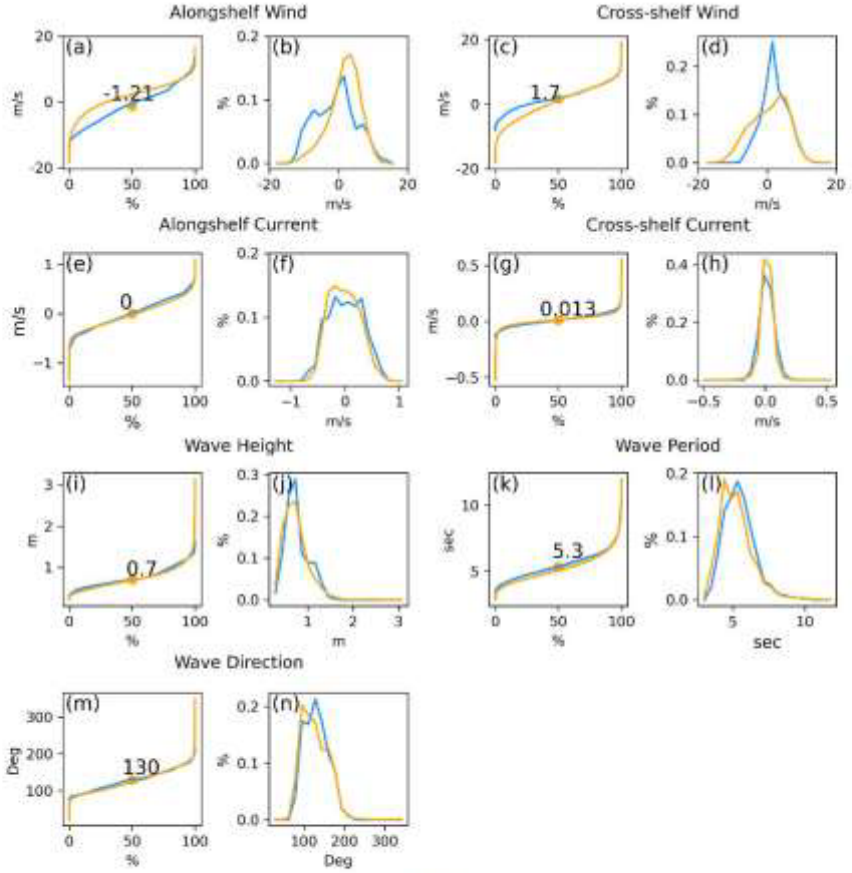


Fig. 4. Duration curve and frequency distributions of the time series presented in Fig. 3 for (a, b) longitudinal and (c, d) transverse wind speed, (e, f) longitudinal and (g, h) transverse current speed, (i, j) wave height, (k, l) wave period, and (m, n) wave propagation direction. The blue lines represent the observed data during the ADCP mooring, and the orange lines represent the historical data series.

Table 1
Median and percentile values for the observed data during the ADCP mooring (M) and for the long-term records from the buoys (LT), for alongshore and cross-shore components of wind and currents, and wave parameters.

Parameter	Period	1st	5th	25th	50th	75th	95th	99th
Alongshore Wind (m/s)	M	−11.9	−10.25	−5.65	−1.21	2.3	8.38	11.04
	LT	−10.61	−6.8	−0.82	2.29	4.88	8.3	10.28
Cross-shore Wind (m/s)	M	−6.28	−3.83	−1.05	1.69	4.95	8.62	10.82
	LT	−11.25	−8.48	−3.21	1.26	4.82	8.37	10.76
Alongshore Current (m/s)	M	−0.66	−0.47	−0.23	0.0	0.26	0.52	0.66
	LT	−0.56	−0.43	−0.24	−0.03	0.19	0.45	0.63
Cross-shore Current (m/s)	M	−0.12	−0.08	−0.03	0.01	0.05	0.11	0.16
	LT	−0.15	−0.06	−0.01	0.01	0.04	0.08	0.14
Wave Height (m)	M	0.34	0.43	0.58	0.7	0.91	1.23	1.36
	LT	0.31	0.38	0.53	0.68	0.87	1.25	1.6
Wave Period (s)	M	3.59	3.95	4.7	5.31	6.07	7.37	8.68
	LT	3.4	3.7	4.4	5.0	5.8	7.3	8.9
Wave Direction (°)	M	81.42	87.15	106.96	129.76	149.9	176.9	198.23
	LT	75.07	84	101	122.8	151.3	180.1	204

cases, the wave orientation was from the southeast quadrant (Fig. 3h). The maximum observed wave height and period were 1.6 m and 10 s, respectively, while the average was 0.7 m and 5.4 s, respectively.

During the observed period, the longitudinal and transverse wind speeds exceeded ±10 m/s for 8 % and 2 % of the time, respectively. There is also a higher frequency of negative longitudinal wind speeds and positive transverse wind speeds compared to the historical series. Approximately 59 % of the observed wind speed data were negative for longitudinal winds, while in the historical series it was about 30 %. On the other hand, observed transverse wind speeds were negative 34 % of the time, while in the historical series it was 43 % of the time. The greatest differences occurred at the 5th and 1st percentiles, where the transverse wind speed in the historical series reached −8 m/s and −11 m/s, while in the observed period, the transverse wind speeds were −3.8 m/s and −6.3 m/s, respectively (Fig. 4 and Table 1).

The observed longitudinal current speed, although not showing significant average trends, exceeded 0.5 m/s for 6 % of the time and −0.5 m/s for 4 % of the time. The histograms estimate also demonstrate this slight tendency of positive velocities (>0.5 m/s). There are no major variations between the observed and historical data, with a maximum difference of 0.1 m/s for the 1st percentile. The observed transverse current speed did not show significant average trends, and moreover, the variations of percentiles between the observed and historical data were less than 0.05 m/s. The greatest differences occurred at the 1st or 99th percentile, where historical transverse current speeds could be > 0.5 m/s, while the observed transverse current speeds were around 0.2 m/s.

The observed significant wave height exceeded 1 m for 20 % of the time and was less than 0.5 m for 12 % of the time. Duration curve shows that the greatest differences between observed and historical data occur after the 1st percentile. The predominant observed wave direction is from the E-SE quadrant, with a median of 130° degrees, while for the historical series, the predominant wave direction is from the E-SE quadrant, with a median of 123° degrees. There is a difference of about 6° degrees between the percentiles of the observed and historical wave directions.

Fig. 5 presents the climatology of the hydrodynamic parameters recorded by the monitoring buoys in terms of monthly frequency distributions, represented by the median and the range of percentiles 1–99, 5–95, and 25–75 %. The results from the monitoring period of the present study (Table 1) are indicated as a red bar for the month of October, with the indication of various percentiles. Overall, the hydrodynamic conditions observed in the experiment reasonably captured the expected variability throughout the year, especially for the longitudinal component of the current (Fig. 5a), and to a lesser extent for the transverse components (Fig. 5b), although for the latter only in April are there more significant occurrences of currents towards the coast. The lowest climatological representativeness occurred with the significant wave height, for percentiles above 5 %, especially when compared to the months of February, April, and July. The representativeness of the wave direction (Fig. 5d) and period (Fig. 5e) parameters was quite satisfactory, with only the months of May and June presenting differentiated extreme situations.

Fig. 6 shows the result of the validation of the vertical SSC profiles generated by the Rouse theory, summarized in Table 2. Out of the total of 1765 profiles recorded during the study period, 55 % were considered valid, 39 % were rejected by the shear stress limit criterion, and 5 % were rejected by the positive mean SSC gradient criterion, considering the hierarchical removal of the total profiles. This means, the first criteria selects the profiles when the environmental conditions are not favorable for sediment mobilization (low bed shear stress). The second criteria selects the profiles when the Rouse Theory does not apply, even under energetic conditions. Considering the overlap of criteria, out of the total profiles rejected by the shear stress criterion, 40 % also had a positive mean SSC gradient. And considering the total profiles rejected by the positive mean SSC gradient criterion (370 profiles), 76 % also had shear stress below the limit value.

The time series of the bottom shear stresses (by currents, τ_c, waves, τ_w, and combined current + waves, τ_{cwm} and τ_{cwmax}), turbulent diffusion coefficient (ε_s), RMSPE, suspended particle size (d_s), and particle terminal velocity (w_s) are presented in Fig. 7, with their respective frequency distributions. The statistical parameters of these time series are summarized in Table 3.

The bottom shear stress by currents and waves presented a relatively similar values, with the ones due to currents being slightly more pronounced. However, the combined effect (τ_{cwm} and τ_{cwmax}), the effect of waves appears to have a minor role. The turbulent diffusion coefficient (ε_s) followed the oscillations of the bottom shear stress, with a mean value of 0.92 cm^2/s and a maximum of 1.77 cm^2/s. The RMSPE of the SSC_{cwmax} estimates in relation to SSC_{ABS} showed a median of 5 %; furthermore, the highest RMSPE values showed a trend with the peaks of τ_{cwmax}, while the lowest values were seen when τ_{cwmax} is less than 0.1–0.2 Pa, approximately (Fig. 7c). Estimates of the mean sediment size (d_s) had a median of 25 μm and a maximum value of 50 μm; the median particle terminal velocity (w_s) was 0.15 cm/s, with a maximum value of 0.7 cm/s.

Fig. 8 presents the time series of mean water column SSC obtained from the inversion of ADCP data and from the Rouse model, along with the respective Hovmöller diagrams showing SSC distributions over time and in the water column. For the most part, the equivalence of SSC values was excellent, with low RMSPE values. However, about 55 % of the SSC_{ABS} time series was used in the Rouse model, while the rest of the series showed higher concentrations near the surface than at the bottom, making it impossible to apply the Rouse model.

The median of the SSC_{ABS} series near the bottom (0.9 m) showed concentrations of 0.31 kg/m^3, and near the surface (14.4 m),

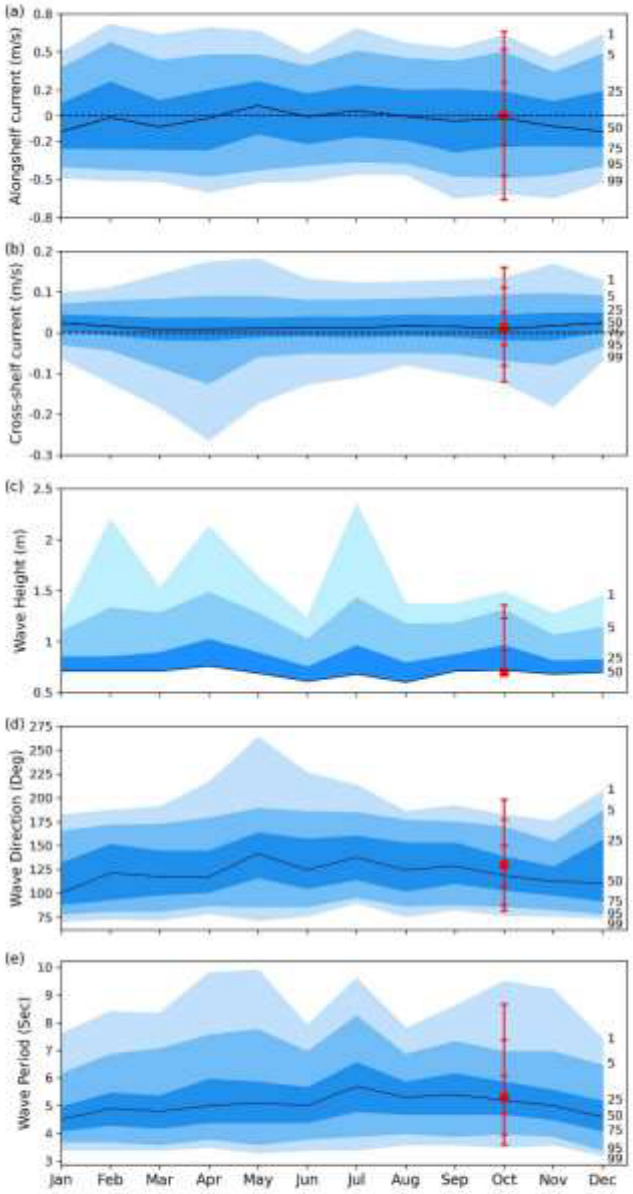


Fig. 5. Monthly climatology of the alongshore (a) and cross-shore (b) components of the mean water column current, and of the wave height (c), direction (d), and period (e). The median value is represented by the black line, and the shades of blue represent the range of percentiles 1–99, 5–95, and 25–75 %. The vertical red line in the month of October represents the data observed during mooring.

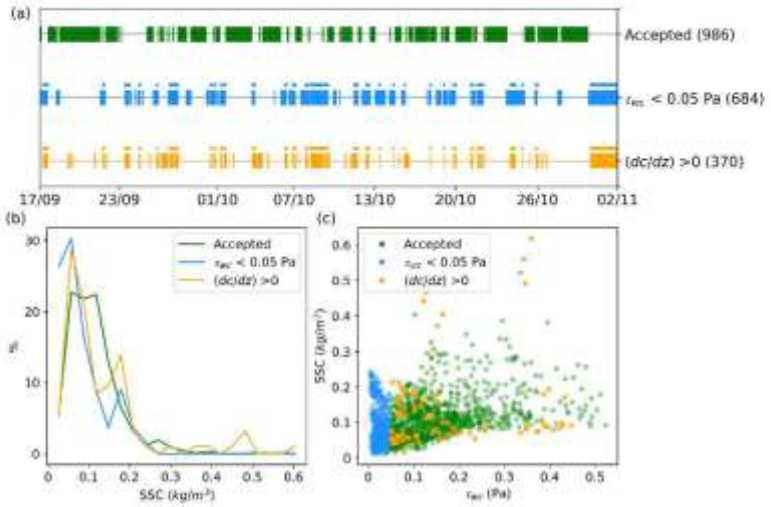


Fig. 6. (a) Temporal indication of accepted and rejected vertical SSC profiles from the validation procedure. The profiles for each criterion are presented with vertical bars, and the points on the bars for the exclusion criteria indicate the overlap with the other criterion. (b) Frequency distributions of mean SSC for each selection category, and (c) relationship between shear stress and mean SSC for each selection category.

Table 2
Summary of the validation results for vertical SSC profiles, including the total number of profiles and the remaining profiles after selection by the criteria of shear stress ($\tau_{wcr} < 0.05$) and positive vertical mean SSC gradient ($\left\langle \frac{dC(z)}{dz} \right\rangle > 0$), also indicating the percentage, mean, and maximum SSC for each subset (SSC and C(z) are in kg/m³ and τ_{wcr} is in Pa).

Condition	#	%	$\overline{SSC}$ (kg/m³)	SSC_{max} (kg/m³)
Total	1765			
$\tau_{wcr} < 0.05$	684	39	0.22	0.46
$\left\langle \frac{dC(z)}{dz} \right\rangle > 0$	95	5	0.3	0.85
Validated	986	55	0.27	0.8

concentrations of 0.15 kg/m³. At some moments, SSC_{ABS} measurements showed higher concentrations in the upper layers compared to the bottom, with maximum differences of up to 0.42 kg/m³ on 01/11. On the other hand, the maximum difference between the bottom and the surface was up to 0.73 kg/m³ on 03/10.

5. Discussion

Rivers are the main sources of sediment for continental shelves (Swift, 1974). Coarse sediments (sands) will be deposited near the sources and become involved in processes related to coastal dynamics, whereas fine sediments (muds) will be transported in suspension and their dispersion will be influenced by factors controlling shelf hydrodynamics (density gradients, wind and tidal currents, and waves) (Swift et al., 1991; Walsh and Nittrouer, 2009). Once released onto the shelf, fine sediments enter a cycle of deposition/erosion/transport depending on the momentary environmental conditions (Wiseman and Garvine, 1995). Thus, although the sediment source is initially rivers, the presence of suspended sediments in the water column at a given location can be interpreted as either horizontal advective processes (transport) or exchange processes with the seafloor (deposition/erosion), with temporal variability ranging from hours to days (Traykovski et al., 2000), which is the scenario captured in our observations.

Our results demonstrated that the use of the inversion method of ABS to estimate the vertical distribution of the SSC, in conjunction with and the application of Rouse theory, are valuable tools for evaluating sediment characteristics and/or examining vertical SSC trends in coastal environments or continental shelves (Lynch et al., 1994; Lee et al., 2002; Shi and Zhou, 2004; Yuan et al., 2008; Liu et al., 2014; Al-Ragum et al., 2014). Rouse theory assumes that vertical SSC profiles are in equilibrium between downward settling flux and upward turbulent diffusion flux, resulting in profiles with an exponential increase in SSC towards the bottom. However, observed SSC profiles can exhibit various shapes (Liu et al., 2014), in situations where the estimated Rouse profile does not reflect the observed profile. We observed profiles where SSC where higher in the upper layers than near the bottom. These situations indicate that the main sediments source for the water column at the position of observation is not the bottom: it could be due to horizontal advection or aerial deposition, and Rouse theory does not apply. The present case, the vertical SSC distribution agreed with the Rouse theory in most of the time when the conditions were energetic enough to mobilize sediments. This supports the idea that the main sediment source for the water column is the seabed. The role of horizontal advection is secondary, even though the study area is relatively close (~10 km) to the mouth of Patos Lagoon and potentially influenced by it (Marques et al., 2010).

A key parameter to apply the Rouse theory is the vertical turbulent diffusion of suspended sediments, which results from the interaction between the fluid and the bottom, and is scaled based on the bottom shear stress. We used the approach proposed by Soulsby and Clarke (2005), to obtain the bottom shear stress, which allowed us to compute the combined effects of waves and currents, over rough or smooth beds. It employs an empirical approach based on the quadratic addition of shear stresses from waves and currents to estimate $\tau_{max,c}$, also accounting for the directional difference between flow and wave action to determine $\tau_{max,cw}$. On the other hand, the method of Grant and Madsen (1979) models the nonlinear interactions between waves and currents based on the fundamental laws of fluid mechanics, including the concept of

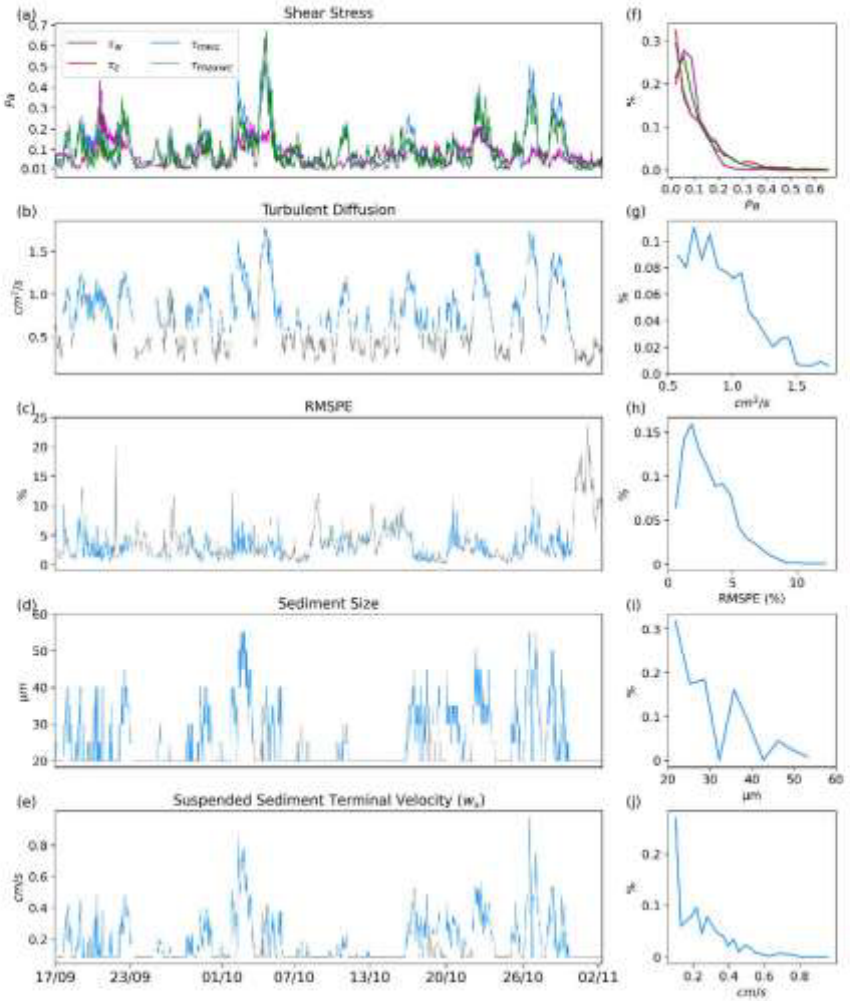


Fig. 7. The left-hand side graphs display the time series of (a) bottom shear stress produced by waves (fuchsia), currents (red), mean wave-current combined (blue) and maximum wave-current combined (green), (b) turbulent diffusion coefficient, (c) root mean square percentage error - RMSPE, (d) sediment size, and (e) particle terminal velocity in suspension. On the right-hand side of each panel, the respective (f, g, h, i, and j) frequency distributions for each parameter from the first column are presented. Valid profile data are shown in blue, and discarded profiles are shown in gray. The frequency distributions are only for valid data.

apparent roughness and considering the angle between the flow and the wave propagation direction. Finally, Mythang and Hansen (1997) employs a probabilistic approach based on the Weibull distribution, where the directional difference between flow and wave action is indirectly accounted for. Long-term time series analyses are ideal for this approach as they include the natural variability of waves and currents. One way to determine the best stress value to use is simply to identify which one best explains the SSC near the bed. In this case, the coefficient of determination (r^2) of SSC with τ_{cmax} and τ_{mcmax} were 0.82 and 0.69, respectively. In Fig. 7a, it can be observed the low contribution of τ_w to the estimates of τ_{cmax} and τ_{mcmax} even with relatively high values of τ_w compared to τ_c, the increment was low and without significant variations between τ_c, τ_{cmax}, and τ_{mcmax}. The greatest variations occurred between the maximum values of τ_c and τ_{mcmax}, 0.64 Pa and 0.53 Pa, respectively.

During the observation period, there was a single short-lived occurrence (1 h on October 27th) where the vertical profile showed indications of disqualification due to a positive vertical gradient, despite energetic environmental conditions ($\tau_{cmax} = 0.38$ Pa). This situation was recorded in only 1 % of the records. During this period, the SSC was -0.9 kg/m^3 at the surface layer and -0.72 kg/m^3 near the bed. The

Table 3
Mean values, standard deviation (σ), and percentiles of shear stress data, turbulent diffusion, RMSPE, sediment size, and particle terminal velocity.

Parameter	Mean	σ	1st	5th	25th	50th	75th	95th	99th
Max Shear-stress wc (Pa)	0.1	0.09	0.01	0.02	0.04	0.07	0.13	0.26	0.44
Mean Shear-stress wc (Pa)	0.1	0.1	0.01	0.01	0.03	0.08	0.15	0.32	0.45
Shear-stress current (Pa)	0.1	0.1	0.01	0.01	0.03	0.07	0.14	0.31	0.44
Shear-stress wave (Pa)	0.08	0.05	0.01	0.02	0.04	0.07	0.11	0.18	0.23
Turbulent diffusion (m^2/s)	0.92	0.26	0.36	0.58	0.72	0.88	1.07	1.43	1.68
RMSPE (%)	5.5	2.8	1.32	1.94	3.3	5.02	7.38	10.69	13.01
Sediment size (μm)	25	6.3	20.0	20.0	20.0	25.0	30.0	40.0	45.0
Settling velocity (cm/s)	0.18	0.11	0.09	0.09	0.09	0.15	0.23	0.38	0.52

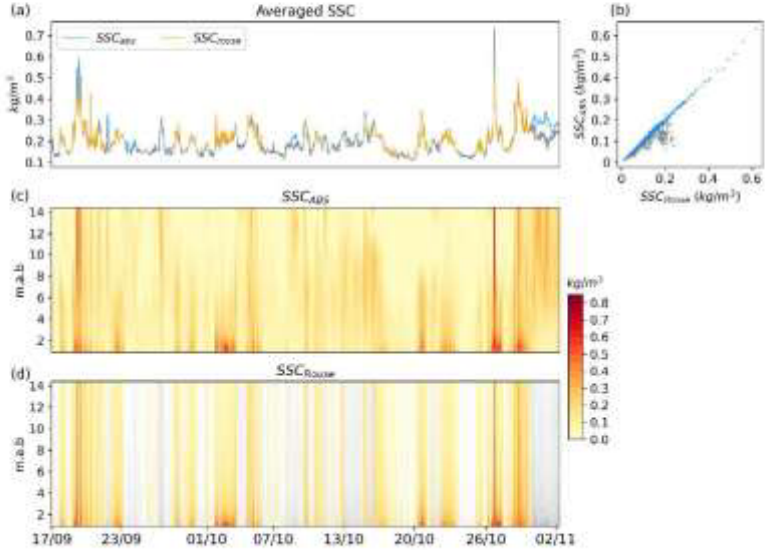


Fig. 8. (a) Time series of mean water column SSC obtained from ABS and Rouse model, and (b) the respective relationship between them. (c) and (d) Hovmöller diagrams for SSC distributions derived from ABS and Rouse, respectively. The gray areas in (d) indicates the discarded profiles.

wind was blowing to the north (velocity = 12 m/s), and the longitudinal component of the current was also to the north (velocity = 0.5 m/s). These conditions, even if for a brief moment, indicate that the input of SSC by horizontal advection was as relevant as by vertical diffusion (Fig. 8c). It is interesting to note that this event indicated transport parallel to the coast, rather than directly associated with an input from the Patos Lagoon plume.

During the period between October 30th and November 2nd, a period was recorded where the SSC_{ABS} near the surface was higher than SSC_{ABS} near the bed, with relatively low bottom shear stress values (−0.02 Pa), an E/NE wind direction (164°), average alongshelf and cross-shelf wind speeds of −0.8 m/s and 4.6 m/s, respectively, and depth averaged alongshelf current speed of 0.06 m/s. As it will be detailed in the next section, these conditions favor the cross-shelf circulation, with the upper layer moving offshore, along with the ebb flow from the Patos Lagoon (Moller et al., 2001), leading to the formation of a sediment-rich buoyancy plume (Marques et al., 2010). These conditions suggest that during this particular period the presence of higher SSC at the upper layer may be explained in terms of horizontal advection (Fig. 8c). In the study by Yuan et al. (2008) in Jiaozhou Bay, China, it was reported that during periods of weak currents (<0.15 m/s), the Rouse model used (Perlin et al., 2005) was not satisfactory and thus disregarded.

Although the data recording period was relatively short (45 days) and covered only the spring period, the estimates generated by the Rouse theory showed good temporal representativeness, as the frequency distributions of oceanographic parameters (waves & currents) were similar to those of long-term series, or even when compared to monthly climatology. Only extreme events where the frequency distribution is >99 % or <1 % were not observed. The greatest discrepancy concerning environmental conditions is related to wave height. However, as seen earlier, the contribution of τ_w to the estimates of τ_{max} was low, meaning that even under extreme wave conditions, the estimates of τ_{max} will not change significantly compared to the maximum values obtained in this study.

Even though it is relatively close to the mouth of Patos Lagoon, sediment dynamics and transport were dominated by processes of exchange with the seafloor. This allows inferring that most of the shelf in the depth range between 15 and 25 m responds similarly. As one approaches the coastline, other mechanisms start to influence the fluid force, such as wave action under storm or low-energy conditions, thus a model that combines diffusion-advection, or solely vertical advection, may provide more realistic estimates (Lee et al., 2002). The buoyant plume coming from the estuary mouth and interacting with shelf currents can be another source of sediment by horizontal advection (Swift

et al., 1991). Therefore, the estimates obtained in this study by the Rouse and Soulsby theories cannot be extrapolated to the region closer to the surf zone or the mouth of Patos Lagoon, as the input of SSC by advection becomes increasingly notable. For deeper regions, the estimates of τ_{max} and τ_{mean} will gradually decrease since the amount of turbulent energy generated by waves and/or currents diminishes gradually with distance from the seafloor. Additionally, the shelf region is dominated by the fluvial influence of the Rio de la Plata and Patos Lagoon, with different quantities and periods, and according to oceanographic conditions (Möller et al., 2001; Piola et al., 2008). Thus, at latitudes greater or lesser than the two estuary mouths, the input of suspended material by horizontal advection becomes less or more noticeable in the surface layers.

5.1. Consequences for sediment transport

Depending on the wind direction and coastline configuration, resultant currents may cause either stacking (water level rise) or subduction (water level decrease) near the coastline, creating a positive or negative pressure gradient favoring transport towards the sea or shore, near the seafloor (Niedoroda et al., 1989; Swift et al., 1985; Austin and Lentz, 2002). Three periods of data records were selected to assess these more energetic hydrodynamic conditions, which exhibited the highest bottom shear stress values, with τ_{max} above 0.2 Pa, and mean longitudinal current velocities above 0.5 m/s (Table 4). Period 1 (October 2nd and 3rd) showed the highest mean values of wave height and sea level oscillation. Period 2 (October 4th and 5th) displayed the highest mean and maximum longitudinal current velocities, and the mean and maximum τ_{mean} were higher compared to periods 1 and 3. Period 3 (October 27th and 28th) exhibited the lowest mean values of sea level oscillation and wave height, and a mean and maximum τ_{mean} similar to period 1 (Table 4).

In period 1, when the wind is coming from the south, at around 9 m/s, the longitudinal current flows northward, and the transverse current in the upper layer moves towards the coast, while that in the lower layer moves towards the open ocean (Fig. 9c). In period 2, when the wind originates from the northeast, at about 10 m/s, the longitudinal current flows southward, and the transverse current separates, with the upper layer flow heading towards the open ocean and the lower layer towards the coast (Fig. 9d). In period 3, when the wind direction is south, at around 12 m/s, the longitudinal current flows northward, and the transverse current in the upper layer moves towards the coast, while that in the lower layer moves towards the open ocean (Fig. 9e).

It was observed that near-bed flow (at 0.9 m depth) transports more suspended sediment material when the flow direction is northward; in periods 1 and 3, the median SSC_{ABS} near the bed was higher compared to period 2 when the flow had a southward direction (Fig. 10c–h-m). Even when the mean τ_{mean} is similar in periods 2 and 3, the mean integrated SSC_{ABS} depth-wise in period 2 was 0.29 kg/m^3, whereas in period 3, it was 0.34 kg/m3. The low values of w_s and d_s in period 2 may be related to the concentration and τ_{mean}; even with similar turbulence forces, at low concentrations, the collision rate is low, preventing the formation of larger flocs, while at high concentrations, flocculation occurs due to the high collision rate. However, this shear stress force promoting flocculation can also be responsible for breaking the flocs, as turbulence forces increase, flocs with lower binding force break apart. According to laboratory studies by Manning et al. (2010), for a mixture of 75 % mud and 25 % sand, the τ required for the initiation of micro-floc breakage is 0.6 Pa, and for macro-flocs, it is 0.35 Pa, with floc breakage facilitated at higher concentrations (5 g/L).

5.2. Approach limitations

The Rouse model assumes equilibrium between settling velocity and turbulent diffusion, and does not consider water stratification, which is a common feature on shelves and can affect considerably the vertical turbulent diffusion (Rippeth, 2005). Low-energy conditions (no turbulent diffusion) and horizontal advection also limits its application, as indicated by the exclusion of 45 % of SSC_{mean} profiles. The threshold value of bottom shear stress to separate 'high' and 'low' energy conditions can vary in time and space, in response to the bottom rheological properties (Winterwerp and van Kesteren, 2004).

The validation of the parameters obtained from the best fit (suspended particle size and settling velocity) can be verified through direct observations; however, their representation remains limited. Particle size can be measured in situ using laser scattering devices (e.g., LISST by Sequoia https://www.sequoiasci.com) and could be moored together with the ADCP, though not without technical challenges related to fouling. Measuring particle settling velocity in coastal waters remains a major challenge. It can be done using a settling tube (Owen tube) or more intricate optical devices operating under calm sea conditions (Dyer et al., 1996).

The interaction between the currents and waves on the bottom shear stress, which ultimately will give the vertical turbulent diffusion, is a complicate matter based on methodological assumptions rather than purely physical processes, differing from each author (Grant and Madsen, 1979; Myrhaug and Hansen, 1997; Soulsby and Clarke, 2005). The SSC_{mean} estimates obtained from acoustic backscatter SSC_{ABS} might be limited to regions with relatively high SSC (>10 mg/L), and it will depend on how satisfactory is the calibration achieved. At low concentrations, estimated SSC_{ABS} may have higher error due to echo attenuation or the equipment limitation to detect smaller particles in clear waters. Furthermore, the empirical relationship used to convert acoustic backscatter to SSC may not fully account for flocculation dynamics or acoustic scattering properties.

6. Conclusions

The approach of coupling the SSC profiles estimated from ADCP records with SSC profiles predicted by Rouse theory provided valuable insights on the continental shelf off the state of Rio Grande do Sul in Brazil. The results indicate that when the environmental conditions are energetic, sediment resuspension and transport were primarily controlled by bottom shear stress generated mainly by currents. The Rouse profile explain satisfactorily the observations, what indicates the balance between settling velocity and turbulent diffusion. Although horizontal advection played a secondary role under most conditions, it became relevant during periods of weak currents and low bottom shear stress.

Periods of high-energy conditions revealed distinct transport

Table 4
Oceanographic parameters for periods 1, 2, and 3 as indicated in Fig. 10. WL represents the sea level oscillation in meters. U and V denote the mean or maximum longitudinal and transverse velocities, respectively (m/s). τ represents the mean or maximum bottom shear stress produced by waves and currents (Pa). w_s is the terminal particle velocity (cm/s), and d_s is the mean particle size (μm).

	WL (m)	U_{mean} (m/s)	U_{max} (m/s)	V_{mean} (m/s)	V_{max} (m/s)	τ_{mean} (Pa)	τ_{max} (Pa)	$Wave_{height}$ (m)	$Wave_{dir}$ (deg)	w_s (cm/s)	d_s (μm)
1	0.44	0.5	0.72	0.03	0.08	0.24	0.44	1.31	145	0.5	41
2	−0.3	−0.55	−0.74	0.09	0.15	0.33	0.52	1.09	114	0.24	29
3	0.13	0.5	0.75	0.04	0.19	0.28	0.5	0.9	155	0.41	38

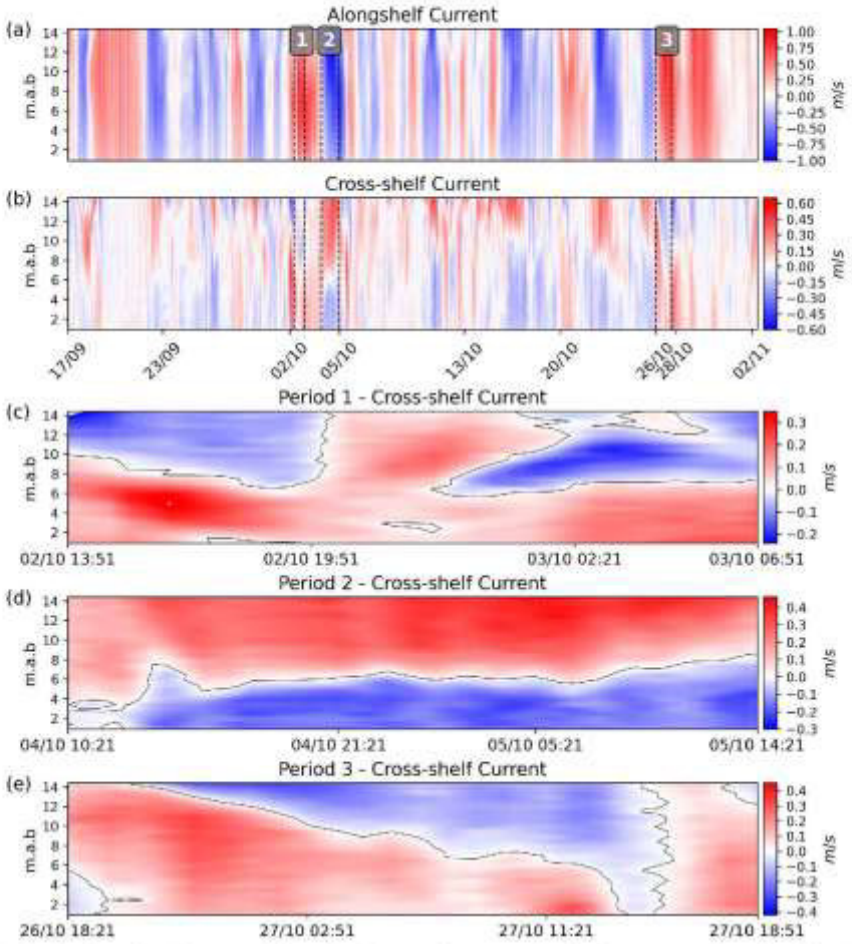


Fig. 9. Hovmöller plot of longitudinal and transversal velocity along the water column. In (a), red colors indicate currents with northward direction, and blue indicates southward direction. In (b) and (c), red colors indicate currents directed towards the coast, and blue indicates currents directed towards the open ocean.

patterns associated with upwelling and downwelling. When the longitudinal current was northward, bottom SSC was higher, enhancing sediment transport along the seabed. Conversely, southward currents corresponded to lower bottom SSC and a more vertically uniform distribution, suggesting reduced resuspension and greater mixing throughout the water column (Fig. 10). These findings align with downwelling conditions enhancing near-bed transport, while upwelling conditions favor a more homogeneous SSC profile.

The study also provided insights into sediment characteristics. The median grain size was 25 μm, with a maximum of 50 μm, and the median settling velocity was 0.15 cm/s, reaching up to 0.7 cm/s. These values are consistent with previously reported sediment characteristics for coastal waters and reinforce the validity of the Rouse-based estimates.

The coupling of ADCP-derived SSC estimates and Rouse theory proved to be an effective framework for assessing suspended sediment dynamics in the inner shelf, providing a valuable tool for future studies.

CRediT authorship contribution statement

Guilherme O. Cruz: Writing – original draft, Visualization, Validation, Software, Methodology, Investigation, Formal analysis. **Carlos A. F. Schettini:** Writing – review & editing, Supervision, Resources, Investigation, Funding acquisition, Conceptualization.

Declaration of competing interest

I, in behalf of my co-author, declare that there is no conflict of interest of any kind regarding the manuscript entitled "The dynamics of the inner-shelf suspended sediments based on ADCP records and Rouse theory".

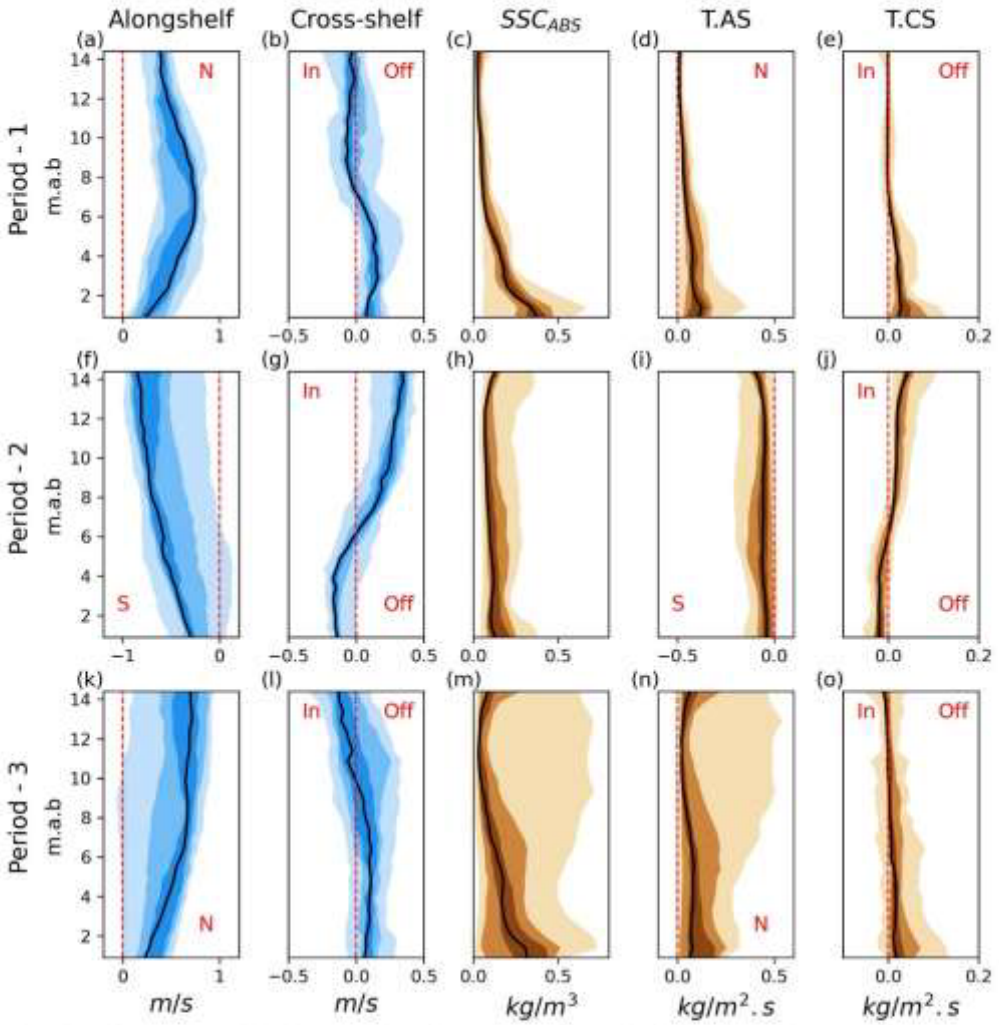


Fig. 10. Plots (a, b, c, d, e) show the calculated duration curve for period 1, plots (f, g, h, i, j) for period 2, and plots (k, l, m, n, o) for period 3. In black, the median, and shades of brown and blue indicate the percentiles 1 %, 20 %, 35 %, 65 %, 80 %, and 99 %. T.AS represents alongshelf sediment transport and T.CS represents cross-shelf sediment transport.

This article does not contain any studies with human or animal subjects.

Acknowledgements

We would like to express our gratitude to all the individuals who provided assistance during the intensive field experiment. We are also thankful for the support from the Office of Naval Research (ONR Grant N62909-19-1-2145), Brazilian National Science Council (CNPq, #316037/2021-4), through INCT-COI and PELD Estuário da Patos Lagoon. To the Coordenação de Aperfeiçoamento de Pessoal de Nível Superior – Brasil (CAPES) for GC's scholarship.

Data availability

Data will be made available on request.

References

Al Ani, S., Dyer, K.R., Huntley, D.A., 1991. Measurement of the influence of salinity on floc density and strength. Geo Mar. Lett. 11 (3–4), 154–158. https://doi.org/10.1007/BF02431002.

Al-Ragum, A., Monge-Ganuzas, M., Amos, C.L., Cuerreta, A., Townend, I., Manca, E., 2014. An evaluation of the Rouse theory for sand transport in the Oka estuary, Spain. Cont. Shelf Res. 39–50, 78. https://doi.org/10.1016/j.csr.2014.01.016.

Andrade Neto, J., Rigon, L., Toldo, E., Schettini, C., 2012. Descarga sólida em suspensão do sistema fluvial do Gasilho, RS, e sua variabilidade temporal. Pesqui. em Geociencias 39 (2), 161. https://doi.org/10.22456/1807-9806.39910.

Austin, A.J., Lentz, S.J., 2002. The inner shelf response to wind-driven upwelling and downwelling. J. Phys. Oceanogr. 32 (7), 2171–2193. https://doi.org/10.1175/1520-0485(2002)032<2171:TISRTW>2.0.CO;2.

Black, K.S., Tolhurst, T.J., Paterson, D.M., Hagerthey, S.E., 2002. Working with natural cohesive sediments. J. Hydraul. Eng. 128 (1), 2–8. https://doi.org/10.1061/(ASCE)0733-9429(2002)128:1(2).

Boudreau, B.P., Hill, P.S., 2020. Rouse revisited: the bottom boundary condition for suspended sediment profiles. Mar. Geol. 419, 106066. https://doi.org/10.1016/j.margeo.2019.106066.

Calliari, L.J., Speranski, N.S., Torronteguy, M., Oliveira, M.B., 2001. The mud banks of cassino beach, southern Brazil: characteristics, processes and effects. Source: J. Coast Res. 318–325. https://www.jstor.org/stable/25736298.

Calliari, L.J., Holland, K.T., Pereira, P.S., Guedes, R.M.C., Santo, R.E., 2007. The influence of mud on the inner shelf, shoreface, beach, and surf zone morphodynamics — cassino, southern Brazil. Coastal Sediments 1455–1465. https://doi.org/10.1061/40926(239)113.

Campos, E.J.D., Mukherjee, S., Pinto, A.R., de Carvalho, F.M.S., 2008. A note on a mineralogical analysis of the sediments associated with the Plata River and Patos Lagoon outflows. Cont. Shelf Res. 28 (13), 1687–1691. https://doi.org/10.1016/j.csr.2008.03.014.

Cerilio, R.O., Dillenburg, S.R., 2019. An ocean wind-wave climatology for the Southern Brazilian Shelf. Part II: variability in space and time. Dynam. Atmos. Oceans 88, 101103. https://doi.org/10.1016/j.dynatmoce.2019.101103.

Choi, W., 2009. Nonlinear surface waves interacting with a linear shear current 80 (1), 29–36. https://doi.org/10.1016/j.matcom.2009.06.021.

Corrêa, I., Westerteider, J., Calliari, L., Toldo, E., Carlos Hanes, J., Buriolli, R., 2013. Plataforma Continental Do Rio Grande Do Sul. PGGM – RS, pp. 74–158.

Costa, R.L., Möller, O., 2011. Estudo da estrutura e da variabilidade das correntes na área da plataforma interna ao largo de Rio Grande (RS, Brasil), no sudoeste do Atlântico Sul, durante a primavera-verão de 2006-2007. Revista de Gestão Costeira Integrada 11 (3), 273–281. https://doi.org/10.5894/rgci256.

Cruzeiro, M.A., Schettini, C.A., 2010. Estudo da dinâmica dos sedimentos em suspensão do estuário do Rio Araranguá (SC): possíveis efeitos da dragagem ácida da atividade de mineração de carvão. Geociencias, UNESP, SP – BR 29 (2), 251–266.

Cuchiara, D., Fernandes, E., Strauch, J.C., Winterwerp, J., Calliari, L., 2009. Determination of the wave climate for the southern Brazilian shelf. Cont. Shelf Res. 29 (3), 545–555. https://doi.org/10.1016/j.csr.2008.09.025.

Downing, J.P., Sternberg, R.W., Lister, C.R.B., 1981. New instrumentation for the investigation of sediment suspension processes in the shallow marine environment. Mar. Geol. 42, 19–34. https://doi.org/10.1016/0025-3227(81)90232-9.

Drake, C.L., Burk, C.A., 1974. Geological significance of continental margins: The Geology of Continental Margins, pp. 3–10. https://doi.org/10.1007/978-3-662-01141-6_1.

Dyer, K.J., Cornelisse, J., Dennaley, M.P., Fennessy, M.J., Jones, S.E., Kappenberg, J., McCave, I.H., Pejrup, M., Puls, W., Van Leussen, W., Wolfstein, K., 1996. A comparison of in situ techniques for estuarine floc settling velocity measurements. J. Sea Res. 36 (1–2), 15–29. https://doi.org/10.1016/S1385-1101(96)90706-3.

Dyer, K.R., Manning, A.J., 1999. Observation of the size, settling velocity and effective density of flocs, and their fractal dimensions. J. Sea Res. 41 (1–2), 87–95. https://doi.org/10.1016/S1385-1101(98)00036-7.

Eisma, D., 1986. Flocculation and de-flocculation of suspended matter in estuaries. Netherlandse J. Sea Res. 20 (2–3), 183–199. https://doi.org/10.1016/0077-7579(86)90041-4.

Fachin, S., 1998. Caracterização do perfil de equilíbrio da antepraia ao norte do Rio Grande do Sul. Porto Alegre, UFRGS, p. 88. Master Thesis.

Gartner, J.W., 2004. Estimating suspended solids concentrations from backscatter intensity measured by acoustic Doppler current profiler in San Francisco Bay, California. Mar. Geol. 211 (3–4), 169–187. https://doi.org/10.1016/j.margeo.2004.07.003.

Grant, D.W., 1979. Combined wave and current interaction with a rough bottom. J. Geophys. Res. 84 (C4), 1797–1808. https://doi.org/10.1029/JC084iC04p01797.

Guillén, J., Bourrin, F., Palanques, A., Durrieu de Madron, X., Puig, P., Buscail, R., 2006. Sediment dynamics during wet and dry storm events on the Têt inner shelf (SW Gulf of Lions). Mar. Geol. 234 (1–4), 129–142. https://doi.org/10.1016/j.margeo.2006.09.016.

Hartmann, C., Calliari, L., Möller, O., 1980. Material em suspensão no estuário da Lagoa dos Patos (RS) Parte I - Observações preliminares - Abril/1979 a Março/1980. Sociedade & Natureza 2 (4). https://doi.org/10.14393/SN-v2-1990-60757.

Ingvova, M.V., Mikhailov, V.N., 2018. Long-term variations of water runoff and suspended sediment yield in the parana and Uruguay rivers. Water Resour. 45 (6), 846–860. https://doi.org/10.1134/S0097807818060088.

Lee, G., Friedrichs, C.T., Vincente, C.E., 2002. Examination of diffusion versus advection dominated sediment suspension on the inner shelf under storm and swell conditions, Duck, North Carolina. J. Geophys. Res.: Oceans 107 (C7). https://doi.org/10.1029/2001JC000918.

Liu, J.H., Yang, S.L., Zhu, Q., Zhang, J., 2014. Controls on suspended sediment concentration profiles in the shallow and turbid Yangtze Estuary. Cont. Shelf Res. 96–108, 90. https://doi.org/10.1016/j.csr.2014.01.021.

Lukawska-Matuszewska, K., Bradtmiller, O., Bolałek, A., Rzepa, G., Manecki, M., Bolałek, J., 2022. Biogeochemical and mineralogical effects of Fe-P-S dynamics in sediments of continental shelf sea: impact of salinity, oxygen conditions, and catchment area characteristics. Sci. Total Environ. 807, 151035. https://doi.org/10.1016/j.scitotenv.2021.151035.

Lynch, J.F., Irish, J.D., Sherwood, C.R., Agrawal, Y.C., 1994. Determining suspended sediment particle size information from acoustical and optical backscatter measurements. Cont. Shelf Res. 14 (10–11), 1139–1165. https://doi.org/10.1016/0278-4343(94)90002-9.

Malarkey, J., Davies, A., 2012. A simple procedure for calculating the mean and maximum bed stress under wave and current conditions for cough turbulent flow based on Soulsby and Clarke's (2005) method. Comput. Geosci. 101–107, 43. https://doi.org/10.1016/j.cageo.2012.02.026.

Manning, A.J., Baugh, J.V., Spearman, J.R., Whitehouse, R.J.S., 2010. Flocculation settling characteristics of mud: sand mixtures. Ocean Dyn. 60 (2), 237–253. https://doi.org/10.1007/s10236-009-0251-9.

Marmin, S., Levoy, F., Dumas, J.C., Samson, S., Tournier, F., Lavaure, A.G., Dubreuil-Brunaud, C., Thouraude, C., 2016. An experimental study on dredge spoil of estuarine sediments in the bay of seine (France): a morphosedimentary assessment. Cont. Shelf Res. 116, 89–102. https://doi.org/10.1016/j.csr.2016.01.010.

Marques, W.C., Möller, O.O., 2008. Variabilidade Temporal em Longo Período da Descarga Fluvial e Níveis de Água da Patos Lagoon, Rio Grande do Sul, Brasil. Revista Brasileira de Recursos Hídricos 13 (3), 155–163. https://doi.org/10.21168/rbrh.v13n3.p155-163.

Marques, W.C., Fernandes, E.H.L., Monteiro, I.O., Möller Jr, O.O., Malhereck, A., 2010. Dynamics of the Patos Lagoon coastal plume and its contribution to the deposition pattern of the southern Brazilian inner shelf. J. Geophys. Res. https://doi.org/10.1029/2010JC006196.

Martins, L.R., Martins, I.R., Urien, C.M., 2003. Aspectos Sedimentares da Plataforma Continental na Área de Influência do Rio de La Plata. Gravel 66–80.

Moller, O.O., Castaing, P., Salomon, J.-C., Lazure, P., 2001. The influence of local and non-local forcing effects on the subtidal circulation of Patos lagoon. Estuaries 24 (2), 297. https://doi.org/10.2307/1352953.

Moreira, D., Simionato, C.G., Gohin, F., Cayocca, F., Luz Clara Tejedor, M., 2013. Suspended matter mean distribution and seasonal cycle in the Río de La Plata estuary and the adjacent shelf from ocean color satellite (MODIS) and in-situ observations. Cont. Shelf Res. 68, 51–66. https://doi.org/10.1016/j.csr.2013.08.013.

Motta, V., 1963. Análise e previsão das alturas de ondas em Tramandaí. IPH. Instituto de Pesquisas Hidráulicas, p. 18.

Myrhaug, D., Holmes, H.E., 1997. Long-term distribution of seabed shear stresses beneath random waves. Coast. Eng. 31, 327–337. https://doi.org/10.1016/S0378-3839(97)00016-5, 1997.

Nieuwenda, A.W., Swift, D.J.P., Figueiredo, A.G., Reed and, G.L., 1989. Modeling shelf storm beds: controls of bed thickness and bedding sequence. In: Shelf Sandstones, Shelf Depositional Sequences and Petroleum Accumulation: a Symposium, pp. 15–39. https://doi.org/10.5724/gcs.89.07.0015.

Palanques, A., Diaz, J.I., 1994. Anthropogenic heavy metal pollution in the sediments of the Barcelona continental shelf (Northwestern Mediterranean). Mar. Environ. Res. 38 (1), 17–31. https://doi.org/10.1016/0141-1136(94)90043-6.

Palma, E., Matano, R., Piola, A., 2008. A numerical study of the Southwestern Atlantic Shelf circulation: stratified ocean response to local and offshore forcing. J. Geophys. Res. 113 (c11). https://doi.org/10.1029/2007JC004720.

Park, H.-R., Lee, G., 2016. Evaluation of ADCP backscatter inversion to suspended sediment concentration in estuarine environments. Ocean Sci. J. 51 (1), 109–125. https://doi.org/10.1007/s12601-016-0010-3.

Pereira, P.S., Calliari, L.J., Holman, R., Holland, K.T., Guedes, R.M.C., Amorim, C.K., Cavalcanti, F.G., 2011. Video and field observations of wave attenuation in a muddy surf zone. Mar. Geol. 279 (1–4), 210–221.

Perlin, A., Moum, J., Klymak, J., Levine, M., Boyd, T., Kosro, P., 2005. A modified law-of-the-wall applied to oceanic bottom boundary layers. J. Geophys. Res.: Oceans 110 (c10), 1–9. https://doi.org/10.1029/2004JC002710.

Piola, A.R., Romero, S.I., Zajaczkovski, U., 2008. Space-time variability of the Plata plume inferred from ocean color. Cont. Shelf Res. 28 (13), 1556–1567. https://doi.org/10.1016/j.csr.2007.03.013.

Reboita, M.S., Krusche, N., 2018. Normais Climatológicas Provisórias de 1991 a 2010 para Rio Grande, RS. Revista Brasileira de Meteorologia 33 (1), 165–179. https://doi.org/10.1590/0102-7786332010.

Ribeiro, R., Milewski, P., Nachbin, A., 2017. Flow structure beneath rotational water waves with stagnation points. J. Fluid Mech. 793–814, 812. https://doi.org/10.1017/jfm.2016.830.

Rippeth, T.P., 2005. Mixing in seasonally stratified shelf seas: a shifting paradigm. Philosophical Transactions of the Royal Society A. https://doi.org/10.1098/rsta.2005.1662.

Rouse, H., 1939. An analysis of sediment transportation in the light of fluid turbulence. California Institute of Technology, Sedimentation Division, p. 38. SCS-TP-25. https://authors.library.caltech.edu/records/0we13-rep55.

Sahin, C., Safak, I., Scheremet, A., Mehta, A., 2012. Observations on cohesive bed reworking by waves: atchafalaya shelf, Louisiana. J. Geophys. Res. v117 (c9). https://doi.org/10.1029/2011JC007821.

Salehi, M., Strom, K., 2012. Measurement of critical shear stress for mud mixtures in the San Jacinto estuary under different wave and current combinations. Cont. Shelf Res. 78–92, 47. https://doi.org/10.1016/j.csr.2012.07.004.

Santos, J.G., Garcia, C.A.E., 2023. Vertical structure and variability of currents on the southern Brazilian inner shelf at 32°S. Ocean and Coastal Res. 71, e23027.
Saraiva, J.M.B., Bedran, C., Cunrico, C., 2003. Monitoring of storm surges on camino beach, RS, Brazil. Proceedings of the brazilian symposium on sandy beaches: morphodynamics: ecology 35 (35), 323–331. https://www.jstor.org/stable/40928726.
Schettini, C.A.F., 2022. Dredging, mud, and dumping-kruger. Acq. Gestão do Mar 55 (Especial), 485–491. https://doi.org/10.22360/arman-r55(Especial.78213.
Schettini, C.A.F., Duarte Pereira, M., Siegle, E., de Miranda, L.B., Silva, M.P., 2013. Residual fluxes of suspended sediment in a tidally dominated tropical estuary. Cont. Shelf Res. 70, 27–35. https://doi.org/10.1016/j.csr.2013.03.006.
Schulkin, M., Marsh, H.W., 1962. Sound absorption in sea water. J. Acoust. Soc. Am. 34 (6), 864–863. https://doi.org/10.1121/1.1918213.
Shi, Z., Zhou, H.J., 2004. Controls on effective settling velocities of mud flocs in the Changjiang Estuary, China. Hydrol. Process. 18 (13). https://doi.org/10.1002/hyp.1500.
Simons, R., Myrhang, D., Thais, L., Chapalain, G., Holmedal, L., MacIver, R., 2000. Bed friction in combined wave-current flows. Coast. Eng. 216–226. https://doi.org/10.1061/40549(276)17.
Soulsby, R., 2006. Simplified calculations of wave orbital velocities (TR155). Sand Transport in Oscillatory Flow Project. HR Wallingford, 20p.
Soulsby, R.L., Clarke, S., 2005. Bed shear-stresses under combined waves and currents on smooth and rough beds (TR137). Estuary Processes Research Project. HR Wallingford. https://eprints.hrwallingford.com/508/.
Soulsby, R., Hamm, L., Klopman, G., Myrhang, D., Simons, R., Thomas, G., 1993. Wave-current interaction within and outside the bottom boundary layer. Coast. Eng. 21 (1–3), 41–69. https://doi.org/10.1016/0378-3839(93)90045-A.
Stech, J.L., Lorenzzetti, J., 1992. The response of the South Brazil Bight to the passage of wintertime cold fronts. J. Geophys. Res.: Oceans 97 (n6), 9507–9520. https://doi.org/10.1029/92JC00486.
Strauch, J.C., 1997. Aquisição e análise de dados de onda em Rio Grande. XII Simpósio Brasileiro de Recursos Hídricos 4, 295–301.
Swift, D.J.P., 1974. Continental shelf sedimentation. In: Burk, C.A., Drake, C.L. (Eds.), The Geology of Continental Margins. Springer, New York, pp. 117–135.
Swift, D.J.P., Hedercda, A.W., Vincent, C.E., Hopkins, T.S., 1985. Barrier island evolution, middle Atlantic shelf, U.S.A. Part I: Shoreface dynamics. Mar. Geol. 63 (1–4), 331–361. https://doi.org/10.1016/0025-3227(85)90089-1.
Swift, D.J.P., Oertel, G.F., Tillman, R.W., Thorne, J.A., 1991. Shelf Sand and Sandstone Bodies: Geometry, Facies and Sequence Stratigraphy. International Association of Sedimentologists, p. 644.
Toldo, E., Dillenburg, S., Dorcis, I., Almeida, L., Weschenfelder, J., Gruber, N., 2006. Sedimentação de Longo e Curto Período na Patos Lagoon, Sul do Brasil. Pesqui. em Geociencias 33 (2), 79. https://doi.org/10.22456/1807-9806.19936.
Traykovski, P., Geyer, W.R., Irish, J.D., Lynch, J.F., 2000. The role of wave-induced density-driven fluid mud flows for cross-shelf transport on the Eel River continental shelf. Cont. Shelf Res. 20 (16), 2113–2140.
Urick, R.J., 1975. Principles of Underwater Sound, second ed. McGraw-Hill.
Urien, C.M., 1972. Rio de la Plata Estuary Environments. Mem. Geol. Soc. Am. 133, 213–234. https://doi.org/10.1130/MEM133-p213.
Van Rijn, L.C., 2005. Note: Critical Bed Shear Stress for Mud And Rods - Literature Review of Critical Bed Shear Stresses for Mud Sand Mixtures.
Vaz, A.C., Möller jr, O.O., de Almeida, T.L., 2006. Análise quantitativa da descarga dos rios afluentes da Patos Lagoon. Atlantica 28 (1), 13–23. https://doi.org/10.5088/atlantica.v28i1.1724.
Walsh, J.P., Nittrouer, C.A., 2009. Understanding fine-grained river sediment dispersal on continental margins. Mar. Geol. 263, 34–45. 2009.
Wang, J., Ma, Q., Yan, S., 2018. A fully nonlinear numerical method for modeling wave-current interactions. J. Comput. Phys. 173–190, 369. https://doi.org/10.1016/j.jcp.2018.04.057.
Williams, A., Rex, M.J., 2001. Delineating fish habitat associations for spatially based management: an example from the south-eastern Australian continental shelf. Mar. Freshw. Res. 52 (4), 513. https://doi.org/10.1071/MF00017.
Winterwerp, J.C., van Kesteren, W.G.M., 2004. Introduction to the Physics of Cohesive Sediment Dynamics in the Marine Environment. Elsevier, 576p.
Wiseman, W.J., Garvine, R.W., 1995. Plumes and coastal currents near large river mouths. Estuaries 18, 509–517.
Yu, J., Jiang, J., Gong, D., Li, S., Xu, Y., 2011. Determining suspended sediment concentration and settling velocity from PC-ADP measurements in the Beibu Gulf, China. Chin. J. Oceanol. Limnol. 29 (3), 691–701. https://doi.org/10.1007/s00343-011-0164-x.
Yuan, Y., Wei, H., Zhao, L., Jiang, W., 2008. Observations of sediment resuspension and settling off the mouth of Jiaozhou Bay, Yellow Sea. Cont. Shelf Res. 28 (19), 2630–2643. https://doi.org/10.1016/j.csr.2008.04.005.
Zavialov, P., Möller, O., Campos, E., 2002. First direct measurements of currents on the continental shelf of Southern Brazil. Cont. Shelf Res. 22 (14), 1975–1986. https://doi.org/10.1016/S0278-4343(02)00049-3.